UAB
Universitat Autònoma de Barcelona

The statistics of stochastic exploration: functionals, resetting, and ergodicity

Rosa Flaquer-Galmés

ADVERTIMENT. L'accés als continguts d'aquesta tesi queda condicionat a l'acceptació de les condicions d'ús establertes per la següent llicència Creative Commons: https://creativecommons.org/licenses/?lang=ca

ADVERTENCIA. El acceso a los contenidos de esta tesis queda condicionado a la aceptación de las condiciones de uso establecidas por la siguiente licencia Creative Commons: https://creativecommons.org/licenses/?lang=es

WARNING. The access to the contents of this doctoral thesis it is limited to the acceptance of the use conditions set by the following Creative Commons license: https://creativecommons.org/licenses/?lang=en

PhD Thesis

The statistics of stochastic exploration: functionals, resetting, and ergodicity

Author:
Rosa Flaquer-Galmés

PhD Advisors:
Prof. Vicenç Méndez López
Prof. Daniel Campos Moreno

UAB
Universitat Autònoma de Barcelona

Department of Physics
08193 Bellaterra, Barcelona
2nd September 2026

"One has to be realistic about these things." — Logen Ninefingers, Joe Abercrombie.

ACKNOWLEDGMENTS

La realització de qualsevol projecte és el resultat de l'esforç combinat de moltes persones qui han fet que la seva culminació sigui possible. Algunes persones han tingut un rol actiu i tangible en el seu desenvolupament, mentre que n'hi ha d'altres qui, de manera silenciosa, tangencial, han fet la seva pròpia aportació, molts cops sense ser conscients, que també ha resultat inestimable perquè l'obra arribi a bon port. Aquesta secció és per agrair-vos-ho a totes de tot cor, intentaré no deixar-me a ningú, però sé que és impossible.

Vull començar per agrair a aquelles persones sense les quals, directament, aquesta tesi no existiria. Gràcies als meus dos supervisors, Vicenç i Daniel, per donar-me l'oportunitat de treballar en aquest projecte i confiar en mi per fer-lo. Gràcies per donar-me les vostres dues maneres d'entendre la recerca, i permetre'm aprendre d'elles. Vicenç, gràcies per guiar-me, ajudar-me i, en definitiva, ensenyar-me el que sé d'aquest fascinant camp de la ciència. Daniel, gràcies per donar-me perspectiva, empènyer-me a anar més enllà i a desenvolupar el meu parer personal. Gràcies als dos per les hores dedicades a què aquesta tesi tiri endavant. Gràcies també pel vostre suport en les iniciatives que he tingut, i en especial, en donar-me l'oportunitat de fer una estada al Wolfson Centre for Mathematical Biology, i gràcies a la gent d'allà per acollir-me, en especial a la Prof. Ruth Baker per mentoritzar-me mentre vaig ser-hi.

Seguidament, vull agrair a totes les persones del departament amb qui he compartit aquests anys i que sempre han tingut un moment quan els he tocat a la porta, o quan ens hem creuat pel passadís. Tal vegada no he treballat directament amb tots vosaltres, però podeu estar segurs que qualque cosa n'he après. Gràcies Albert, Javier, Juan i Xavi. Gràcies especialment al Javier Cristín, qui aquest darrer any de treball m'ha permès enfortir mancances i veure les coses des d'un altre punt de vista. Als companys i companyes de doctorat, als que ja heu acabat i els que heu passat aquests anys amb mi, és un plaer haver treballat al vostre costat. Axel, Lluc, Marta, Daniela i Almudena creieu-me quan us dic que el meu dia a dia ha estat millor perquè vosaltres hi éreu. Jordi, per totes les vegades que hem treballat braç a braç, gràcies.

Mo mare i mon pare, gràcies per confiar en mi, donar-me ales per volar i donar suport als meus projectes que, encara que no necessàriament són el que vosaltres haguéssiu triat, els he pogut tirar endavant perquè sé que me recolzau. Miquel, ets l'alegria de la casa, se'm fa estrany pensar que quan me'n vaig anar a estudiar tu no anaves a l'institut i ara podràs entendre el contingut d'aquestes pàgines, sort de tu algú de casa ho entendrà! Per descomptat, moltes gràcies a la meva família, la que

ho ha estat sempre i qui he triat, no sempre us he sabut explicar a què em dedicava *exactament*, entre les mans teniu una prova tangible de què alguna cosa estava fent.

Martí, tu et mereixes més que uns agraïments, no tinc paraules per expressar-te com som d'afortunada de tenir-te al meu costat. No és exagerar dir que aquesta tesi existeix en gran part gràcies a tu també. M'has recolzat quan més ho necessitava, has estat fort quan jo no podia, m'has cuidat quan m'ha fet falta, has fet que tornàs a riure quan plorava, has cregut en jo quan jo ja no ho feia. Gràcies.

Als meus amics i amigues, els de tota la vida, gràcies per fer-me sentir una més sempre que torn, malgrat estar lluny us seguesc sentint a prop. A les nines, Inés, Marina, Pascu i Sastre, gràcies per la paciència que teniu amb jo, som conscient que no sempre us he pogut dedicar tot el temps que m'agradaria i que us mereixeu, això és el que estava fent mentre no ens veiem. A la gent de Barcelona, gràcies per acollir-me i fer-me sentir a casa. David i Pau, voltros, gràcies per escoltar-me sempre i empatitzar amb mi, per totes les vegades que hem passat hores parlant, i perquè sé que si me gir, hi sereu.

I en general, gràcies a totes aquelles persones que heu aportat el vostre granet de sorra. Als companys i professors de la UB i de l'IFISC, que de manera directa o indirecta heu ajudat a que el meu camí em porti a ser allà on som. A les persones amb qui compartim aficions, perquè el temps que passam juntes fa que els dies siguin més amens. I als autors i autores de ficció que m'han acompanyat en els meus viatges en tren fins al despatx, per omplir el meu món de llum i colors.

ABSTRACT

Stochastic processes provide a mathematical framework to describe systems whose dynamics are affected by randomness. Although the trajectory of a single particle cannot usually be predicted in detail, its statistical properties can often be characterized. This allows us to study how random walkers explore space, and how their behavior changes when additional mechanisms are introduced. These questions are motivated, among others, by biological and ecological systems, where molecules, cells, or animals search for targets, return to familiar regions, or move in heterogeneous environments.

In this thesis, we study diffusion and anomalous diffusion processes through quantities that describe the trajectory beyond its position at a given time. We focus on two main questions. The first one concerns the efficiency of stochastic processes, as characterized in terms of its first-passage properties. We study this problem for different random-walk models and investigate how stochastic resetting, returning the walker at random times to prescribed positions or states, modifies the search process.

The second question concerns how stochastic trajectories explore space over time. To address this, we study stochastic functionals, which are observables defined along the whole trajectory of the walker. In particular, we focus on occupation times, which measure the time spent by a particle in a given region of space, and on area observables, which quantify accumulated properties of the trajectory. These quantities provide information that is not contained in the propagator or in the mean squared displacement alone. They are especially useful in anomalous diffusion, where different microscopic mechanisms may lead to similar transport properties but different trajectory-to-trajectory fluctuations. To characterize these functionals, we study their ergodic properties. We analyze whether time-averaged observables obtained from a single long trajectory are equivalent to ensemble-averaged observables. This distinction proves relevant in systems where long memory, broad waiting-time distributions, spatial heterogeneity, or non-stationary dynamics are present. Throughout the thesis, we use Feynman-Kac formalisms, renewal theory, and asymptotic methods to derive probability distributions, their moments, and ergodicity breaking parameters for different stochastic functionals.

Overall, in this thesis, we characterize stochastic trajectories through their first-passage properties, residence times, and stochastic functionals in general. The aim is to understand how random walkers search, how they occupy space, and under which conditions their long-time statistical properties can be inferred from individual trajectories. In this context, stochastic resetting appears both to modify search efficiency and to alter the statistical and ergodic properties of such processes.

Resum en Català, per a aquelles persones que sempre m'han demanat a què dedico el meu temps

La natura està plena de processos que es poden descriure com a aleatoris, des de la distribució de partícules en un gas, la cerca d'aliment d'organismes, o el plegament de proteïnes. Segons el DIEC, el terme *aleatori* es defineix com aquell "Que depèn d'un esdeveniment incert, d'una contingència o de l'atzar." En aquest sentit, una podria pensar que tots aquells processos que es poden descriure com a aleatoris són, per definició, incerts i imprevisibles.

No obstant això, durant més d'un segle, s'han desenvolupat eines i models per a descriure i entendre aquests processos, i treure'n l'entrellat dels mecanismes subjacents que els governen. Si bé és cert que aquests processos són aleatoris, també ho és que no són completament imprevisibles. De fet, molts d'aquests processos segueixen patrons i lleis que es poden descriure matemàticament, i que ens permeten fer prediccions sobre el seu comportament a llarg termini. Malgrat que no necessàriament podem saber exactament el comportament d'una partícula individual, sí que podem arribar a tenir una bona descripció del comportament de moltes d'aquestes partícules en conjunt, i fins i tot, d'algunes de les propietats d'una trajectòria individual.

Els mecanismes que generen aquests processos aleatoris poden ser més o menys sofisticats, i, a més, tenir origen en mecanismes molt distints a nivell microscòpic, que, per altra banda, poden donar lloc a comportaments a gran escala molt similars. És per això que, a l'hora d'estudiar-los, s'han desenvolupat eines que permetin descriure diferents propietats dels sistemes, depenent de les preguntes que es vulguin respondre.

En aquesta tesi, ens centrem en dues qüestions principals: la primera és la caracterització dels processos a través de la seva eficiència, entesa com el temps que es triga, en mitjana, un grup de partícules a arribar a un punt de l'espai. Veurem que, mecanismes com el retorn estocàstic, que consisteix a interrompre el procés a temps aleatoris i tornar-lo a un estat predefinit, poden ajudar a optimitzar aquesta eficiència.

La segona qüestió que tractarem és com aquestes partícules que es mouen de manera aleatòria exploren l'espai (a través d'uns objectes matemàtics anomenats funcionals estocàstics) i, en concret, ens centrarem en els temps de residència en unes regions de l'espai definides. Estudiarem les distribucions i propietats estadístiques d'aquests temps de residència i, a més, en determinar les seves propietats ergòdiques. És a dir, si quan el temps d'observació és prou llarg, podem intercanviar l'estudi d'una trajectòria molt llarga amb l'estudi de moltes trajectòries més curtes. Veurem que en molts casos aquesta hipòtesi no es compleix, i per tant no podem fer aquest intercanvi. A més, veurem com distints mecanismes de retorn estocàstic poden alterar aquestes propietats.

En definitiva, en aquesta tesi aprofundirem en la comprensió de com els processos aleatoris es poden descriure i entendre a través de diferents eines, i com aquestes eines ens permeten fer prediccions sobre el seu comportament a llarg termini. A més, veurem com aquests processos poden ser optimitzats a través de mecanismes com el retorn estocàstic, i com aquests mecanismes poden alterar les propietats estadístiques dels processos.

PUBLICATIONS

The articles detailed below, in chronological order by date of publication, form the basis of this thesis.

1. R. Flaquer-Galmés, D. Campos, and V. Méndez. "Intermittent random walks under stochastic resetting". In: *Physical Review E* 109 (3 Mar. 2024), p. 034103. DOI: 10.1103/PhysRevE.109.034103.

2. V. Méndez, R. Flaquer-Galmés Rosa, and D. Campos. "First-passage time of a Brownian searcher with stochastic resetting to random positions". In: *Physical Review E* 109 (4 Apr. 2024), p. 044134. DOI: 10.1103/PhysRevE.109.044134.

3. V. Méndez, R. Flaquer-Galmés, and A. Pal. "Occupation-time statistics for non-Markovian random walks". In: *Physical Review E* 111 (4 Apr. 2025), p. 044119. DOI: 10.1103/PhysRevE.111.044119.

4. V. Méndez and R. Flaquer-Galmés. "Statistical properties of stochastic functionals under general resetting". In: *Physical Review E* 112 (4 Oct. 2025), p. 044123. DOI: 10.1103/pcm7-bw2y.

5. V. Méndez, C. Hervás, and R. Flaquer-Galmés. "Ergodic properties of functionals of Gaussian processes". In: *Physical Review E* 112 (6 Dec. 2025), p. 064111. DOI: 10.1103/qpkk-mgt6.

6. V. Méndez and R. Flaquer-Galmés. "Ergodic properties of occupation times in heterogeneous media". In: *Journal of Statistical Mechanics: Theory and Experiment* 2026.1 (Jan. 2026), p. 013203. DOI: 10.1088/1742-5468/ae337d.

7. V. Méndez, R. Flaquer-Galmés, and J. Cristín. "Area under subdiffusive random walks". In: *Physica A: Statistical Mechanics and its Applications* (June 2026), p. 131719. DOI: 10.1016/j.physa.2026.131719.

Other works published during the PhD period are:

1. E. Barkai, R. Flaquer-Galmés, and V. Méndez. "Ergodic properties of Brownian motion under stochastic resetting". In: *Physical Review E* 108 (6 Dec. 2023), p. 064102. DOI: 10.1103/PhysRevE.108.064102.

2. R. Flaquer-Galmés, D. Campos, and J. Cristín. “Magneticlike model for chemotactic navigation in ants”. In: *Physical Review Research* 8 (1 Jan. 2026), p. 013116. DOI: 10.1103/fdhh-5jpy.

Finally, articles under preparation as a result of ongoing work, with the following tentative titles and author lists, are:

1. Rosa Flaquer-Galmés and Daniel Campos. “The effect of inertia and cognitive processing on patterns of chemical navigation in ants.”

2. Vicenç Méndez, Rosa Flaquer-Galmés, and Javier Cristín. “Occupation time statistics of geometric Brownian motion.”

CONTENTS

Acknowledgments v

Abstract vii

Publications ix

List of figures xx

Acronyms xxi

I Foundations

1 Introduction 3

2 Background 7

2.1 Diffusion processes 7

2.1.1 Anomalous diffusion 9

2.2 First-passage times 14

2.3 Stochastic resetting 16

2.4 Stochastic functionals and the Feynman-Kac formula 20

2.4.1 Half occupation time 21

2.4.2 Occupation time in an interval 22

2.4.3 Area under the trajectory 23

2.5 Ergodicity and ergodicity breaking 24

II Efficiency

3 Intermittent random walks under stochastic resetting 33
3.1 Introduction . . . 34
3.2 The IRW model without resetting . . . 34
3.2.1 Mean squared displacement . . . 37
3.2.2 First-passage time . . . 38
3.3 The IRW model with resetting . . . 40
3.3.1 Mean squared displacement . . . 41
3.3.2 Non-equilibrium steady state . . . 42
3.3.3 First-passage time . . . 43
3.3.4 Optimal reset rate . . . 45
3.3.5 Global optimization of the MFPT . . . 47
3.4 Summary of results . . . 49

4 Stochastic resetting to random positions . . . 51
4.1 Introduction . . . 52
4.2 Averaged mean first-passage time . . . 52
4.2.1 Effect of the resetting distribution on the first-passage PDF . . . 55
4.2.2 Symmetric reset-point PDF in an interval and $x_t \notin \mathscr{D}$ . . . 56
4.2.3 Symmetric reset-point PDF in an interval and $x_t \in \mathscr{D}$ . . . 59
4.2.4 Resetting to two points . . . 62
4.3 Equivalent resetting point . . . 65
4.4 Fluctuations of the MFPT . . . 69
4.4.1 Example: Uniform resetting PDF with $x_t > L$ . . . 70
4.4.2 Example: Uniform resetting PDF with $x_t \in \mathscr{D}$ . . . 71
4.5 Summary of results . . . 72

III Ergodic properties

5 Occupation time statistics for non-Markovian random walks . . . 79
5.1 Introduction . . . 80
5.2 Non-Markovian random walks . . . 80
5.3 The Feynman-Kac equation . . . 83
5.4 Occupation time in an interval . . . 85
5.4.1 Moments of T_a . . . 86
5.4.2 PDF of T_a . . . 91
5.4.3 Ergodic properties of T_a . . . 94

5.5 Half occupation time . . . 94
5.5.1 Moments of T_+ . . . 95
5.5.2 PDF of T_+ . . . 96
5.5.3 Ergodic properties of T_+ . . . 97
5.6 Poissonian resetting . . . 97
5.6.1 Moments – General expressions and asymptotics . . . 98
5.6.2 PDF . . . 101
5.6.3 Ergodic properties . . . 102
5.7 Summary of results . . . 104

6 Stochastic functionals under general resetting . . . 107
6.1 Introduction . . . 108
6.2 Characteristic function . . . 108
6.2.1 Moments . . . 110
6.3 Limiting PDF for a finite moment resetting distribution . . . 111
6.4 Moments in the long-time limit . . . 113
6.5 Application: Half occupation time . . . 115
6.5.1 The first two moments and EB . . . 115
6.5.2 Limiting PDF . . . 118
6.6 Summary of results . . . 124

7 Occupation times in heterogeneous media . . . 125
7.1 Introduction . . . 125
7.2 Generating function and $D(x)$ . . . 126
7.3 Half occupation time . . . 128
7.3.1 Piecewise heterogeneity . . . 128
7.3.2 Power law heterogeneity . . . 131
7.4 Occupation time in an interval . . . 134
7.4.1 Piecewise heterogeneity . . . 135
7.4.2 Power law heterogeneity . . . 136
7.5 Summary of results . . . 139

8 Occupation and area observables in Gaussian anomalous diffusion . . . 141
8.1 Introduction . . . 142
8.2 The first two moments . . . 142
8.2.1 Gaussian processes . . . 145

8.3 Stationary processes . . . 146
8.4 Occupation-time statistics . . . 147
8.4.1 Half occupation time . . . 150
8.4.2 Occupation time in an interval . . . 153
8.4.3 Scaling of the PDF . . . 156
8.5 Area observables . . . 158
8.5.1 Area . . . 159
8.5.2 Absolute Area . . . 160
8.5.3 Scaling of the PDF . . . 163
8.6 Summary of results . . . 165

IV Concluding statements

9 Conclusions . . . 169

A Numerical simulation methods . . . 173
A.1 Trajectory generation . . . 174
A.1.1 Chapter 3: Intermittent random walks under stochastic resetting 174
A.1.2 Chapter 4: Stochastic resetting to random positions . . . 174
A.1.3 Chapter 5: Occupation time statistics for non-Markovian random walks . . . 175
A.1.4 Chapter 6: Stochastic functionals under general resetting . 176
A.1.5 Chapter 7: Occupation times in heterogeneous media . . . 176
A.1.6 Chapter 8: Occupation and area observables in Gaussian anomalous diffusion . . . 177
A.2 Numerical evaluation of functionals . . . 177
A.3 Ensemble statistics . . . 178

B PDF of the occupation time in an interval . . . 179
B.1 Left edge regime . . . 180
B.2 Right edge regime . . . 182
B.3 Central bulk regime . . . 183

C Limiting PDF for a finite moment resetting distribution 185

D Limiting PDF of the half occupation time under general resetting . . . 187

E Probability density functions of occupation times in heterogeneous media 191

E.1 Derivation of the half occupation time distribution 191

E.1.1 Piecewise heterogeneity 192

E.1.2 Power-law heterogeneity 193

E.2 Derivation of the distribution of the occupation time in an interval 194

E.2.1 Piecewise heterogeneity 194

E.2.2 Power-law heterogeneity 195

F Second moment of the absolute area under a SBM 197

Bibliography 219

LIST OF FIGURES

1.1 Recording of Brownian trajectories by Jean Baptiste Perrin 4

2.1 Example Brownian trajectories 8
2.2 MSD of anomalous diffusion. 10
2.3 Examples of anomalous trajectories 11
2.4 Schematics of a CTRW. 12
2.5 Example first-passage time for Brownian trajectories 15
2.6 Example resetting for Brownian trajectories 16
2.7 MFPT of a BM with reset rate r 18
2.8 Half occupation time. 21
2.9 Occupation time in an interval. 22
2.10 Area under the trajectory 23
2.11 Time and ensemble averages. 25

3.1 Scheme of the IRW 35
3.2 Trajectory of the IRW without resetting 36
3.3 MSD of the IRW without resetting 38
3.4 IRW trajectory with resetting 40
3.5 MSD of the IRW with resetting 41
3.6 NESS of the IRW with resetting 42
3.7 FPT PDF of the IRW with resetting. 44
3.8 MFPT of the IRW with resetting. 46
3.9 Phase diagram of the MFPT for the IRW. 47

4.1 Example trajectory of diffusion with resetting to distributed positions 53
4.2 Uniformly distributed reset points in an interval 56
4.3 AMFPT for uniformly distributed reset-point PDF with $x_t \notin \mathscr{D}$. 57

4.4 r_{opt} for uniformly distributed reset points in an interval 58
4.5 Uniformly distributed reset points in an interval containing the target. 59
4.6 AMFPT for uniformly distributed reset points in a finite interval containing the target. 60
4.7 Infinite support with exponential reset points 61
4.8 AMFPT for uniformly distributed reset-point PDF in an infinite support. 62
4.9 Diagram $L\sqrt{r/D}$ vs p for asymmetric resetting points in an interval with $x_t > L$ 63
4.10 Optimal reset rate for asymmetric resetting points in an interval with $x_t > L$ 64
4.11 Optimal reset rate exponent for asymmetric resetting points in an interval with $x_t > L$ 65
4.12 First-passage PDFs. 66
4.13 Diagram x_r/x_t vs L/x_t for the ERP with $x_t \notin \mathscr{D}$. 67
4.14 Diagram x_r/L vs x_t/L for the ERP when $x_t \in \mathscr{D}$. 68
4.15 CV for the uniform resetting PDF with $x_t > L$ 71
4.16 CV for the uniform resetting PDF with $x_t < L$ 72

5.1 Mean squared displacement 88
5.2 Mean occupation time in an interval. 89
5.3 Mean squared occupation time in an interval. 90
5.4 Scaled PDF of occupation time $Q(y,t)$ as a function of $y = T_a/t$ for $\varphi(s)$ with finite first moment. 92
5.5 Scaled PDF of occupation time $Q(y,t)$ as a function of $y = T_a/t$ for $\varphi(s)$ with diverging moments. 93
5.6 Moments of the half occupation time. 95
5.7 Universality of the *arcsine* distribution. 97
5.8 Moments of the occupation time with resetting. 100
5.9 Scaled PDF $Q_r(Z/t,t)$ of the occupation time in the presence of stochastic resetting. 103

6.1 Limiting PDF of Z for exponentially distributed resetting in Laplace space 113
6.2 Exponent ω (of $\sim t^{\omega}$) of the first and second moments of the observables for a Brownian Walker with fat-tailed resetting 114
6.3 First moment, second moment, and EB parameter of the half occupation time with fat-tailed resetting. 117

6.4 Limiting PDF of the half occupation time of a Brownian motion with resetting for a variety of resetting distributions. 120

6.5 Limiting PDF of the half occupation time of a CTRW with resetting for a variety of resetting distributions. 123

7.1 Limiting distribution of the half occupation time for the piecewise heterogeneity 128

7.2 Moments and EB parameter of the half occupation time for the piecewise heterogeneity. 129

7.3 PDF of the time averaged half occupation time for the piecewise heterogeneity. 130

7.4 Limiting distribution of the half occupation time for the power-law heterogeneity. 131

7.5 Moments and EB parameter of the half occupation time for the power-law heterogeneity. 132

7.6 PDF of the time averaged half occupation time for the power-law heterogeneity. 133

7.7 Distribution of the occupation time in the interval for the piecewise heterogeneity. 134

7.8 Moments and EB parameter of the half occupation time for the piecewise heterogeneity 135

7.9 Limiting distribution of the occupation time in an interval for the power-law heterogeneity. 136

7.10 Moments and EB parameter of the occupation time in an interval for the power-law heterogeneity 137

7.11 PDF of the time averaged occupation time in the interval for the power-law heterogeneity 138

8.1 Moments and EB of the half occupation time for the SBM 151

8.2 Moments and EB of the half occupation time for the fBM 152

8.3 Moments and EB of the occupation time in an interval for the SBM 154

8.4 Moments and EB of the occupation time in an interval for the fBM. 155

8.5 Scaling form for T_+ and T_a for the SBM 156

8.6 Scaling form for T_+ and T_a for the fBM 157

8.7 Second moment of the area for the SBM and fBM 159

8.8 Moments and EB of the absolute area for the SBM 160

8.9 Moments and EB of the absolute area for the fBM 161

8.10 Scaling form for A and $\mathscr{A}$ for the SBM 164

8.11 Scaling form for A and $\mathscr{A}$ for the fBM 165

ACRONYMS

AMFPT averaged mean first-passage time

BM Brownian motion

CTRW continuous-time random walk

CV coefficient of variation

EB ergodicity breaking

ERP equivalent resetting point

fBM fractional Brownian motion

FK Feynman-Kac

FPT first-passage time

GME generalized master equation

HDP heterogeneous diffusion process

i.i.d. independent identically distributed

IRW intermittent random walk

l.h.s. left-hand side

MFPT mean first-passage time

MGF moment generating function

ML Mittag-Leffler

MSD mean squared displacement

NESS non-equilibrium steady state

PDF probability density function

r.h.s. right-hand side

SBM scaled Brownian motion

TAMSD time-averaged mean squared displacement

Foundations

1 **Introduction** 3

2 **Background** 7

2.1 Diffusion processes 7
2.2 First-passage times 14
2.3 Stochastic resetting 16
2.4 Stochastic functionals and the Feynman-Kac formula 20
2.5 Ergodicity and ergodicity breaking 24

1

INTRODUCTION

Stochastic processes are mathematical models for physical phenomena that appear to be dominated by randomness. Examples range from the motion of molecules in a gas, the molecular dynamics of biomolecules, and molecular binding/unbinding processes to population growth in viruses and bacteria, disease spreading, atmospheric dynamics, geophysical motions, and stock-market prices. The most famous example, however, is the motion of pollen grains in water, and diffusion processes in general.

The interest in diffusion processes dates back to the beginning of the 1900s, with the works of Einstein [10], Smoluchowski [11], and Langevin [12], among others, who provided a theoretical framework that could explain the inherent and incessant jiggling motion of pollen particles suspended in a fluid, observed experimentally by Robert Brown in 1828 [13]. The early developments of the theory came at a time when the atomistic nature of matter was being disputed, bringing further support to it. Experimental works such as those of J. Perrin and students [14], as presented in Fig. 1.1, allowed for a determination of the Avogadro number, which they estimated to be $N_A \simeq (6.4-6.9)\times 10^{23}[\text{mol}]^{-1}$ inspired by Einstein's works on diffusion. Thus, the problem of Brownian motion (BM) has played a central role in the development of both the foundations of thermodynamics and the dynamical interpretation of statistical physics, providing a link between underlying microscopic dynamics and macroscopic observable phenomena [15]. For a more extensive historical background on the early developments, see the introductory chapter of [16].

Since these early developments, the theory of diffusive processes, and of stochastic processes more generally, has been widely developed and applied across many fields. A telling sign of the field's activity is the periodic focus issues and reviews that are published on significant dates. Examples include the special issue "100 years of Brownian motion" published in 2005 [15], the review "111 years of Brownian motion"

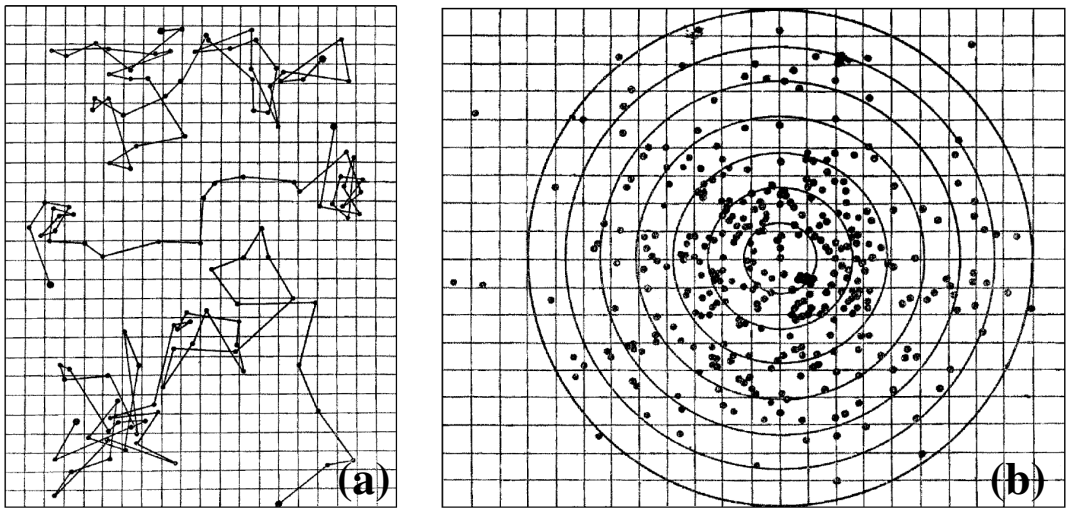


Figure 1.1: **Recording of Brownian trajectories by Jean Baptiste Perrin.** [14]. (a) Three designs obtained by tracing a small grain of putty (mastic, used for varnish) at intervals of 30 s. (b) The starting point of each motion event is shifted to the origin. Image taken from [17].

published in 2016 [18], both of them to celebrate the anniversary of Einstein's 1905 article, or the thematic collection *250 Years of Brownian Motion* [19], to commemorate Brown's birth. These reviews and collections discuss a large variety of topics under the umbrella of Brownian motion, including granular systems, soliton diffusion, quantum phenomena, life sciences, and fluid physics, which illustrates the broad applications of the field. What is more, after more than a century, there still is a debate on the true origin of irregularity that causes the stochastic, random character of Brownian trajectories [15, 20], showing that in spite of the great progress made, there are still unknowns at a fundamental level, which lead to fruitful scientific discussions.

Standard Brownian diffusion is typically characterized by two properties: a linear growth in time of the MSD of the particles (sometimes called Fickian diffusion), and a probability density function to find the diffusive particle at a certain point in space and time that follows Gaussian statistics. After the first works on BM, empirical evidence has shown that in many cases, especially in complex systems, the dynamics deviate from standard diffusion; either by a non-linear MSD with time, or non-Gaussian statistics. This behavior is often referred to as anomalous diffusion [21, 22]. There is a wide variety of mechanisms that can lead to such deviations, such as the presence of correlations in the dynamics of the system, heterogeneity in the medium, external forces, memory effects, etc. Generalizations and alternate models of the standard BM have been developed to account for these deviations, and have been observed in a huge variety of systems, from the diffusion of molecules in crowded environments to the diffusion of animals in their habitats, with the continuous-time random walk (CTRW), developed by Montroll and Weiss in 1965 [23], being one of the most well-known generalizations.

A general question is what information can be extracted from the trajectory of a stochastic process. In a first approach one might try to study the propagator, the distri-

bution in space of an ensemble of particles at a given time, of the process. However, in many physical, biological, or ecological systems the dynamics are not straightforward. The particle may move through different phases, return repeatedly to previously visited regions, diffuse in a heterogeneous environment, or display memory effects and temporal correlations. In these situations, getting the exact propagator of the underlying process is not always a feasible option, nor answers the relevant questions under study, and other strategies are needed. Luckily, the trajectory is not only characterized by how far particles have moved or where they are at a given time, but also by how it has explored phase space in time, which provides complementary information on the dynamics of the system.

Extensive work has been done to develop tools and frameworks to characterize stochastic trajectories, and the applicability of each framework depends on the specific question being addressed. In this thesis, we focus on two main areas: first-passage problems and ergodic properties of functionals of random walks. In the former, the focus is to study when a certain process attains a value for the first time [24], and more specifically, one is typically interested in the distribution and its mean value as performance metrics of the system. The second approach is through stochastic functionals in general. The prototypical example of a stochastic functional is the Brownian functional, defined as the time integral over the trajectory of a walker when it is Brownian [25]. Stochastic functionals provide a way to characterize random walks beyond standard quantities such as the MSD or the propagator. Since they are defined as time integrals along a trajectory, they naturally appear when studying time-averaged (in contrast to ensemble-averaged) observables, occupation times, first-passage quantities, or accumulated areas. This is especially relevant in anomalous diffusion, where different stochastic models may show similar scaling of the MSD but differ in their trajectory-to-trajectory fluctuations, and the ergodicity of the system may be absent. Therefore, the study of stochastic functionals allows us to obtain information on how the particle explores the phase space in time, and on whether the corresponding time-averaged observables converge to their ensemble averages in the long-time limit.

This thesis characterizes diffusion and anomalous diffusion processes through first-passage characteristics, residence times, and area functionals. Moreover, we examine how the presence of stochastic resetting, a mechanism by which a process is restarted at random times, changes the statistical and ergodic properties of the system under consideration. Through the work presented here, we aim to enlarge the current knowledge on stochastic processes by providing specific results on models of interest, but also to give general frameworks that can be used in generic contexts.

Biological systems provide a natural motivation for these ideas. At the scale of organisms, animal movement is rarely a purely Brownian process: individuals may alternate between local exploration and long relocations, return repeatedly to nests or previously visited regions, or move under the influence of memory and environmental constraints. At smaller scales, the motion of molecules, proteins, or vesicles inside living cells is also affected by crowding, transient binding, viscoelasticity, and spatial heterogeneity, which often lead to anomalous diffusion and non-ergodic behavior.

The text is structured as follows: Part I aims to be introductory, laying the foundations for the work that we present; in particular, in Chapter 2 we establish the background information and known results that the rest of the thesis builds upon. In

Part II, we study two random walk models undergoing stochastic resetting, and we characterize them by their first-passage properties: first for intermittent random walks, and then for Brownian searchers resetting to random positions. In Part III, we turn to stochastic functionals and ergodic properties, studying non-Markovian random walks, general resetting protocols, heterogeneous media, and Gaussian anomalous diffusion through occupation-time and area observables. Finally, in Part IV, we present the conclusions. The numerical methods used throughout the thesis are collected in Appendix A, and in Appendix B to F we include derivations of analytical results. We finish the document with the Bibliography.

2 BACKGROUND

This introductory chapter presents the concepts this thesis builds upon. We introduce the stochastic dynamics studied in the following chapters, together with first-passage times and stochastic resetting. We then define stochastic functionals and the main observables analyzed later in the thesis. Finally, we discuss ergodicity and ergodicity breaking in the context of stochastic functionals.

2.1 Diffusion processes . . . 7
2.1.1 Anomalous diffusion . . . 9
2.2 First-passage times . . . 14
2.3 Stochastic resetting . . . 16
2.4 Stochastic functionals and the Feynman-Kac formula . . . 20
2.4.1 Half occupation time . . . 21
2.4.2 Occupation time in an interval . . . 22
2.4.3 Area under the trajectory . . . 23
2.5 Ergodicity and ergodicity breaking . . . 24

2.1 Diffusion processes

> **Note 2.1** For convinience of the caluclations, all discussions and results in this work are given for one-dimensional processes.

Brownian motion (BM) is a paradigmatic stochastic process and the basis of many more elaborate models. It therefore provides a natural starting point for textbooks on stochastic processes and diffusion [26, 27]. In the earliest formulation of BM by Einstein, he took a probabilistic description of an ensemble of particles instead of de-

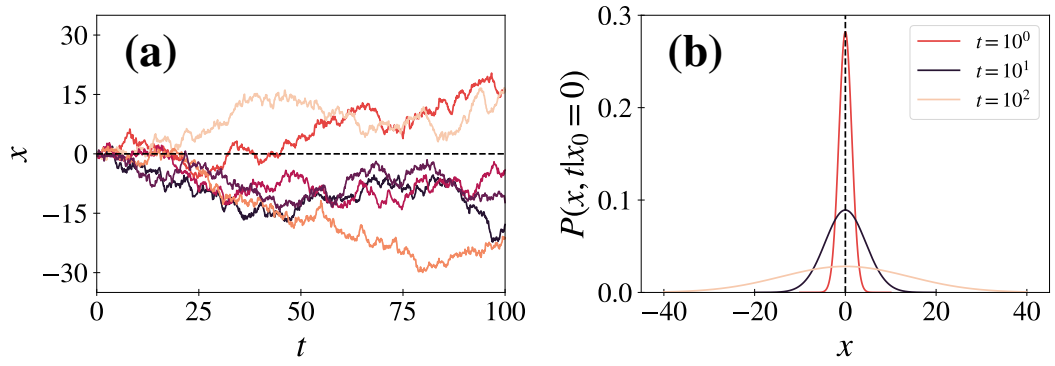


Figure 2.1: **Example Brownian trajectories** (a) 6 Brownian trajectories. (b) Gaussian propagator Eq. (2.2) for Brownian particles at three different times $t = 10^0, 10^1, 10^2$. For both figures $D = 1$, and $x_0 = 0$.

scribing the trajectory of every single particle. His derivation assumes (i) the trajectory of every particle can be divided into discrete intervals τ, so that the displacements of the particle in different time intervals of length τ can be considered statistically independent; (ii) at each time interval of length τ, the distance traveled by the particle is Δ, where Δ is a random variable sampled from a symmetric distribution with zero mean and finite variance (note that one does not need to consider the distribution to be Gaussian); (iii) consider an ensemble of N large enough independent particles, and spatial scales much larger than the typical size and distance Δ. Finally, by taking the limit of $\tau \to 0$ and $\Delta \to 0$ while keeping the ratio Δ^2/τ finite, Einstein arrived at the diffusion equation for the evolution of the PDF $P(x,t)$ of the particle's position over time

$$\frac{\partial P(x,t)}{\partial t} = D\frac{\partial^2 P(x,t)}{\partial x^2}, \tag{2.1}$$

where D is the well-known diffusion coefficient, $D = \langle \Delta^2 \rangle / (2\tau)$. The solution of the diffusion equation with the initial condition $P(x,t=0) = \delta(x-x_0)$ and boundary conditions $P(x,t) \to 0$ as $x \to \pm\infty$ is given by

$$P(x,t) = \frac{1}{\sqrt{4\pi D t}} \exp\left(-\frac{(x-x_0)^2}{4Dt}\right), \tag{2.2}$$

which is the characteristic Gaussian distribution with mean x_0 and variance $2Dt$. In Fig. 2.1, we include an illustrative example of Brownian trajectories in panel (a) and of the propagator at different times in panel (b). From this solution, the MSD of the process, when $x_0 = 0$ is

$$\langle x(t)^2 \rangle = 2Dt, \tag{2.3}$$

Note 2.2 Through all this work, we use $\langle \cdot \rangle$ to denote the average over the re-

alizations of the stochastic process, and $\bar{\cdot}$ to denote the time average of a single realization.

giving the well-known linear growth of the MSD with time, which is a hallmark of standard diffusion processes. More generally, the n-th moment of the process can be obtained from the Fourier transform $P(k,t) = \mathscr{F}_{x\to k}[P(x,t)]$ of the propagator, as

$$\langle x(t)^n \rangle = \frac{1}{(-i)^n} \left[\frac{\partial^n P(k,t)}{\partial k^n} \right]_{k=0}. \tag{2.4}$$

While Einstein took a mesoscopic approach, representing the system at the population level, Langevin, on the other hand, considered the process from the microscopic point of view, describing the dynamics of the individual particles. He formulated the problem as the dynamics of a single Brownian particle subjected to a random force. In its more general form, the Langevin equation can be written as

$$\frac{dx(t)}{dt} = q(x,t) + g(x,t)\xi(t), \tag{2.5}$$

where $q(x,t)$ is the drift, representing the deterministic contributions to the dynamics of the system, for example if a particle is moving in some potential; $g(x,t)$ is the noise amplitude, which sets the local intensity of the random fluctuations acting on the particle, and $\xi(t)$ is a stochastic noise term.

In the simplest case of a free Brownian particle, $q(x,t) = 0$, $g(x,t) = \sqrt{2D}$, and $\xi(t)$ a Gaussian white noise with $\langle \xi \rangle = 0$ and autocorrelation $\langle \xi(t)\xi(t') \rangle = \delta(t-t')$, then the Langevin equation, in its overdamped form, reduces to

$$\frac{dx(t)}{dt} = \sqrt{2D}\xi(t). \tag{2.6}$$

Note 2.3 To simplify the notation, and unless otherwise specified, we will denote the Fourier and Laplace transforms of a function by the arguments of the function, that is, if $f(x)$ is a function of x, then its Fourier transform will be denoted by

$$f(k) = \int_{-\infty}^{\infty} f(x) e^{-ikx} dx,$$

with its inverse being

$$f(x) = \frac{1}{2\pi} \int_{-\infty}^{\infty} f(k) e^{ikx} dk.$$

Similarly if $f(t)$ is a function of t, then its Laplace transform will be denoted by

$$f(s) = \int_{0}^{\infty} f(t) e^{-st} dt.$$

2.1.1 Anomalous diffusion

As hinted in the introduction, many systems in nature deviate from standard diffusive behavior, and are mainly referred to as anomalous diffusion processes. Anomalous transport is a hallmark of complex media, from crowded intracellular environments to

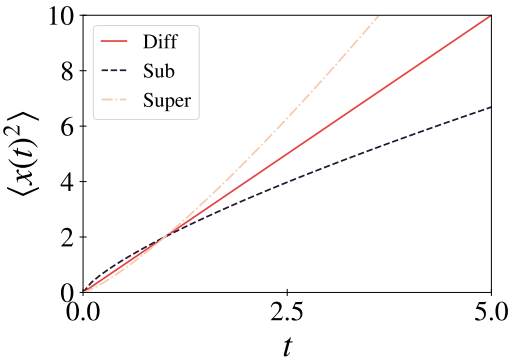


Figure 2.2: **MSD of anomalous diffusion.** For diffusion, $D = 1$, for subdiffusion the anomalous exponent is $\nu = 3/4$, and for superdiffusion $\nu = 5/4$.

porous and fractal substrates [21, 28, 29, 30, 31, 32, 33]. While there is a wide variety of underlying mechanisms that give rise to anomalous diffusion, and the resulting processes exhibit different characteristics, they are all defined by a scaling of the MSD that deviates from linearity as a power-law of time, that is

$$\langle x(t)^2 \rangle \sim t^{\nu}, \tag{2.7}$$

where ν is the anomalous diffusion exponent. If $\nu < 1$, the process is known to be subdiffusive, while if $1 < \nu < 2$, the process is superdiffusive, and for $\nu > 2$ the process is hyperdiffusive. In Fig. 2.2 we illustrate the MSD of a diffusive process with $D = 1$, a subdiffusive, and a superdiffusive one.

On top of the deviation from linearity, the propagator $P(x,t)$ for these systems is not necessarily Gaussian. Notice that according to the Central Limit Theorem Gaussian statistics emerge as a limit distribution of independent identically distributed (i.i.d.) random variables with finite variance; then any system where one, or both, of these assumptions is not fulfilled, will deviate from Gaussianity [21]. In fact, the scaling of the MSD as some power of t in anomalous diffusion is deeply connected with the breakdown of the Central Limit Theorem, caused by either broad distributions or long-range correlations. Instead, anomalous diffusion relies on the validity of the Lévy-Gnedenko generalized Central Limit Theorem, for when not all moments of the underlying elementary transport events exist [17].

Anomalous diffusion, where the MSD goes as some power of t, is not the only known deviation from standard diffusion. In some highly disordered systems, the MSD grows even slower with time, typically as some function of the logarithm of t, which appears in amorphous semiconductors, porous media, or biological transport [17, 34]. While we are not going to deal with these types of systems known as "ultraslow diffusion", it is worth noting that other mechanisms exist that do not yield a power-law MSD scaling. Moreover, systems can exhibit a crossover between different scaling regimes, typically when the time evolution of the system exceeds some characteristic correlation time or length scale [35]. "Brownian yet non-Gaussian diffusion" is also known to arise in some systems with spatial or temporal heterogeneity [36] with a MSD that grows linearly with time but with a non-Gaussian propagator at finite times.

In the following, we will briefly review the main mathematical descriptions of anomalous diffusion that we will study in the next chapters and summarize their main features in Table 2.1 at the end of this section. Here, we present examples of

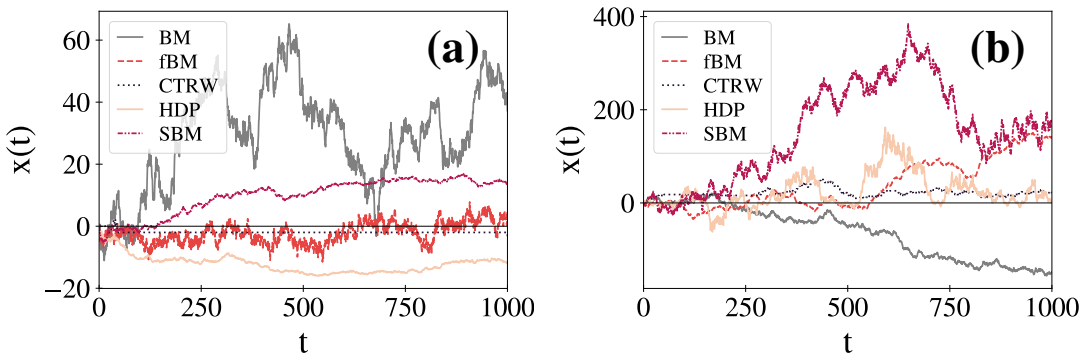


Figure 2.3: **Examples of anomalous trajectories.** In both panels $D = 1$ for BM, $K = 1$ for SBM, $D_H = 1$ for fBM, $D_0 = 1$ for HDP, and $\Phi(\Delta) = 0.5\delta(\Delta) + 0.5\delta(-\Delta)$ with $\Delta = 2$ for CTRW. In panel (a) $\alpha = 1/2$ for the SBM, $H = 1/4$ for the fBM, $\alpha = -2$ for the HDP and $\alpha = 1/2$ for the CTRW. In panel (b) $\alpha = 3/2$ for the SBM, $H = 3/4$ for the fBM, $\alpha = 2/3$ for the HDP and $\alpha = 3/2$ for the CTRW.

trajectories generated by those diffusion mechanisms in Fig. 2.3. In panel (a), all trajectories except the BM are computed with model parameter values that yield a subdiffusive scaling of the MSD of $\nu = 1/2$. On the other hand, in panel (b) all trajectories have a superdiffusive scaling of $\nu = 3/2$ except for the BM and CTRW, which both have a linear scaling in t.

A Continuous time random walk

The CTRW is a generalization of the standard random walk, first introduced by Montroll and Weiss in 1965 [23], see [17] for an extensive review of this subject. In a CTRW, as its name implies, time is treated as a continuous variable, with the walker waiting a time τ between jumps, where τ is a random variable drawn from a waiting time distribution $\varphi(\tau)$. The jump lengths Δ are also random variables drawn from a step length distribution $\Phi(\Delta)$. In Fig. 2.4 we illustrate the CTRW process. Depending on the choice of the waiting time and step length distributions, the CTRW can exhibit subdiffusive, superdiffusive, or normal diffusive behavior. For instance, if the waiting time distribution has a heavy tail (e.g., $\varphi(\tau) \sim \tau^{-1-\alpha}$ with $0 < \alpha < 1$), the resulting process is subdiffusive, [37]; this can be the case of particles diffusing in a quenched energy landscape, where the distribution of trapping times is very broad [38]. On the other hand, if the step length distribution has a heavy tail (e.g., $\Phi(\Delta) \sim |\Delta|^{-1-\beta}$ with $0 < \beta < 2$), the process can be superdiffusive, giving rise to what is known as Lévy flights [39, 40]. The CTRW has been used to describe a wide variety of phenomena, from transport in disordered and porous media [41, 42], electron transport [43], epidemic modeling [44], to finance and economics [45, 46].

B Scaled Brownian motion

The scaled Brownian motion (SBM) is a non-stationary Gaussian process with time-dependent diffusivity. In particular, the SBM fulfills the Langevin Eq. (2.5) with $q(x,t) = 0$ and $g(x,t) = \sqrt{2D(t)}$, and $\xi(t)$ a white Gaussian noise with zero mean and unit autocorrelation $\langle \xi(t)\xi(t')\rangle = \delta(t-t')$. In the case of SBM, the diffusion

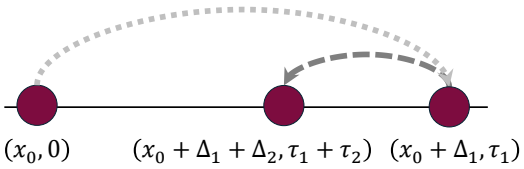


Figure 2.4: **Schematics of a CTRW.**

coefficient is given by a power law of time, that is

$$D(t) = \alpha K t^{\alpha-1}, \tag{2.8}$$

with $\alpha \in (0,2)$. The MSD of this process is given by

$$\left\langle x(t)^2 \right\rangle = 2Kt^{\alpha}, \tag{2.9}$$

which can be derived by integrating Eq. (2.5) with (2.8). It is straightforward to note that $\alpha = 1$ corresponds to normal diffusion, $\alpha < 1$ to subdiffusion, and $\alpha > 1$ to superdiffusion. This model has been used to describe fluorescence recovery after photobleaching in various settings [47] as well as anomalous diffusion in various biophysical contexts [22, 48, 49]. In other branches of physics, SBM has been applied to study the scaled voter model [50] and to model turbulent flows observed by Richardson [51]. Moreover, the diffusion of particles in granular gases with relative speed dependent restitution coefficients follows SBM [52].

C Fractional Brownian motion

The fractional Brownian motion (fBM) is a self-similar Gaussian process with zero mean and autocorrelation

$$C(t_1, t_2) = D_H \left(t_1^{2H} + t_2^{2H} - |t_1 - t_2|^{2H} \right), \tag{2.10}$$

with $H \in (0,1)$, which is sometimes referred to as the Hurst exponent. In this way, for $H > 1/2$ the increments are positively correlated, for $H < 1/2$ they are anticorrelated, and for $H = 1/2$ the correlations vanish and the usual Brownian motion is recovered. One way of understanding how the fBM is generated is by considering it as the sum of Gaussian increments, which are not, in general, independent, but are generated by a fractional Gaussian noise. Therefore, contrary to SBM, the anomalous diffusion of fBM is not generated by a time-dependent diffusion coefficient but by the temporal correlations between the increments.

The fBM was first introduced by Kolmogorov [53] and later studied by Mandelbrot and van Ness [54]. It has been observed to generate the subdiffusion of various tracers in complex environments both in vivo and in vitro [55, 56, 57, 58, 59], but also for completely different stochastic processes such as electronic network traffic [60] or financial time series [61, 62]. In the superdiffusive regime ($1/2 < H < 1$), positive

increment correlations and single-trajectory power spectra consistent with fBM were observed for the actively driven motion of endogenous granules inside amoeba cells as well as for the motion of the amoeba themselves [63, 64]. In addition, it has been extensively studied in mathematical literature [62, 65].

The MSD of the fBM can be derived from its autocorrelation function, giving

$$\langle x(t)^2 \rangle = 2D_H t^{2H}, \tag{2.11}$$

again we see that, in this case, $H < 1/2$ yields subdiffusion, $H = 1/2$ regular diffusion, and $H > 1/2$ is superdiffusive.

D Heterogeneous diffusion processes

While the previous models of anomalous diffusion are based on temporal heterogeneity, meaning that the dynamics of the process change over time, there are many systems in nature where the dynamics change over space, this is the case of the heterogeneous diffusion processs (HDPs). One way of modeling such systems is by considering a space-dependent diffusion coefficient, that is, by considering the Langevin Eq. (2.5) with $q(x,t) = 0$ and $g(x,t) = \sqrt{2D(x)}$, where $D(x)$ is a function of the position, and again with a Gaussian white noise with zero mean and unit autocorrelation. In this case, since now $g(x,t)$ depends on x, the noise is said to be multiplicative, and we need to specify the interpretation of the stochastic integral. In what follows, we will consider the Itô interpretation. The particular example we will consider in this work is the power-law heterogeneous diffusion process, where the diffusion coefficient is given by a power law of the position [66, 67, 68, 69, 70, 71], that is

$$D(x) = D_0 |x|^\alpha \tag{2.12}$$

with $\alpha < 2$. The MSD of this process is [71]

$$\langle x(t)^2 \rangle = \left[D_0 (2-\alpha)^2 \right]^{\frac{2}{2-\alpha}} \frac{\Gamma\left(\frac{3-\alpha}{2-\alpha}\right)}{\Gamma\left(\frac{1-\alpha}{2-\alpha}\right)} t^{\frac{2}{2-\alpha}}. \tag{2.13}$$

Thus, for $\alpha < 0$ we find subdiffusion, and superdiffusion for $\alpha > 0$. Brownian motion with normal diffusion emerges for $\alpha = 0$, and $\alpha = 1$ produces diffusive ballistic motion. This model has been used successfully in several contexts [68], such as Richardson diffusion in turbulence [51], mesoscopic transport in disordered porous media [72], and diffusion on random fractal structures [73], random walks in an inhomogeneous medium [74, 75, 76], chemical reactions [77], diffusion (in momentum space) in laser cooling processes [78], dissipative particle dynamics [79], vortex-antivortex annihilation [80], biophysics [81, 82, 83] e.g. measurements of proteins' diffusivity in mammalian cells [83], and modeling of $1/f$ noise [84].

The corresponding Fokker-Planck equation for $P(x,t)$ in the Itô interpretation is

$$\frac{\partial P(x,t)}{\partial t} = D_0 \frac{\partial^2}{\partial x^2} \left[|x|^\alpha P(x,t) \right], \tag{2.14}$$

Model	$\langle \mathbf{x}(\mathbf{t})^2 \rangle$	**Diffusion type**	**Source of anomalous diffusion**
BM	$\sim t$	standard	none
CTRW	deppends on $\varphi(\tau)$ and $\Phi(\Delta)$	sub. for $\varphi(\tau) \sim \tau^{-1-\alpha}$, with $\alpha \in (0,1)$	heavy-tailed waiting times
SBM	$\sim t^{\alpha}$, $\alpha \in (0,2)$	sub. for $\alpha \in (0,1)$, super. for $\alpha \in (1,2)$	time dependent diffusion coefficient
fBM	$\sim t^{2H}$, $H \in (0,1)$	sub. for $H \in (0,1/2)$, super. for $H \in (1/2,1)$	long-range temporal correlations
HDP	$\sim t^{\frac{2}{2-\alpha}}$, $\alpha < 2$	sub. for $\alpha < 0$, super. for $\alpha > 0$	power-law spatial heterogeneity

Table 2.1: Summary of the main features of the different diffusion processes discussed in this section.

whose solution is (see Appendix C in Ref. [71])

$$P(x,t) = \frac{N}{|x|^{\alpha} t^{\frac{1-\alpha}{2-\alpha}}} e^{-\frac{|x|^{2-\alpha}}{D_0(2-\alpha)^2 t}}, \tag{2.15}$$

where

$$N = \frac{(2-\alpha)^{\frac{\alpha}{2-\alpha}}}{2D_0^{\frac{1-\alpha}{2-\alpha}} \Gamma\left(\frac{1-\alpha}{2-\alpha}\right)}.$$

However, not all spatial heterogeneity gives rise to anomalous diffusion, for example, a choice of the spatial dependence of the diffusion coefficient as a piecewise constant [85, 86, 87]

$$D(x) = \begin{cases} D_-, & x < 0 \\ D_+, & x > 0 \end{cases} \tag{2.16}$$

With $D_{\pm} > 0$, yields a MSD in the Itô interpretation

$$\langle x(t)^2 \rangle = 2\sqrt{D_+ D_-}\, t, \tag{2.17}$$

which is diffusive [86] for any $D_+, D_- > 0$. This form of position-dependent diffusion coefficient was previously used to find the solution of the Langevin equation in an open system, without a trapping potential [86].

2.2 First-passage times

Many processes in nature rely on a variable reaching a specific value for the first time [24, 88, 89] , from the firing of a neuron, to a chemical reaction, to the search for a target by an animal [27]. In those situations, the characterization of the MSD or the propagator of the process is not what gives the most insights, but instead one turns to the first-passage time (FPT) of the process, which is the random variable that measures

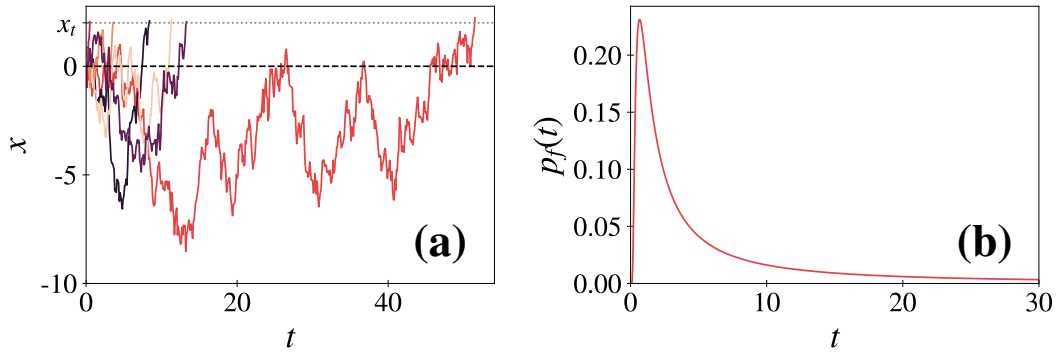


Figure 2.5: **Example first-passage time for Brownian trajectories.** (a) 6 Brownian trajectories that end when they reach x_t. (b) FPT PDF Eq. (2.18) for Brownian trajectories. In both figures $D = 1$, $x_0 = 0$, and $x_t = 2$.

the time it takes for a stochastic process to reach a predefined state or threshold for the first time [24]. The distribution of the arrival times, namely the FPTs and, in particular, their mean value, the MFPT, can provide insights into the underlying dynamics of the system and are often used to characterize the efficiency of search processes, reaction kinetics, and other phenomena where timing is crucial.

First-passage densities $p_f(t)$ can be obtained in a variety of ways, one of which is by introducing an absorbing boundary at the target state and then writing the Fokker–Planck equation for the probability density of the process $P(x,t)$ with such boundary condition [24]. A well-known result of particular interest for this work is that the FPT distribution of a Brownian particle with diffusion coefficient D starting at x_0 to reach a target x_t in an unbounded domain, as illustrated in Fig. 2.5(a), is given by [24]

$$p_f(t) = \frac{|x_t - x_0|}{\sqrt{4\pi D t^3}} \exp\left(-\frac{(x_t - x_0)^2}{4Dt}\right) \sim \frac{1}{t^{1+1/2}} \quad \text{as} \quad t \to \infty. \tag{2.18}$$

From this distribution, plotted in Fig. 2.5(b), we get that the MFPT of a Brownian particle to reach a target in an unbounded domain is infinite. Indeed,

$$\langle T \rangle = \int_0^\infty t p_f(t)\, dt \sim \int_0^\infty t^{-3/2} t\, dt = 2t^{1/2}\Big|_0^\infty = \infty.$$

Related to the FPT is the survival probability, which is the probability that a stochastic process has not yet reached a predefined state or threshold by a given time. The survival probability is closely related to the FPT distribution, and in many cases, it can be easier to compute than the FPT distribution itself. Then the survival probability $G(t)$ can be expressed as:

$$G(t) = 1 - \int_0^t p_f(t')dt', \tag{2.19}$$

or

$$p_f(t) = -\frac{\partial G(t)}{\partial t}. \tag{2.20}$$

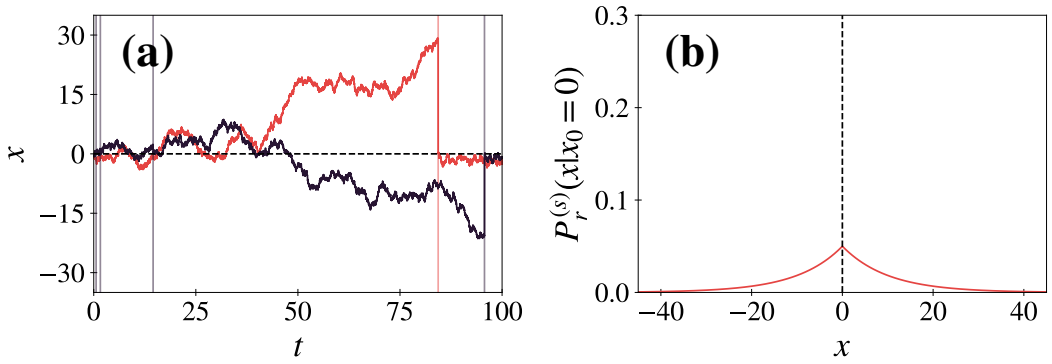


Figure 2.6: **Example resetting for Brownian trajectories.** (a) 2 Brownian trajectories with resetting, the vertical lines indicate the times when a reset happens. (b) PDF with resetting Eq. (2.23) for Brownian particles. For both figures $D = 1$, $x_0 = 0$, and reset rate $r = 0.01$.

We can further write the MFPT in terms of the survival probability as:

$$\langle T \rangle = \int_0^\infty t p_f(t) dt = \int_0^\infty G(t) dt = G(s=0), \tag{2.21}$$

where $G(s=0)$ is the Laplace transform of the survival probability evaluated at $s = 0$, and assuming $\lim_{t\to\infty} tG(t) = 0$.

2.3 Stochastic resetting

From the discussion above, we have seen that for a standard BM the mean search time of a target is infinite in unbounded domains. However, there are mechanisms that can modify this behavior; and stochastic resetting is one such mechanism. By means of stochastic resetting, a stochastic process is interrupted at random times and brought back to a prescribed state, which is often, but not necessarily, its initial condition. This mechanism has been studied in different contexts [90, 91, 92, 93, 94, 95, 96, 97, 98, 99], the reason being that, by restarting the evolution of the process, resetting can modify in a fundamental way how the spatial domain is explored.

The idea was first introduced for standard BM [90, 100], and it has later been extended to many other stochastic processes, such as Lévy flights [101, 102, 103], run-and-tumble motion [104], subdiffusive processes [105], diffusion in various potentials [93, 106, 107], among others. Stochastic resetting is appealing in many contexts, for example in search optimization problems, where it has been seen experimentally that halting a process and restarting it anew helps speed up the search process [90], since resetting can prevent trapping in metastable states. Another field of application where resetting has drawn interest is in the study of chemical and biochemical reactions, where the binding/unbinding dynamics of chemical species can be thought of as a resetting problem [106, 108]. Moreover, one can think that a physical phenomenon undergoing a sudden change over time, in a timescale substantially shorter than the typical dynamical timescale of such a system, can be, in a way, described by stochastic resetting [109].

In many situations, one of the main consequences of stochastic resetting is the emergence of NESSs. In addition, under suitable conditions, resetting can be used to optimize search processes by minimizing the MFPT [110, 111]. Both of these features arise because the particle is repeatedly returned to a particular position or region. Similar effects can also appear in heterogeneous media with space-dependent diffusion coefficients following a power law [68], or in the presence of external force fields [112, 113], where the system can also reach a steady state and display a finite MFPT.

A seminal and particularly influential contribution to this field was the work of Evans and Majumdar [100]. In their work, they considered a Brownian particle initially located at x_0 at time $t = 0$, diffusing with diffusion coefficient D, and resetting to its initial position at random times drawn from an exponential distribution re^{-rt}, where r is the reset rate. We exemplify this process in Fig. 2.6(a), where we plot the resetting process of two Brownian trajectories, where the colored vertical lines represent the resetting events for each particular trajectory. In their work, they proposed that the propagator of the particle follows the following master equation

$$\frac{\partial P_r(x,t|x_0)}{\partial t} = D\frac{\partial^2 P_r(x,t|x_0)}{\partial x^2} - rP_r(x,t|x_0) + r\delta(x-x_0), \tag{2.22}$$

the first two terms correspond to the standard diffusion equation, see Eq. (2.1), while the last two account for the resetting mechanism: the term $-rP_r(x,t|x_0)$ accounts for the loss of probability due to resetting, while the term $r\delta(x-x_0)$ accounts for the gain of probability at the reset position.

By solving the above equation, they found that the system reaches a NESS, with a non-Gaussian distribution given by

$$P_r^{(s)}(x|x_0) = \frac{1}{2}\sqrt{\frac{r}{D}}e^{-\sqrt{\frac{r}{D}}|x-x_0|}. \tag{2.23}$$

In Fig. 2.6(b) we represent the NESS on the same scale as Fig. 2.1 for easier comparison with the reset-free case. From the existence of this NESS, it follows that the MSD in the long-time limit of the process with resetting, instead of following Eq. (2.3), it converges to a constant value

$$\langle x^2\rangle = \int_{-\infty}^{\infty} x^2 P_r^{(s)}(x|0)\,dx = 2\frac{D}{r}, \quad \text{as} \quad t\to\infty, \tag{2.24}$$

thus, the range in which the diffusive particles move is, in this case, finite. This feature of the exponential resetting effectively delimits a range where the particles are localized, which is of interest in some ecological applications, where this length scale can define a home range of organisms.

On top of the NESS and MFPT, in their work [100], Evans and Majumdar also find the first passage properties to the origin, $x_t = 0$, of a BM with resetting to x_0 that starts at $x > 0$. They write the following backward master equation for the survival probability $G(x,t)$ of the process

$$\frac{\partial G(x,t)}{\partial t} = D\frac{\partial^2 G(x,t)}{\partial x^2} - rG(x,t) + rG(x_0,t), \tag{2.25}$$

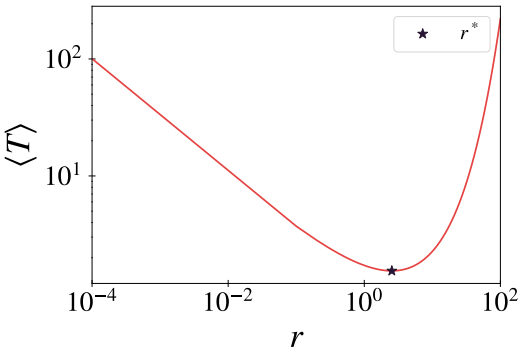


Figure 2.7: **MFPT of a BM with reset rate r.** Eq. (2.26) $x_0 = 0$, $D = 1$, and $x_t = 1$.

with boundary and initial conditions $G(0,t) = 0$, $G(x,0) = 1$. Notice that the second term on the right-hand side (r.h.s.) corresponds to the loss of probability at x due to resetting to the initial condition from x to x_0, and the fourth term is the corresponding gain at x_0. By solving this equation in Laplace space, they find that for Brownian motion with Poissonian resetting, the MFPT to reach a target at x_t is given by [1]

$$\langle T \rangle = \frac{1}{r}\left(e^{\sqrt{\frac{r}{D}}|x_0 - x_t|} - 1\right). \tag{2.26}$$

Now we see that in the presence of exponential resetting, not only is the MFPT finite, but also that it can be optimized by tuning the reset rate r. In Fig. (2.7) we show the value of the MFPT as a function of the reset rate r. From the figure and from Eq. (2.23) we can see that the value of $\langle T \rangle$ diverges as $r \to 0$, and $r \to \infty$ this is because at low values of the reset rate the effect of resetting is very small, and the system behaves as if it was a reset-free situation, for which the MFPT is infinite, see Sec. 2.2. On the other hand, for frequent enough resetting, the particle is unable to leave the vicinity of the resetting point. Notice that at $r \to \infty$ Eq. (2.24) goes to 0, and thus the finding of the target is also hindered. Therefore, there is a value of r that optimizes the MFPT, which is given by $r^* = z^{*2} D/|x_0 - x_t|^2$, with $z^*/2 = 1 - e^{-z^*}$, where $z^* \approx 1.59362$ [100].

The previous discussion corresponds to the particular case of Poissonian resetting. More generally, however, one can consider processes where the resetting times are drawn from a generic distribution $\phi(t)$ with Poissonian resetting being a particular case [90, 109]. When the resetting distribution $\phi(t)$ is not exponential, the properties discussed above (the presence of a non-equilibrium steady state, the optimization of the MFPT, or a constant MSD at long times) are not necessarily guaranteed, and depend on the properties of the resetting distribution. For example, for resetting times drawn from a power law $\tau^{-1-\gamma}$ if $\gamma < 1$, that is, when the first moment is infinite, resetting does not optimize the MFPT, nor does a steady state distribution exist [109]. Such broad tail distributions for the resetting rate can represent extreme events, like a sudden drop in population size due to catastrophes, or crashes in stock exchanges [109].

The generalization of resetting processes with arbitrary resetting distributions is naturally described in terms of renewal theory, since each reset interrupts the evolution and makes the process start again from the reset position. Then, the full trajectory can

[1] In their original work $x_t = 0$, here we write the MFPT in a more general way, for an arbitrary x_t.

be decomposed into intervals between consecutive reset events, and the dynamics with resetting can be related to the corresponding reset-free dynamics, see [90, 114]. In this formulation, the propagator $P_r(x,t|x_0)$ of the process with resets is related to the propagator of the free process $P_0(x,t|x_0)$ as

$$P_r(x,t|x_0) = \phi^*(t)P_0(x,t|x_0) + \int_0^t \phi(t')P_r(x,t-t'|x_r)dt', \tag{2.27}$$

where $\phi(t)$ is the reset PDF, $\phi^*(t) = \int_t^\infty \phi(t')dt'$ is the probability that no reset has occurred up to time t, and x_r is the reset position. Written in this way, this is known as a first renewal equation, where the first term accounts for the trajectories where no resetting event has occurred up to time t, and the second term is the contribution of trajectories with the first reset occurring between time t' and $t'+dt'$.

Another way of writing Eq. (2.27) is considering the last reset instead of the first one, which leads to the last renewal equation

$$P_r(x,t|x_0) = \phi^*(t)P_0(x,t|x_0) + \int_0^t K(t')\phi^*(t-t')P_0(x,t-t'|x_r)dt', \tag{2.28}$$

where $K(t')$ is the probability density for a reset to occur in $(t',t'+dt']$ and $\phi^*(t-t')$ is the probability that there are no further resets after this. $K(t')$ is related to the reset PDF through its Laplace transform $K(s) = \mathscr{L}[K(t')]_{t'\to s} = \phi(s)/(1-\phi(s))$ [90]. Notice that, unlike the first renewal equation, now the reset-free propagator is inside the integral. It can be shown that Eqs. (2.27) and (2.28) are equivalent [90].

Analogously, one can get the first and the last renewal equations for the survival probability $G_r(x_0,t)$ in the presence of an absorbing target for the process with resetting [90] in terms of the survival probability of the reset-free process $G_0(x_0,t)$. The first renewal equation reads

$$G_r(x_0,t) = \phi^*(t)G_0(x_0,t) + \int_0^t \phi(t')G_0(x_0,t')G_r(x_r,t-t')dt', \tag{2.29}$$

where again the first term accounts for the trajectories in which there has been no resetting. The second term represents trajectories in which resetting has occurred and we have a convolution of survival probabilities: survival starting from x_0 with no resetting up to time t' (the time of the first reset) and survival starting from x_r with resetting during $t-t'$.

If the resetting is Poissonian $\phi(t) = re^{-rt}$, there is a very simple relation in Laplace space between the survival probability with and without reset [90]

$$G_r(x_0,s) = \frac{G_0(x_0,r+s)}{1-rG_0(x_r,r+s)}. \tag{2.30}$$

This relation proves useful since many processes had been studied in their reset-free version, and, for the Poissonian resetting case, the properties of the process with resets can be straightforwardly unveiled by means of Eq. (2.30).

Further extensions of the resetting problem have been, and are being, studied. Processes where resetting is non-instantaneous [115, 116], or the particle has a refractory period after the reset event [117]. Systems with space-dependent reset rates [118, 119],

time-dependent reset rates [96, 114], or the cost associated to resetting [120] are also being discussed. Moreover, in many-body systems with non-interacting particles, when they are subjected to simultaneous resetting at constant rates, long-range correlations emerge [121]. It is worth mentioning that resetting is not always beneficial to the search process [106], as we have seen for the case of Poissonian resetting, where too frequent resetting can hinder the search process. Another situation might be when the searcher moves deterministically at a constant speed, and resetting only brings it back to the initial position, thus hindering the search process. In general, the effect of resetting on the search process will depend on the properties of the underlying dynamics, and on the resetting mechanism itself.

2.4 Stochastic functionals and the Feynman-Kac formula

Besides observables such as the MSD or the first-passage time, stochastic trajectories can also be characterized through other quantities accumulated along the path. These quantities are known in general as stochastic functionals [122, 123]. The paradigmatic example is the Brownian functional, defined as the time integral over the path of a Brownian walker. More generally, the stochastic functional can be defined over a general random walker, Brownian or not. The stochastic functional, then, is defined as the time integral of a function, often positive, of the path of a random walk up to a measurement time. Consider a random walk $x(t)$, and a non-negative function $U(x)$, then the stochastic functional $Z(t)$ is

$$Z(t) = \int_0^t U(x(t'))dt', \tag{2.31}$$

where t is the measurement time. Since $x(t)$ is a random variable, $Z(t)$ is also a random variable, and its distribution $Q(Z,t|x_0)$ can provide insights into the underlying dynamics of the system. Moreover, the measurement time t can, in turn, be a random variable itself, for example, if it corresponds to the FPT of the process to reach a certain state. This type of functionals are known as first-passage functionals, and are useful to extract information about systems that do not have a predefined lifetime, such as DNA breathing dynamics [124].

The prototypical example of a stochastic functional is the so-called Brownian functional, when the random walk is a BM with diffusion coefficient D. In 1949 [25] Kac, influenced by Feynman's thesis about Schrödinger's equation, found that the statistical properties of one-dimensional Brownian functionals can be studied by the Feynman-Kac (FK) formula, which is a Schrödinger-like equation derived by Kac following Feynman's path integral method. Since then, Brownian functionals have found widespread applications across diverse fields, including probability theory [125, 126], finance [127], disordered systems and mesoscopic physics [128], computer science [129], hydrodynamics [130], and meteorology [131]. These ideas have subsequently been extended to subdiffusive dynamics [122, 132], within the context of fractional calculus. By means of the FK formula, one can compute the PDF of the stochastic functional $Z(t)$ [122, 129]. The backward FK formula states that the characteristic



Figure 2.8: **Half occupation time.** The trajectory is a BM with $D = 1$ and in gray we highlight when $x > 0$.

function of the positive functional $Z(t)$ can be obtained by solving the following partial differential equation:

$$\frac{\partial Q(p,t|x_0)}{\partial t} = D\frac{\partial^2 Q(p,t|x_0)}{\partial x_0^2} - pU(x_0)Q(p,t|x_0), \tag{2.32}$$

where $Q(p,t|x_0)$ is the Laplace transform with respect to Z of the PDF $Q(Z,t|x_0)$, which satisfies the initial condition $Q(p,t=0|x_0) = 1$. Since the spatial derivatives are taken with respect to the initial position, Eq. (2.32) is the backward FK equation.

In order to solve the FK equation, it is often convenient to take a further Laplace transform with respect to time, which gives

$$sQ(p,s|x_0) - 1 = D\frac{\partial^2 Q(p,s|x_0)}{\partial x_0^2} - pU(x_0)Q(p,s|x_0). \tag{2.33}$$

This equation needs to be solved with the appropriate boundary conditions, which depend on the specific functional under study, and hence on every individual $U(x)$. Once solved, in principle one can obtain the PDF of the functional $Z(t)$ by performing the double inverse Laplace transform with respect to p and s, which is not generally straightforward.

2.4.1 Half occupation time

Some of the widely studied functionals in different fields are the occupation times [70, 129, 133, 134, 135, 136, 137], which are defined as the time that a random walk spends in a given region of space. It is of particular interest the occupation of the positive half-line, namely the half-occupation time T_+ of a Brownian particle, as illustrated in Fig. 2.8, where we present a Brownian trajectory and highlight in gray when $x > 0$. For this functional, $U(x) = \Theta(x)$, where $\Theta(x)$ is the Heaviside step function, then

$$T_+(t) = \int_0^t \Theta(x(t'))dt'. \tag{2.34}$$

The half-occupation time has been widely studied in the context of BM, and its distribution is given by the celebrated arcsine law given by Lévy [138], which states that the PDF of $y = T_+/t$ at sufficiently large t is given by

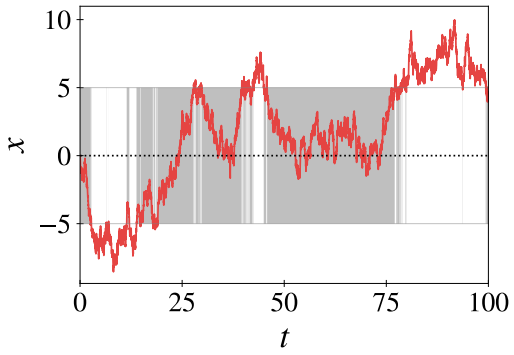


Figure 2.9: **Occupation time in an interval.** The trajectory is a BM with $D = 1$ and in gray we highlight when $-5 < x < 5$.

$$Q(y|0) = \frac{1}{\pi\sqrt{y(1-y)}}. \tag{2.35}$$

Note that this distribution is bimodal with peaks at $y = 0$ and $y = 1$, which means that, while the average time spent by the collective of Brownian particles on the positive half-line is $y = 1/2$, the distribution of the occupation time is such that it is more likely that a Brownian particle spends a large fraction of time on one side of the origin than to spend equal time on both sides. Indeed, the first and second moments of this distribution are

$$\langle T_+(t)\rangle = \frac{1}{2}t, \qquad \langle T_+(t)^2\rangle = \frac{3}{8}t^2. \tag{2.36}$$

Extensions of this law have been derived beyond the Brownian case, the most relevant for this work being applied to renewal processes with power-law waiting times with exponent α, this includes the CTRW with power-law waiting times as a particular case [139, 140, 141]. In this case, the distribution of $y = T_+/t$ at sufficiently large t is given by the Lamperti PDF

$$Q(y|0) = \frac{\sin(\alpha\pi/2)}{\pi}\frac{[y(1-y)]^{\frac{\alpha}{2}-1}}{y^\alpha + (1-y)^\alpha + 2[y(1-y)]^{\frac{\alpha}{2}}\cos(\alpha\pi/2)}. \tag{2.37}$$

Again, this distribution is still bimodal with peaks at $y = 0$ and $y = 1$, which means that a single trajectory spends a larger fraction of time on one side of the origin than on the other. However, its first two moments are [140]

$$\langle T_+(t)\rangle = \frac{1}{2}t, \qquad \langle T_+(t)^2\rangle = \frac{4-\alpha}{8}t^2, \quad 0 < \alpha < 1 \tag{2.38}$$

where we see again that collectively the average time spent on the positive half-line is $y = 1/2$, which is not the representative behavior of any single trajectory.

2.4.2 Occupation time in an interval

Another functional of interest is the occupation time in an interval T_a [133, 141, 142, 143, 144], which is defined as the time that a random walk spends in a given interval of space, which in this work we have considered the symmetric interval $[-a, a]$, as

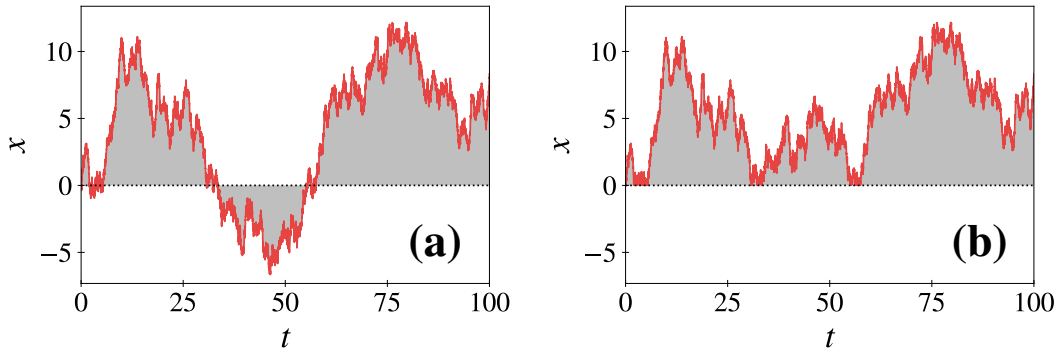


Figure 2.10: **Area under the trajectory.** (a) area. (b) absolute area. In both panels, the trajectory is a BM with $D = 1$.

illustrated by Fig. 2.9. In this case, $U(x) = \Theta(a - |x|)$, where $\Theta(x)$ is the Heaviside step function, and the occupation time in the interval is given by

$$T_a(t) = \int_0^t \Theta(a - |x(t')|)dt'. \tag{2.39}$$

In [8] we showed that for a free Brownian particle with diffusion coefficient D, the PDF of the half occupation time in an interval follows, in the long time limit, a half Gaussian

$$Q(T_a, t|0) \approx \left(\frac{D}{\pi a^2 t}\right)^{1/2} \exp\left(-\frac{DT_a^2}{4a^2 t}\right), \tag{2.40}$$

with first and second moments, in the long-time limit given by

$$\langle T_a(t)\rangle \approx \frac{2a}{\sqrt{\pi D}} t^{1/2}, \qquad \langle T_a(t)^2\rangle \approx \frac{2a^2}{D} t. \tag{2.41}$$

2.4.3 Area under the trajectory

Finally, another functional of interest is the area under the trajectory A [129], which is defined as the time integral of the position of a random walk, as illustrated in Fig. 2.10. This functional is defined as

$$A(t) = \int_0^t x(\tau)d\tau, \tag{2.42}$$

where, in this case, $U(x) = x$. If one considers the absolute value of the position, then we get the absolute area under the trajectory, which is defined as

$$\mathscr{A}(t) = \int_0^t |x(\tau)|d\tau, \tag{2.43}$$

where now $U(x) = |x|$. These functionals have been studied particularly for the standard BM [131, 145, 146, 147] in DNA breathing dynamics [124]. The absolute area

functional was first studied in the context of economics [148] and later extensively in probability [145, 147]. The same functional was also studied in the context of electron-electron and phase coherence in a one-dimensional weakly disordered quantum wire [149]. These functionals are closely related to integrated random motion and random acceleration problems [130, 150].

For the standard BM the moments of the area read

$$\langle A(t)\rangle = 0, \qquad \langle A(t)^2\rangle = \frac{2Dt^3}{3}. \tag{2.44}$$

This result was originally derived by Lévy [151]. Further, the distribution of the area under the trajectory of a Brownian is given by

$$Q(A,t|0) = \frac{1}{\sqrt{4\pi Dt^3/3}} e^{-\frac{3A^2}{4Dt^3}}. \tag{2.45}$$

Regarding the absolute area of a Brownian motion, the characteristic function of $\mathscr{A}(t)$ and its moments were derived in [145, 147] but the exact Laplace inversion to find $P(\mathscr{A},t)_{\mathrm{BM}}$ is not known. However, using large deviation theory it has been possible to obtain some scaling properties of $P(\mathscr{A},t)_{\mathrm{BM}}$ [131]. Thus, the first and second moments of the absolute area of a Brownian motion are given by

$$\langle \mathscr{A}(t)\rangle = \frac{4}{3}\sqrt{\frac{D}{\pi}} t^{\frac{3}{2}}, \quad \langle \mathscr{A}(t)^2\rangle = \frac{3Dt^3}{4}. \tag{2.46}$$

2.5 Ergodicity and ergodicity breaking

The ergodic hypothesis is a fundamental concept in statistical mechanics, which states that the time average of a physical observable over a single trajectory of a system is equal to the ensemble average over many realizations of the system. This implies that the long-term behavior of a single trajectory can be representative of the behavior of the entire ensemble. In the context of stochastic functionals, ergodicity implies that the time average of a functional over a single trajectory will converge to the ensemble average as the measurement time goes to infinity.

However, many systems deviate from the ergodic hypothesis and are known as non-ergodic, such as spin glasses [152], or blinking quantum dots [140, 153]. In the classical setting of statistical mechanics, ergodicity is broken when the phase space is decomposed into different regions, where the system cannot access one part of the phase space if it started in a different region. Yet, there is a different type of non-ergodicity, often called weak-ergodicity breaking. Introduced by Bouchaud in 1992 in the context of glassy dynamics [152], weak ergodicity breaking refers to systems where the phase space is not broken a priori, but nonetheless a long trajectory fails to explore the entirety of the phase space in a finite time [22, 152, 154, 155, 156]. This type of ergodicity breaking is found in systems whose dynamics are characterized by power-law waiting times, such as the average trapping time in the theory of laser

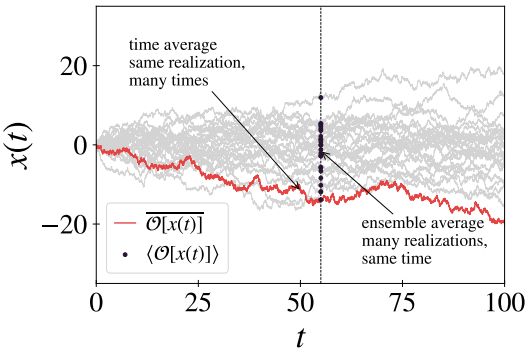


Figure 2.11: **Time and ensemble averages.** The trajectories are a BM with $D = 1$.

cooling [140, 157]. It is in this weak sense that we study ergodicity breaking in this thesis. Below we define the EB parameter [158], which is a dimensionless measure of the ergodicity of a system regarding a particular observable.

To define EB, let us first consider a stochastic trajectory $x(\tau)$ observed from $\tau = 0$ up to time $\tau = t$. Next, consider an observable $\mathscr{O}[x(\tau)]$, a function of the trajectory $x(\tau)$. Since $x(\tau)$ is stochastic in nature, the observable $\mathscr{O}[x(\tau)]$ will also be fluctuating between the realizations. If $P(x,t)$ is the propagator of the process, that is the probability to find the walker at the point x at time t, and if the observable is integrable with respect to the density $P(x,t)$, then the ensemble average of $\mathscr{O}[x(t)]$ is given by

$$\langle \mathscr{O}[x(t)] \rangle = \int_{-\infty}^{\infty} \mathscr{O}[x] P(x,t) dx. \tag{2.47}$$

On the other hand, the time average of $\mathscr{O}[x(t)]$ is defined as

$$\overline{\mathscr{O}[x(t)]} = \frac{1}{t} \int_0^t \mathscr{O}[x(\tau)] d\tau. \tag{2.48}$$

In Fig. 2.11, we illustrate the difference between time and ensemble averages taking BM trajectories as an example. As discussed above, this observable is said to be ergodic if

$$\langle \mathscr{O} \rangle = \lim_{t \to \infty} \overline{\mathscr{O}}. \tag{2.49}$$

An implication of this property is that if $\mathscr{O}[x(\tau)]$ is ergodic, then its time average $\overline{\mathscr{O}}$ is not a random variable. As a consequence, the PDF of $\overline{\mathscr{O}}$ in the long-time limit is given by

$$Q(\overline{\mathscr{O}}, t \to \infty) = \delta\left(\overline{\mathscr{O}} - \langle \mathscr{O} \rangle\right). \tag{2.50}$$

For non-ergodic observables, since $\overline{\mathscr{O}}$ is stochastic, its variance $\mathrm{Var}(\overline{\mathscr{O}})$ is non-zero in the long-time limit. Otherwise, for an ergodic observable $\mathrm{Var}(\overline{\mathscr{O}}) = 0$ in the long-time limit. With this, one can define the EB parameter [158] in the following way

$$\mathrm{EB} = \lim_{t \to \infty} \frac{\mathrm{Var}(\overline{\mathscr{O}})}{\langle \overline{\mathscr{O}} \rangle^2} = \lim_{t \to \infty} \frac{\left\langle \overline{\mathscr{O}}^2 \right\rangle - \langle \overline{\mathscr{O}} \rangle^2}{\langle \overline{\mathscr{O}} \rangle^2}. \tag{2.51}$$

For ergodic observables, it is clear that EB $= 0$, then any nonzero EB is a measure of non-ergodicity. When the observable considered is a stochastic functional as defined in Eq. (2.31) $\mathscr{O}[x(t)] = U[x(t)]$, then Eq. (2.48) becomes

$$\overline{\mathscr{O}[x(t)]} = \frac{1}{t}\int_0^t U[x(\tau)]d\tau = \frac{Z(t)}{t}, \tag{2.52}$$

and therefore, the first and second moments of the functional

$$\left\langle \overline{\mathscr{O}} \right\rangle = \frac{\langle Z(t)\rangle}{t}, \quad \left\langle \overline{\mathscr{O}}^2 \right\rangle = \frac{\left\langle Z(t)^2 \right\rangle}{t^2}. \tag{2.53}$$

Finally, from (2.51), the ergodicity breaking parameter can be expressed in terms of the first and second moments

$$\mathrm{EB} = \lim_{t\to\infty} \frac{\left\langle Z(t)^2 \right\rangle}{\langle Z(t)\rangle^2} - 1. \tag{2.54}$$

Note from the definition (2.54) that to study the ergodic properties of a random walk using the ergodicity breaking parameter, it is necessary to choose a specific observable $\mathscr{O}$ [159, 160, 161]. A functional that traditionally has been used to study the ergodic properties of a system is the time-averaged mean squared displacement (TAMSD), alongside the MSD; however, complementary metrics have been proposed [162, 163, 164, 165]. In this context, we will focus on the functionals defined in sections 2.4.1, 2.4.2, and 2.4.3: the half occupation time, the occupation time in an interval, and the area, which are relevant for characterizing the ergodic properties of a system. Then, with this definition of the ergodicity breaking parameter, the value of EB for the half occupation time, the occupation time in an interval, and the absolute area one gets for a free Brownian particle

$$\mathrm{EB}(T_+) = \frac{1}{2}, \quad \mathrm{EB}(T_a) = \frac{\pi}{2} - 1, \quad \mathrm{EB}(\mathscr{A}) = \pi\left(\frac{3}{4}\right)^3 - 1. \tag{2.55}$$

Thus, we see that, even for standard diffusion, the ergodicity breaking parameter is different from 0. This means that, for observables such as T_+, T_a, or $\mathscr{A}$, time and ensemble averages cannot be treated as interchangeable, and care must be taken when analyzing experimental results. To understand this feature, let us focus on the observable T_+. As discussed below Eq. (2.35), a trajectory of a Brownian walker typically spends most of its time either on the positive or on the negative half-line. Therefore, for individual trajectories one usually finds either $T_+ \approx t$ or $T_+ \approx 0$, whereas the ensemble average, given by Eq. (2.36), yields $\langle T_+(t)\rangle = t/2$. Thus, at the ensemble level, one could wrongly interpret that a Brownian walker spends half of its time on each side of $x = 0$, while at the single-particle level, many trajectories spend most of their time either at $x > 0$ or at $x < 0$. These discrepancies are what the parameter EB captures, and the higher the value of EB, the larger the difference between time and ensemble averages. In particular, this behavior is related to the divergence of the MFPT

of a free Brownian particle, since part of the ensemble performs long excursions in the half-space where the target is not located, yielding an infinite MFPT. Finally, from Eq. (2.55) we also see that EB computed for different functionals gives different results. This illustrates what we had anticipated, namely that the value of EB is not universal for all observables of the same underlying random walk.

Another quantity of interest to characterize ergodicity is the PDF of the time-averaged observable $\overline{\mathscr{O}[x(t)]}$ around its mean in the long-time limit. For this purpose, lets define the dimensionless random variable

$$\eta = \lim_{t\to\infty} \frac{\overline{\mathscr{O}}}{\left\langle \overline{\mathscr{O}} \right\rangle} \tag{2.56}$$

and from (2.52) and (2.53), the relative time averaged observable $U[x(t)]$ is defined by

$$\eta = \lim_{t\to\infty} \frac{Z(t)}{\langle Z(t) \rangle}. \tag{2.57}$$

Once $Q(Z,t|0)$ is known, the PDF of η follows from

$$Q(\eta) = Q(Z = \eta \langle Z(t) \rangle, t) \langle Z(t) \rangle . \tag{2.58}$$

Note that the variance of η is nothing but the ergodicity breaking parameter:

$$\mathrm{Var}(\eta) = \left\langle \eta^2 \right\rangle - \langle \eta \rangle^2 = \left\langle \eta^2 \right\rangle - 1 = \frac{\left\langle Z(t)^2 \right\rangle}{\langle Z(t) \rangle^2} - 1 = \mathrm{EB}.$$

Therefore, for ergodic observables (EB = 0) one has that the limiting PDF of the time averaged observable is $Q(\eta) = \delta(\eta - 1)$. In the case where the underlying process is a renewal process, the fluctuations of η can be related to the fluctuations of the number of renewal events $N(t)$ up to time t. If the times between consecutive events are i.i.d. random variables, and if these waiting times are given by a power-law PDF $\varphi(t) \sim t^{-1-\alpha}$, with $\alpha \in (0,1)$, then from [68, 141, 158] it is known that in the limit of long times η follows a Mittag-Leffler distribution

$$\lim_{t\to\infty} Q(\eta|0) = \mathscr{M}_\alpha(\eta) = \frac{\Gamma^{1/\alpha}(1+\alpha)}{\alpha \eta^{1+1/\alpha}} \ell_\alpha \left[\frac{\Gamma^{1/\alpha}(1+\alpha)}{\alpha \eta^{1/\alpha}} \right], \tag{2.59}$$

where $\ell_\alpha(z)$ is the one-sided Lévy stable distribution of order α, defined through its characteristic function as

$$\int_0^\infty \ell_\alpha(t) e^{-st} dt = e^{-s^\alpha}, \tag{2.60}$$

see Ref. [166] and references therein for more mathematical details on this function. Indeed, Eq. (2.59) tends to a Dirac delta for $\alpha \to 1$. Finally, the ergodicity breaking parameter EB follows from Eq. (2.59) [158]

$$\mathrm{EB} = 2\frac{\Gamma^2(1+\alpha)}{\Gamma(1+2\alpha)} - 1. \tag{2.61}$$

Notice that for the particular case $\alpha = 1$ Eq. (2.61) is 0, implying an ergodic behavior consistent with the Dirac form of Eq. (2.59).

II Efficiency

3 Intermittent random walks under stochastic resetting 33

3.1 Introduction 34
3.2 The IRW model without resetting . 34
3.3 The IRW model with resetting 40
3.4 Summary of results 49

4 Stochastic resetting to random positions 51

4.1 Introduction 52
4.2 Averaged mean first-passage time 52
4.3 Equivalent resetting point 65
4.4 Fluctuations of the MFPT 69
4.5 Summary of results 72

In this part of the thesis, we mainly focus on search processes, where the relevant quantity is not only how a particle spreads, but how long it takes to find a target. This kind of question appears in many physical and biological applications. A molecule diffusing in a medium may need to find another molecule before a reaction occurs. A protein searching along DNA has to locate a specific binding site. A forager moving in a heterogeneous landscape has to encounter food, and a tracer in a reactive material may be useful only when it reaches a particular region. In all these cases, the efficiency of the process is related to the time needed to complete the search, and this is why the MFPT is a natural observable to quantify it [24, 90, 167, 168].

However, many searchers do not move as simple Brownian particles. In several situations the motion is intermittent, meaning that the walker alternates between phases with different roles. There can be a slow phase in which the target can be detected, and a faster relocation phase which allows the searcher to explore new regions but during which detection is not possible. This type of motion is common in animal locomotion and foraging, but it also appears in protein search on DNA, particle motion close to interfaces, transport in disordered media, and in some algorithmic search strategies [167, 169, 170, 171]. Then, the efficiency of the search depends on the balance between spending enough time searching locally and avoiding the oversampling of the same region. This is the main motivation for studying IRWs, where diffusive and ballistic phases are combined in a minimal model [167, 172, 173, 174].

Another way to improve the efficiency of a search process is to introduce stochastic resetting. If the walker moves for too long without finding the target, a reset can bring it back to a region from where the search is more likely to succeed. This mechanism is relevant for recurrent movement patterns, returns to nests or familiar places, spatial memory, and also for restart protocols in experiments or computational searches [90, 91, 100, 175]. In intermittent walks, resetting can affect not only the position of the walker but also the state in which it restarts. Therefore, the search efficiency can depend on whether the walker is reset to a state where it can detect the target, or to a relocation state, where it first explores new regions.

Finally, in many realistic systems the reset is not made to a single exact point. An animal may return to a known territory rather than to a precise location, and an experimental or algorithmic reset may have some uncertainty. This motivates considering a Brownian searcher that resets to positions drawn from a distribution. The resetting distribution can represent spatial memory, site fidelity, or imperfect control, and introduces a new length scale that can modify the optimal search strategy [176, 177, 178, 179, 180, 181]. Thus, in this first part of the thesis, we address the general question of how is efficiency of a search process affected promoted or hindered.

3

INTERMITTENT RANDOM WALKS UNDER STOCHASTIC RESETTING

In this chapter, we explore the main transport properties of an IRW model combining diffusive and relocation modes and study its dynamics under stochastic Poissonian resetting. We demonstrate that the resetting mechanism leads to a NESS also for the IRW. We further compute the distribution of the FPT to a target along with its mean and show the existence of an optimal reset rate. We prove that because of the resetting mechanism, the initial state of the walker can significantly affect the long-time properties of the search process. Finally, we demonstrate the presence of distinct parameter regimes for the global optimization of the MFPT when ballistic and diffusive movements are in direct competition.

3.1 Introduction 34
3.2 The IRW model without resetting 34
3.2.1 Mean squared displacement 37
3.2.2 First-passage time 38
3.3 The IRW model with resetting 40
3.3.1 Mean squared displacement 41
3.3.2 Non-equilibrium steady state 42
3.3.3 First-passage time 43
3.3.4 Optimal reset rate 45
3.3.5 Global optimization of the MFPT 47
3.4 Summary of results 49

3.1 Introduction

The IRW is a movement model within the class of intermittent search strategies, where organisms alternate between distinct motion modes [173, 182]. In behavioral ecology, such strategies have been studied as mechanisms to optimize search efficiency, both theoretically [183] and experimentally [27, 168, 169, 184].

IRWs extend Brownian motion in multiple contexts [185]. In biology, they have been proposed to describe seed and copepod dispersal [186, 187], or protein site location in DNA under the name of teleportation models [170, 188]. In physical systems, they model particle dynamics at liquid–solid interfaces [189], supercooled liquids [190], colloidal suspensions [191], and disordered media [192, 193, 194, 195], and have been explored in energy minimization algorithms [196]. Connections with self-trapping and self-avoiding mechanisms at microscopic scales have also been suggested [197].

Specifically, the IRW considered here alternates between two phases. The extensive phase consists of fast ballistic relocations, typically insensitive to the presence of targets and mainly serving to reach new regions, with reduced cognitive processing during transit [167]. It is followed by an intensive local search phase, characterized by slower diffusive motion during which targets can be detected upon encounter [167].

Theoretically, IRWs provide efficient search strategies in many scenarios [171, 172, 173, 174, 198, 199, 200]. With Poissonian switching between relocation and diffusion, an optimal balance of switching rates minimizes the mean search time in bounded domains [172]. However, as in Brownian motion, the mean search time diverges in unbounded domains. Stochastic resetting resolves this issue by suppressing arbitrarily long excursions, and potentially enabling search optimization. In biological foraging, resetting captures recurrent returns to nests or previously visited sites [175].

This chapter opens Part II by applying the first-passage and renewal ideas introduced in Chapter 2 to an IRW with diffusive and relocation modes under Poissonian stochastic resetting. We examine how the presence of an unresponsive relocation phase affects first-passage statistics. In Sec. 3.2, we present the IRW model without resetting, compute its MSD, and discuss its first-passage properties. In Sec. 3.3, we introduce Poissonian resetting to the model presented in the previous section and derive its NESS induced by resetting, the modified first-passage statistics, and their dependence on initial conditions, including an analysis of the optimal MFPT and the trade-off between switching rates. In Sec. 3.4, we summarize the main results.

3.2 The IRW model without resetting

The IRW model studied in this chapter follows the standard two-mode intermittent-search construction, with a slow diffusive search phase and a fast nonreactive relocation phase [167, 171, 172]. Specifically, the walker alternates between two modes: a diffusive mode with diffusion coefficient D and a ballistic relocation mode with velocity v. The walker switches from the diffusive to the ballistic mode at a rate τ_D^{-1} and from the ballistic to the diffusive mode at a rate τ_v^{-1}, as portrayed in Fig. 3.1. Let $P_0(x,t)$ be the PDF of finding the walker at position x at time t in the diffusive mode, $P_+(x,t)$ be the PDF of the walker in the ballistic mode with $+v$ velocity, and $P_-(x,t)$ be the PDF

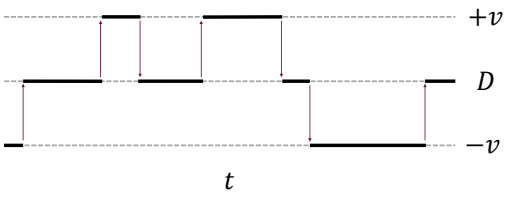


Figure 3.1: **Scheme of the IRW.**

of the walker in the ballistic mode with $-v$ velocity. Then, the full PDF of the walker is given by $P(x,t) = P_0(x,t) + P_+(x,t) + P_-(x,t)$. The evolution of these probabilities is given by the set of coupled Fokker-Planck equations

$$\frac{\partial P_+(x,t)}{\partial t} = -v\frac{\partial P_+(x,t)}{\partial x} - \frac{1}{\tau_v}P_+(x,t) + \frac{1}{2\tau_D}P_0(x,t), \tag{3.1}$$

$$\frac{\partial P_-(x,t)}{\partial t} = v\frac{\partial P_-(x,t)}{\partial x} - \frac{1}{\tau_v}P_-(x,t) + \frac{1}{2\tau_D}P_0(x,t), \tag{3.2}$$

$$\frac{\partial P_0(x,t)}{\partial t} = D\frac{\partial^2 P_0(x,t)}{\partial x^2} + \frac{1}{\tau_v}\big(P_+(x,t) + P_-(x,t)\big) - \frac{1}{\tau_D}P_0(x,t). \tag{3.3}$$

In Eqs. (3.1) and (3.2), the ballistic mode equations, the first term on the r.h.s. accounts for the ballistic relocation, the second for the loss of probability due to walkers switching from the relocation to the diffusive phase, and the last term is the gain of probability due to walkers switching from diffusion to relocation. The factor $1/2$ in the last term implies that a walker in the diffusive mode has an equal probability of switching to right or left ballistic modes, with no preferred direction. In systems where right-left symmetry is broken in the relocation phase, Eqs. (3.1)-(3.3) can be generalized by introducing the corresponding probability p of relocating in one direction and $1-p$ of relocating in the other. In Eq. (3.3), the diffusive equation, the first term on the r.h.s. accounts for the particles diffusing (notice that without the other terms this equation is Eq. (2.1)), the second term is the gain of probability from particles switching from both ballistic phases, and the last term accounts for switching from diffusion to relocation.

Instead of dealing with the set of coupled equations, we can get a single evolution equation for $P_0(x,t)$ by transforming Eqs. (3.1)-(3.3) in space by Fourier ($x \to k$) and time by Laplace ($s \to t$), to get

$$\begin{aligned} sP_0(k,s) - P_0(k,t=0) = \quad & -Dk^2P_0(k,s) + \frac{1}{\tau_D}\left[\frac{(s\tau_v+1)-(s\tau_v+1)^2-(kv\tau_v)^2}{(s\tau_v+1)^2+(kv\tau_v)^2}\right]P_0(k,s) \\ & + \frac{(s\tau_v+1)[P_+(k,t=0)+P_-(k,t=0)]}{(s\tau_v+1)^2+(kv\tau_v)^2} + ikv\tau_v\frac{[P_+(k,t=0)-P_-(k,t=0)]}{(s\tau_v+1)^2+(kv\tau_v)^2}, \end{aligned} \tag{3.4}$$

where $P_i(k,t=0)$ is the Fourier transform of the initial condition at state i. To proceed further, we need to specify the initial condition of the walker. In our work, we deal

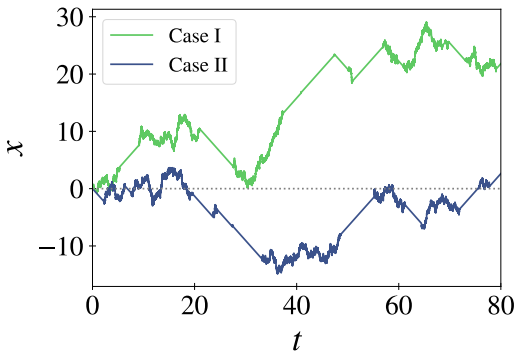


Figure 3.2: **Trajectory of the IRW without resetting.** The model parameters used are $D = v = 1$, $\tau_D = 3.8$, $\tau_v = 3.3$ and $x_0 = 0$.

with two cases: one for walkers that start relocating and the other for walkers that start by diffusing, in this way, we have

- Case I: Diffusive initial condition. Then, $i = 0$, so that $P_0(k, t = 0) = e^{-ikx_0}$ and $P_+(k, t = 0) = P_-(k, t = 0) = 0$.
- Case II: Ballistic initial condition, starting in the $+v$ or $-v$ mode with equal probability. Then, $i = +$ or $i = -$, so that $P_0(k, t = 0) = 0$ and $P_+(k, t = 0) = P_-(k, t = 0) = e^{-ikx_0}/2$.

In the following, we use the superscripts ^{D} and ^{v} (referring to the initial state, diffusive or ballistic, in each case) to identify our results for cases I and II, respectively. The distinction between the different initial conditions is not very relevant for the long-time properties of the reset-free process. However, as we have anticipated in the introduction, and will show in the next section, the presence of resetting will induce the system to revisit the initial condition multiple times, leading to a non-negligible effect of the initial condition on the long-time properties of the process. To illustrate the system we are dealing with, in Fig. 3.2 we show example trajectories for the two initial conditions under consideration.

With the initial conditions specified, we can obtain the full propagator $P(k, s)$ of the process for the two cases from Eq. (3.4) after some algebraic manipulations. For case I, we get

$$P^D(k,s) = P_0^D(k,s)\left[1 + \frac{\tau_v}{\tau_D}\frac{s\tau_v + 1}{(s\tau_v+1)^2 + (v\tau_v k)^2}\right], \tag{3.5}$$

where $P_0^D(k, s)$, the propagator of the diffusing phase when the system at $t = 0$ starts diffusing, is

$$P_0^D(k,s) = \frac{e^{-ikx_0}}{s + Dk^2 + \frac{1}{\tau_D}\left[1 - \frac{s\tau_v+1}{(s\tau_v+1)^2+(vk\tau_v)^2}\right]}. \tag{3.6}$$

Analogously, for case II these expressions are

$$P^v(k,s) = P_0^v(k,s)\left[1 + \frac{\tau_v}{\tau_D}\frac{s\tau_v+1}{(s\tau_v+1)^2+(v\tau_v k)^2}\right] + \tau_v e^{-ikx_0}\frac{s\tau_v+1}{(s\tau_v+1)^2+(v\tau_v k)^2}, \tag{3.7}$$

with

$$P_0^v(k,s) = P_0^D(k,s)\frac{(s\tau_v+1)}{(s\tau_v+1)^2+(vk\tau_v)^2}, \tag{3.8}$$

which is the propagator of the diffusing phase when the initial condition starts by relocating.

3.2.1 Mean squared displacement

To characterize the transport properties of this system, we start by computing its MSD [171, 199]. We can do so by recalling that the moments of a distribution are related to the Fourier transform of the propagator through Eq. (2.4). Because the process is symmetric, it is straightforward to see that the first moment is zero $\langle x\rangle = 0$. The second moment, after inverting the Laplace transform and after taking $x_0 = 0$, reads

$$\langle x(t)^2\rangle \;\; = 2\tfrac{D\tau_D+(v\tau_v)^2}{\tau_D+\tau_v}t + A_1^i + A_2^i e^{-\frac{t}{\tau_v}} + A_3^i e^{-(\frac{1}{\tau_v}+\frac{1}{\tau_D})t}, \tag{3.9}$$

where the coefficients A_j^i with $j = 1,2,3$ and $i = v,D$ take different values depending on whether the walker is initially in the diffusive or relocation state. In particular, if the walker starts in the diffusive state (case I)

$$A_1^D = 2\frac{\tau_v^2}{\tau_D}\frac{D-2\tau_v v^2-\frac{(\tau_v v)^2}{\tau_D}}{(1+\frac{\tau_v}{\tau_D})^2}, \tag{3.10}$$

$$A_2^D = 2(\tau_v v)^2, \tag{3.11}$$

$$A_3^D = -2\frac{\tau_v^2}{\tau_D}\frac{(D+\tau_D v^2)}{(1+\frac{\tau_v}{\tau_D})^2}. \tag{3.12}$$

Instead, if it is initially at the relocation state (case II),

$$A_1^v = 2\frac{{\tau_v}^2(v^2-\frac{D}{\tau_v})-\frac{{\tau_v}^3 v^2}{\tau_D}(1+\frac{\tau_v}{\tau_D})}{(1+\frac{\tau_v}{\tau_D})^2}, \tag{3.13}$$

$$A_2^v = 2\tau_v v^2(\tau_v-\tau_D), \tag{3.14}$$

$$A_3^v = 2\tau_v\frac{(D+\tau_D v^2)}{(1+\frac{\tau_v}{\tau_D})^2}. \tag{3.15}$$

Notice that regardless of the initial condition and the specific values of the A_j^i coefficients, in the long-time limit, this system behaves in a diffusive manner,

$$\langle x(t)^2\rangle \approx 2\frac{D\tau_D+(v\tau_v)^2}{\tau_D+\tau_v}t, \quad \text{as} \quad t\to\infty. \tag{3.16}$$

Indeed, we find the signature diffusive scaling $\langle x^2(t)\rangle \sim t$ with an effective diffusion coefficient $D_{eff} = \frac{D\tau_D+(v\tau_v)^2}{\tau_D+\tau_v}$ [171, 199]. On the other hand, in the short time limit, we

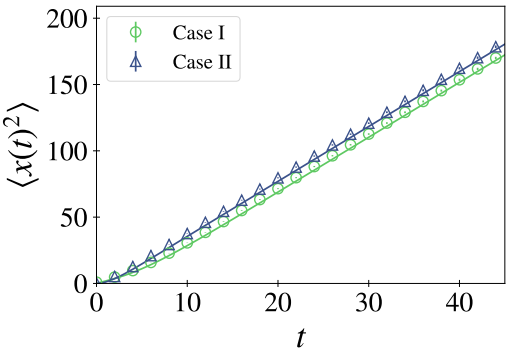


Figure 3.3: **MSD of the IRW without resetting.** The symbols are numerical simulations and in solid lines the analytical prediction Eq. (3.9). The model parameters are $D = v = 1$, $\tau_D = 3.8$, $\tau_v = 3.3$ and $x_0 = 0$. The number of trajectories is 10^5.

recover a diffusive regime for case I and a ballistic one for case II, as one might expect from their initial condition

$$\langle x(t)^2 \rangle^D \approx 2Dt, \quad \text{as} \quad t \to 0, \tag{3.17}$$

$$\langle x(t)^2 \rangle^v \approx \left(v^2 + \frac{D}{\tau_v} \right) t^2 \quad \text{as} \quad t \to 0. \tag{3.18}$$

In Fig. 3.3, we have compared Eq. (3.9) for cases I and II with numerical simulations. We thus see that the switching processes between diffusive and relocation states affect only the transient temporal behavior of the MSD.

3.2.2 First-passage time

As discussed in the previous chapter, the FPT to a target is a widely used measure of the efficiency of a process in which attaining a certain value for the first time is key; this is the case of search processes, with biological foraging being an example. For the IRW studied in this chapter, we work under the assumption that the target can only be detected when the walker is in the diffusive phase, since the speed at which it moves during the relocation phase prevents it from detecting the target [167, 172, 173], and that the process is terminated when the target is found. For simplicity, we consider walkers starting at an initial condition $x = x_0$ and a target located at the origin $x_t = 0$, which works like an absorbing boundary. Now, Eq. (3.3) has to be rewritten to account for the presence of the target, while Eqs. (3.1) and (3.2) remain unchanged, since the target cannot be detected in the relocation phase. The new Eq. for $P_0(x,t)$ is

$$\frac{\partial P_0(x,t)}{\partial t} = D\frac{\partial^2 P_0(x,t)}{\partial x^2} + \frac{(P_+(x,t) + P_-(x,t))}{\tau_v} - \frac{P_0(x,t)}{\tau_D} - p_f(x_0,t)\delta(x), \tag{3.19}$$

where $p_f(x_0,t)$ is the FPT density to the target. Eq. (3.19) is Eq. (3.3) but with the extra term in the r.h.s., which removes the particle once it arrives at the origin. The FPT density can be computed by again transforming (3.19) to Fourier-Laplace space, to get an equation analogous to Eq. (3.4) with an extra $-p_f(x_0,s)$ in the r.h.s..

Next, we can integrate this equation over k and using

$$\frac{1}{2\pi}\int_{-\infty}^{\infty} P_0(k,s)dk = P_0(x=0,s) = 0$$

we can get an expression for the FPT density $p_f(x_0,s)$ in Laplace space. For case I, we get

$$p_f^D(x_0,s) = \frac{I(x_0,s)}{I(x_0=0,s)}, \tag{3.20}$$

where we have defined

$$\begin{aligned} I(x_0,s) &= \tfrac{1}{2\pi}\int_{-\infty}^{\infty} P_0^D(k,s)dk = \tfrac{1}{2\pi}\int_{-\infty}^{\infty} \tfrac{A(k,s)e^{-ikx_0}}{\left[k^2+\lambda_+^2(s)\right]\left[k^2+\lambda_-^2(s)\right]}dk \\ &= \tfrac{1}{2(\lambda_+^2(s)-\lambda_-^2(s))}\left[\tfrac{\psi_-(s)e^{-|x_0|\lambda_-(s)}}{D} - \tfrac{\psi_+(s)e^{-|x_0|\lambda_+(s)}}{D}\right], \end{aligned} \tag{3.21}$$

and $A(k,s)$, $\lambda_\pm$, and $\psi_\pm$ are defined as

$$\begin{aligned} A(k,s) &= \frac{(1+s\tau_v)^2}{D(v\tau_v)^2} + \frac{k^2}{D}, \quad \lambda_\pm = \left[\frac{B(s) \pm \sqrt{B(s)^2 - 4C(s)}}{2}\right]^{1/2}, \\ \psi_\pm(s) &= \frac{(1+s\tau_v)^2}{(v\tau_v)^2\lambda_\pm(s)} - \lambda_\pm(s), \end{aligned} \tag{3.22}$$

and

$$B(s) = \frac{1+s\tau_D}{D\tau_D} + \frac{(1+s\tau_v)^2}{(v\tau_v)^2}, \quad C(s) = \frac{(1+s\tau_v)\left[s\tau_v + s\tau_D(1+s\tau_v)\right]}{D\tau_D(v\tau_v)^2}. \tag{3.23}$$

It is not difficult to show that $B^2(s) > 4C(s)$ so that $\lambda_\pm$ are always real values. From this, after computing the integral $I(x_0,s)$, the FPT density for case I reads in Laplace space

$$p_f^D(x_0,s) = \frac{\psi_-(s)e^{-|x_0|\lambda_-(s)} - \psi_+(s)e^{-|x_0|\lambda_+(s)}}{\psi_-(s) - \psi_+(s)}. \tag{3.24}$$

An identical procedure can be followed to get the FPT density for case II. Now the FPT density is

$$p_f^v(x_0,s) = \frac{J(x_0,s)}{I(x_0=0,s)}, \tag{3.25}$$

where $J(x_0,s)$ is defined as

$$\begin{aligned} J(x_0,s) &= \frac{1}{2\pi}\frac{1+s\tau_v}{D(v\tau_v)^2}\int_{-\infty}^{\infty}\frac{e^{-ikx_0}}{k^4 + B(s)k^2 + C(s)}dk \\ &= \frac{1+s\tau_v}{D(v\tau_v)^2}\frac{\lambda_+(s)e^{-|x_0|\lambda_-(s)} - \lambda_-(s)e^{-|x_0|\lambda_+(s)}}{2\left(\lambda_+^2(s) - \lambda_-^2(s)\right)\lambda_-(s)\lambda_+(s)}. \end{aligned} \tag{3.26}$$

Finally, the FPT for case II reads

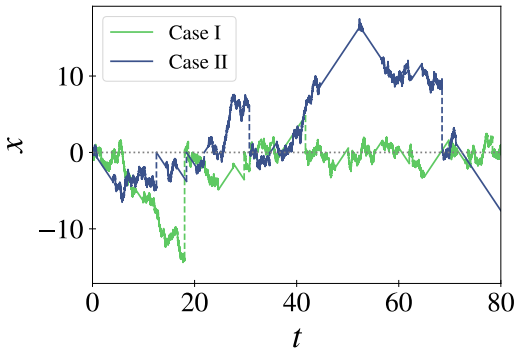


Figure 3.4: **IRW trajectory with resetting.** Sample trajectory of the IRW for case I green and case II blue. The model parameters are $D = v = 1$, $\tau_D = 3.8$, $\tau_v = 3.3$ and $x_0 = 0$.

$$p_f^v(x_0,s) = \frac{1+s\tau_v}{(v\tau_v)^2}\frac{\lambda_+(s)e^{-|x_0|\lambda_-(s)} - \lambda_-(s)e^{-|x_0|\lambda_+(s)}}{\lambda_+(s)\lambda_-(s)(\psi_-(s)-\psi_+(s))}. \tag{3.27}$$

If we compute the MFPT for any of the initial conditions, which we can do by means of Eqs. (2.19) and (2.21), we find that it is infinite. This is analogous to the standard Brownian motion in an unbounded domain, Sec. 2.2. However, in other works, see [167, 172, 174], they have studied the IRW as a means to optimizing a search. The difference is that, in those works, the space is restricted to a confined interval, and thus they find that the relocations help to minimize the MFPT, since they move the searcher to new unexplored regions of space faster, where the target might be located. In unbounded domains, however, as is in our case, the relocations do not suffice to optimize the search.

3.3 The IRW model with resetting

As we have shown, in unbounded domains the MFPT to a hidden target diverges. We expect, and will later demonstrate, that introducing Poissonian stochastic resetting to the initial position renders the MFPT finite, as observed in many previous studies (see, for example, Refs. [91, 100]). As described in Sect. 2.3, the resetting dynamics are defined as follows. The walker starts at position x_0 in either the diffusive state (case I) or the relocating state (case II). After a random time drawn from an exponential distribution $\phi(t) = re^{-rt}$, the walker is instantaneously returned to its initial position corresponding to that case, after which the dynamics restart. Importantly, resetting enforces a revisiting of the initial condition: a walker that initially diffuses resumes diffusion after each reset, while a walker that initially relocates returns to the relocating state.

One could also consider a third scenario in which, after each reset, the walker randomly selects between the diffusive and relocating states with some probability q and $1-q$ respectively. We have examined this case; however, since the propagator in this case would be $P_r(k,s) = qP_r^D(k,s) + (1-q)P_r^v(k,s)$, where the subindex $_r$ indicates the propagator of the process with resetting, many of the results are simple linear combinations of the solutions obtained for cases I and II. For this reason, we restrict our analysis to the two already mentioned initial conditions.

To illustrate the resetting mechanism in the IRW model, we present two sample

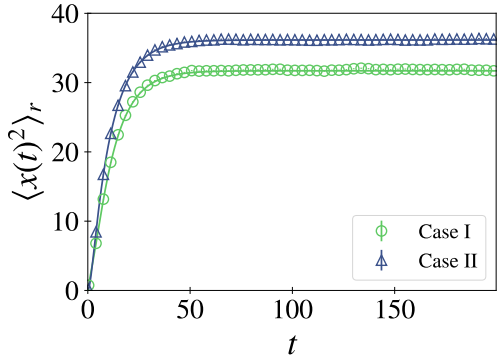


Figure 3.5: **MSD of the IRW with resetting.** The symbols are numerical simulations and in solid lines the analytical prediction Eq. (3.9). The model parameters are $D = v = 1$, $\tau_D = 3.8$, $\tau_v = 3.3$ and $x_0 = 0$. The number of trajectories is 10^5.

trajectories in Fig. 3.4, where dashed lines indicate the occurrence of reset events. A comparison with the reset-free trajectories in Fig. 3.2 seems to indicate that resetting induces localization around x_0, in stark contrast to the unbounded spreading observed in the free process.

To compute observables in the presence of resetting, we rely on the renewal approach, which expresses the propagator of the reset process in terms of the reset-free propagator, as given in Eq. (2.27)

$$P_r(x,t) = e^{-rt}P(x,t) + r\int_0^t e^{-rt'}P_r(x,t-t')\,dt', \tag{3.28}$$

where $P(k,s)$ is the reset-free propagator, given by Eqs. (3.5) and (3.7) for cases I and II, respectively.

3.3.1 Mean squared displacement

To quantify how Poissonian resetting influences the transport properties of the IRW, we begin by computing its MSD. Since the reset-free process is diffusive in the long-time limit, we anticipate a behavior qualitatively similar to that of standard Brownian motion. The convenience of the renewal equation as written in Eq. (3.28) is that it enables the computation of the MSD of the process with reset in terms of the reset-free MSD, Eq. (3.9). Indeed, by multiplying Eq. (3.28) by x^2 and integrating over all x, we get, after taking the Laplace transform, and transforming back to the time domain, that the MSD of the process with resetting is given by

$$\langle x(t)^2 \rangle_r = \int_0^t F(t-t')e^{-rt'}\left\langle x(t')^2\right\rangle dt', \tag{3.29}$$

where $F(t-t')$ is the resetting rate function, defined via its Laplace transform as $F(s) = \frac{1}{1-\phi(s)} = \frac{s+r}{s}$. Inserting this expression for $F(t-t')$ into Eq. (3.29) we get

$$\begin{aligned}\langle x(t)^2 \rangle_r \quad &= 2\frac{D+\frac{\tau_v^2 v^2}{\tau_D}}{(1+\frac{\tau_v}{\tau_D})}\tau_r\left(1-e^{-t/\tau_r}\right) + A_1^i + \frac{A_2^i}{1+\frac{\tau_r}{\tau_v}}\left(1+\frac{\tau_r}{\tau_v}e^{-t\frac{(\tau_r+\tau_v)}{\tau_r\tau_v}}\right) \\ &\quad + \frac{A_3^i\left[1+\frac{\tau_r}{\tau_v}\left(1+\frac{\tau_v}{\tau_D}\right)e^{-t\frac{(\tau_r+\tau_v+\tau_D)}{\tau_D\tau_r\tau_v}}\right]}{1+\frac{\tau_r}{\tau_v}\left(1+\frac{\tau_v}{\tau_D}\right)},\end{aligned} \tag{3.30}$$

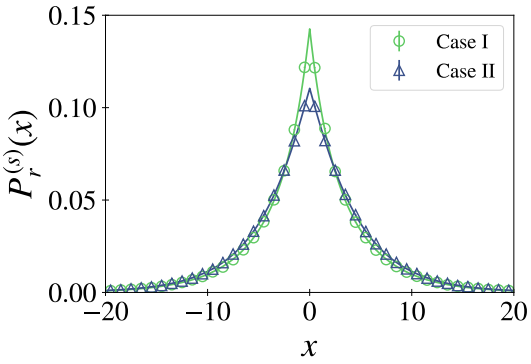


Figure 3.6: **NESS of the IRW with resetting.** The symbols are numerical simulations and the solid lines Eqs. (3.33) and (3.34). The model parameters are $D = v = 1$, $\tau_D = 3.8$, $\tau_v = 3.3$ and $x_0 = 0$. The number of trajectories used for the MSD is 10^6.

where A_j^i are the same coefficients defined in Eqs. (3.10)-(3.12) for case I, and in Eqs. (3.13)-(3.15) for case II. As we had anticipated, in the long-time limit, we obtain that the MSD of the process with resetting reaches a constant value, given by

$$\langle x(t)^2\rangle_r = 2\frac{D+\frac{\tau_v^2 v^2}{\tau_D}}{(1+\frac{\tau_v}{\tau_D})}\tau_r + A_1^i + \frac{A_2^i}{1+\frac{\tau_r}{\tau_v}} + \frac{A_3^i}{1+\frac{\tau_r}{\tau_v}\left(1+\frac{\tau_v}{\tau_D}\right)}, \text{ as } t\to\infty.$$

In Fig. 3.5, we have compared Eq. (3.30) with numerical simulations for both cases I and II, finding an excellent agreement between the two. We see then that the presence of resetting induces a localization of the process near the initial position, in contrast to the free process, which is diffusive in the long-time limit.

3.3.2 Non-equilibrium steady state

Since the mean time between resets is finite, we expect that the process reaches a NESS [96]. In Eq. (3.28), we have the propagator of the process with resetting in terms of the reset-free propagator, which, in Fourier-Laplace space, reads

$$P_r(k,s) = \frac{s+r}{s}P(k,s+r). \tag{3.31}$$

The NESS of the process can be obtained by taking the $s\to 0$ limit, which is equivalent to taking $t\to\infty$ in $P_r(k,s)$, which yields

$$P_r^{(s)}(k) = \lim_{s\to 0} sP_r(k,s) = rP(k,s+r), \tag{3.32}$$

where the superscript (s) stands for the steady state. Inverting the Fourier transform of $P_r^{(s)}(k)$ we get the NESS of the process in real space, $P_r^{(s)}(x)$. Note that since the propagator of the process without reset is different depending on the initial condition, the long-time limit of the process with resetting, and thus its NESS, will also depend on the initial condition. In particular, for case I, we get

$$P_r^{(s),D}(x) = r\left[\frac{1}{2\pi}\int_{-\infty}^{\infty} P^D(k,s)e^{ikx}dk\right]_{s=r} = r\left[I(|x-x_0|,r) + \frac{\tau_v}{\tau_D}J(|x-x_0|,r)\right] \tag{3.33}$$

where $I(|x-x_0|,r)$ and $J(|x-x_0|,r)$ are the same integrals defined in Eqs. (3.22) and (3.26), but with s replaced by r. In the absence of relocations ($\tau_D \to \infty$), we recover the result for standard diffusion, Eq. (2.23) as reported in [100]. On the other hand, for case II, the propagator at the stationary state is given by

$$\begin{aligned} P_r^{(s),v}(x) &= r\left[\frac{1}{2\pi}\int_{-\infty}^{\infty} P^v(k,s)e^{ikx}dk\right]_{s=r} = \\ &= r\left[J(|x-x_0|,r) + \frac{\tau_v(r\tau_v+1)^2}{2D\tau_D(v\tau_v)^4}\left(\frac{e^{-|x-x_0|\lambda_-}}{\lambda_-(\lambda_+^2-\lambda_-^2)(\kappa^2-\lambda_-^2)} + \right.\right. \\ &- \left.\left.\frac{e^{-|x-x_0|\lambda_+}}{\lambda_+(\lambda_+^2-\lambda_-^2)(\kappa^2-\lambda_+^2)}\right)\right], \end{aligned} \tag{3.34}$$

where $\kappa \equiv (r\tau_v+1)/(v\tau_v)$.

In Fig. 3.6 we show the comparison between the NESS and numerical simulations, confirming the validity of our results. We can see that, as expected, the NESS is different depending on the initial condition of the walker. This behavior reappears in all other quantities computed in this chapter. This is due to the fact that resetting makes the walker return to the initial condition and so, its effect is not smoothed out at long times as is expected in IRW processes without resetting. For long distances, the NESS of both cases decays exponentially as $P_r^{(s)}(x) \sim e^{-|x-x_0|\lambda_-(r)}$, with different prefactors for each case, that deppend on the model parameters. This behavior is similar to that of standard diffusion with resetting, which also decays exponentially, as shown in Eq. (2.23).

3.3.3 First-passage time

Next, we proceed to compute the FPT PDF for the IRW under resetting. We do so in Laplace space in terms of the FPT PDF of the system without resetting. Following [90], let $G_0(x_0,t)$ be the survival probability for the system without resetting and $G_r(x_0,t)$ the one for the system with resetting; both magnitudes are related via a last renewal equation, which in Laplace space is Eq. (2.30). Next, we note that the FPT PDF is related to the survival probability which, in Laplace space is given by $p_f(s) = -sG(s)+1$, so that,

$$p_f(s)_r = \frac{(s+r)p_f(s+r)_0}{s+rp_f(s+r)_0}, \tag{3.35}$$

where $p_f(s)$ is the first-passage probability density without resetting.

In principle (3.35) can be transformed back to real space, via the inverse Laplace transform. In Fig. 3.7(a) we present a particular case for the FPT PDF for case I and II in real space from simulation data. We have checked that the FPT PDF decays exponentially, though there is not a simple relation between the decaying constant and the model's parameters. Even if we cannot compute the FPT PDF in real space, we can still compute its mean MFPT $\langle T(x_0)\rangle_r$ from the first-passage probability density

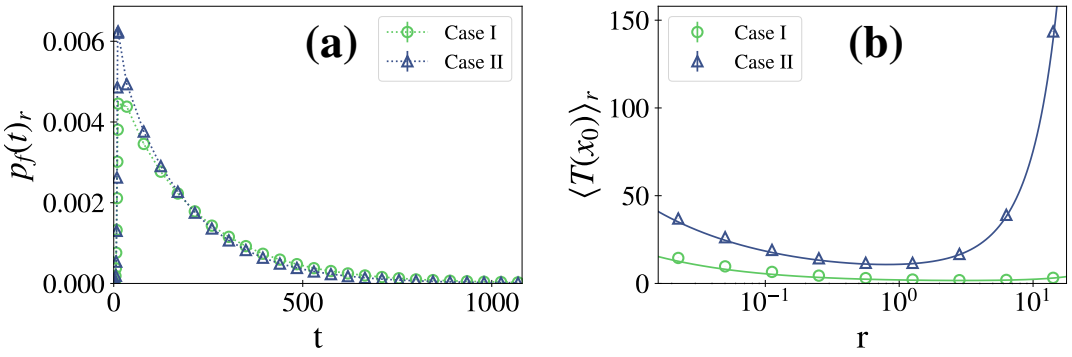


Figure 3.7: **FPT PDF of the IRW with resetting.** In both panels case I is in green and case II in blue. (a) FPT PDF in the presence of resetting obtained from numerical simulations. The dotted lines are added as a visual guide. (b) In all panels the parameters used in the simulations are $D = v = 1$, $\tau_D = 3.8$, $\tau_v = 3.3$, $x_0 = 10$, $r = 0.1$, and $N = 10^6$ trajectories.

$$\langle T(x_0)\rangle_r = \int_0^\infty t p_f(x_0,t)_r dt = G_r(x_0, s=0) = \frac{G_0(x_0, s=r)}{1 - rG_0(x_0, s=r)} = \frac{1 - p_f(s=r)_0}{r p_f(s=r)_0}. \tag{3.36}$$

Combining Eqs. (3.24) and (3.36) the expression of the MFPT for the case I is given by

$$\left\langle T^D(x_0)\right\rangle_r = \frac{1}{r}\left[\frac{\psi_-(r) - \psi_+(r)}{\psi_-(r)e^{-|x_0|\lambda_-(r)} - \psi_+(r)e^{-|x_0|\lambda_+(r)}} - 1\right] \tag{3.37}$$

where $\psi_+(r)$, $\psi_-(r)$, $\lambda_+(r)$ and $\lambda_-(r)$ are as in Eqs. (3.23) but setting $s = r$.

If the searcher does not relocate ($\tau_D \to \infty$), i.e., only diffuses then $\lambda_+(r) \simeq \sqrt{r/D}$ and $\psi_-(r) \simeq 0$. Therefore, (3.37) reduces to the well-known case of Brownian walkers with stochastic resetting, Eq. (2.26) [100]. Analogously, for case II the MFPT reads

$$\langle T^v(x_0)\rangle_r = \frac{1}{r}\left[\frac{(v\tau_v)^2(\psi_-(r) - \psi_+(r))/(r\tau_v + 1)}{\lambda_-^{-1}(r)e^{-|x_0|\lambda_-(r)} - \lambda_+^{-1}(r)e^{-|x_0|\lambda_+(r)}} - 1\right]. \tag{3.38}$$

We note that this result is different from that obtained in Eq. (3.37), which reveals the explicit dependence of the MFPT on the initial condition, i.e., if the walker is initially either relocating or diffusing. In this case, in the limit of no relocation, $\tau_D \to \infty$, the MFPT goes to

$$\left\langle T^v(x_0)\right\rangle_r \simeq \frac{1}{r}\left[\frac{\lambda_+^2(r) - \lambda_-^2(r)}{\lambda_+(r)e^{-|x_0|\lambda_-(r)} + \lambda_-(r)e^{-|x_0|\lambda_+(r)}} - 1\right]. \tag{3.39}$$

This shows that the MFPT is dependent on the initial condition also in this limit. It can easily be understood by noticing that $\tau_D \to \infty$ means that the searcher only diffuses,

so in case I the walkers do not relocate. It is not the case for case II, where the walkers initially relocate at rate τ_v^{-1} before switching to diffusion state. In the opposite limit, when $D = 0$ the searcher only relocates, i.e., it never detects the target, so that the MFPT (3.37) and (3.38) diverge. Effectively, if $D = 0$ then $\lambda_{\pm}(r) \to \infty$ and $\langle T(x_0)\rangle_r \to \infty$. Furthermore, one may notice that while $\langle T^D(x_0)\rangle_r \to 0$ as $x_0 \to 0$, $\langle T^v(x_0)\rangle_r$ tends to a constant value given by

$$\langle T^v(x_0)\rangle_r \simeq \frac{1}{r}\left[\frac{(v\tau_v)^2}{r\tau_v+1}\frac{(\psi_-(r)-\psi_+(r))\lambda_+(r)\lambda_-(r)}{\lambda_+(r)-\lambda_-(r)}-1\right] \tag{3.40}$$

in the same limit.

This difference arises because for case II the walkers do a relocation first (during which target detection is not possible), so in general this is detrimental in order to find the target for $x_0 \to 0$. More interesting is the case for $x_0 \to \infty$, which satisfies

$$\frac{\langle T^D(x_0)\rangle_r}{\langle T^v(x_0)\rangle_r} \simeq \frac{r\tau_v+1}{(v\tau_v)^2}\frac{1}{\psi_-(r)\lambda_-(r)}. \tag{3.41}$$

In general, $\langle T^D(x_0)\rangle_r \neq \langle T^v(x_0)\rangle_r$ showing that the effect of the initial condition is not smoothed out. As we have mentioned, this behavior arises because, in the presence of resetting, the walker is consistently returned to its initial condition during the time evolution.

3.3.4 Optimal reset rate

In Sec. 3.3.1, 3.3.2, and 3.3.3, we have seen that the IRW displays similar features under Poissonian resetting to those of regular Brownian walkers [100]. In this section, we will show that in this case, there also exists an optimal value of the reset rate r that minimizes the MFPT. In the absence of resetting the walker takes an infinite time to reach the target due to the non-recurrent nature of Brownian particles, and the heavy-tailed FPT distribution. On the other hand, for large reset rates, the walker's motion is localized near the reset point, also resulting in a very large MFPT. To analytically explore the existence of this optimal rate, we begin by analyzing Eq. (3.37) both for small and large r. Let us first expand the MFPT for large r. From Eq. (3.23) we have $B(r) \simeq r^2/v^2$ and $C(r) \simeq r^3/Dv^2$ so that

$$\lambda_+(r) \simeq r/v, \qquad \lambda_-(r) \simeq \sqrt{r/D} \quad \text{as } r \to \infty \tag{3.42}$$

which yields a MFPT,

$$\langle T^D(x_0)\rangle_r \simeq \frac{1}{r}e^{|x_0|\sqrt{r/D}} \quad \text{as } r \to \infty \tag{3.43}$$

so that the MFPT tends to infinity as r does.

This is the same behavior as in the absence of resetting. To prove that the optimal reset rate exists, we just need to verify if the MFPT decreases with r for small values of r, that is, if the condition

$$\lim_{r\to 0}\left(\frac{\partial\langle T^D(x_0)\rangle_r}{\partial r}\right) < 0 \tag{3.44}$$

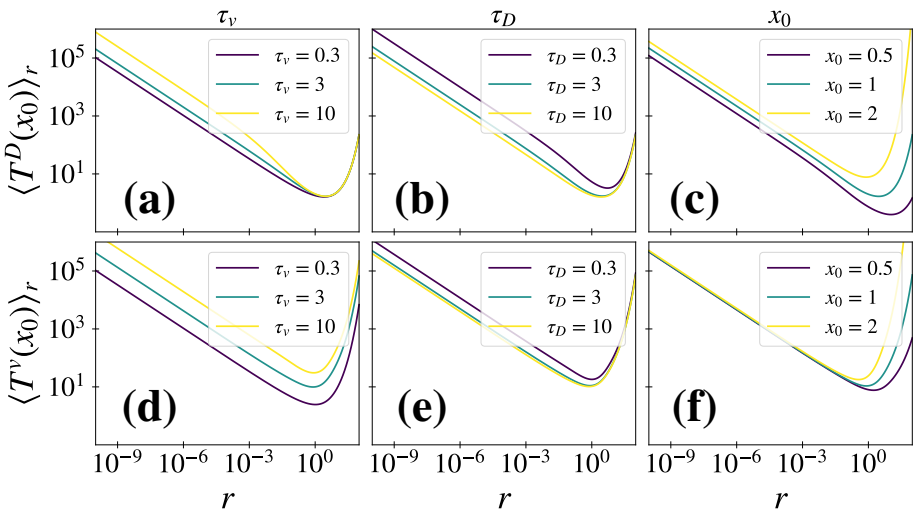


Figure 3.8: **MFPT of the IRW with resetting** as a function of the reset rate, fixing different parameter values. The top row corresponds to case I, where the lines are obtained from Eq. (3.37); the bottom row corresponds to case II, where the lines are obtained from Eq. (3.38). The parameters used to obtain all curves are $D = v = 1$, $\tau_D = 3.8$, $\tau_v = 3.3$, and $x_0 = 1$ unless stated otherwise in the corresponding captions.

is met. Expanding $\lambda_\pm(r)$ for small r we find

$$\lambda_+(r) \simeq \lambda_0 + O(r), \quad \lambda_-(r) \simeq \lambda_1\sqrt{r} + O(r), \tag{3.45}$$

where

$$\lambda_0 = \sqrt{\frac{1}{D\tau_D} + \frac{1}{(v\tau_v)^2}}, \quad \lambda_1 = \sqrt{\frac{\tau_D + \tau_v}{(v\tau_v)^2 + D\tau_D}}.$$

After some calculations, the dominant term in the expansion of the MFPT for small r reads

$$\left\langle T^D(x_0)\right\rangle_r \simeq \frac{T_0}{\sqrt{r}} \quad \text{as } r \to 0, \tag{3.46}$$

where

$$T_0 = \lambda_1 (v\tau_v)^2 \left[\left(e^{-|x_0|\lambda_0} - 1\right)\left(\frac{1}{\lambda_0 (v\tau_v)^2} - \lambda_0\right) + \frac{|x_0|}{(v\tau_v)^2}\right].$$

Finally, the condition (3.44) applied to (3.46) is equivalent to $T_0 > 0$, or simply

$$\frac{|x_0|\lambda_0}{1 - e^{-|x_0|\lambda_0}} > -\frac{(v\tau_v)^2}{D\tau_D},$$

which is always fulfilled, confirming the existence of the optimal reset rate.

One can also prove that (3.38) has an optimal reset rate following an analogous procedure. In the limit of large reset rate r, using (3.42) we find that

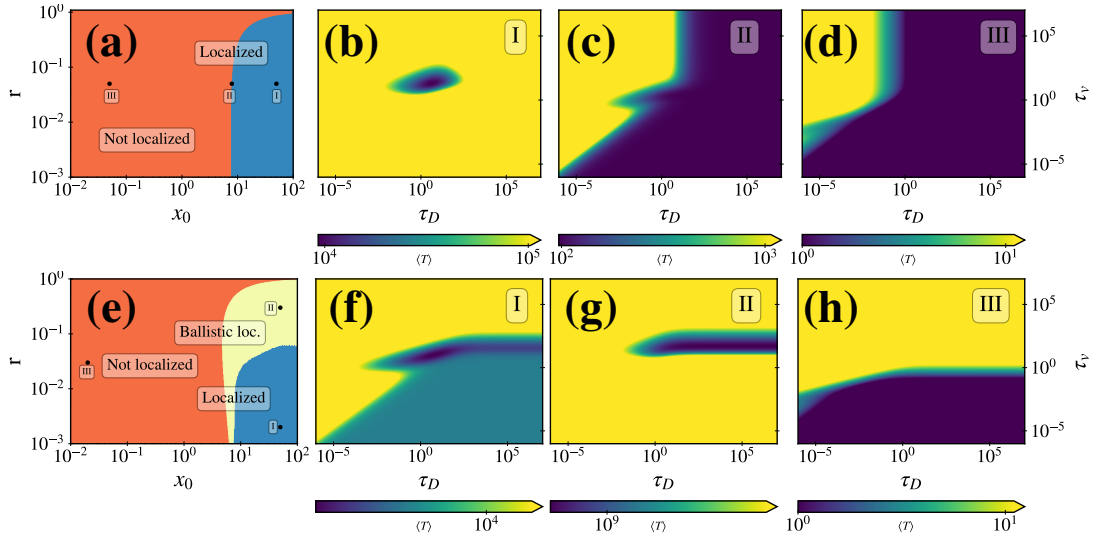


Figure 3.9: **Phase diagram of the MFPT for the IRW.** In the top row we plot case I. (a) Phase diagram of the behavior of MFPT in (x_0, r) space. Panels (b), (c), and (d) are representative examples of the MFPT in each phase and the interphase in (τ_D, τ_v) space for a given x_0 and r. The Roman number shows their corresponding position in the phase diagram. In panel (b) $x_0 = 50$, $r = 0.05$; In panel (c) $x_0 = 7.9$, $r = 0.05$; And in panel (d) $x_0 = 0.05$, $r = 0.05$. In the bottom row we plot case II. Panel (e) Phase diagram of the behavior of MFPT in (x_0, r) space. Panels (f), (g), and (h) are representative examples of the MFPT in each phase in (τ_D, τ_v) space for a given x_0 and r. In panel (f) $x_0 = 50$, $r = 0.002$; In panel (g) $x_0 = 50$, $r = 0.3$; And in panel (h) $x_0 = 0.02$, $r = 0.03$. For all plots $D = 1$ and $v = 1$.

$$\langle T^v(x_0)\rangle_r \simeq \tau_r e^{|x_0|\sqrt{r/D}} \quad \text{as } r \to \infty. \tag{3.47}$$

Analogously, using (3.45) we find that when $r \to 0$ the MFPT is given by (3.38) and behaves as in (3.46) but with

$$T_0 = \frac{\lambda_1}{\lambda_0}\left[\frac{(v\tau_v)^2}{D\tau_D} + \lambda_0|x_0| + e^{-|x_0|\lambda_0}\right].$$

Since T_0 is positive, the optimal reset rate also exists when the walkers start by relocating. In Fig. 3.8 we present some illustrative cases of the dependence of the MFPT with r computed from Eq. (3.37) and Eq. (3.38) for case I and case II, respectively, to check the existence of the optimal value of r. Though we are not able to find a compact relationship between the model parameters and the minimal MFPT, in the next section, we numerically identify the existence of different regime behaviors of the MFPT.

3.3.5 Global optimization of the MFPT

Above, we have seen that indeed, like in the standard Brownian case, IRWs also optimize their MFPT in the presence of stochastic resetting. However, a further question is, how does the MFPT behave when varying other model parameters, like τ_D, τ_v, or x_0, since they encode relevant space and time scales of this system. In our analysis, we

have $v = 1$ and $D = 1$, this allows us to focus the study on the most interesting regime in which ballistic and diffusive movements are in direct competition (note that one may change x and t to nondimensional variables $x \to x\frac{v}{D}$ and $t \to t\frac{v^2}{D}$). We have centered our study on finding the combination of parameter values that globally minimizes the MFPT. The analysis was conducted in the following manner: for a set of (τ_D, τ_v) in the range from 10^{-4} to 10^7 we used Eq. (3.37) and Eq. (3.38) to compute the MFPT for different combinations within the ranges $r \in [10^{-3}, 10^0]$ and $x_0 \in [10^{-2}, 10^2]$.

For the diffusive initial condition, two distinct phases can be observed (distinguished by the colors red and cyan in Fig. 3.9(a)). For the phase in cyan, which we name the *localized phase*, the MFPT presents a well-localized minimum in the (τ_D, τ_v) phase space. This can be better identified in Fig. 3.9(b), where we directly show for a specific choice of (x_0, r) values that the minimum value lies in a confined region of the space (τ_D, τ_v). On the other hand, for x_0 small we obtain the red (*non-localized*) phase, for which the MFPT does not have a well-defined minimum but rather there exists a plateau region of (τ_D, τ_v) values for which the MFPT becomes minimum. In particular, any combination of (τ_D, τ_v) out of the region $\tau_v \gg \tau_D$ will suffice to optimize the MFPT, as can be seen for the case depicted in Fig. 3.9(d). In this region of the phase-space what we have is that the specific amount of time that the walker spends either relocation or diffusing does not greatly impact the value of the MFPT. Noting that this is for x_0 small, and that the walker initially starts diffusing, this region represents a regime where the target is found after the walker starts diffusing from the initial condition, or after a reset. For the sake of completeness, in panel 3.9(c) we show the behavior of the MFPT for the interface between both (localized and non-localized) phases, where we observe the transition from one behavior to the other.

In the bottom row of Fig. 3.9, we present the same analysis for the relocation initial condition, case II. In this case, we observe three different phases. Apart from the localized and non-localized phases above, we observe an intermediate situation, which we call *ballistic localization*, in light yellow in Fig. 3.9(e). For this region, the minimum of the MFPT is confined to a fine line of (τ_D, τ_v) values where τ_v is (regardless of the value of τ_D) at least of the order of the timescale x_0/v, which corresponds to the case where the target can be reached on average in a single relocation. Similarly to case I, in panels (f)-(h) of Fig. 3.9 we show the behavior of the MFPT for the three different phases. Remarkably, the behavior for the non-localized phase is slightly different now: the region where the minimum MFPT occurs does not include the region where τ_v is large. This is because for x_0 small a very large value of τ_v now implies that the walker will depart on average much from the target position before switching to diffusive motion when the target can be detected.

All in all, we have seen that when ballistic and diffusive movements directly compete, the parameter combination that maximizes its global optimization of the MFPT directly depends on the initial condition of the system. For case I, we have observed two distinct behaviors. The *localized* phase in which the MFPT exhibits a well-localized minimum in (τ_D, τ_v) phase space. On the other hand, for small x_0 or large r the *non-localized* phase in which a plateau region of values (τ_D, τ_v) optimizes the MFPT. In this phase, the specific combination of (τ_D, τ_v) is not relevant for optimizing the search. For case II a third intermediate phase arises, *ballistic localization*. Here the minimum of the MFPT is restricted to a fine line region of (τ_D, τ_v) values, corresponding

to the situation where the target can be reached on average in a single relocation.

3.4 Summary of results

In this chapter, we have studied a IRW that stochastically switches between a diffusive phase, modeling an intensive local search phase, where a target can be detected; and a rapid ballistic relocation phase, where the speed hinders target detection. To this known model our contribution has been to add exponential stochastic resetting and analyze the transport properties and FPT of the resulting random walk in an unbounded domain. We have seen that, like in the standard BM with Poissonian resetting, the IRW exhibits a NESS, and that resetting not only makes the MFPT finite, but also there exists a value of the resetting rate r that minimizes it. We have also seen that since resetting induces a revisiting of the initial condition, all the long-time properties of the system are dependent on whether the walker starts in a diffusion or relocating state. Finally, we have numerically studied the global optimization of the MFPT with all model parameters. The existence of the *localized phase* for a non-trivial combination of (τ_D, τ_v) reveals that having an unresponsive relocation phase is beneficial for the optimization of the MFPT of the search process for 1D IRW in unbounded domains in the presence of resetting in agreement with [171, 172, 174, 199].

Having shown that resetting to a fixed position and state can make the initial condition relevant even at long times, in the next chapter, we consider a complementary question: how the first-passage properties change when the reset position itself is not fixed, but sampled from a distribution.

4

STOCHASTIC RESETTING TO RANDOM POSITIONS

In this chapter, we study the effect of Poissonian resetting to points randomly distributed around the origin on the MFPT of a Brownian searcher moving in one dimension. We compare the search efficiency with that corresponding to resetting to the origin and find that the MFPT of the latter can be larger or smaller than the distributed case, depending on whether the resetting points are symmetrically or asymmetrically distributed. We see that the existence of an optimal reset rate depends on whether the target position belongs to the resetting interval. We also see that the FPT density averaged over the resetting points depends on its first moment only. As a consequence, there is an equivalent point such that the FPT problem with resetting to that point is statistically equivalent to the case of distributed resetting. We end our study by analyzing the fluctuations of the FPTs.

4.1 Introduction . . . 52
4.2 Averaged mean first-passage time . . . 52
4.2.1 Effect of the resetting distribution on the first-passage PDF . . . 55
4.2.2 Symmetric reset-point PDF in an interval and $x_t \notin \mathscr{D}$ . . . 56
4.2.3 Symmetric reset-point PDF in an interval and $x_t \in \mathscr{D}$ . . . 59
4.2.4 Resetting to two points . . . 62
4.3 Equivalent resetting point . . . 65
4.4 Fluctuations of the MFPT . . . 69
4.4.1 Example: Uniform resetting PDF with $x_t > L$ . . . 70
4.4.2 Example: Uniform resetting PDF with $x_t \in \mathscr{D}$ . . . 71
4.5 Summary of results . . . 72

4.1 Introduction

The previous chapter considered resetting to a prescribed position and internal state. Here we keep the focus on first-passage properties under Poissonian stochastic resetting, but turn to a standard BM whose resetting position is itself drawn from a distribution. Despite their relevance, the phenomenology of processes where the resetting point can vary is far less known. Distributed resetting was discussed formally for Brownian motion in the seminal paper by Evans and Majumdar [100]. Since then, several works have considered different choices of the resetting position, such as already visited places [201], resetting to the maximum visited position [202], or partial resetting, where the particle is returned only to a fraction of its distance to the origin [203]. It is also highly natural to assume that in experiments or nature resets cannot be performed with perfect precision, giving rise to a distribution of return points [204]. In addition, from a theoretical perspective, the resetting distribution introduces new length scales into the problem, which can give rise to interesting phenomena [179, 204]. Recent studies have also addressed Poissonian resetting to multiple nodes in networks [178, 205], interval based resetting [206], the thermodynamic aspects of distributed resetting [180, 207], and the converse case of a moving target [208] or a spatially distributed one. However, studies on the fundamental properties of distributed resetting points are still scarce [181].

In this chapter, we focus on the efficiency issue by studying the MFPT of a Brownian searcher moving in one dimension when it resets its position at a constant rate to randomly distributed points x_0 sampled from a PDF $f(x_0)$. This PDF may account for a known territory that is revisited as a consequence of spatial memory or site fidelity [176, 177]. We further compare the efficiency (MFPT) and performance (coefficient of variation) of the search process between resetting to a single point located at the origin or resetting to randomly distributed points.

The chapter is organized as follows. In Sec. 4.2 we obtain exact analytic expressions for the first two moments of the FPT PDF for the Brownian walker resetting to distributed points and we study some particular cases, specifically: the case where the resetting points are symmetrically distributed in an interval, the case where the resets are distributed along the whole real line, and the case of asymmetric resetting points. Next, in Sec. 4.3 we study the properties of the equivalent resetting point (ERP), for which resetting to that point results in the same MFPT as for the case of distributed resets to an interval. In Sec. 4.4 we study the corresponding fluctuations of the MFPT for the most interesting cases above. Finally, in Sec. 4.5 we conclude with a brief recapitulation of the main results of this chapter.

4.2 Averaged mean first-passage time

Consider a random walker such that at a constant rate r its location resets to a random position x_0 drawn from the PDF $f(x_0)$. The trajectory of the searcher is terminated whenever it hits the target position, x_t. The first-passage problem for this situation states that the master equation for the probability of finding the searcher at point x at time t is given by

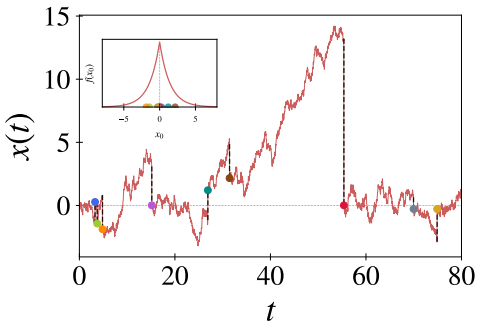


Figure 4.1: **Example trajectory of diffusion with resetting to distributed positions.** The main panel represents a trajectory that resets at rate r to points drawn from a distribution $f(x_0)$, represented by the colored points. In the inset, the resetting distribution.

$$\frac{\partial P(x,t)}{\partial t} = D\frac{\partial^2 P(x,t)}{\partial x^2} - rP(x,t) + rf(x)G(t) - p_f(t)\delta(x-x_t), \tag{4.1}$$

where D is the diffusion coefficient, $G(t)$ is the survival probability up to time t, and the rightmost term represents the absorbing boundary condition $P(x=x_t,t)=0$, with $p_f(t)$ the FPT PDF. Compared with Eq. (2.22), the first two terms on the right-hand side are unchanged. The third term, instead of a delta function at the origin, is written in terms of the resetting-point distribution $f(x)$ and is multiplied by the probability $G(t)$ that the searcher has not yet encountered the target. Finally, the last term $p_f(t)\delta(x-x_t)$ accounts for the absorbing boundary at the target position x_t.

To solve Eq. (4.1) we perform a Fourier transform in space $x \to k$ and a Laplace transform in time $t \to s$ with the initial condition $P(x,0)=\delta(x-x_0)$, where x_0 is a random variable sampled from $f(x_0)$, then Eq. (4.1) becomes

$$P(k,s) = \frac{e^{-ikx_0} - e^{-ikx_t}}{s+r+Dk^2} + \frac{rf(k)+se^{-ikx_t}}{s+r+Dk^2}G(s), \tag{4.2}$$

where we have used

$$p_f(s) = 1 - sG(s) \tag{4.3}$$

to relate the survival probability and the FPT PDF. The absorbing boundary condition $P(x=x_t,s)=0$ turns into

$$\int_{-\infty}^{\infty} e^{ikx_t}P(k,s)dk = 0. \tag{4.4}$$

So by multiplying Eq. (4.2) by e^{ikx_t} and integrating over k we get

$$G(s) = \frac{\int_{-\infty}^{\infty}\frac{1-e^{-ik(x_0-x_t)}}{s+r+Dk^2}dk}{\int_{-\infty}^{\infty}\frac{rf(k)e^{ikx_t}+s}{s+r+Dk^2}dk} = \frac{1-e^{-|x_0-x_t|\sqrt{\frac{r+s}{D}}}}{s+r\int_{-\infty}^{\infty}f(x_0)e^{-|x_t-x_0|\sqrt{\frac{r+s}{D}}}dx_0}, \tag{4.5}$$

which has to be solved for a specific $f(x_0)$. From Eq. (2.21) we know that the MFPT can be computed from the Laplace transform of survival probability $G(s)$, in fact, all moments of the FPT PDF can be computed from $G(s)$.

Moreover, note that the Laplace transform of $p_f(t)$ is

$$p_f(s) = \int_0^\infty e^{-st} p_f(t) dt = \langle e^{-st} \rangle_{p_f} = \sum_{n=0}^{\infty} \frac{(-s)^n}{n!} T^n, \tag{4.6}$$

where $T^n \equiv \langle t^n \rangle_{p_f}$ are the n-th moments. Now, since in Laplace space $p_f(s)$ and $G(s)$ are related by Eq. (4.3), performing a small-s expansion on $G(s)$ one gets

$$p_f(s) = 1 - sG(s) = 1 - s\left[G(s=0) + sG'(s=0) + \frac{s^2}{2!}G''(s=0) + \cdots\right], \tag{4.7}$$

thus, equating the coefficients of the powers of s in Eqs. (4.6) and (4.7) one finds that the moments of the first-passage PDF can be written in terms of the derivatives of $G(s)$

$$T^n = n(-1)^{n+1}\left[\frac{d^{n-1}G(s)}{ds^{n-1}}\right]_{s=0}, \quad n \geq 1. \tag{4.8}$$

From (4.5) and (4.8) the MFPT is then given by

$$T(x_0) = G(s=0) = \frac{1 - e^{-|x_0 - x_t|\sqrt{\frac{r}{D}}}}{r\int_{-\infty}^{\infty} e^{-|x_0 - x_t|\sqrt{\frac{r}{D}}} f(x_0) dx_0}, \tag{4.9}$$

provided that $|x_0 - x_t| = |x_t - x_0|$. However, since x_0 is a random variable drawn from $f(x_0)$ we need to define the averaged mean first-passage time (AMFPT) over the possible values of x_0

$$\langle T \rangle_{x_0} = \int_{-\infty}^{\infty} T(x_0) f(x_0) dx_0 = \frac{1}{r}\left[\frac{1}{I(r,x_t)} - 1\right] \tag{4.10}$$

with

$$I(r,x_t) \equiv \int_{-\infty}^{\infty} e^{-|x_0 - x_t|\sqrt{\frac{r}{D}}} f(x_0) dx_0, \tag{4.11}$$

which corresponds to the result found by Evans and Majumdar in [91]. Without loss of generality, we assume $x_t > 0$ and denote by $\mathscr{D}$ the support of $f(x_0)$ from now on.

Note 4.1 Before continuing, we need to prove, for sanity, that $I(r,x_t) < 1$ so that $\langle T \rangle_{x_0} > 0$. We consider two different situations, firstly $x_0 \in \mathscr{D}$ with $x_t \notin \mathscr{D}$ but $x_t > 0$ and secondly $x_t \in \mathscr{D}$. In the former case, since $x_t > x_0$, $\forall x_0 \in \mathscr{D}$, we have $|x_0 - x_t| = |x_t - x_0| = x_t - x_0$ so that

$$\begin{aligned} I(r,x_t) &= e^{-x_t\sqrt{\frac{r}{D}}} \int_{\mathscr{D}} e^{x_0\sqrt{\frac{r}{D}}} f(x_0) dx_0 < e^{-x_t\sqrt{\frac{r}{D}}} \max_{x_0 \in \mathscr{D}}\left(e^{x_0\sqrt{\frac{r}{D}}}\right) \int_{\mathscr{D}} f(x_0) dx_0 \\ &= e^{-x_t\sqrt{\frac{r}{D}}} \max_{x_0 \in \mathscr{D}}\left(e^{x_0\sqrt{\frac{r}{D}}}\right) < 1. \end{aligned}$$

In the latter case let us say $\mathscr{D} = [a,b]$ and so $a < x_t < b$. Hence,

$$
\begin{aligned}
I(r,x_t) &= \int_a^{x_t} e^{(x_0-x_t)\sqrt{\frac{r}{D}}} f(x_0)dx_0 + \int_{x_t}^{b} e^{-(x_0-x_t)\sqrt{\frac{r}{D}}} f(x_0)dx_0 \\
&< e^{-x_t\sqrt{\frac{r}{D}}} \max_{x_0\in(a,x_t)} \left(e^{x_0\sqrt{\frac{r}{D}}}\right) \int_a^{x_t} f(x_0)dx_0 \\
&+ e^{x_t\sqrt{\frac{r}{D}}} \max_{x_0\in(x_t,b)} \left(e^{-x_0\sqrt{\frac{r}{D}}}\right) \int_{x_t}^{b} f(x_0)dx_0 \\
&= \int_a^{x_t} f(x_0)dx_0 + \int_{x_t}^{b} f(x_0)dx_0 = 1.
\end{aligned}
$$

If the support of $f(x_0)$ is the real line, then the above proof still holds by doing $a=-\infty$ and $b=+\infty$.

4.2.1 Effect of the resetting distribution on the first-passage PDF

Here, we examine several relevant properties of the survival probability derived above. If we average over the reset-point PDF $f(x_0)$ by multiplying Eq. (4.5) by $f(x_0)$ and integrating over x_0 we obtain

$$
\langle G(s)\rangle_{x_0} = \frac{1-I(s+r,x_t)}{s+rI(s+r,x_t)} \tag{4.12}
$$

where $I(r+s,x_t)$ is given in Eq. (4.11) replacing r by $r+s$. We note that since the averaged survival probability only depends on the resetting distribution through the integral $I(s,x_t)$, a fixed form of this integral determines the survival properties of the target completely (and then the first-passage time PDF). Putting this together with the result in Eq. (4.10), we find that specifying the value of the AMFPT (which is equivalent to fixing $I(s,x_t)$), the first-passage properties become unequivocally determined. This means that any resetting point PDF $f(x_0)$ leading to the same AMFPT will follow exactly the same first-passage statistics, revealing a somewhat universal behavior of the averaged first-passage distribution.

Moreover, we can write Eq. (4.12) in terms of $\langle T\rangle_{x_0}$ by inverting Eq. (4.10). While a closed expression cannot be found in general, in the limit $s \ll r$, that is at long times, it is easy to see that one obtains

$$
\langle G(s)\rangle_{x_0} \simeq \frac{\langle T\rangle_{x_0}}{1+s\langle T\rangle_{x_0}}. \tag{4.13}
$$

Similarly, the first-passage PDF (in the Laplace space) will read

$$
\left\langle p_f(s)\right\rangle_{x_0} = 1 - s\left\langle G(s)\right\rangle_{x_0} \simeq \frac{1}{1+s\langle T\rangle_{x_0}}. \tag{4.14}
$$

Thus, one finds that both the survival probability and the first-passage distribution averaged over the resetting-point distribution are always exponential in the long-time limit ($s \ll r$), and their dependence on r and $f(x_0)$ is exclusively contained within the first moment $\langle T\rangle_{x_0}$ independently of $f(x_0)$. To proceed further, we consider specific functions for $f(x_0)$ to be able to solve Eq. (4.10).

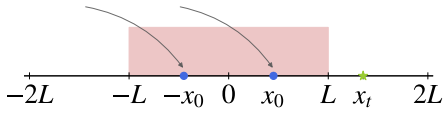


Figure 4.2: **Uniformly distributed reset points in an interval.**

4.2.2 Symmetric reset-point PDF in an interval and $x_t \notin \mathscr{D}$

Let us consider that the resetting process is symmetric, and that the walker resets to x_0 and $-x_0$ with equal probability, then $f(x_0)$ is an even function. Additionally, we assume that the target is not contained in the domain of the resetting distribution. $x_t \notin \mathscr{D}$, so from Eq. (4.11) we get

$$I(r,x_t) = e^{-x_t\sqrt{\frac{r}{D}}} \int_{\mathscr{D}} e^{x_0\sqrt{\frac{r}{D}}} f(x_0)dx_0. \tag{4.15}$$

Then (4.10) becomes

$$\langle T\rangle_{x_0} = \frac{1}{r}\left[\frac{e^{x_t\sqrt{\frac{r}{D}}}}{\int_{\mathscr{D}} f(x_0)\exp\left(x_0\sqrt{\frac{r}{D}}\right)dx_0} - 1\right]. \tag{4.16}$$

Using for instance $\mathscr{D} = [-L,L]$, then

$$\langle T\rangle_{x_0}(r,L) = \frac{1}{r}\left[\frac{e^{x_t\sqrt{\frac{r}{D}}}}{\int_{-L}^{L} f(x_0)e^{-x_0\sqrt{\frac{r}{D}}}dx_0} - 1\right]. \tag{4.17}$$

To compute the specific expression of the AMFPT we need to specify a particular form for $f(x_0)$, but this is not necessary to prove the existence of an optimal reset rate r that minimizes $\langle T\rangle_{x_0}$, when the resetting PDF is symmetric, and the target is outside the resetting domain. To do so, we analyze the limits $r \to 0^+$ and $r \to \infty$. In the limit $r \to 0^+$ the integral in Eq. (4.17) tends to 1 so that $\langle T\rangle_{x_0} \sim r^{-1}$; this means that the AMFPT diverges to $+\infty$ in this limit. On the other hand, for the limit $r \to \infty$ we can find a lower bound for $\langle T\rangle_{x_0}$, so if we prove that the lower bound diverges as $r \to \infty$, then $\langle T\rangle_{x_0}$ diverges too. If we consider

$$\int_{-L}^{L} f(x_0)e^{-x_0\sqrt{\frac{r}{D}}}dx_0 \quad < \quad \max_{x_0}\left(e^{-x_0\sqrt{\frac{r}{D}}}\right)\int_{-L}^{L} f(x_0)dx_0 = e^{L\sqrt{\frac{r}{D}}}$$

then we see that

$$\langle T\rangle_{x_0}(r,L) > \frac{1}{r}\left[e^{(x_t-L)\sqrt{\frac{r}{D}}} - 1\right].$$

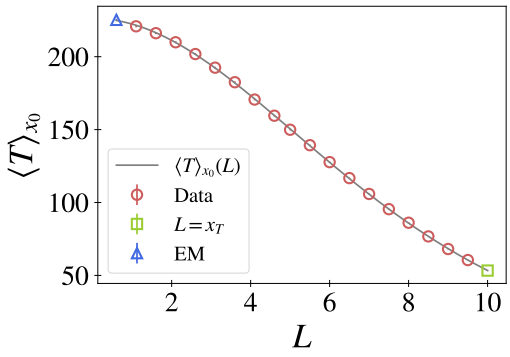


Figure 4.3: **AMFPT for uniformly distributed reset-point PDF with $x_t \notin \mathscr{D}$.** The solid line represents Eq. (4.19) and the symbols numerical simulations. In blue (triangle) $L \to 0$, Eq. (2.26), and in green (square) the case $L \to x_t$, Eq. (4.20). The parameters are $D = 1$, $r = 0.1$, and $x_t = 10$. We have averaged over $N = 10^5$ trajectories.

is satisfied. Since $x_t > L$, in the limit $r \to \infty$ the lower bound tends to infinity and thus $\langle T \rangle_{x_0} \to \infty$. Therefore, we can conclude that there exists a value of r which optimizes the AMFPT when the resetting points are symmetrically distributed in a finite interval. This is the first main result of this chapter.

A Uniformly distributed reset points in an interval

Next, we study how the AMFPT depends on L and find the optimal reset rate r; to this end, we need to consider specific choices for $f(x_0)$. Let $f(x_0)$ be a uniform distribution in $[-L, L]$. That is, $f(x_0) = 1/2L$ if $x_0 \in [-L, L]$, and zero otherwise, as shown in Fig. 4.2. Therefore, from Eq. (4.11)

$$I(r, x_t, L) = \frac{1}{L}\sqrt{\frac{D}{r}} e^{-x_t\sqrt{\frac{r}{D}}} \sinh\left(L\sqrt{\frac{r}{D}}\right), \tag{4.18}$$

thus (4.16) reduces to

$$\langle T \rangle_{x_0}(r, L) = \frac{1}{r}\left[L\sqrt{\frac{r}{D}}\frac{e^{x_t\sqrt{\frac{r}{D}}}}{\sinh\left(L\sqrt{\frac{r}{D}}\right)} - 1\right]. \tag{4.19}$$

When $L \to 0$, the PDF of resetting points tends to a Dirac delta function, and Eq. (4.19) reduces to the well-known result by Evans and Majumdar (EM) [100]. That is, when $L \to 0$ Eq. (4.19) becomes Eq. (2.26). On the other hand, when $x_t \to L$, the AMFPT is

$$\langle T \rangle_{x_0}(r, L = x_t) = \frac{1}{r}\left[x_t\sqrt{\frac{r}{D}}\frac{2}{1 - e^{-2x_t\sqrt{\frac{r}{D}}}} - 1\right]. \tag{4.20}$$

In Fig. 4.3 we plot $\langle T \rangle_{x_0}(r, L)$ with respect to L for fixed values of the rest of parameters. The agreement between the simulation symbols and (4.19) is excellent. In blue we plot the particular case of $L \to 0$, Eq. (2.26), and in green the case for $x_t \to L$ Eq. (4.20). As can be seen, the AMFPT decreases monotonically with the width of the resetting points interval, i.e., resetting to a point (this is the case $L = 0$) is less effective, it has a higher AMFPT than resetting to uniformly distributed points.

Above, we have seen that for a symmetric $f(x_0)$ and $x_t \notin \mathscr{D}$ there exists a value of the reset rate that minimizes the AMFPT, namely r_{opt}. In order to compute it, we define the following dimensionless quantities

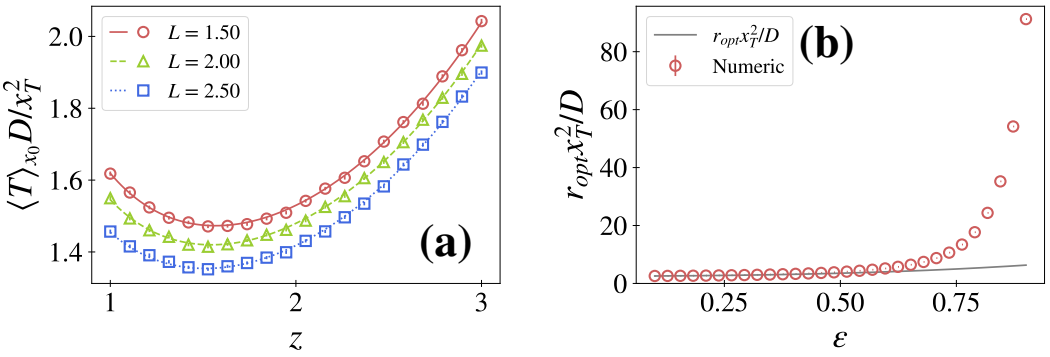


Figure 4.4: r_{opt} **for uniformly distributed reset points in an interval.** (a) $\frac{D}{x_t^2}\langle T\rangle_{x_0}$ as function of the parameter $z = x_t\sqrt{r/D}$ for three values of L, $L = 1.50$ (red), $L = 2.00$ (green) and $L = 2.50$ (blue). The lines represent Eq. (4.22) while the symbols are obtained from numerical simulations. The parameter values are $D = 1$, $r = 0.1$, and x_t is computed given a fixed value of z. We have averaged over $N = 10^5$ trajectories. (b) $r_{opt}x_t^2/D$ vs ε. The solid line is computed using Eq. (4.24) while the data points are obtained by numerically computing $d\langle T\rangle_{x_0}/dz = 0$.

$$\varepsilon = L/x_t \quad x_t > L \Rightarrow 0 < \varepsilon < 1, \quad z = x_t\sqrt{r/D} \tag{4.21}$$

then from Eq. (4.19)

$$\frac{D}{x_t^2}\langle T\rangle_{x_0} = \frac{\varepsilon e^z}{z\sinh(\varepsilon z)} - \frac{1}{z^2}, \tag{4.22}$$

where $\varepsilon = 0$ reduces to the EM case. In Fig. 4.4(a), we observe the existence of an optimal reset rate, r_{opt}, for different values of L and compare the result given in Eq. (4.22) with numerical simulations. In agreement with Fig. 4.3(a), we observe that curves with large L lead to lower values of the AMFPT.

To compute r_{opt} we do $d\langle T\rangle_{x_0}/dz = 0$, from which we obtain a transcendental equation for z whose solution, namely z_{opt}, allows us to compute the optimal reset rate as

$$r_{opt} = \frac{D}{x_t^2}z_{opt}^2. \tag{4.23}$$

We can obtain approximated analytic results for the optimal reset rate by introducing the perturbative expansion $z = z_0 + z_1\varepsilon + z_2\varepsilon^2 + \ldots$ into the equation for $d\langle T\rangle_{x_0}/dz = 0$. Equating the coefficients of the powers of ε we can calculate z_0, z_1, ... The $O(0)$ coefficient is $2 + (z_0 - 2)e^{z_0} = 0$ whose solution is $z_0 = 1.5936$ and corresponds to the value found in [91]. The next order, $O(1)$ gives $z_1 = 0$ while the second order gives

$$z_2 = -\frac{z_0^3\left(z_0e^{z_0} - 4e^{z_0} + 4\right)}{6\left(z_0^2e^{z_0} + 4 - 4e^{z_0} + z_0e^{z_0}\right)} = 1.1363.$$

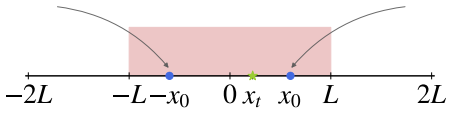


Figure 4.5: **Uniformly distributed reset points in an interval containing the target.**

Finally, we find an approximation for the optimal value of r from (4.21)

$$r_{opt} = 2.5396\frac{D}{x_t^2}\left[1+0.713\left(\frac{L}{x_t}\right)^2+...\right]^2 \tag{4.24}$$

where the prefactor corresponds to the value of the optimal reset rate found by EM, and we have found the lowest order correction term due to the uniform resetting in the interval $[-L,L]$. We compare in Fig. 4.4(b) the numerical solution to the equation $d\langle T\rangle_{x_0}/dz = 0$ (circles) with the approximation provided by Eq. (4.24) (curve). We note that when the target is far from the resetting interval, $x_T \gg L$ that is $\varepsilon \to 0$, the optimal situation takes place when the reset rate is low, and so the searcher has enough time to reach the target. Then, as $\varepsilon \to 0$ we expect $r_{opt} \to 0$. This is observed in Fig. 4.4(b). Contrarily, as $x_t \to L$, i.e., $\varepsilon \to 1$, to increase the chance of reaching the target, the optimal strategy is to avoid large excursions, which implies increasing the reset rate. This is also observed in Fig. 4.4(b) where r_{opt} increases with ε.

4.2.3 Symmetric reset-point PDF in an interval and $x_t \in \mathscr{D}$

We can now consider that the support of the resetting PDF contains the target, that is, $x_t \in \mathscr{D}$. We will consider two different cases: the first one when the resetting points are symmetrically distributed in an interval (i.e., $f(x_0)$ has finite support), or symmetrically distributed in the real line ($f(x_0)$ has infinite support).

A Finite support: Uniformly distributed points in an interval

We will start by writing $I(r,x_t)$ for a general symmetric distribution with support $\mathscr{D} = [-L,L]$, where now $-L < x_t < L$, thus $L \in (x_t,\infty)$. From the first equality of the last equation in Note 4.1 and considering that $f(x_0)$ is an even function we get

$$I(r,x_t,L) = e^{-x_t\sqrt{\frac{r}{D}}}\int_{-L}^{x_t} f(x_0)e^{x_0\sqrt{\frac{r}{D}}}dx_0 + e^{x_t\sqrt{\frac{r}{D}}}\int_{x_t}^{L} f(x_0)e^{-x_0\sqrt{\frac{r}{D}}}dx_0. \tag{4.25}$$

In the specific case that the reset-point PDF $f(x_0)$ is uniform in $[-L,L]$, as shown in Fig. 4.5, then

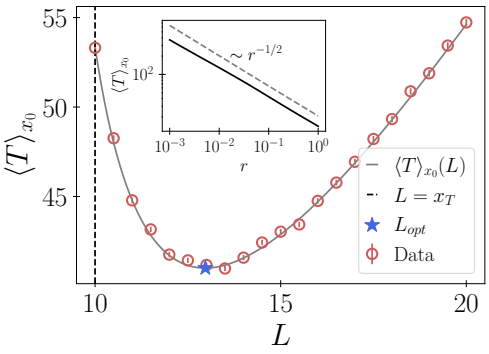


Figure 4.6: **AMFPT for uniformly distributed reset points in a finite interval containing the target.** The symbols are obtained from simulations and the solid line represents Eq. (4.27). The blue star is $L_{opt} = 12.97$. The parameters values are $D = 1$, $r = 0.1$, $x_t = 10$, and $N = 10^5$ trajectories are used. In the inset, the solid line represents the AMFPT as a function of the resetting rate r for $L = 15$ from Eq. (4.27), and the dashed line shows the predicted scaling as $r^{-1/2}$.

$$I(r,x_t,L) = \frac{1}{L}\sqrt{\frac{D}{r}}\left[1 - e^{-L\sqrt{\frac{r}{D}}}\cosh\left(x_t\sqrt{\frac{r}{D}}\right)\right] \tag{4.26}$$

and from (4.10) the AMFPT reads

$$\langle T\rangle_{x_0}(r,L) = \frac{1}{r}\left[\frac{L\sqrt{\frac{r}{D}}}{1 - e^{-L\sqrt{\frac{r}{D}}}\cosh\left(x_t\sqrt{\frac{r}{D}}\right)} - 1\right]. \tag{4.27}$$

In Fig. 4.6 we check Eq. (4.27) with numerical simulations, for both the behavior of the AMFPT with respect to r and with respect to L, showing an excellent agreement. Moreover, we see that there seems to exist an optimal value of L which minimizes the AMFPT. To check that this is a general result, and not the particular case for the parameters used for the plot, we study the AMFPT both for $L \to x_t$ and for large L. On one hand, it can be shown that $\left[\partial \langle T\rangle_{x_0}(L)/\partial L\right]_{L=x_t} < 0$. On the other hand, from Eq. (4.27) it is easy to see that $\langle T\rangle_{x_0}(L) \sim L$ as $L \to \infty$. The optimal resetting domain width, say L_{opt}, can be found from (4.27) by solving the equation $\partial \langle T\rangle_{x_0}/\partial L = 0$ to get

$$L_{opt} = \sqrt{\frac{D}{r}}\left[-1 - W_{-1}\left(-\frac{1}{e\cosh\left(x_t\sqrt{\frac{r}{D}}\right)}\right)\right], \tag{4.28}$$

where $W_{-1}(\cdot)$ is the lower branch of the Lambert function. For example, for the data used in Fig. 4.6 from (4.28) we find $L_{opt} = 12.97$, which is marked as a blue star in the figure. The existence of this minimum can be easily understood; at large values of L the probability of large excursions is not negligible, so the confining benefits of Poissonian resetting are lost, and thus the AMFPT diverges. For $L \to x_t$ Eq. (4.27) is (4.20), and for some values of $L \gtrapprox x_t$ the AMFPT decreases, this is because in this regime trajectories can start near the target both from the right and from the left, thus the existence of L_{opt} for $x_t \in [-L, L]$. Combining the results from Eq. (4.19) and Eq. (4.27) we have found that the AMFPT is smaller than the localized reset for any finite length of the interval

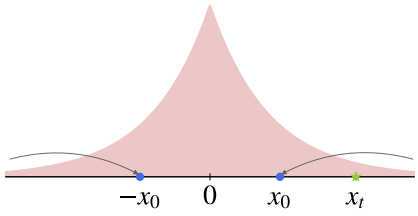


Figure 4.7: **Infinite support with exponential reset points.**

when the target is outside such interval, then, as L increases to contain the target, the AMFPT reaches a minimum for L_{opt} given by Eq. (4.28) and finally diverges at large values of L.

That the AMFPT diverges for large values of L is consistent with the mechanism discussed in Chapter 3: when resets or relocations place the walker arbitrarily far from the target in an unbounded domain, the search process again undergoes arbitrarily long excursions. In the present distributed-resetting problem, increasing L weakens the effective localization induced by resetting, and the AMFPT therefore diverges in the large-L limit.

Next, we check if for this case there also exists an optimal reset rate. In the limit where r approaches 0 from the left we find the behavior $\langle T\rangle_{x_0} \sim r^{-1/2}$, so that (4.27) diverges in this limit. In the limit $r \to \infty$ then it is shown that $\langle T\rangle_{x_0} \sim r^{-1/2}$ as well. Altogether, no optimal reset rate exists, and the scaling behavior $\langle T\rangle_{x_0} \sim r^{-1/2}$ is observed both for small and large r. This is shown in the inset of Fig. 4.6 where the scaling $r^{-1/2}$ is observed within some orders of magnitude.

B Infinite support

The second case of $x_t \in \mathscr{D}$ that we consider takes $\mathscr{D} = \mathbb{R}$ and assumes exponentially distributed resetting points as shown in Fig. 4.7, that is

$$f(x_0) = \frac{\lambda}{2} e^{-\lambda|x_0|}, \quad \lambda > 0. \tag{4.29}$$

From Eq. (4.11), we get

$$I(r,x_t,\lambda) = \frac{\lambda}{\lambda^2 - \frac{r}{D}} \left(\lambda e^{-x_t\sqrt{\frac{r}{D}}} - \sqrt{\frac{r}{D}} e^{-x_t\lambda} \right), \tag{4.30}$$

and finally, the AMFPT reads from (4.10)

$$\langle T\rangle_{x_0}(r,\lambda) = \frac{1}{r} \left(\frac{\lambda^2 - \frac{r}{D}}{\lambda^2 e^{-x_t\sqrt{\frac{r}{D}}} - \lambda\sqrt{\frac{r}{D}} e^{-x_t\lambda}} - 1 \right). \tag{4.31}$$

From (4.31) it results that $\langle T\rangle_{x_0} \sim \lambda^{-1}$ as $\lambda \to 0^+$, while in the limit $\lambda \to \infty$ the exponential function in Eq. (4.29) tends to a delta function so $\langle T\rangle_{x_0}$ tends to a constant

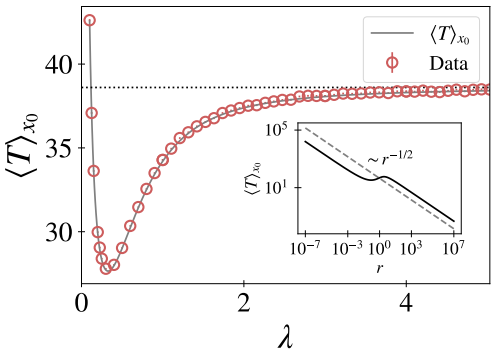


Figure 4.8: **AMFPT for uniformly distributed reset-point PDF in an infinite support.** The symbols are obtained from simulations and the solid line represents Eq. (4.31), and the dotted line represents the AMFPT for Eq. (2.26). The parameters used for the simulations are $D = 1$, $r = 0.1$, $x_t = 5$, and $N = 5 \cdot 10^5$ trajectories are used. In the inset, the solid line represents the AMFPT as a function of the resetting rate r for $\lambda = 1$ from Eq. (4.31). The dashed line shows the decaying as $r^{-1/2}$.

value corresponding to the EM result in Eq. (2.26), as shown in Fig. 4.8 by the dashed line. In this case, we have not been able to prove the existence of the λ_{opt} in general, however from the discussion on the previous case, we expect that it exists. We also check the existence of an optimal reset rate. Taking the limit $r \to 0^+$ to Eq. (4.31) we find $\langle T \rangle_{x_0} \sim r^{-1/2}$. Taking the limit $r \to \infty$ to (4.31), one has $\langle T \rangle_{x_0} \sim r^{-1/2}$ as well, and then no optimal reset rate exists. This scaling can be seen in the inset of Fig. 4.8.

4.2.4 Resetting to two points

Next, we consider the situation in which the resetting process is not symmetric. We cannot use Eq. (4.16) since it only holds for symmetric $f(x_0)$, therefore we need to get the AMFPT from the general expression (4.11). Let us consider that the searcher either resets to the point $x_0 = +L$ with probability p, or to the point $x_0 = -L$ with probability $1-p$, then

$$f(x_0) = p\delta(x_0 - L) + (1-p)\delta(x_0 + L), \tag{4.32}$$

if $x_t > L$. Then, from (4.10) and (4.32)

$$\langle T \rangle_{x_0}(r, L) = \frac{1}{r}\left[\frac{e^{x_t\sqrt{\frac{r}{D}}}}{(1-p)e^{-L\sqrt{\frac{r}{D}}} + pe^{L\sqrt{\frac{r}{D}}}} - 1\right]. \tag{4.33}$$

Again, it can be shown that $\langle T \rangle_{x_0}$ approaches EM result (2.26) in the limit $L \to 0$. Next we study the behavior of the AMFPT for a finite value of L in terms of the probability p. For $L > 0$, if $0 < p < 1/2$ the AMFPT reaches a maximum value at

$$L = L_c = \sqrt{\frac{D}{r}} \ln\left(\frac{\sqrt{p(1-p)}}{p}\right), \quad 0 < p < 1/2. \tag{4.34}$$

This maximum does not exist when $1/2 < p < 1$, and the maximum of $\langle T \rangle_{x_0}$ is attained at $L = 0$. Moreover, when $0 < p < 1/2$ it can be shown that the AMFPT of resetting to a single point in the origin $L = 0$ is smaller than the distributed case for $0 < L < L^*$, this is $\langle T \rangle_{x_0}(L = 0) < \langle T \rangle_{x_0}(L)$. However, for $L^* < L < x_t$ the AMFPT of the distributed case is smaller $\langle T \rangle_{x_0}(L = 0) > \langle T \rangle_{x_0}(L)$ where we have defined

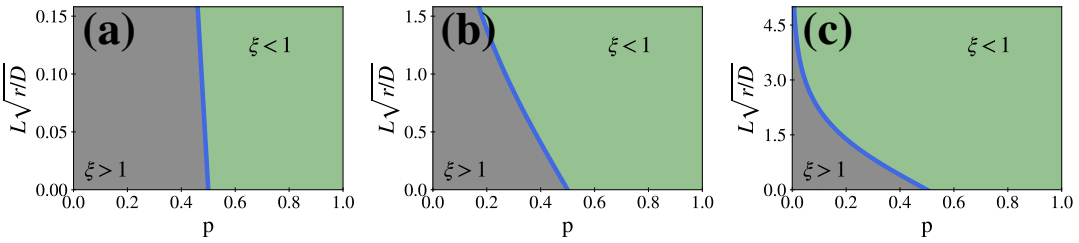


Figure 4.9: **Diagram $L\sqrt{r/D}$ vs p for asymmetric resetting points in an interval with $x_t > L$.** The parameter ξ is defined as $\xi = \langle T \rangle_{x_0}(L) / \langle T \rangle_{x_0}(L=0)$. We have obtained the value of ξ numerically from Eq. (2.26) and Eq. (4.33). The green region ($\xi < 1$) corresponds to the case where the asymmetric resetting strategy is more efficient, while in the gray region the most efficient strategy is to reset to $x_0 = 0$. The blue line, computed through Eq. (4.35), represents $L^*\sqrt{r/D}$ vs p. Panel (a) is for a reset rate $r = 0.01$, panel (b) for $r = 0.1$ and panel (c) for $r = 1$.

$$L^* = \sqrt{\frac{D}{r}} \ln\left(\frac{1-p}{p}\right). \tag{4.35}$$

Then, given a value of $p < 1/2$, resetting to the origin will be more optimal for all $L < L^*$. On the other hand, for $1/2 < p < 1$, L_c does not exist and the maximum of $\langle T \rangle_{x_0}$ is attained at $L = 0$, meaning that for any finite length $L > 0$ the AMFPT of resetting to two points is always smaller than the case of resetting to the origin. In Fig. 4.9 we summarize these results graphically, where we can see that the distributed resetting yields a smaller value of the AMFPT (green region) for small values of p given that $L^* < L < x_t$. What this shows is that just a small chance of starting the trajectory closer to the target, p, even if it is less than half the time, is enough to reduce the AMFPT.

For the case when the target lies between the resetting points, that is, for $x_t < L$ from Eqs. (4.10) and (4.32) we get

$$\langle T \rangle_{x_0}(r,L) = \frac{1}{r}\left[\frac{e^{L\sqrt{\frac{r}{D}}}}{(1-p)e^{-x_t\sqrt{\frac{r}{D}}} + pe^{x_t\sqrt{\frac{r}{D}}}} - 1\right] \tag{4.36}$$

which yields a AMFPT that is monotonically increasing with L for $L \in (x_t, \infty)$. Note that this expression is the same as Eq. (4.33) but exchanging x_t and L.

As we have done for the previous cases, we want to study, if it exists, the optimal reset rate that minimizes the AMFPT, so we proceed as above. It is easy to show that in the limit $r \to 0^+$ the AMFPTs given by (4.33) and (4.36) go as r^{-1} as in the previous examples. Hence, the AMFPT diverges when r approaches 0. In the limit $r \to \infty$ from (4.33) we have $\langle T \rangle_{x_0} \sim \frac{e^{(x_t-L)\sqrt{r/D}}}{r}$, and this goes to infinity provided that $x_t > L$. For $x_t < L$, using (4.36) we have $\langle T \rangle_{x_0} \sim \frac{e^{(L-x_t)\sqrt{r/D}}}{r}$ as $r \to \infty$, so the existence of an optimal reset rate is proven if $x_t \neq L$. However, for the specific case $x_t = L$ we have $\langle T \rangle_{x_0} \sim r^{-1}$ and no optimal reset rate exists; the minimum value of the AMFPT is zero, and it is attained as $r \to \infty$. This means that the optimal reset rate diverges as L tends to x_t. We can get at which rate r_{opt} diverges by proposing the ansatz for r

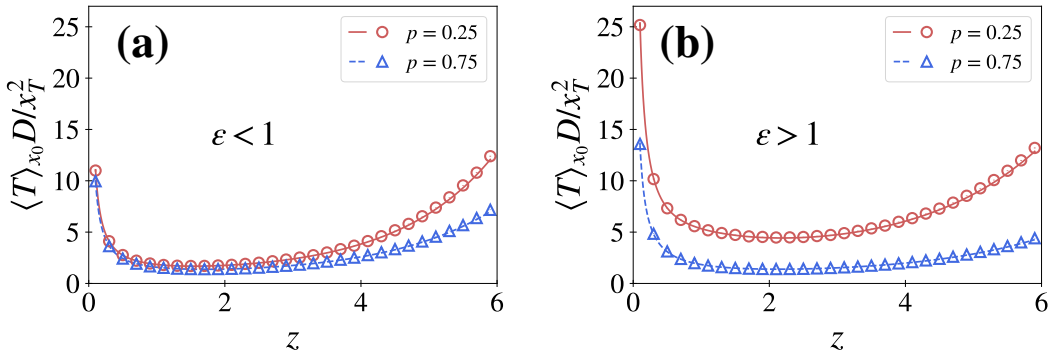


Figure 4.10: **Optimal reset rate for asymmetric resetting points in an interval with $x_t > L$.** $\frac{D}{x_t^2}\langle T\rangle_{x_0}$ as function of the parameter $z = x_t\sqrt{r/D}$ for $p = 0.25$ (red) and $p = 0.75$ (blue). The lines represent Eq. (4.38) while the points (circles and triangles) are data from numerical simulations. The parameters used for obtaining the data are $D = 1$, $x_t = 2$, and r is computed given a fixed value of z. In panel (a) $\varepsilon = 0.2$, therefore $L = 0.2$. In panel (b) $\varepsilon = 1.8$, therefore $L = 3.6$. For the simulations, we have used $N = 10^5$ trajectories.

$$r_{opt} \sim |\varepsilon - 1|^{-\beta}, \quad \text{as} \quad \varepsilon \to 1 \tag{4.37}$$

in order to compute the exponent β, which we can do numerically. Considering Eqs. (4.21), (4.33), and (4.36) we find

$$\frac{D}{x_t^2}\langle T\rangle_{x_0} = \begin{cases} \frac{1}{z^2}\left[\frac{e^z}{(1-p)e^{-\varepsilon z}+pe^{\varepsilon z}} - 1\right], & 0 < \varepsilon < 1 \\ \frac{1}{z^2}\left[\frac{e^{\varepsilon z}}{(1-p)e^{-z}+pe^{z}} - 1\right], & \varepsilon > 1. \end{cases} \tag{4.38}$$

In Fig. 4.10 we compare this result against numerical simulations. The agreement is excellent for both cases $\varepsilon < 1$ and $\varepsilon > 1$. In agreement with our reasoning, in both cases there is an optimal reset rate that minimizes the AMFPT. In the case $\varepsilon \to 1$, that is, when $L \approx x_t$ we observe (see Fig. 4.11) that

$$r_{opt} \sim \frac{D/x_t^2}{|\varepsilon - 1|^2} \tag{4.39}$$

so that the exponent $\beta = 2 \pm 10^{-7}$. We can show this analytically, by means of Eq. (4.23) and (4.37) and writing $z_{opt} \sim |\delta|^{-\beta}$, where $\delta = \varepsilon \pm 1$. It is important to note that there will appear terms proportional to z and to $z\delta$ and in the limit $\varepsilon \to 1^{\pm}$, i.e., $\delta \to 0$, we have $z \to \infty$ and $z \gg z\delta$. Let us deal with the cases $\varepsilon > 1$ and $\varepsilon < 1$ separately. By taking the derivative of (4.38) respect to z for $\varepsilon < 1$ we find that the z_{opt} is solution to

$$p(\delta z - 2)e^{4z}e^{-3z\delta} + (1-p)(-2+2z-\delta z)e^{2z}e^{-z\delta} = 2\left(pe^{2z}e^{-2z\delta} + 1 - p\right)^2. \tag{4.40}$$

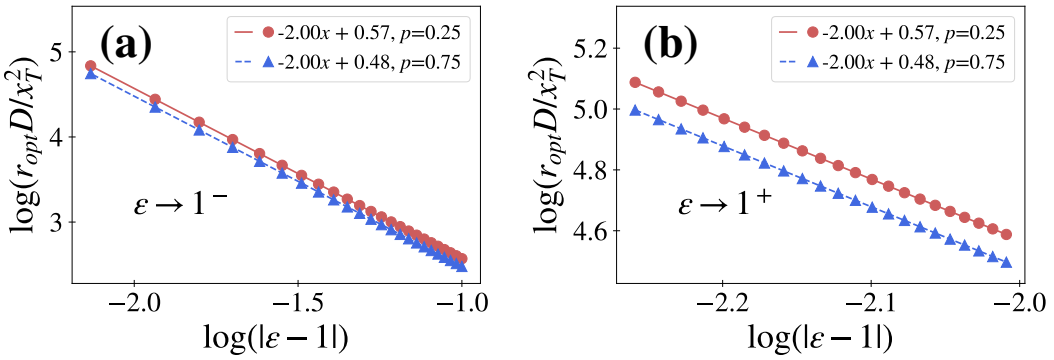


Figure 4.11: **Optimal reset rate exponent for asymmetric resetting points in an interval with $x_t > L$.** $r_{opt}(\varepsilon)$ for $\varepsilon \to 1$ for $p = 0.25$ (red circles) and $p = 0.75$ (blue triangles). The dots are obtained by numerically minimizing Eq. (4.38) and the lines are linear regressions to the data, for each curve the correlation coefficient $R^2 = 0.9999$. In panel (a) $\varepsilon \to 1^-$. In panel (b) $\varepsilon \to 1^+$.

It is not difficult to see that the first term on the left-hand side (l.h.s.) of Eq. (4.40) is much higher than the second term in the limit $\delta \to 0$ ($z \to \infty$) where $\delta = 1 - \varepsilon$. The term on the r.h.s. of Eq. (4.40) approaches $2p^2 e^{4z}$. Eq. (4.40) reduces then to $\delta z_{opt} \sim 2p(1+p)$, so that $\delta^{1-\beta/2} \sim O(\delta^0)$, leading to $\beta = 2$. We can proceed analogously for $\varepsilon > 1$. Taking the derivative of (4.38) with respect to z we find

$$(1-p)(2-2z-z\delta)e^{2z}e^{z\delta} + p(2-\delta z)e^{4z}e^{\delta z} = 2\left(pe^{2z}+1-p\right)^2 \tag{4.41}$$

for $\varepsilon > 1$ where now $\delta = \varepsilon - 1$. In the limit $\delta \to 0$, we see that the second term of the l.h.s. of Eq. (4.41) is larger than the first one. So that, $p(2-\delta z_{opt}) \sim 2p^2$, i.e., $\delta z_{opt} \sim 2(1-p)$, which leads to $\delta^{1-\beta/2} \sim O(\delta^0)$ and then to $\beta = 2$ again.

4.3 Equivalent resetting point

In the previous sections, we have been comparing the AMFPT obtained after averaging over distributed reset points with the MFPT for resetting to a single point at the origin, and we have seen that resetting to a distribution can be more efficient in some cases. This raises the question: given a specific resetting point PDF $f(x_0)$, what is the specific value of a single reset point x_e such that the resulting MFPT is the same as the AMFPT obtained for the distributed case with $f(x_0)$? The value of x_e can be denoted as an ERP with respect to the PDF $f(x_0)$. As we have seen in Sec. 4.2.1, any choice of $f(x_0)$ with a given MFPT will lead to the same first-passage PDF as another choice of $f(x_0)$ with the same mean value, so we expect that the first-passage statistics of resetting to the ERP will be completely equivalent to the case of distributed resetting, independent of $f(x_0)$. To compute the MFPT for the ERP consider Eq. (4.10) with the reset point distribution $f(x_0) = \delta(x_0 - x_e)$, then

$$\langle T_e \rangle_{x_0} = \frac{1}{r}\left(e^{|x_e - x_t|\sqrt{\frac{r}{D}}} - 1\right). \tag{4.42}$$

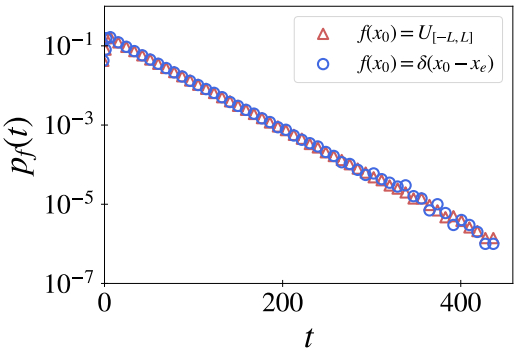


Figure 4.12: **First-passage PDFs.** In red triangles the FPT PDF for distributed symmetric resetting points in the interval $[-L,L]$. In blue circles, the FPT PDF to its ERP. The parameters used for the simulations are $x_t = 5$, $D = 1$, $r = 0.1$, $L = 2$ and $N = 10^7$ trajectories.

Consequently, by the definition of x_e, equating (4.42) to (4.10) the following relation has to be satisfied

$$|x_e - x_t| = -\sqrt{\frac{D}{r}} \ln\left[I(r,x_t)\right]. \tag{4.43}$$

As we have proven, $I(r,x_t) < 1$ so that the sign of the right-hand side of Eq. (4.43) is positive. Solving Eq. (4.43) for x_e we find two possible solutions:

$$x_e^{\pm} = x_t \mp \sqrt{\frac{D}{r}} \ln\left[I(r,x_t)\right]. \tag{4.44}$$

Both solutions for the ERP are at the same distance from the target, the positive (negative) solution corresponding to the ERP at the right (left) side of the target, respectively. Let us now compute the specific values of the x_e for the $f(x_0)$ discussed above. The ERP corresponding to the symmetric reset-point PDF in the interval $[-L,L]$ with $x_t \notin \mathscr{D}$, is from (4.15) and (4.44)

$$\begin{aligned} x_e^{+} &= 2x_t - \sqrt{\frac{D}{r}} \ln\left[\int_{-L}^{L} f(x_0) e^{x_0\sqrt{\frac{r}{D}}} dx_0\right] \\ x_e^{-} &= \sqrt{\frac{D}{r}} \ln\left[\int_{-L}^{L} f(x_0) e^{x_0\sqrt{\frac{r}{D}}} dx_0\right]. \end{aligned} \tag{4.45}$$

In particular, for a uniform resetting-points PDF in $[-L,L]$ with $x_t > L$, and using (4.45), we obtain

$$\begin{aligned} x_e^{+} &= 2x_t - \sqrt{\frac{D}{r}} \ln\left[\frac{1}{L}\sqrt{\frac{D}{r}} \sinh\left(L\sqrt{\frac{r}{D}}\right)\right] \\ x_e^{-} &= \sqrt{\frac{D}{r}} \ln\left[\frac{1}{L}\sqrt{\frac{D}{r}} \sinh\left(L\sqrt{\frac{r}{D}}\right)\right]. \end{aligned} \tag{4.46}$$

Alternatively, for the case in Eq. (4.32) where the searcher resets to $-L$ or to L with probabilities $1-p$ and p, with $x_t > L$, using Eq. (4.44) we get

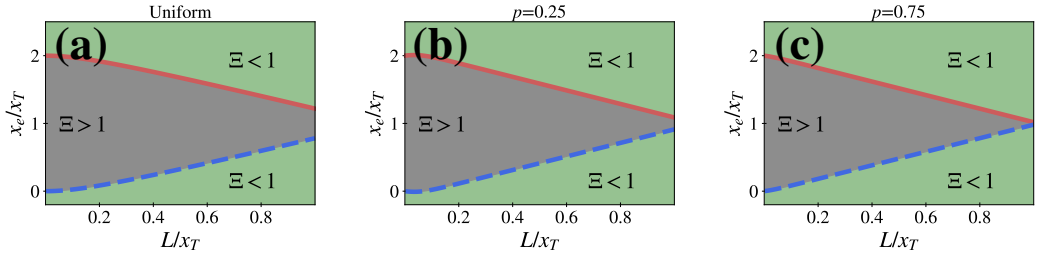


Figure 4.13: **Diagram x_r/x_t vs L/x_t for the ERP with $x_t \notin \mathscr{D}$.** We have obtained the value of Ξ, defined in Eq. (4.52), numerically using Eq. (2.26) and Eq. (4.19) in panel (a) and Eq. (2.26) and Eq. (4.33) in panels (b) and (c). In the green region ($\Xi < 1$), it is more efficient to reset to random distributed points. However, in the gray region, the efficient strategy is to reset to x_r. The red solid line represents x_e^+ while the blue dashed line represents x_e^-. Panel (a) corresponds to a uniform reset-point PDF in $[-L,L]$ the red and blue lines being computed with Eq. (4.46). Panels (b) and (c) the searcher resets to $-L$ or L with probabilities $1-p$ and p, respectively. Then the red and blue lines are computed with Eq. (4.47). Panel (b) is for $p = 0.25$ and panel (c) is for $p = 0.75$.

$$\begin{aligned} x_e^+ &= 2x_t - \sqrt{\frac{D}{r}} \ln\left[p e^{L\sqrt{\frac{r}{D}}} + (1-p) e^{-L\sqrt{\frac{r}{D}}} \right] \\ x_e^- &= \sqrt{\frac{D}{r}} \ln\left[p e^{L\sqrt{\frac{r}{D}}} + (1-p) e^{-L\sqrt{\frac{r}{D}}} \right] \end{aligned} \tag{4.47}$$

In Fig. 4.12 we confirm with numerical simulations that not only are the mean values the same, but also that the PDFs are the same, as anticipated. We do so for the case where $f(x_0)$ is taken as a uniform distribution in the interval $(-L,L)$. We simulate the resetting process to a point x_0 randomly sampled from the symmetric reset-point PDF in the interval $[-L,L]$ and we compute the first-passage PDF, represented in red triangles. We then simulate the resetting process to the ERP obtained from Eq. (4.46) and compute its first-passage PDF, in blue circles. We see that not only the PDFs coincide, but also that at long times the decay is exponential, as discussed in Sec. 4.2.1.

Next, we consider the case when $x_t \in \mathscr{D}$ the ERP given by Eq. (4.44) can be written as

$$\begin{aligned} x_e^+ &= x_t - \Delta(x_t) \\ x_e^- &= x_t + \Delta(x_t) \end{aligned} \tag{4.48}$$

where $\Delta(x_t) = \sqrt{D/r}\ln[I(r,x_t)]$. If we consider the uniform reset-point PDF in $[-L,L]$ with $-L < x_t < L$, the integral $I(r,x_t)$ is given by (4.26) and

$$\Delta(x_t) = \sqrt{\frac{D}{r}} \ln\left\{ \frac{1}{L}\sqrt{\frac{D}{r}} \left[1 - e^{-L\sqrt{\frac{r}{D}}} \cosh\left(x_t \sqrt{\frac{r}{D}} \right) \right] \right\}. \tag{4.49}$$

When the reset-point PDF is given by Eq. (4.29) then

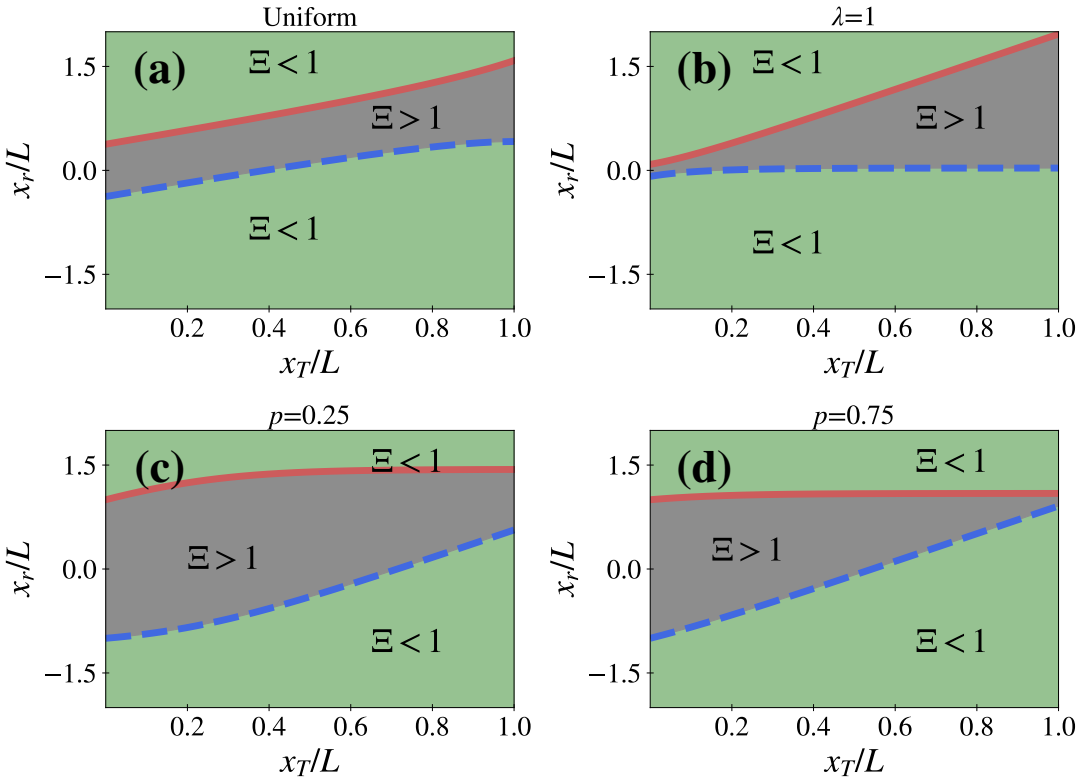


Figure 4.14: **Diagram x_r/L vs x_t/L for the ERP when $x_t \in \mathscr{D}$.** We have obtained the value of Ξ, defined in Eq. (4.52), numerically using Eq. (2.26) and Eq. (4.27) in panel (a), Eq. (2.26) and Eq. (4.31) in panel (b), and Eq. (2.26) and Eq. (4.36) in panels (c) and (d). In the green region ($\Xi < 1$), it is more efficient to reset to distributed random points. However, in the gray region ($\Xi > 1$), the efficient strategy is to reset to x_r. The red solid line represents x_e^+ while the blue dashed line represents x_e^- computed with Eq. (4.48). We make use of (4.49) in panel (a), (4.50) in panel (b) and (4.51) in panels (c) and (d).

$$\Delta(x_t) = \sqrt{\frac{D}{r}} \ln\left\{ \frac{\lambda}{\lambda^2 - \frac{r}{D}} \left(\lambda e^{-x_t\sqrt{\frac{r}{D}}} - \sqrt{\frac{r}{D}} e^{-x_t\lambda} \right) \right\}. \tag{4.50}$$

Finally, for the asymmetric case given by Eq. (4.32) with $x_t < L$, we get

$$\Delta(x_t) = \sqrt{\frac{D}{r}} \ln\left[e^{-L\sqrt{\frac{r}{D}}} \left(p e^{x_t\sqrt{\frac{r}{D}}} + (1-p) e^{-x_t\sqrt{\frac{r}{D}}} \right) \right]. \tag{4.51}$$

From the analysis above we have seen that we can always find a x_e so that the distributed resetting and the resetting to a single point have the same first-passage statistics. Now, in order to compare the AMFPT of resetting to distributed points $\langle T \rangle_{x_0}$ with the AMFPT of resetting to a fixed point, say x_r, $\langle T_r \rangle_{x_0}$, we define the dimensionless quantity

$$\Xi = \frac{\langle T \rangle_{x_0}}{\langle T_r \rangle_{x_0}} \tag{4.52}$$

where $\langle T_r \rangle_{x_0} = \left(e^{|x_r - x_t|\sqrt{\frac{r}{D}}} - 1 \right) / r$. Ξ has been defined so that $x_r = x_e$ leads immediately to $\Xi = 1$.

In Figs. 4.13 and 4.14 we illustrate a comparison between both resetting protocols. In the former we plot the diagram x_r/x_t versus L/x_t for the equivalent resetting point when $x_t \notin \mathscr{D}$ where the blue and red curves have been plotted from Eq. (4.47). In the latter we show a diagram for x_r/x_t versus L/x_t when $x_t \in \mathscr{D}$ with the curves corresponding to the results found in Eq. (4.48) together with (4.49), (4.50) and (4.51). In the gray region, $(\Xi > 1)$ resetting to x_r yields a smaller AMFPT, however in the green region, the distributed resetting is more efficient.

4.4 Fluctuations of the MFPT

In the previous section, we have been discussing how the mean of the first-passage time PDF for the distributed resetting case is larger or smaller than resetting to a single point, and we have argued that under some circumstances, resetting to a distributed PDF can be beneficial when it comes to the mean. This however, raises the question of what happens to the fluctuations of the AMFPT. In this section, to complete the study of the AMFPT we will characterize the corresponding fluctuations for the case of a Brownian searcher with distributed resetting. By averaging over $f(x_0)$ and by taking $n = 2$ from Eq. (4.8) we have that the second moment $\langle T^2 \rangle_{x_0}$ is given by

$$\langle T^2 \rangle_{x_0} = \frac{2}{r I(r,x_t)} \left\{ \partial_r I(r,x_t) + \frac{1 + r\partial_r I(r,x_t)}{r I(r,x_t)} \left[1 - I(r,x_t) \right] \right\}. \tag{4.53}$$

Accordingly, the variance of the first-passage time is

$$\sigma^2 = \langle T^2 \rangle_{x_0} - \langle T \rangle_{x_0}^2 = \frac{1}{r^2}\left[\frac{1+2r\partial_r I(r,x_t)}{I(r,x_t)^2} - 1\right] \tag{4.54}$$

and the coefficient of variation (CV), defined as the quotient between the standard deviation and the AMFPT, can be expressed as

$$\mathrm{CV} = \frac{\sigma}{\langle T \rangle_{x_0}} = \frac{\sqrt{1 - I(r,x_t)^2 + 2r\partial_r I(r,x_t)}}{1 - I(r,x_t)}. \tag{4.55}$$

First, we note that the condition for the optimal resetting rate, i.e., $\partial \langle T \rangle_{x_0} / \partial r = 0$ can be combined with (4.55) to find $\mathrm{CV} = 1$, in agreement with [97], that is, CV is universally equal to 1 at the optimal resetting rate. Next, we study the behavior of the CV with the width of the resetting interval L and the resetting rate r for the examples provided above.

4.4.1 Example: Uniform resetting PDF with $x_t > L$

We first consider the case when $f(x_0)$ is uniform in, $(-L, L)$, with $x_t > L$. From the definitions in (4.21), together with (4.18), we get

$$I(\varepsilon, z) = \frac{\sinh(\varepsilon z)}{\varepsilon z e^z}, \quad 2r\frac{\partial I(r,x_t)}{\partial r} = z\frac{\partial I(\varepsilon,z)}{\partial z} = e^{-z}\left[\cosh(\varepsilon z) - \frac{1+z}{\varepsilon z}\sinh(\varepsilon z)\right] \tag{4.56}$$

Plugging these results into (4.55) we get the expression for the CV corresponding to the uniform resetting PDF with $0 < L < x_t$ (or $0 < \varepsilon < 1$), namely $\mathrm{CV}(\varepsilon, z)$. For fixed x_t the limit $L \to 0$, that is, $\varepsilon \to 0$ we find

$$\mathrm{CV}_{EM} = \mathrm{CV}(\varepsilon = 0, z) = \frac{\sqrt{e^{2z} - ze^z - 1}}{e^z - 1}, \tag{4.57}$$

which corresponds to the EM limit found in Eq. (3) in Ref. [97]. On the other hand, in the opposite limit $L \to x_t$ one has $\varepsilon \to 1$ so that

$$\mathrm{CV}(\varepsilon = 1, z) = \frac{\Phi(z)}{1 + (2z-1)\,\mathrm{e}^{2z}},$$

where we have defined

$$\Phi(z) \equiv \sqrt{(4z^2 + 2z + 2)\,e^{2z} - 1 + (4z^2 - 2z - 1)\,e^{4z}}.$$

Although it can be numerically proven that $\mathrm{CV}(\varepsilon = 1, z) > \mathrm{CV}(\varepsilon = 0, z)$ for any $z \in (0, \infty)$ and $\varepsilon \in [0, 1]$ using the results above, it does not prove in general that a minimum value for $\mathrm{CV}(\varepsilon, z)$ exists, for a given ε, in this case. However, analyzing the behavior of $\mathrm{CV}(\varepsilon, z)$ near $\varepsilon = 0$, it can be shown that $[\partial \mathrm{CV}(\varepsilon, z)/\partial \varepsilon]_{\varepsilon=0} = 0$ but the second derivative $\left[\partial^2 \mathrm{CV}(\varepsilon, z)/\partial \varepsilon^2\right]_{\varepsilon=0} > 0$ if $z \in (0, z^*)$ and $\left[\partial^2 \mathrm{CV}(\varepsilon, z)/\partial \varepsilon^2\right]_{\varepsilon=0} < 0$ if $z \in (z^*, \infty)$, where $z^* = 3.83$. Therefore, there is an optimal value L_{opt} for L which

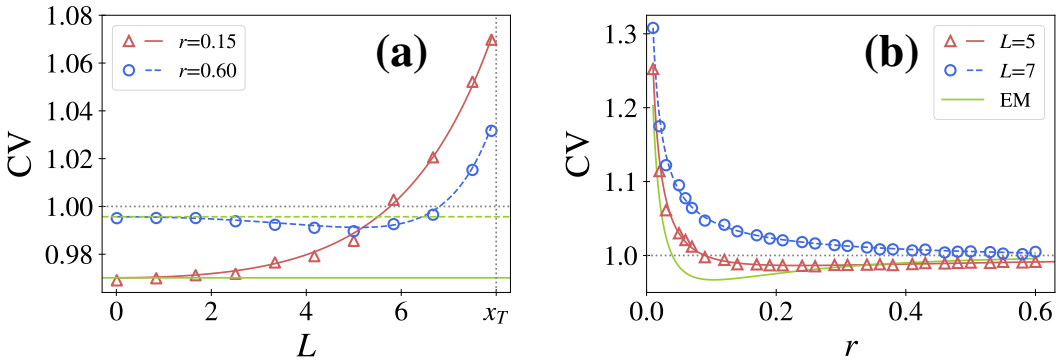


Figure 4.15: **CV for the uniform resetting PDF with $x_t > L$** The red and blue lines are obtained from Eq. (4.55) while the points are data obtained from numerical simulations (a) CV as a function of L for $r = 0.15$, $r < r_c$, (red solid line and triangles) and $r = 0.60$, $r > r_c$ (blue dashed line and circles). The green horizontal lines represent the EM case. (b) Coefficient of variation CV as a function of r for $L = 5$, (red solid line and triangles) and $L = 7$ (blue dashed line and circles). In all panels the parameters used are $x_t = 8$, $D = 1$ and $N = 10^6$ trajectories. Therefore, $r_c = 0.23$ and the value of r at which CV$= 1$ is $r_{opt} = 0.044$.

minimizes CV(ε, z) if and only if $r > r_c$, where $r_c = 14.67D/x_t^2$. We conclude that if $r > r_c$ the fluctuations of the FPT when the searcher resets to points uniformly distributed with $L = L_{opt}$ are smaller than when resetting to a point ($L = 0$). Otherwise, when $r < r_c$ the resetting process to a point has smaller fluctuations than resetting to points uniformly distributed, regardless of the value of L. In Fig. 4.15(a) we compare CV computed from ((4.55)-(4.56)) (solid curves) with numerical simulations (symbols), showing an excellent agreement. It is shown that for $r > r_c$ (in blue) the CV reaches a minimum value, while for $r < r_c$ (in red) such a minimum does not exist. We also plot (green lines) the CV corresponding to the EM case, i.e., where the searcher resets to the origin ($L = 0$), computed from (4.57). When $r < r_c$ we have CV $>$ CV$_{EM}$ while if $r > r_c$ then this condition depends on L.

Next, we explore how the CV depends on the reset rate r. To do this, we let $z \to 0$ (with the rest of the values fixed) and obtain from (4.56) that CV $\simeq z^{-1/2} \sim r^{-1/4}$, so that the CV diverges as r tends to 0. This is equivalent to $z \to \infty$, and from (4.56) we find that the CV tends to 1. In this case, although we have numerically observed that there is always a minimum for the CV, we are not able to prove its existence rigorously. In Fig. 4.15(b), we plot the CV as a function of r for two values of L. We show in green the case CV$_{EM}$, which allows us to see that depending on the values of r, the CV can be higher or lower than CV$_{EM}$.

4.4.2 Example: Uniform resetting PDF with $x_t \in \mathscr{D}$

As a second example, we study the case for which $x_t \in \mathscr{D}$. Recall that we had set $x_t > 0$ for simplicity, but we could do the same discussion for $x_t < 0$. Introducing the dimensionless parameters (4.21) into Eq. (4.26) we get

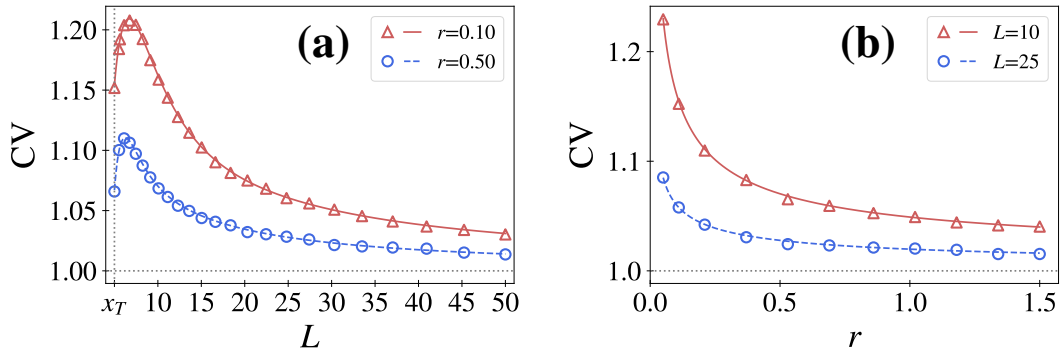


Figure 4.16: **CV for the uniform resetting PDF with** $x_t < L$ The red and blue lines are obtained from Eq. (4.55) while the points are data obtained from numerical simulations (a) CV as a function of L for $r = 0.1$ (red solid line and triangles) and $r = 0.50$ (blue dashed line and circles). The green horizontal lines represent the EM case. (b) Coefficient of variation CV as a function of r for $L = 10$ (red solid line and triangles) and $L = 25$ (blue dashed line and circles). In all panels the parameters used are $x_t = 5$, $D = 1$ and $N = 10^6$ trajectories.

$$I(\varepsilon, z) = \frac{1}{\varepsilon z}\left[1 - e^{-\varepsilon z}\cosh(z)\right]. \tag{4.58}$$

Since $x_t > 0$ and $-L < x_t \leq L$, then $\varepsilon \in [1, \infty)$ holds. We can then compute the CV from Eq. (4.55). To analyze the behavior of the CV with L we fix a value of z and vary ε. We note that $\mathrm{CV}(\varepsilon \to 1^+, z) > 1$ and $\mathrm{CV}(\varepsilon \to \infty, z) \sim 1 + 1/2z\varepsilon + \ldots$. Since $[\partial \mathrm{CV}(\varepsilon, z)/\partial \varepsilon]_{\varepsilon=1} > 0$, then we conclude that CV reaches a maximum value for a specific value of L.

In Fig. 4.16(a) we compare the CV for the uniform reset-point PDF computed from (4.55) with numerical simulations for two different values of r. It confirms the decay $\mathrm{CV} \sim L^{-1}$ towards CV$= 1$. On the other hand, if we fix L and vary r we see that CV$\sim r^{-1/4}$ as $r \to 0$ and CV~ 1 as $r \to \infty$. Moreover, we have numerically checked that $[\partial \mathrm{CV}/\partial r] < 0$, so that CV decreases monotonically with r towards CV $= 1$. So, there is no value for r such that CV$= 1$, which is in agreement with the fact that there is no optimal reset rate that minimizes the AMFPT. In Fig. 4.16(b) we compare the CV computed from (4.55) for the uniform reset-point PDF with numerical simulations, confirming the scaling of CV with r.

4.5 Summary of results

In this chapter we have studied the effect of a distributed reset-point PDF on the AMFPT of a Brownian searcher moving in one dimension. We have compared the search efficiency given by the AMFPT of resetting to the origin with the efficiency of resetting to randomly distributed points, either symmetrically or asymmetrically distributed around the origin.

We have proved the existence of an optimal reset rate, which minimizes the AMFPT,

when the resetting points are symmetrically distributed in an interval if the target position lies outside the interval. In this case, we have shown that resetting to the origin is always less efficient than resetting uniformly on an interval. When the resetting points are symmetrically distributed, but the target is located inside the domain of the reset-point PDF, we have proven that there is no optimal reset rate, but there is still an optimal interval width or an optimal characteristic resetting length which minimizes the AMFPT.

We have also considered an asymmetric resetting mechanism with different probabilities to two reset points located at the same distance to the left and right from the origin. For this case, we have proved the existence of an optimal reset rate, except when the target is located on one of the resetting points. In addition, we have shown that the optimal reset rate diverges as a power law as the target position approaches the position of a resetting point. Moreover, we have seen that in the long time limit the first-passage PDF averaged over the resetting points depends on the AMFPT only, revealing a somewhat universal behavior. This also allows us to define an equivalent resetting point for which the first-passage statistics coincide with those obtained under distributed resetting.

Finally, we have studied the fluctuations of the MFPT as a consequence of resetting to randomly distributed points and observed that they can be higher or lower than the fluctuations of the FPT of resetting to the origin depending on the reset rate and the resetting interval width. Together with Chapter 3, from these results we see that stochastic resetting modifies search efficiency not only through the resetting rate, but also through the structure of the state or position to which the process is reset.

III Ergodic properties

5 Occupation time statistics for non-Markovian random walks 79

5.1 Introduction 80
5.2 Non-Markovian random walks ... 80
5.3 The Feynman-Kac equation 83
5.4 Occupation time in an interval .. 85
5.5 Half occupation time 94
5.6 Poissonian resetting 97
5.7 Summary of results 104

6 Stochastic functionals under general resetting 107

6.1 Introduction 108
6.2 Characteristic function 108
6.3 Limiting PDF for a finite moment resetting distribution 111
6.4 Moments in the long-time limit .. 113
6.5 Application: Half occupation time 115
6.6 Summary of results 124

7 Occupation times in heterogeneous media 125

7.1 Introduction 125
7.2 Generating function and $D(x)$ .. 126
7.3 Half occupation time 128
7.4 Occupation time in an interval . 134
7.5 Summary of results 139

8 Occupation and area observables in Gaussian anomalous diffusion 141

8.1 Introduction 142
8.2 The first two moments 142
8.3 Stationary processes 146
8.4 Occupation-time statistics 147
8.5 Area observables 158
8.6 Summary of results 165

In Part II we have used first-passage observables to quantify the efficiency of search processes, and we have mainly focused on the resetting mechanism as a way to optimize it. In the current part we shift this focus, to analyze instead how a random walker distributes its time in space. In many physical applications, the relevant quantity is not only whether a particle arrives somewhere, but how long it remains there. A molecule diffusing inside a cell may need to spend sufficient time near a binding site before a reaction occurs. A tracer in a porous or nanoporous material may contribute to transport or catalysis only during the time it occupies a reactive region. A searcher that repeatedly returns to a preferred location may be efficient not because it reaches every point quickly, but because its residence time is concentrated in favorable zones. These examples motivate the study of time-integrated observables rather than only propagators, MSDs, or first-passage times [83, 209, 210].

The mathematical object used to describe these questions is the stochastic functional of the trajectory $x(t)$, as introduced in Chapter 2

$$Z(t) = \int_0^t U[x(\tau)]\, d\tau.$$

For suitable choices of U, this includes occupation times, residence fractions, local-time-like observables, and areas under the trajectory. The occupation time is particularly useful because it has a direct physical interpretation: it measures the time during which the walker experiences a given environment, reaction condition, mobility state, or spatial domain. In single-particle tracking, for example, two trajectories may have comparable displacement statistics but very different residence times in confined, crowded, or low-mobility regions [209, 211]. In fact, occupation time in a finite interval and the occupation time of the half space are among the most extensively studied examples of stochastic functionals [141]. Occupation-time statistics have been investigated far beyond standard Brownian motion, encompassing renewal processes [141, 212], active particles [104, 136], fractional Brownian motion [213, 214], subdiffusive walkers [122], as well as various experimental systems such as blinking quantum dots [215], colloids in optical traps [216], light resonators in cavities [217], and deterministic dynamics displaying weak ergodicity breaking [218].

These observables are relevant specially in the context of anomalous diffusion, where in general time averages and ensemble averages need not agree. For an ordinary ergodic process, the fraction of time spent in a region is expected to become reproducible at long times, converging to a deterministic value fixed by the stationary measure. In systems with long trapping times, aging, renewal memory, or spatially dependent mobility, this expectation can fail. The occupation fraction may remain random even in the long-time limit, so two nominally identical particles can give different empirical averages. This is not a technical subtlety: it affects how one interprets experiments based on individual trajectories. A time average measured from a single molecule, tracer particle, or search path may not represent the ensemble behavior if the process is weakly non-ergodic [22, 122, 134].

The models considered in this part are therefore motivated by different physical mechanisms that can make residence statistics nontrivial. In non-Markovian random walks transport occurs in trapping-dominated media or in systems where immobilization events are broadly distributed. Heterogeneous diffusion represents media in which

the local mobility depends on position, a common idealization for crowded cellular environments, porous materials, and complex fluids [67, 83, 210, 219]. Gaussian anomalous diffusion provides a complementary setting in which anomalous scaling may come from temporal correlations or from a time-dependent diffusivity rather than from explicit trapping. Moreover, as we have seen in the previous part, stochastic resetting can significantly alter the dynamics of a system, therefore we are also going to study how it can modify the statistics of stochastic functionals and their ergodic properties.

5

OCCUPATION TIME STATISTICS FOR NON-MARKOVIAN RANDOM WALKS

In this chapter, we study the occupation time statistics, occupation time in an interval, and half occupation time, for non-Markovian random walkers based on the formalism of the generalized master equation for the Continuous-Time Random Walk. We analyze the behavior of the PDFs, the moments, the limiting distributions and the ergodic properties for both occupation times when the underlying random walk is normal or anomalous. For the half occupation time, we revisit the arcsine law and examine its validity pertaining to various regimes of the rest period of the walker. Finally, we analyze how Poissonian resetting modifies these occupation-time statistics and drives the long-time distributions toward deterministic, ergodic behavior.

5.1 Introduction . . . 80
5.2 Non-Markovian random walks . . . 80
5.3 The Feynman-Kac equation . . . 83
5.4 Occupation time in an interval . . . 85
5.4.1 Moments of T_a . . . 86
5.4.2 PDF of T_a . . . 91
5.4.3 Ergodic properties of T_a . . . 94
5.5 Half occupation time . . . 94
5.5.1 Moments of T_+ . . . 95
5.5.2 PDF of T_+ . . . 96
5.5.3 Ergodic properties of T_+ . . . 97

5.6 Poissonian resetting 97
5.6.1 Moments – General expressions and asymptotics 98
5.6.2 PDF 101
5.6.3 Ergodic properties 102
5.7 Summary of results 104

5.1 Introduction

We start the first chapter of Part III by developing a framework to study positive stochastic functionals and apply it to the half occupation time and the occupation time in an interval for generic random walkers that may exhibit either Markovian or non-Markovian dynamics. To this end, we derive the FK equation for positive stochastic functionals within the framework of the CTRW, allowing for arbitrary waiting time distributions. Extending the classical FK formalism, originally formulated for Brownian motion (see Sec. 2.4), to generic non-Markovian settings enables the systematic treatment of systems where long-term memory effects are present and prevail. Moreover, we further study how Poissonian resetting, as introduced in the previous chapters, modifies the statistical and ergodic properties of these functionals.

Non-Markovian processes are relevant because many physical systems retain memory of their past evolution and therefore cannot be reduced to a memory-less diffusion with independent increments. In random-walk models, this memory may arise from broad waiting-time distributions, correlations between successive steps, or internal states that persist over finite time intervals, leading to anomalous transport and relaxation laws that differ from the Brownian case [17, 23, 220]. In this context, the CTRW framework as presented in Sec. 2.1.1 provides a convenient way to encode non-Markovianity through its waiting time and jump lengths PDFs.

This chapter is organized as follows. In Sec. 5.2 we review the derivation of the generalized master equation for the CTRW. In Sec. 5.3, we derive the FK equation for the characteristic function of a general stochastic functional when the random walk is described by the generalized master equation of the CTRW. In Sections 5.4 and 5.5 we apply the derived formalism to study the statistical properties (mean, fluctuation, and the PDF) for the occupation time in an interval and for the half occupation time respectively. Next, in Sec. 5.6 we analyze how the results from the previous two sections are modified by Poissonian resetting. Finally, in Sec. 5.7 we summarize the main results of this chapter.

5.2 Non-Markovian random walks

In this chapter, we describe non-Markovian random walks by means of the CTRW framework as introduced in Sec. 2.1.1. This formalism assumes that the walker starts at the initial position at time $t = 0$ and waits a random time before performing the first jump to a new position. It then waits again for a time interval before proceeding to the next jump. Jump lengths and waiting times are independent and identically distributed random variables according to the PDFs $\Psi(x)$ and $\varphi(t)$, respectively. In this

context, only when the waiting time PDF is exponential is the random walk Markovian, otherwise, it is non-Markovian. The propagator $P(x,t|x_0)$ that describes the position of the walker at time t given that it had started at the location x_0 is given by the famous Montroll-Weiss equation [23], which in Fourier-Laplace space reads

$$P(k,s|x_0) = \frac{e^{ikx_0}\left[1-\varphi(s)\right]}{s\left[1-\varphi(s)\Psi(k)\right]}, \tag{5.1}$$

where $\varphi(s)$ is the Laplace transform of the waiting time PDF and $\Psi(k)$ is the Fourier transform of the jump length PDF. Rearranging Eq. (5.1) we get

$$sP(k,s|x_0) - e^{ikx_0} = K(s)\left[\Psi(k)-1\right]P(k,s|x_0), \tag{5.2}$$

where $K(s)$ is the memory kernel in Laplace space

$$K(s) = \frac{s\varphi(s)}{1-\varphi(s)}. \tag{5.3}$$

Note that when the random walk is Markovian, that is $\varphi(t) = e^{-t/\langle\tau\rangle}/\langle\tau\rangle$, the memory kernel $K(t)$ is a Dirac delta function. Otherwise, the random walk is considered to be non-Markovian.

If the PDF of jumps $\Psi(x)$ has finite moments, we can consider the continuum limit in space and expand it in the Fourier space up to the second order in k. Then,

$$\Psi(k) = 1 - M_2\frac{k^2}{2} + \cdots = 1 - \frac{(k\sigma)^2}{2} + \cdots \tag{5.4}$$

where $M_2 = \int_{-\infty}^{\infty} x^2\Psi(x)dx$ is the mean square jump distance (second moment), and σ is the characteristic motion distance defined as $\sigma = \sqrt{M_2}$. Then, if the walker jumps a distance l to the right or left with probability 1/2, $\Psi(k) = \cos(kl) = 1 - k^2l^2/2 + \cdots$, and in this case $\sigma = l$. On setting $\Psi(k) \approx 1 - (\sigma k)^2/2$ in Eq. (5.2) and inverting in Fourier-Laplace we obtain the generalized master equation (GME) for random walks [220]

$$\frac{\partial P(x,t|x_0)}{\partial t} = \frac{\sigma^2}{2}\int_0^t K(t-t')\frac{\partial^2 P(x,t'|x_0)}{\partial x^2}dt'. \tag{5.5}$$

> **Note 5.1** We want to note that Eq. (5.5) can be expressed within the fractional calculus framework, even if we are not going to work within it directly, and would be known as the fractional diffusion equation [17, 221].

By means of Eq. (2.4) it is easy to find the MSD from the propagator in the Fourier-Laplace space

$$\langle x(s)^2\rangle = -\left(\frac{\partial^2 P(k,s|x_0)}{\partial k^2}\right)_{k=0}. \tag{5.6}$$

Using Eq. (5.5) and Eq. (5.6), the MSD, when the continuous space assumption holds and assuming that the walker starts from the origin, can be obtained in terms of the waiting time PDF as

$$\langle x(t)^2 \rangle = \sigma^2 \mathscr{L}^{-1}_{s\to t}\left[\frac{\varphi(s)}{s(1-\varphi(s))}\right]. \tag{5.7}$$

For a Markovian random walk the waiting time PDF, which we will refer to as FM (in reference to the Finite Moments) in the rest of this chapter, is

$$\varphi(t) = e^{-t/\langle\tau\rangle}/\langle\tau\rangle, \tag{5.8}$$

and thus, from Eq. (5.7) the MSD is $\langle x(t)^2\rangle = \sigma^2 t/\langle\tau\rangle$, where $\langle\tau\rangle = \int_0^\infty t\varphi(t)dt$ is the first moment of the waiting time PDF, i.e., the mean waiting time. If the waiting time PDF has all the moments finite then, for small s, one can do the following expansion

$$\varphi(s) = \int_0^\infty \left(1 - st + \frac{1}{2!}s^2t^2 + ...\right)\varphi(t)dt = 1 - \langle\tau\rangle s + O(s^2), \tag{5.9}$$

and thus the memory kernel is

$$K(s) \approx 1/\langle\tau\rangle \tag{5.10}$$

which, when inverting the Laplace transform yields $K(t) \approx \delta(t)/\langle\tau\rangle$ as we had anticipated. In this case, Eq. (5.5) reduces to the diffusion equation Eq. (2.1). Moreover by inserting Eq. (5.9) into Eq. (5.7) we obtain the same MSD in the long-time limit as for the exponential waiting time PDF. This means that the MSD for any random walk with a waiting time PDF with finite moments, at large times and when the continuous space assumption holds, converges to $\langle x(t)^2\rangle = \sigma^2 t/\langle\tau\rangle = 2Dt$ with $D = \sigma^2/(2\langle\tau\rangle)$, which corresponds to the MSD of normal diffusion.

Once we have discussed the Markovian case, we examine the anomalous case, focusing on subdiffusion. To account for the anomalous diffusion of the walker's movement, we first consider the waiting time PDF with power-law tails. In the long-time limit

$$\varphi(t) \sim \frac{1}{t^{1+\alpha}}. \tag{5.11}$$

We consider two cases of power-law waiting-times PDFs that fulfill Eq. (5.11). The first example is the fat-tailed PDF [17], which we will denote as (FT) in the rest of this chapter

$$\varphi(t) = \begin{cases} 0, & t < t_0 \\ \frac{\alpha t_0^\alpha}{t^{1+\alpha}}, & t > t_0, \end{cases} \tag{5.12}$$

where the index $0 < \alpha < 2$ and t_0 is a timescale. Note that for $0 < \alpha < 1$ the waiting time PDF lacks finite moments while for $1 < \alpha < 2$ only the first moment is finite. The Laplace transform of Eq. (5.12) is given by

$$\varphi(s) = \alpha e^{-st_0} U(1, 1-\alpha, st_0), \tag{5.13}$$

where $U(a,b;z)$ is the Tricomi confluent hypergeometric functions of the second kind [222]. Using the Tauberian theorem [223] in Eq. (5.13), we find the following expansion in Laplace space for small s

$$\varphi(s) \approx \begin{cases} 1 - b_\alpha s^\alpha, & 0 < \alpha < 1 \\ 1 - \langle\tau\rangle s + b_\alpha s^\alpha, & 1 < \alpha < 2 \end{cases} \tag{5.14}$$

where $b_\alpha = t_0^\alpha |\Gamma(1-\alpha)|$ and $\langle\tau\rangle = \alpha t_0/(\alpha-1)$. From this, the memory kernel $K(s)$ is in the small s limit

$$K(s) = \begin{cases} \frac{s^{1-\alpha}}{b_\alpha} + \ldots, & 0 < \alpha < 1 \\ \frac{1}{\langle\tau\rangle} + \frac{b_\alpha s^{\alpha-1}}{\langle\tau\rangle^2} + \ldots, & 1 < \alpha < 2 \end{cases} \tag{5.15}$$

which is clearly not a Dirac delta in t.

The second example of a power-law waiting-time PDF that we consider is the Mittag-Leffler (ML) PDF

$$\varphi(t) = \frac{t^{\alpha-1}}{\tau^{*\alpha}} E_{\alpha,\alpha}\left(-\frac{t^\alpha}{\tau^{*\alpha}}\right), \tag{5.16}$$

with $0 < \alpha < 1$ and $E_{\alpha,\beta}(\cdot)$ is the two-parametric Mittag-Leffler function [224]. The PDF takes the following form in Laplace space

$$\varphi(s) = \frac{1}{1 + (s\tau^*)^\alpha}, \tag{5.17}$$

so its memory kernel $K(s)$ reads

$$K(s) = \frac{s^{1-\alpha}}{(\tau^*)^\alpha}. \tag{5.18}$$

Once we have established the CTRW framework and the corresponding GME, we are now in a position to derive the FK equation.

5.3 The Feynman-Kac equation

We use the stochastic functional introduced in Eq. (2.31) and derive its backward Feynman-Kac, extending Eq. (2.32) to a general non-markovian case, in the context of the CTRW. In what follows, we denote by $Q(Z,t|x_0)$ the PDF of the functional, and by $Q(p,t|x_0)$ its Laplace transform in $Z \to p$. In the CTRW framework, we consider a walker performing jumps of constant length σ. The walker is initially at x_0 and after waiting a time t, randomly distributed according to $\varphi(t)$, it performs a jump to either $x_0 + \sigma$ or $x_0 - \sigma$ (with the same probability each) or it stays at x_0 during this time t. Hence, we can write the following evolution equation

$$Q(Z,t|x_0) = \int_0^t \varphi(\tau)\left\{\frac{1}{2}Q(Z-\tau U(x_0),t-\tau|x_0+\sigma)\right. \tag{5.19}$$
$$\left. + \frac{1}{2}Q(Z-\tau U(x_0),t-\tau|x_0-\sigma)\right\}d\tau + \varphi^*(t)\delta\left[Z-tU(x_0)\right],$$

where $\varphi^*(t) = \int_t^\infty \varphi(\tau)d\tau$ is the probability that the walker does not perform any jump during the measurement time $[0,t]$. Note that $tU(x_0)$ is the contribution to the observable Z cumulated while being at x_0 during the time interval $[0,t]$ as indicated by the last term on the r.h.s..

Next, taking the Laplace transform on both sides of Eq. (5.19) with respect to Z, we find

$$Q(p,t|x_0) = \int_0^t \varphi(\tau)e^{-p\tau U(x_0)}\left\{\frac{1}{2}Q(p,t-\tau|x_0+\sigma)\right.$$
$$\left. + \frac{1}{2}Q(p,t-\tau|x_0-\sigma)\right\}d\tau + \varphi^*(t)e^{-ptU(x_0)}. \tag{5.20}$$

Written in this way, $Q(p,t|x_0)$ is known as the characteristic function of the functional Z. Taking another Laplace transform in Eq. (5.20) with respect to t, we find

$$Q(p,s|x_0) = \varphi(s+pU(x_0))\left[\frac{1}{2}Q(p,s|x_0+\sigma)+\frac{1}{2}Q(p,s|x_0-\sigma)\right]$$
$$+ \frac{1-\varphi(s+pU(x_0))}{s+pU(x_0)}. \tag{5.21}$$

Considering the continuum limit as in the previous section, that is, we assume that the jump size σ is smaller than any other length scale of the system, i.e., $x_0 \gg \sigma$, so that we expand $Q(p,s|x_0\pm\sigma)$ up to $O(\sigma^2)$ to arrive at

$$Q(p,s|x_0\pm\sigma) = Q(p,s|x_0) \pm \sigma\frac{\partial Q(p,s|x_0)}{\partial x_0} + \frac{1}{2}\sigma^2\frac{\partial^2 Q(p,s|x_0)}{\partial x_0^2} + ..., \tag{5.22}$$

which upon inserting into Eq. (5.21) yields

$$sQ(p,s|x_0) - 1 = \frac{\sigma^2}{2}K(s+pU(x_0))\frac{\partial^2 Q(p,s|x_0)}{\partial x_0^2} - pU(x_0)Q(p,s|x_0), \tag{5.23}$$

which is the backward Feynman-Kac equation for a stochastic functional of a non-Markovian random walker. Note that if the random walk is Markovian, that is $K(s)$ is given by Eq. (5.10), then the expression above reduces to Eq. (2.32). In the time domain, the expression above reads

$$\frac{\partial Q(p,t|x_0)}{\partial t} = \frac{\sigma^2}{2}\int_0^t K(t')e^{-pt'U(x_0)}\frac{\partial^2 Q(p,t-t'|x_0)}{\partial x_0^2}dt' - pU(x_0)Q(p,t|x_0). \tag{5.24}$$

The moments of $Z(t|x_0)$ can be obtained from the derivatives of $Q(p,s|x_0)$ in a systematic manner, as we have already done in Eq. (4.8). To do this, we first define the Laplace transform of the moments

$$\langle Z(s|x_0)^n\rangle \equiv \mathscr{L}_{t\to s}[\langle Z(t|x_0)^n\rangle] = \int_0^\infty dt\, e^{-st} \int_0^\infty Z(t|x_0)^n Q(Z,t|x_0) dZ. \tag{5.25}$$

Since

$$\langle Z(s|x_0)^n\rangle = \int_0^\infty dt e^{-st} \int_0^\infty \left[(-1)^n \frac{\partial^n}{\partial p^n} e^{-pZ}\right]_{p=0} Q(Z,t|x_0) dZ, \tag{5.26}$$

it is then straightforward to show that the moments are represented in terms of $Q(p,s|x_0)$ in the following way

$$\langle Z(s|x_0)^n\rangle = (-1)^n \frac{\partial^n Q(p,s|x_0)}{\partial p^n}\bigg|_{p=0}. \tag{5.27}$$

In what follows, we consider two specific stochastic functionals that are interesting in analyzing the properties of the search processes: the occupation time in an interval and the occupation time along the half-positive real line, as illustrated in Fig. 2.8 and Fig. 2.9. For each case, we solve for the moment generating function (MGF) from Eq. (5.23) using suitable boundary conditions, and then use Eq. (5.27) to derive the moments, which we analyze in detail.

Note 5.2 In this chapter, we are focusing on occupation times, which are non-negative functionals. If instead one considers a functional that can take both positive and negative values, then rather than a Laplace transform of Z, one needs to work with Fourier transforms, and the non-Markovian backward FK equation, Eq. (5.23), reads

$$sQ(\omega,s|x_0) - 1 = \frac{\sigma^2}{2} K(s + i\omega U(x_0)) \frac{\partial^2 Q(\omega,s|x_0)}{\partial x_0^2} - i\omega U(x_0) Q(\omega,s|x_0),$$

where ω is the Fourier pair of Z. In this case, the n-th order moment is computed by

$$\langle Z(s|x_0)^n\rangle = (i)^n \frac{\partial^n Q(\omega,s|x_0)}{\partial \omega^n}\bigg|_{\omega=0}.$$

instead.

5.4 Occupation time in an interval

We first consider the occupation time $T_a(t|x_0)$ of the random walker, starting initially from x_0, in an interval $[-a,a]$ up to an observation time t, as defined in Sec. 2.4.2. The

corresponding Feynman-Kac equation, Eq. (5.23), needs to be solved with suitable boundary conditions. Specifically, if the starting point is at infinity i.e., $x_0 \to \pm\infty$ the walker will never reach the interval so that $P(T_a,t|x_0 \to \pm\infty) = \delta(T_a)$, i.e., $Q(p,s|x_0 \to \pm\infty) = 1/s$. Skipping details of this computation, which can be found in Appendix B of [3], and taking $x_0 = 0$ without any loss of generality, the solution to the characteristic function, Eq. (5.23), in Laplace space is

$$Q(p,s) = Q(p,s|x_0=0) = \frac{1}{s+p}\left[1+\frac{p/s}{F(s,p)}\right], \tag{5.28}$$

where

$$F(s,p) = \cosh\left(\lambda(s+p)\right) + \frac{\lambda(s+p)}{\lambda(s)}\sinh\left(\lambda(s+p)\right), \tag{5.29}$$

and

$$\lambda(s) = a\sqrt{\frac{2s}{\sigma^2 K(s)}}. \tag{5.30}$$

Eq. (5.28) is the characteristic function of the occupation time in an interval in Laplace space for both T_a and t. With this expression we now can compute the moments of T_a for different waiting time distributions and analyze their behavior in the long-time limit. While inverting from Laplace space to the time and T_a domains proves not trivial, we can still compute the PDF in relevant limits, as we will see in the next sections.

5.4.1 Moments of T_a

We can compute the moments of T_a by means of Eq. (5.27) where $Q(p,s)$ is given by Eq. (5.28). The first moment is therefore

$$\langle T_a(s)\rangle = \frac{1}{s^2}\left[1-e^{-\lambda(s)}\right], \tag{5.31}$$

and the second moment reads

$$\left\langle T_a(s)^2\right\rangle = \frac{2}{s^3}\left[1-e^{-\lambda(s)} - \Phi(s)e^{-\lambda(s)}\left(\lambda(s)+\frac{1}{2}-\frac{e^{-2\lambda(s)}}{2}\right)\right], \tag{5.32}$$

where we have defined

$$\Phi(s) = \frac{1}{2} - \frac{s}{2K(s)}\frac{dK(s)}{ds}. \tag{5.33}$$

As $\varphi(s)$ is a monotonically increasing function of s, one can easily show that $\lambda(s)$ also increases monotonically with s. Then, $\lambda(s)$ goes to zero as $s \to 0$. Using this

argument, we can approximate the expressions in Eq. (5.31) and Eq. (5.32) in the long-time limit. Expanding the exponential functions of $\lambda(s)$ we find

$$\langle T_a(s)\rangle \approx \frac{\lambda(s)}{s^2}, \tag{5.34}$$

and

$$\left\langle T_a(s)^2\right\rangle \approx \frac{2\lambda(s)}{s^3}\left[1-\frac{\lambda(s)}{2}-\Phi(s)\left(2-3\lambda(s)\right)\right], \tag{5.35}$$

as $s\to 0$, which corresponds to the long-time limit $t\to\infty$ in Laplace space. With these expressions now we have the first and second moments of the occupation time in an interval in terms of the memory kernel $K(s)$. With this we need to consider a specific choice of the waiting time PDF $\varphi(t)$ to proceed further.

A Finite moments PDF

First, we consider the case of a waiting time PDF with finite moments (FM) as in Eq. (5.9). From $K(s)$ as given by Eq. (5.10), then Eq. (5.30) yields $\lambda(s)\approx a\sqrt{2s\langle\tau\rangle/\sigma^2}$ as $s\to 0$ where from Eq. (5.34) the mean occupation time for a diffusing walker is given by

$$\langle T_a(t)\rangle_{\mathrm{FM}} \approx \frac{2a\sqrt{t}}{\sqrt{\pi D}}, \tag{5.36}$$

in the long-time limit. Following a similar derivation for the second moment using Eq. (5.35) and Eq. (5.30), we find

$$\left\langle T_a(t)^2\right\rangle_{\mathrm{FM}} \approx \frac{2a^2}{D}t. \tag{5.37}$$

Eq. (5.36) and (5.37) coincide with the expressions for the occupation time in an interval of the BM, Eq. (2.41), which is expected since the CTRW with exponential waiting times PDF and a jump length PDF with finite moments yields standard diffusion. Indeed, we derived these results, Eq. (5.36) and (5.37), for a BM, in Ref. [8].

B Power-law tails PDF

Next, we consider the two examples of waiting-time PDFs with power-law tails given by Eqs. (5.12) and (5.16). For the first case, inserting Eqs. (5.3) and (5.14) in Eq. (5.34) and inverting the Laplace transform (see Appendix C of [3] for derivation), we find

$$\langle T_a(t)\rangle_{\mathrm{FT}} \approx \begin{cases} a\sqrt{\frac{2b_\alpha}{\sigma^2}}\frac{t^{1-\frac{\alpha}{2}}}{\Gamma\left(2-\frac{\alpha}{2}\right)}, & 0<\alpha<1 \\ \frac{2a\sqrt{t}}{\sqrt{\pi D}}, & 1<\alpha<2 \end{cases}, \tag{5.38}$$

in the $t\to\infty$ limit, which agrees with [122]. It is useful to note that for a fat-tailed waiting time PDF with $1<\alpha<2$ the mean occupation time is the same as for the case

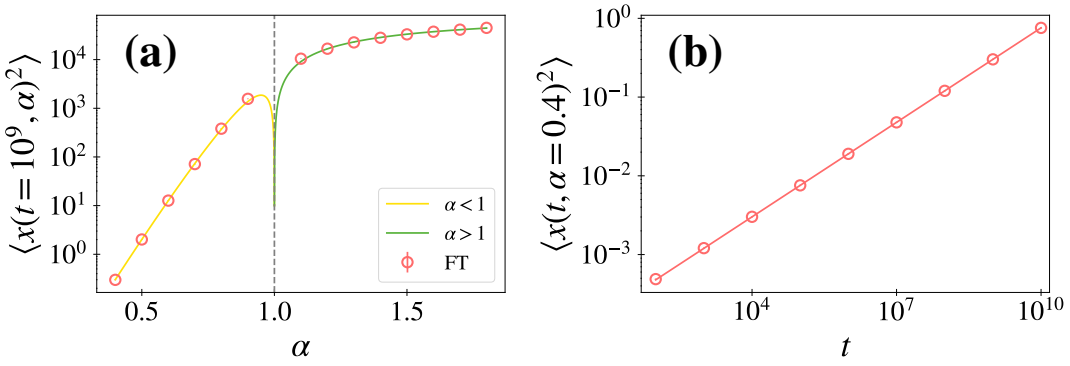


Figure 5.1: **Mean squared displacement (MSD).** The symbols are computed with numerical simulations with the FT waiting time PDF, Eq. (5.12), and the lines represent Eq. (5.40). (a) we fix the maximum simulation time to $t = 10^9$ and compute $\langle x^2 \rangle$ for different values of α; the dotted vertical line represents the transition value $\alpha = 1$. The value $\alpha = 1$ is not included in Eq. (5.40) so that the solid line does not hold in the vicinity of $\alpha = 1$. (b) we fix $\alpha = 0.4$ and show the time evolution of $\langle x^2(t) \rangle$. The parameters used are $a = 0.055$, $x_0 = 0$, $\sigma = 0.01$, and $t_0 = 1$. The number of walkers for the simulations is $N = 10^7$.

of normal diffusion given by Eq. (5.36). Similarly, we can compute the second moment $\langle T_a(t)^2 \rangle$ by inserting Eq. (5.14) in (5.35), where we obtain in the long-time limit

$$\langle T_a(t)^2 \rangle_{\text{FT}} \approx \begin{cases} \frac{2a(1-\alpha)\sqrt{2b_\alpha/\sigma^2}}{\Gamma(3-\alpha/2)} t^{2-\frac{\alpha}{2}}, & 0 < \alpha < 1 \\ \frac{2a^2}{D} t + \frac{2a(\alpha-1)b_\alpha}{\Gamma\left(\frac{7}{2}-\alpha\right)\langle\tau\rangle\sqrt{D}} t^{\frac{5}{2}-\alpha}, & 1 < \alpha < 2. \end{cases} \tag{5.39}$$

From Eq. (5.38) and Eq. (5.39) we can see that the mean and squared mean of the occupation time display a cross-over at the transition point $\alpha = 1$ where they switch from subdiffusive to diffusive behavior in time. This transition is at the value of α for which the waiting time PDF $\varphi(t)$ switches from diverging first moment, for $0 < \alpha < 1$, to a finite one, for $1 < \alpha < 2$. To better illustrate this behavior, we examine the spatial properties of the walker, namely the MSD. From Eq. (5.7) with $\varphi(s)$ given by Eq. (5.14) we get

$$\langle x(t)^2 \rangle_{\text{FT}} \approx \begin{cases} \frac{\sigma^2 (t/t_0)^\alpha}{|\Gamma(1-\alpha)|\Gamma(1+\alpha)}, & 0 < \alpha < 1 \\ \frac{\sigma^2}{\langle\tau\rangle} t, & 1 < \alpha < 2. \end{cases} \tag{5.40}$$

Clearly, for $0 < \alpha < 1$ the walker moves subdiffusively while for $1 < \alpha < 2$ it moves diffusively. In Fig. 5.1 we compare the previous result for the MSD with numerical simulations. In panel (a) we fix $t = 10^9$ and plot the MSD for different values of α ranging from 0 to 2. The value $\alpha = 1$ is not included in Eq. (5.40) so that the solid line does not hold in the vicinity of $\alpha = 1$. In panel (b) we plot the MSD as a function of time in a log-log plot for $\alpha = 0.4$. Upon first glance, one could expect for $1 < \alpha < 2$ the $\langle T_a(t) \rangle_{\text{FM}}$, and $\langle T_a(t)^2 \rangle_{\text{FM}}$ to coincide with the ones derived for the

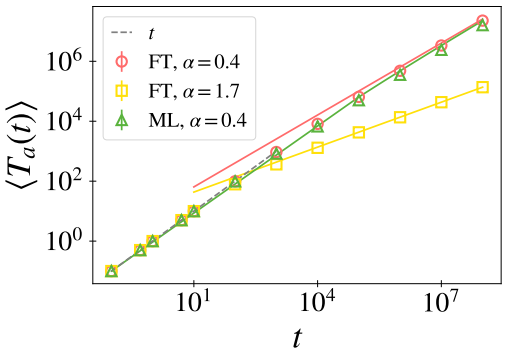


Figure 5.2: **Mean occupation time in an interval.** The symbols are from numerical simulations: the $\varphi(t)$ for the circles and the squares (FT) is Eq. (5.12), and for the triangles (ML) is Eq. (5.16). The solid lines represent Eqs. (5.38) and (5.43) respectively. Note that the FT and ML solutions coincide in the long-time limit. The parameters used are $a = 0.055$, $x_0 = 0$, $\sigma = 0.01$, $t_0 = 1$ for the FT, and $\tau^* = |\Gamma(1-\alpha)|^{1/\alpha}$ for the ML. The number of walkers in the simulations is $N = 10^5$.

finite moments PDF, Eqs. (5.36) and (5.37), since in this regime the MSD exhibits a diffusive scaling. This reasoning is fulfilled for the mean occupation time, since Eq. (5.38) coincides with Eq. (5.36) in the large time limit for $1 < \alpha < 2$. However, this is not fulfilled for the second moment. Eq. (5.39) for $1 < \alpha < 2$ coincides with Eq. (5.37) for $3/2 < \alpha < 2$ only. Note that of the two terms on the right side of the equality in (5.39) the dominant term at long times is the one with the larger exponent, i.e., $\langle T_a(t)^2 \rangle \sim t^{\max\{1, \frac{5}{2}-\alpha\}}$. Then, for $1 < \alpha < 2$ one has $\langle T_a(t)^2 \rangle \sim t$ if $3/2 < \alpha < 2$. Summarizing, we can rewrite Eq. (5.39) in the form

$$\langle T_a(t)^2 \rangle_{\rm FT} \approx \begin{cases} \frac{2a(1-\alpha)}{\Gamma(3-\frac{\alpha}{2})\sqrt{K_\alpha}} t^{2-\frac{\alpha}{2}}, & 0 < \alpha < 1 \\ \frac{2a^2}{D} t + \frac{2a(\alpha-1)b_\alpha}{\Gamma(\frac{7}{2}-\alpha)\langle\tau\rangle\sqrt{D}} t^{\frac{5}{2}-\alpha}, & 1 < \alpha < \frac{3}{2} \\ \frac{2a^2}{D} t, & \frac{3}{2} < \alpha < 2 \end{cases} \tag{5.41}$$

with $K_\alpha = \sigma^2/2b_\alpha$.

If the waiting time PDF is given instead by Eq. (5.16), now it is possible to obtain an exact solution for the mean occupation time in an interval. Combining Eqs. (5.3), (5.17) and (5.30), Eq. (5.31) turns into

$$\langle T_a(s) \rangle_{\rm ML} = \frac{1}{s^2} \left[1 - e^{-\frac{a\sqrt{2}}{\sigma}(s\tau^*)^{\alpha/2}} \right], \tag{5.42}$$

which can be Laplace inverted to find the temporal behavior in terms of the one-sided Lévy function $l_{\alpha/2}(t)$ of index $\alpha/2$

$$\langle T_a(t) \rangle_{\rm ML} = \int_0^t \left\{ 1 - L_{\frac{\alpha}{2}} \left[\left(\frac{\sigma}{a\sqrt{2}} \right)^{\frac{2}{\alpha}} \frac{t'}{\tau^*} \right] \right\} dt', \tag{5.43}$$

where $L_\alpha(t)$ is the one-sided stable cumulative distribution $L_\alpha(t) = \int_0^t l_\alpha(t')dt'$ and where the one-sided Lévy function $l_\alpha(t)$ is defined by its characteristic function, Eq. (2.60). In the large time limit ($s\tau^* \ll 1$) Eq. (5.42) reduces to

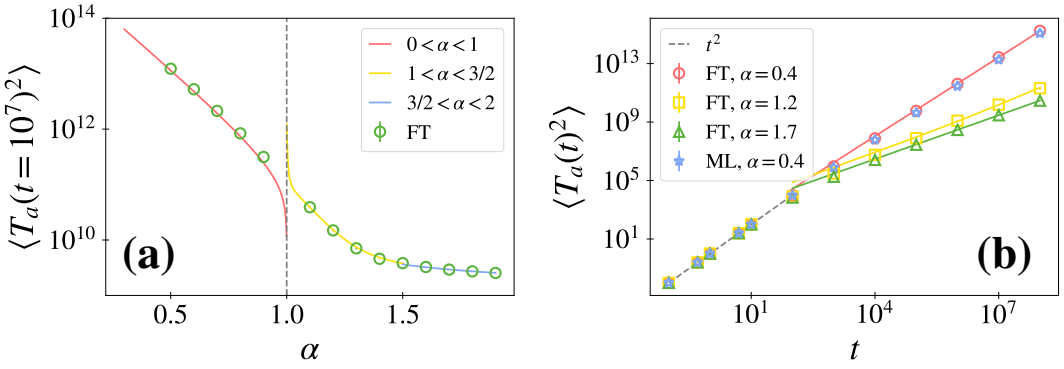


Figure 5.3: **Mean squared occupation time in an interval.** The symbols are computed with numerical simulations and the solid lines represent Eq. (5.41). (a) $\langle T_a(t)^2\rangle$ as a function of α, for PL data. The dashed line marks the transition value $\alpha = 1$. The parameters used are $a = 0.055$, $x_0 = 0$, $\sigma = 0.01$, and $t_0 = 1$. The number of walkers for the simulations is $N = 10^6$ and the maximum simulation time is $t = 10^7$. (b) $\langle T_a(t)^2\rangle$ as a function of time t. The circles, squares, and triangles are computed using the FT waiting time PDF, Eq. (5.12), while the stars with (5.16). The parameters used here are $a = 0.055$, $x_0 = 0$, $\sigma = 0.01$, $t_0 = 1$ for the PL data, and $\tau^* = |\Gamma(1-\alpha)|^{1/\alpha}$ for the ML.

$$\langle T_a(s)\rangle_{\mathrm{ML}} \approx \frac{a\sqrt{2}\tau^{*\alpha/2}}{\sigma} s^{-2+\alpha/2} \tag{5.44}$$

which back to real time is exactly the result found in Eq. (5.38) for $0 < \alpha < 1$ but replacing b_α by $\tau^{*\alpha}$. This behavior is shown in Fig. 5.2, where we plot $\langle T_a(t)\rangle$ found in Eqs. (5.38) and (5.43) together with numerical simulations in a log-log plot. We can see that the red (FT) and green (ML) lines converge to each other for long times. Note also that in the long-time limit we can keep the first term of the series expansion in Eq. (5.43), obtaining the same result. Therefore, the mean occupation time in an interval found from the waiting times PDF (5.12) and (5.16) is the same when $t \to \infty$. This means that the long-time behavior of the mean occupation time in an interval is governed only by the tails of the waiting time PDF. Then, for $\langle T_a(t)^2\rangle_{\mathrm{ML}}$ we get the same result as in Eq. (5.41) for $0 < \alpha < 1$ in the long-time limit [122, 134]. This can be observed in Fig. 5.3(a), where we plot with blue star symbols numerical simulations for $\alpha = 0.4$ using the waiting time PDF given in Eq. (5.17). It can be appreciated that these symbols coincide with values (in red circles) obtained for the waiting time (5.12).

In Fig. 5.3(a) we check the exponents of the temporal dependence of the mean square occupation time given by Eq. (5.41) (solid lines) against the numerical simulations (symbols). We note that close to $\alpha = 1$ the analytical results diverge. This case should be computed separately, which we have not done. On the other hand, it is interesting to observe that the short time behavior of the occupation time in an interval is not affected by the underlying random walk, i.e., does not depend on the details of the waiting time PDF. Since the walker is initially at $x_0 = 0$ (inside the interval), as long as the measurement time is less than the first escape time of the interval $[-a, a]$, the time elapsed by the walker within the interval will be equal to

t. Therefore, if the measurement time is small enough (smaller than the first escape time of the interval) then $T_a \sim t$ so that $\langle T_a(t)\rangle \sim t$ and $\langle T_a(t)^2\rangle \sim t^2$. This can be checked from Eqs. (5.31) and (5.32). In the short time limit ($s \to \infty$) Eqs. (5.31) and (5.32) reduce to $\langle T_a(s)\rangle \approx s^{-2}$ and $\langle T_a(s)^2\rangle \approx 2s^{-3}$ since $\lambda(s) \to \infty$ as $s \to \infty$. Finally, inverting the Laplace transform we find $\langle T_a(t)\rangle \approx t$ and $\langle T_a(t)^2\rangle \approx t^2$ as $t \to 0$. We have checked this behavior in Figs. 5.2 and 5.3(b).

5.4.2 PDF of T_a

We now continue our analysis of the occupation time in an interval, focusing on the behavior of $Q(T_a,t)$. Since the double Laplace inversion of Eq. (5.28) is not generically tractable, we will need to analyze the behavior of $Q(T_a,t)$ in some limits. In particular, we take $t \to \infty$, since as we have seen before for short times the particles would not have had enough time to escape the interval. Still we need further approximations, for this, we will consider three regimes: left edge, when the occupation time is much smaller than the measurement time $T_a \ll t$, bulk, when the occupation time is comparable to the measurement time, and right edge, when the occupation time is close to the measurement time $t - T_a \ll 1$. The details of the inversions involve several limits and approximations, and can be found in Appendix B. Below, we go directly to the main results.

We will consider the finite moments FM Eq. (5.8) and the fat-tailed FT, Eq. (5.12) separately. The ML case is not directly discussed since it yields the same results as the FT as we are dealing with the long-time limit (after replacing b_α by τ^α, and for $0 < \alpha < 1$). This is in agreement with what we have discussed in Sec. 5.4.1, where we have seen that the long-time behavior of the waiting-time PDF was sufficient to determine the first and second moments of T_a.

A Finite moments

For the case of a waiting time PDF with finite moments, we find that the PDF of the occupation time in an interval is given by

Left edge regime

$$Q(T_a,t)_{\rm FM} \approx \frac{2}{\pi\sqrt{tT_a}} e^{-\frac{a^2}{4DT_a}}. \tag{5.45}$$

In Fig. 5.4 we compare Eq. (5.45) (in dashed lines) with the numerical simulations. As can be seen in the inset, the validity of (5.45) is restricted to a narrow region very close to $T_a/t = 0$. The agreement is good until the numerical curve reaches a maximum. After that, the approximation breaks down, and the numerical curve starts to deviate from the analytical one. This is expected since the approximation leading to Eq. (5.45) is valid only for $T_a \ll t$.

Right edge regime

$$Q(T_a,t)_{\rm FM} \approx \sqrt{\frac{D}{4a^2\pi}} \frac{t}{(t-T_a)^{\frac{3}{2}}} e^{-\frac{t^2 D}{4a^2(t-T_a)}}. \tag{5.46}$$

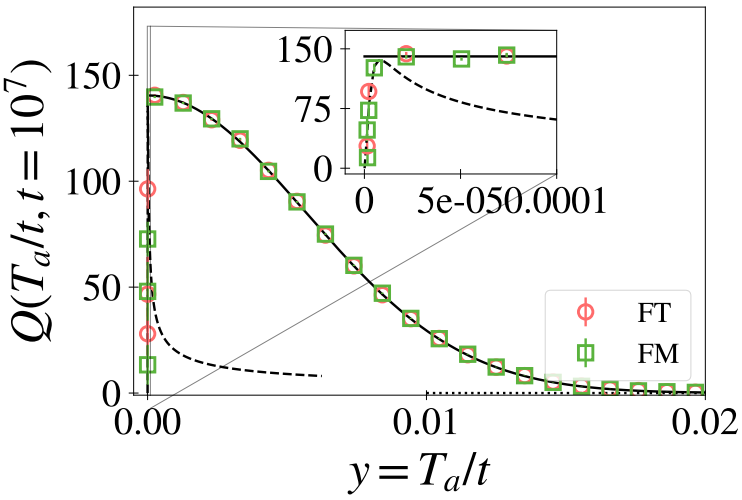


Figure 5.4: **Scaled PDF of occupation time $Q(y,t)$ as a function of $y = T_a/t$ for $\varphi(s)$ with finite first moment.** The red circles (FT) are for the waiting time PDF in Eq. (5.12) with $\alpha = 1.6$; the green squares (FM) are numerically generated from Eq. (5.8) with $\langle\tau\rangle = \alpha/(\alpha-1)$. Theoretical predictions: The solid line represents Eq. (5.47), the dashed line Eq. (5.45), and the dotted line represents Eq. (5.46). Inset is used to magnify the results from the left edge. The parameters used for the numerical simulations are $a = 0.055$, $x_0 = 0$, $\sigma = 0.01$, $t_0 = 1$, the number of walkers for the simulation $N = 10^6$, and the maximum time $t = 10^7$.

In Fig. 5.4 we plot Eq. (5.46) with a dotted line. As can be seen $Q(T_a,t)_{\rm FM}$ vanishes in this limit, meaning that the probability that the walker spends all the time within the interval is vanishingly small.

Central bulk regime

$$Q(T_a,t)_{\rm FM} \approx \sqrt{\frac{D}{a^2\pi(t-T_a)}}\, e^{-\frac{T_a^2 D}{4a^2(t-T_a)}}. \tag{5.47}$$

Which is the half-Gaussian distribution. In Fig. 5.4 we compare Eq. (5.47) (in solid lines) with numerical simulations. The agreement is again excellent along the central bulk region, corresponding with the results for the occupation time in an interval of a BM, Eq. (2.40).

B Fat-tailed distribution

The results for the case of a fat-tailed waiting time PDF are more involved, since we have to consider $0 < \alpha < 1$, all moments divergent, and $1 < \alpha < 2$, finite first moment, separately. However, the results for $1 < \alpha < 2$ are the same as for the finite moments case, as we show in Fig. 5.4. Thus, below only focus on the case of $0 < \alpha < 1$.

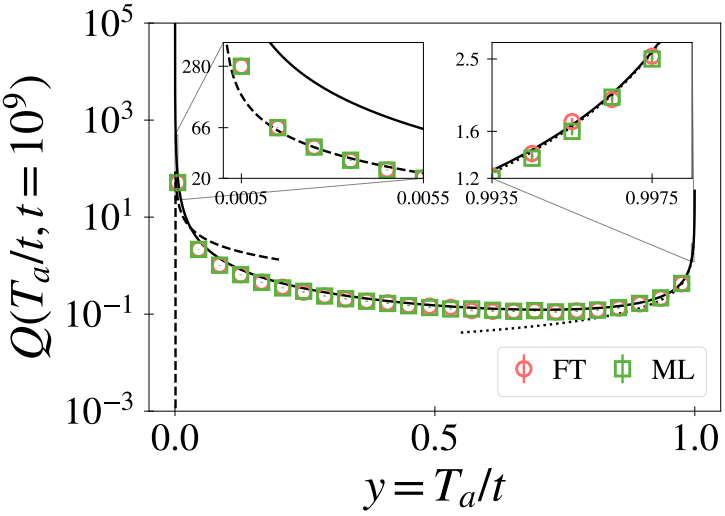


Figure 5.5: **Scaled PDF of occupation time $Q(y,t)$ as a function of $y = T_a/t$ for $\varphi(s)$ with diverging moments.** The points are generated from numerical simulations: the red circles with the waiting time PDF Eq. (5.12) (FT) and the green squares with Eq. (5.16) (ML). Theoretical predictions: The dashed line is computed with Eq. (5.48), the dotted line with Eq. (5.49), and the solid line with Eq. (5.51). Insets are used to magnify the results from left and right edge regimes. The parameters used are $a = 0.055$, $x_0 = 0$, $\sigma = 0.01$, $\alpha = 0.4$, $t_0 = 1$ for the power-law data, and $\tau^* = |\Gamma(1-\alpha)|^{1/\alpha}$ for the Mittag-Leffler. The number of walkers for the numerical simulations is $N = 10^6$ and the final time of the simulation is $t = 10^9$.

Left edge regime

$$Q(T_a,t)_{\mathrm{FT}} \approx \frac{2\sin\left(\frac{\pi\alpha}{2}\right)}{\pi} \frac{(T_a/t)^{\frac{\alpha}{2}}}{\left(a/\sqrt{K_\alpha}\right)^{\frac{2}{\alpha}}} \int_0^1 \frac{l_{\alpha/2}\left[\frac{T_a z}{\left(a/\sqrt{K_\alpha}\right)^{\frac{2}{\alpha}}}\right]}{(1-z)^{1-\frac{\alpha}{2}}} dz, \tag{5.48}$$

which holds for $T_a \ll (a/\sqrt{K_\alpha})^{2/\alpha}$, i.e., in a narrow region very close to $y = T_a/t = 0$. Again, is expected since in this approximation $T_a \ll t$. In Fig. 5.5 we compare numerical simulations with the analytical result in Eq. (5.48) in a dashed curve. As can be seen from the plot, the agreement is very good (see the left inset).

Right edge regime

$$Q(T_a,t)_{\mathrm{FT}} \approx \frac{\mathscr{B}_\alpha}{t^\alpha (t-T_a)^{1-\frac{\alpha}{2}}}, \quad 0 < \alpha < 1 \tag{5.49}$$

where

$$\mathscr{B}_\alpha = \frac{a}{\sqrt{K_\alpha}\Gamma(\frac{\alpha}{2})\Gamma(1-\alpha)}. \tag{5.50}$$

In contrast with the finite moments case, we see that the PDF does not vanish as T_a approaches t, revealing that for power-law waiting times with $0 < \alpha < 1$ the probability

that the walker spends all the time within the interval is non-negligible. In Fig. 5.5 we compare Eq. (5.49) (in dotted lines) with numerical simulations. The agreement is very good (see the right inset).

Central bulk regime

$$Q(T_a,t)_{\rm FT} \approx \mathscr{B}_\alpha \frac{(t-T_a)^{\frac{\alpha}{2}}}{T_a^{1+\alpha}} \left(2+\frac{T_a}{t-T_a}\right). \tag{5.51}$$

Finally, we compare in Fig. 5.5 Eq. (5.51) (in solid lines) with numerical simulations. We see that the agreement is very good even in the region where $T_a/t \approx 1$.

5.4.3 Ergodic properties of T_a

We finish the discussion of the half occupation time by computing its ergodic properties. From the first and second moments, we can characterize the ergodic properties of such observables as defined in Sec. 2.5. We compute the ergodicity breaking parameter EB from Eq. (2.51) and Eqs. (5.36) and (5.37) for FM together with Eqs. (5.38) and (5.41) for FT we find

$$\mathrm{EB} = \begin{cases} \sim t^{\alpha/2}, & 0<\alpha<1 \\ \sim t^{\frac{3}{2}-\alpha}, & 1<\alpha<3/2 \\ \frac{\pi}{2}-1, & 3/2<\alpha<2. \end{cases} \tag{5.52}$$

From the results of EB above, we see that the occupation time in an interval for both Markovian and non-Markovian random walks is non-ergodic, regardless of the interval width a. In fact, for values of $\alpha \in (0,3/2)$ we see that the EB parameter increases with time, which means that, contrary to ergodic behavior, the longer the trajectory, the larger the differences between averages over realizations and time averages. On the other hand, the value of EB for $\alpha \in (3/2,2)$ corresponds to the value of a standard Brownian motion [8]. This result is in agreement with the discussion below Eq. (5.40), where we have seen that the first and second moments of T_a have the same long-time behavior as the Brownian case when $\alpha > 3/2$.

5.5 Half occupation time

We consider now the occupation time $T_+(t|x_0)$ of the walker above the origin (i.e., on the positive half-space) within a time window of size t if it was at $x = x_0$ at $t = 0$, as defined in Sec. 2.4.1 under the appropriate boundary conditions [129]. If the starting point $x_0 \to +\infty$ the walker will stay on the positive side with $x(t) > 0$ for all finite t implying $T^+(t|x_0 \to +\infty) = t$ and accordingly $P(T_+,t|x_0 \to +\infty) = \delta(T_+ - t)$, i.e., $Q(p,s|x_0 \to +\infty) = 1/(s+p)$. On the other hand, if the starting point $x_0 \to -\infty$ the walker will never reach the positive side and it will stay on the negative half-space implying $T^+(t|x_0 \to -\infty) = 0$ and hence $Q(T_+,t|x_0 \to -\infty) = \delta(T_+)$, so that $Q(p,s|x_0 \to -\infty) = 1/s$. The solution for the characteristic function under the above boundary conditions reads

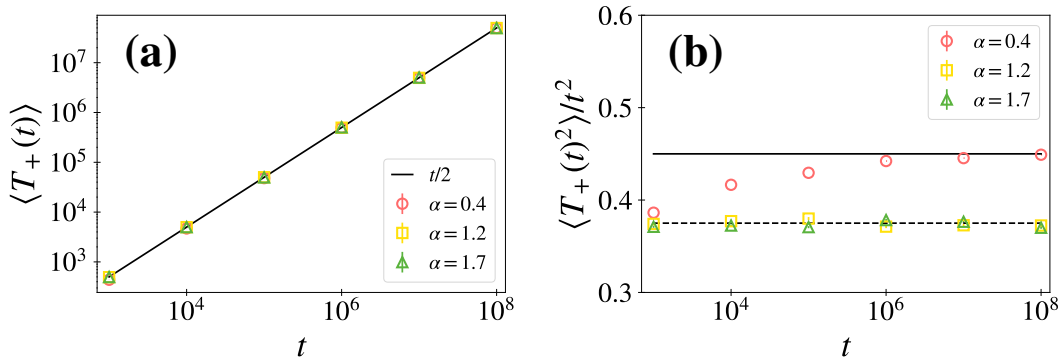


Figure 5.6: **Moments of the half occupation time.** All the data points are generated with the FT $\varphi(t)$ in Eq. (5.12). The circles with $\alpha = 0.4$, the squares with $\alpha = 1.2$, and the triangles with $\alpha = 1.7$. (a) First moment. The solid line is Eq. (5.54). (b) Second moment. The lines are Eq. (5.56): the solid line for $\alpha = 0.4$ and the dashed line for $1 < \alpha < 2$. The parameters used for the numerical simulations are $x_0 = 0$, $\sigma = 0.01$, $t_0 = 1$, and the number of walkers for the simulation $N = 10^5$.

$$Q(p,s) = \frac{1}{s+p}\left[1 + \frac{p}{s + \sqrt{\frac{s(s+p)K(s)}{K(s+p)}}}\right], \tag{5.53}$$

5.5.1 Moments of T_+

Again, the moments of the half occupation time can be computed by means of Eq. (5.27) with $Q(p,s)$ given by Eq. (5.53). Hence, the first moment in Laplace space is given by $\langle T^+(s)\rangle = 1/2s^2$. Inverting, we find

$$\left\langle T^+(t)\right\rangle = \frac{t}{2}, \tag{5.54}$$

which is independent of the waiting time PDF $\varphi(t)$. This means that for any isotropic random walk, the mean half occupation time up to a time t is simply $t/2$. This result is in line with what was known from Eqs. (2.36) and (2.38) for specific waiting time distributions. Here we have seen that it holds in general, regardless of $\varphi(t)$. For completeness, in Fig. 5.6(a) we show this result against numerical simulations, and we see that regardless of the value of α, the data points collapse onto a single curve. This universal behavior however, is not present in the second moment. Taking the second derivative of Eq. (5.53) with respect to p and taking $p = 0$ we find the general expression in Laplace space

$$\left\langle T^+(s)^2\right\rangle = \frac{1}{4s^3}\left[3 + \frac{s}{K(s)}\frac{dK(s)}{ds}\right]. \tag{5.55}$$

For a waiting time PDF with finite moments $\langle T^+(t)^2\rangle \approx 3t^2/8$ as in Eq. (2.36). For the case of a walker performing rests of power-law distributed duration, using the expression in Eq. (5.15) for $K(s)$ and substituting in Eq. (5.55), one finds

$$\langle T^+(t)^2\rangle_{\rm FT} \approx \begin{cases} \frac{4-\alpha}{8}t^2, & 0<\alpha<1 \\ \frac{3}{8}t^2, & 1<\alpha<2 \end{cases} \tag{5.56}$$

in the long-time limit. The result for $0<\alpha<1$ matches with Eq. (2.38) as expected, while for $1<\alpha<2$ with Eq. (2.36). Note that, unlike the case of T_a there is not a transition in the value of the second moment at long times for $\alpha = 3/2$; when the waiting time PDF has a finite first moment, then the first and second moment of T_+ behave like the Brownian case. The same result for $0<\alpha<1$ is obtained in the case of the ML PDF. Inserting Eq. (5.17) into Eq. (5.55) we find

$$\langle T^+(t)^2\rangle_{\rm ML} = \frac{4-\alpha}{8}t^2. \tag{5.57}$$

For this observable it is possible to obtain the n-order moment $\langle T^+(t)^n\rangle$ both for FM and ML waiting times

$$\langle T^+(t)^n\rangle_{\rm FM} \approx \frac{\Gamma\left(n+\frac{1}{2}\right)}{n!\sqrt{\pi}}t^n \tag{5.58}$$

in the long-time limit and

$$\langle T^+(t)^n\rangle_{\rm ML} = \frac{\mathscr{C}_n(\alpha)}{n!}t^n \tag{5.59}$$

with

$$\mathscr{C}_n(\alpha) = \sum_{j=0}^{\infty}(-1)^j\left[\left(1+\frac{\alpha j}{2}\right)_n + \left(\frac{\alpha}{2}+\frac{\alpha j}{2}\right)_n\right] \tag{5.60}$$

where $(a)_n = \Gamma(a+n)/\Gamma(a)$ is the Pochhammer symbol. The second moment in Eq. (5.56) is verified with numerical simulations in Fig. 5.6(b). As predicted in Eq. (5.56) the coefficient is the same for $\alpha = 1.2$ and $\alpha = 1.7$, with no transition at $\alpha = 3/2$, in contrast to the behavior of T_a.

5.5.2 PDF of T_+

The PDF of the occupation time can be computed by inverting Eq. (5.53) with an explicit memory kernel. This means that the half occupation time statistics are governed by the statistics of the resting periods of the random walk. When the waiting time PDF has finite moments, the PDF for the half occupation time $Q(T_+,t)$ admits a limiting distribution in the limit $T_+ \to \infty$ and $t \to \infty$ so that it converges to

$$Q(y) = \frac{1}{\pi\sqrt{y(1-y)}},$$

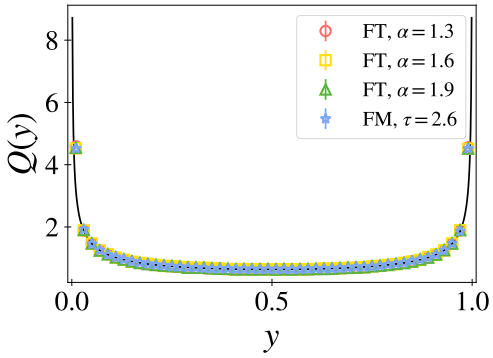


Figure 5.7: **Universality of the *arcsine* distribution.** The circles, squares, and triangles are computed with $\varphi(t)$ from Eq. (5.12) for $\alpha = 1.3$, $\alpha = 1.6$, and $\alpha = 1.9$ respectively. The stars are computed with $\varphi(t)$ from Eq. (5.8) with $\langle \tau \rangle = 2.6$. The solid line is the arcsine distribution (2.35). The parameters used for the numerical simulations are $x_0 = 0$, $\sigma = 0.01$, $t_0 = 1$, the number of walkers for the simulation $N = 10^6$, and the maximum time $t = 10^7$.

where $y = T_+/t$. This is the limiting *arcsine distribution*, Eq. (2.35), as one would expect for a diffusive random walker [129, 138].

On the other hand, when the waiting time PDF is a power-law we can find a range of behaviors. For instance, if it is given by Eq. (5.16), then the characteristic function $Q(p,s)$ possesses a limiting distribution (the Lamperti PDF [122, 139], as presented in Eq. (2.37)) namely

$$Q(y) = \frac{\sin(\frac{\alpha\pi}{2})}{\pi} \frac{y^{\frac{\alpha}{2}-1}(1-y)^{\frac{\alpha}{2}-1}}{y^\alpha + (1-y)^\alpha + 2y^{\frac{\alpha}{2}}(1-y)^{\frac{\alpha}{2}}\cos(\frac{\alpha\pi}{2})},$$

which is also the case for Eq. (5.12) with $0 < \alpha < 1$. However, for Eq. (5.12) when $1 < \alpha < 2$ (so that the first moment is finite), $Q(T,t)$ still follows the *arcsine law* given by Eq. (2.35). The arcsine PDF (2.35) is then an *attractor* for the PDF of half occupation time of a random walker having rest periods with finite first moments. This result is in line with the discussion of the moments of T_+ done in the section above. We show that this is the case in Fig. 5.7.

5.5.3 Ergodic properties of T_+

From the moments above we can write the EB parameter for this functional, which yields

$$\mathrm{EB} = \begin{cases} 1 - \frac{\alpha}{2}, & 0 < \alpha < 1 \\ \frac{1}{2}, & 1 < \alpha < 2. \end{cases} \tag{5.61}$$

Consequently, the half occupation time for both Markovian and non-Markovian random walks is also non-ergodic, with the EB parameter for $1 < \alpha < 2$ coinciding with the value of a standard Brownian motion Eq. (2.55).

5.6 Poissonian resetting

In this section, we examine how the occupation time statistics of the random walker studied above change when it is subjected to a stochastic resetting mechanism. The resetting mechanism examined here is the same protocol as in Chapter 3, where the resetting time distribution is given by an exponential distribution with rate r that reverts

the walker to its initial position x_0. In this case, the generating function of a functional $Q_r(p,s)$ of the resetting process can be expressed in terms of the generating function $Q(p,s)$ of the underlying reset-free process through the following renewal relation in the Laplace space [212, 225, 226]

$$Q_r(p,s) = \frac{Q(p,s+r)}{1-rQ(p,s+r)}, \tag{5.62}$$

where again $x_0 = 0$. By means of Eq. (5.62), the generating function of any functional under resetting, as well as its moments, is fully determined if we know its generating function for the reset-free case.

5.6.1 Moments – General expressions and asymptotics

We start by noting that Eq. (5.27) is valid for the process with resetting, but now the generating function has to be $Q_r(p,s)$, which we can get in terms of $Q(p,s)$ by means of Eq. (5.62). With this, the first moment of the PDF $Q_r(Z,t)$ can be written in Laplace space, with $x_0 = 0$, as

$$\langle Z(s)\rangle_r = \frac{\langle Z(s+r)\rangle}{[1-rQ(p=0,s+r)]^2}. \tag{5.63}$$

The characteristic function evaluated at $p = 0$ is given by

$$Q(p=0,t) = \int_0^\infty e^{-pZ} Q(Z,t)dZ\Big|_{p=0} = 1 \tag{5.64}$$

which in Laplace space yields $Q(p=0,s) = s^{-1}$, then $Q(p=0,s+r) = (s+r)^{-1}$ and the first moment is therefore

$$\langle Z(s)\rangle_r = \left(\frac{s+r}{s}\right)^2 \langle Z(s+r)\rangle, \tag{5.65}$$

which connects the first moment between the two processes. In the long-time limit, we can use $s \to 0$ as this implies $\langle Z(s)\rangle_r \approx r^2 \langle Z(s=r)\rangle / s^2$ which after transforming back to t gives

$$\langle Z(t)\rangle_r \approx r^2 \langle Z(s=r)\rangle t + O(0) \quad \text{as } t \to \infty. \tag{5.66}$$

Proceeding similarly for the second moment we find the following general relation

$$\langle Z(s)^2\rangle_r = \left(\tfrac{s+r}{s}\right)^2 \left[\langle Z(s+r)^2\rangle + \tfrac{2r}{s}(s+r)\langle Z(s+r)\rangle^2\right] \tag{5.67}$$

which in the long-time limit i.e., $s \to 0$ yields $\langle Z^2(s)\rangle_r \approx 2r^4 \langle Z(s=r)\rangle^2 s^{-3}$, so that

$$\langle Z(t)^2\rangle_r \approx r^4 \langle Z(s=r)\rangle^2 t^2 + O(t), \quad \text{as } t\to\infty \tag{5.68}$$

after Laplace inversion. We can compute the variance of $Z(t)_r$ in the presence of resetting. From Eqs. (5.66) and (5.68) we see that the terms $O(t^2)$ cancel and the variance grows linearly with time in the large time limit. In particular, from Eqs. (5.65) and (5.67) and expanding in Taylor series for small s we readily find

$$\mathrm{Var}(Z(t))_r \;=\; \langle Z(t)^2\rangle_r - \langle Z(t)\rangle_r^2 = r^2 A t + O(0), \quad \text{as } t\to\infty \tag{5.69}$$

where

$$A = \langle Z(s=r)^2\rangle + 2r\langle Z(s=r)\rangle^2 + 2r^2\langle Z(s=r)\rangle \left(\frac{d\langle Z(s)\rangle}{ds}\right)_{s=r}. \tag{5.70}$$

Note that in the long-time limit, the time dependence of the functionals with resetting does not depend on the details of the underlying random walk.

A Occupation time in an interval

Particularizing for the case of the occupation time in the full interval. Using Eq. (5.31), Eqs. (5.66) and (5.68) read

$$\langle T_a(t)\rangle_r \approx \left(1 - e^{-a\sqrt{\frac{2r}{\sigma^2 K(r)}}}\right) t, \quad \text{as } t\to\infty \tag{5.71}$$

and

$$\langle T_a(t)^2\rangle_r \approx \left(1 - e^{-a\sqrt{\frac{2r}{\sigma^2 K(r)}}}\right)^2 t^2, \quad \text{as } t\to\infty \tag{5.72}$$

respectively. With this, we get a general expression for the first two moments in terms of the memory kernel $K(s=r)$, which for the cases studied above is given in Eqs. (5.10), (5.15), and (5.18). The variance of the occupation time in an interval follows from Eqs. (5.69) and (5.70)

$$\mathrm{Var}(T_a(t))_r \approx r^2 A_a t, \tag{5.73}$$

with

$$A_a = \frac{2e^{-\lambda(r)}}{r^3}\left\{1 - (1+\lambda(r)\Phi(r))\, e^{-\lambda(r)} - \frac{\Phi(r)}{2}\left(1 - e^{-2\lambda(r)}\right)\right\}, \tag{5.74}$$

where $\lambda(r)$ and $\Phi(r)$ are given by Eqs. (5.30) and (5.33). In general, it can be shown from Eq. (5.27) that in the long-time limit all moments of T_a fulfill the relation

$$\langle T_a(t)^n\rangle_r \simeq r^{2n}\langle T_a(r)\rangle^n t^n. \tag{5.75}$$

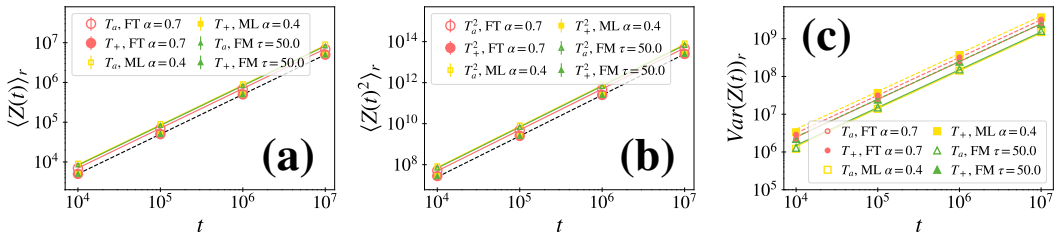


Figure 5.8: **Moments of the occupation time with resetting.** First moment (a), second moment (b), and variance (c) of the occupation time in an interval T_a (empty symbols), and of the half occupation time, T_+ (full symbols) in the presence of stochastic resetting, with reset rate $r = 0.001$. The circles (FT) are computed with $\varphi(t)$ given by Eq. (5.12) with $\alpha = 0.7$ and $t_0 = 1$, the squares (ML) with $\varphi(t)$ given by Eq. (5.16) with $\alpha = 0.4$ and $\tau^* = |\Gamma(1-\alpha)|^{1/\alpha}$, and the triangles (FM) with $\varphi(t)$ given by Eq. (5.8) with $\langle\tau\rangle = 50$. The solid lines are theoretical predictions for T_a: The solid lines represent Eq. (5.71) in panel (a), Eq. (5.72) in panel (b), and Eq. (5.73) in panel (c); the colors correspond to the specific waiting time of the matching colored data points. The dashed lines are theoretical predictions for T_+: Eq. (5.76) in panels (a), and (b), and Eq. (5.77) in panel (c). The parameters used for the numerical simulations are $a = 0.055$, $x_0 = 0$, $\sigma = 0.01$, and the number of walkers for the simulation $N = 10^6$.

B Half occupation time

In the case of the half occupation time, (5.66), (5.68) and (5.69) can be computed using Eq. (5.55) and we get

$$\langle T^+(t)\rangle_r \approx \frac{t}{2}, \quad \langle T^+(t)^2\rangle_r \approx \frac{t^2}{4}, \tag{5.76}$$

and the variance follows

$$\mathrm{Var}(T^+(t))_r \approx r^2 A_+ t, \tag{5.77}$$

with

$$A_+ = \frac{1}{4r^3}\left[1 + \frac{r}{K(r)}\frac{dK(r)}{dr}\right]. \tag{5.78}$$

For the half occupation time we are also able to find in the long-time limit a general relation for all moments from Eq. (5.27)

$$\langle T_+(t)^n\rangle_r \simeq \left(\frac{t}{2}\right)^n, \tag{5.79}$$

In Fig. 5.8 we compare the expressions for the first moment, the second moment, and the variance of both the occupation time of an interval and the half occupation time against numerical simulations. Since the first and second moments scale as a power of time, they appear as linear functions in the log-log scale of Fig. 5.8. Moreover, the slopes of the lines in each panel are the same, which indicates that the temporal scaling is independent of the underlying random walk.

5.6.2 PDF

In this section, we present the results for the PDF of the occupation times under resetting dynamics. In principle $Q_r(Z,t)$ can be obtained from Eq. (5.62) via

$$Q_r(Z,t) = e^{-rt}\mathscr{L}^{-1}_{p\to T}\mathscr{L}^{-1}_{s\to t}\left[\frac{Q(p,s)}{1-rQ(p,s)}\right], \tag{5.80}$$

however performing the double inverse Laplace transform can be cumbersome, as we have seen in Section 5.4. It can be done for the half occupation time T_+ in the case of a ML waiting-time PDF with $\alpha = 1$ which yields a solution in terms of the modified Struve $L_0(\cdot)$ and Bessel $I_0(\cdot)$ functions

$$\begin{aligned} Q_r(y,\xi) = \xi e^{-\xi}\sum_{k=0}^{\infty}\frac{\left[\xi^2 y(1-y)\right]^{\frac{k-1}{2}}}{\Gamma\left(\frac{k+1}{2}\right)^2} = \frac{e^{-\xi}}{\pi\sqrt{y(1-y)}} \\ + \xi e^{-\xi}\left[L_0\left(2\xi\sqrt{y(1-y)}\right) + I_0(2\xi\sqrt{y(1-y)})\right], \end{aligned} \tag{5.81}$$

with $\xi = rt$. This result holds for all t and agrees with the result found in Ref. [225].

The exact solution for FT for general ML waiting-time turns out to be intractable, as is the case for T_a. We can however find the limiting distribution in the long-time limit. To this end we express $Q_r(p,s)$ in a moment generating form

$$Q_r(p,s) = \sum_{n=0}^{\infty}\frac{(-p)^n}{n!}\langle Z^n(s)\rangle_r, \tag{5.82}$$

where the expression for the moments $\langle Z^n(s)\rangle_r$ in the long-time limit are given by Eq. (5.75) or Eq. (5.79). Thus, for the occupation time in an interval from the expression of the n-th moment in the long-time limit given by Eq. (5.82), it follows

$$Q_r(p,t) \approx \sum_{n=0}^{\infty}\frac{1}{n!}\left(-pr^2\langle T_a(r)\rangle t\right)^n = e^{-pr^2\langle T_a(r)\rangle t}. \tag{5.83}$$

Finally, inverting $p \to T_a$

$$Q_r(T_a,t) \approx \delta\left(T_a - \langle T_a(t)\rangle_r\right), \tag{5.84}$$

where $\langle T_a(t)\rangle_r$ is given by Eq. (5.71). This means that in the long-time limit (i.e., when there have been a sufficiently large number of resetting events $rt \gg 1$) the occupation time in the interval $[-a,a]$ is given its mean value.

Proceeding analogously for the half occupation time, where now the n-th moment is given by Eq. (5.79) we get

$$Q_r(p,t) = \sum_{n=0}^{\infty}\frac{(-p)^n}{n!}\left\langle T^+(t)^n\right\rangle_r \approx e^{-pt/2}, \tag{5.85}$$

and Laplace inverting the PDF of the half occupation time under resetting is given by

$$Q_r(T_+,t) \approx \delta(T_+ - t/2). \tag{5.86}$$

So we have seen that both T_a and T_+ tend to a Dirac delta centered at their mean in the long-time limit when resetting is present. These results can be explained in terms of the NESS that resetting induces. Indeed the walker propagator in terms of resetting, namely $P(x,t)_r$, goes to a steady state [115] given by

$$P_r^{ss}(x) = P_r(x, t\to\infty) = \sqrt{\frac{r}{2\sigma^2 K(r)}} e^{-|x|\sqrt{\frac{2r}{\sigma^2 K(r)}}}. \tag{5.87}$$

Hence, in the long-time limit, the occupation time fraction is nothing but

$$\lim_{t\to\infty} \frac{T_a}{t} = \int_{-a}^{a} P_r(x)dx = 1 - e^{-a\sqrt{\frac{2r}{\sigma^2 K(r)}}}, \tag{5.88}$$

for the case of the occupation time in an interval and

$$\lim_{t\to\infty} \frac{T_+}{t} = \int_0^\infty P_r^{ss}(x)dx = \frac{1}{2}, \tag{5.89}$$

for the half occupation time. We note, as suggested by Eqs. (5.84) and (5.86), that whenever Poissonian resetting induces a NESS then the PDF of any stochastic functional (without having explicit time dependence on an external parameter) should attain the form $Q_r(Z,t) \approx \delta(Z - \langle Z(t)\rangle_r)$ in the long-time limit, under suitable conditions. In the following chapter, we will prove this claim.

5.6.3 Ergodic properties

When Poissonian resetting is present, we have seen that the limiting PDF of the time-averaged observable is a Dirac delta function centered at the mean value for T_a and T_+. This means that the ensemble average and the time average are interchangeable in the long-time limit, and Eq. (2.50) is fulfilled. This result is also found for the half occupation time of a Brownian walker in an arbitrary confining (stable) potential (see Section 2 in Ref. [134]). This fact stems from the idea that the effect of a confining potential (or a force field towards a point) is equivalent to a Poissonian resetting process to a point [93, 113]. However, this equivalence is not fulfilled for a subdiffusive random walk (see Section 3.1 in Ref. [134]). The difference lies in the fact that this correspondence can be established when the process is ergodic only. Moreover, the ergodicity breaking parameter is defined for specific observables; then, while we have seen that the occupation time functionals are ergodic in the presence of Poissonian resetting, it has also been seen that Poissonian resetting renders ergodicity breaking in the TAMSD [227]. Moreover, as we are going to discuss in the next chapter, if the resetting times are not Poissonian but rather drawn from a power-law distribution, then the occupation times become non-ergodic as well.

Since we have seen that the occupation times are ergodic in the presence of Poissonian resetting, we can now find a transient PDF for T_a and T_+ by means of the Central

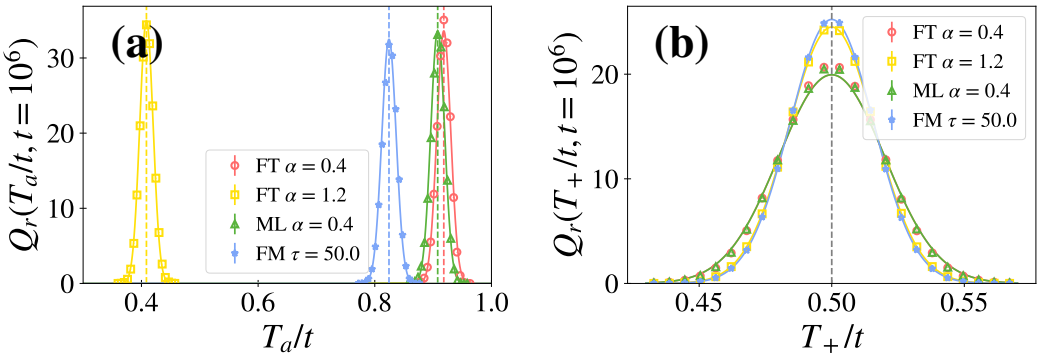


Figure 5.9: **Scaled PDF $Q_r(Z/t,t)$ of the occupation time in the presence of stochastic resetting.** (a) $Z = T_a$, and (b) $Z = T_+$. All symbols come from numerical simulations. The circles and squares (FT) are computed from a $\varphi(t)$ given by Eq. (5.12) with $t_0 = 1$, $\alpha = 0.4$ and $\alpha = 1.2$ respectively; the triangles (ML) with $\varphi(t)$ given by Eq. (5.16) with $\alpha = 0.4$ and $\tau^* = |\Gamma(1-\alpha)|^{1/\alpha}$; and for the stars (FM) $\varphi(t)$ is given by Eq. (5.3) with $\langle\tau\rangle = 50$. The vertical dashed lines represent the means $\langle Z(t)\rangle_r/t$, Eq. (5.71) in (a), and Eq. (5.76) in (b). The solid lines are plotted using Eq. (5.91) in (a) and Eq. (5.92) in (b). The parameters used for the numerical simulations are $a = 0.055$, $x_0 = 0$, $\sigma = 0.01$, $r = 0.001$, $t = 10^6$ and the number of walkers for each simulation $N = 10^6$. To compute T_+, we added $1/2$ of the residence time at $x = 0$ to the total time in the positive axis.

Limit Theorem. This result is not very surprising since each reset renews the process in its entirety. As a result, the occupation times accumulated in the consecutive intervals and the rest are statistically independent and identical to each other. Let T^{in} and T^{out} be the occupation times spent by the walker inside and outside the interval $[-a,a]$, or the positive half line. If τ_i^{in} and τ_i^{out} and denote the times spent by the walker inside and outside the interval between the $i-1$-th and i-th resets, respectively, then the time between two consecutive resettings is $\tau_i = \tau_i^{\text{in}} + \tau_i^{\text{out}}$ and $T^{\text{in}} = \sum_{i=1}^{n(t)} \tau_i^{\text{in}}$, $T^{\text{out}} = \sum_{i=1}^{n(t)} \tau_i^{\text{out}}$, where $n(t)$ is the number of resets up to time t. Since τ_i are exponentially distributed, the times τ_i^{in} and τ_i^{out} have finite moments so that the occupation time in an interval T can be expressed as the sum of i.i.d. random variables with finite mean. Therefore, by virtue of the Central Limit Theorem the PDF for T follows the Gaussian PDF

$$Q_r(T,t) \approx \frac{1}{\sqrt{2\pi \text{Var}(T)_r}} \exp\left[-\frac{(T - \langle T(t)\rangle_r)^2}{2\text{Var}(Z)_r}\right], \tag{5.90}$$

where T is either T_a or T_+. The general expressions for $\langle T(t)\rangle_r$ and $\text{Var}(T)_r$ are given by Eqs. (5.66) and (5.69), respectively. Such Gaussian limit for the observable PDF was also observed earlier [212, 228].

We can further specify Eq. (5.90) for both occupation times. For T_a, we find

$$Q_r(y,t) \approx \frac{1}{\sqrt{2\pi r^2 A_a/t}} \exp\left[-\frac{\left(y-1+e^{-\lambda(r)}\right)^2}{2r^2A_a/t}\right], \tag{5.91}$$

where $y = T_a/t$ and A_a is given by Eq. (5.74). Similarly for T_+, we have

$$Q_r(y,t) \approx \frac{1}{\sqrt{2\pi r^2 A_+/t}} \exp\left[-\frac{\left(y-\frac{1}{2}\right)^2}{2r^2A_+/t}\right], \tag{5.92}$$

where $y = T_+/t$ and A_+ is given by Eq. (5.78). Note that the Gaussian regime is actually the *transient solution* towards the Dirac-Delta limiting PDF at the large time by virtue of

$$\begin{aligned} \lim_{t\to\infty} Q_r(y,t) &= \lim_{t\to\infty} \frac{1}{\sqrt{2\pi r^2 A/t}} \exp\left[-\frac{\left(y-r^2\langle T(r)\rangle\right)^2}{2r^2A/t}\right] \\ &= \delta\left(y-r^2\langle T(r)\rangle\right), \end{aligned} \tag{5.93}$$

where y is either $y = T_a/t$ or $y = T_+/t$. In Fig. 5.9 we show these arguments using numerical simulations. In particular, we compare Eqs. (5.91) and (5.92) with numerical simulations for T_a and T_+ for the different waiting times at the long-time limit $t = 10^6$. We find that a Gaussian PDF can successfully represent the data, which confirms our theoretical predictions.

5.7 Summary of results

In this chapter we presented a comprehensive analysis of the occupation time statistics of a random walker, considering both Markovian and non-Markovian dynamics. Within the CTRW framework, we derived the backward Feynman-Kac equation for a functional of a generic non-Markovian random walk. We then studied two specific observables: the occupation time in an interval T_a and the half occupation time T_+. Their characteristic functions were obtained in terms of the memory kernel, together with exact and asymptotic expressions for the first two moments.

For Mittag–Leffler and power-law waiting-time PDFs, we showed that the mean $\langle T_a(t)\rangle$ converges to the same long-time value when $0 < \alpha < 1$. For the power-law case, with $1 < \alpha < 2$, we have seen that $\langle T_a(t)\rangle$ instead approaches the value corresponding to Brownian motion. In the short-time limit, we see that both $\langle T_a(t)\rangle$ and $\langle T_a(t)^2\rangle$ are independent of the underlying random walk, and scale as t and t^2, respectively. Although an exact expression for $Q(T_a,t)$ over the full domain could not be obtained, exact solutions were derived in the left ($T_a \ll t$), right ($T_a \to t$), and central regimes for both waiting-time distributions.

For T_+, the PDF converges in the long-time limit to a scaling form in the variable T_+/t. When the rest periods have finite first moment, the limiting distribution is the

arc-sine law. For power-law ($0 < \alpha < 1$) and Mittag–Leffler waiting times, the limiting distribution instead becomes the Lamperti law. We also derived expressions for the general moments $\langle T_a(t)^n \rangle$ for systems with finite or divergent rest-period moments. This analysis concludes with a detailed study of the ergodic properties of the occupation times and their relation to the limiting distributions.

Finally, we examined occupation time statistics in the presence of stochastic resetting with exponentially distributed reset times. In this case, the moments scale as $\langle Z(t)^n \rangle_r \sim t^n$. Moreover, the occupation times satisfy a Central Limit Theorem, and the PDFs of both functionals converge in the long-time limit to Dirac delta functions centered at their mean values with a Gaussian PDF as a transient solution.

6

STOCHASTIC FUNCTIONALS UNDER GENERAL RESETTING

In this chapter we derive the characteristic function of stochastic functionals of a random walk whose position is reset to the origin at random times drawn from a general probability distribution. When the resetting PDF has a power law tail, we obtain the temporal scaling of the first two moments of any stochastic functional. We also prove that when the resetting-time PDF has finite moments, the probability density of any functional converges to a delta function centered at its mean, indicating an ergodic phase. Next, we apply these general expressions to the specific case of the half occupation time deriving the ergodicity breaking parameter, the first two moments, and the limiting distribution when the resetting time distribution follows a power-law tail, for both Brownian and subdiffusive random walks. We characterize the three different shapes of the limiting distribution as a function of the exponent of the resetting distribution.

6.1 Introduction . . . 108
6.2 Characteristic function . . . 108
6.2.1 Moments . . . 110
6.3 Limiting PDF for a finite moment resetting distribution . . . 111
6.4 Moments in the long-time limit . . . 113
6.5 Application: Half occupation time . . . 115
6.5.1 The first two moments and EB . . . 115
6.5.2 Limiting PDF . . . 118
6.6 Summary of results . . . 124

6.1 Introduction

In the previous chapters, we have seen how stochastic resetting can significantly alter fundamental properties of the underlying random walk. As discussed earlier, this mechanism can lead to the emergence of a NESS [110, 229] and can optimize the MFPT [97]. Moreover, in Chapter 5 we have seen that Poissonian resetting can also modify the statistical properties of stochastic functionals of a random walker, driving a transition from non-ergodic to ergodic behavior.

Most existing works on stochastic functionals under resetting assume Poissonian resetting [225, 226], while much less attention has been given to resetting processes governed by general probability density functions. Only a few studies consider reset times drawn from arbitrary distributions. In particular, when the resetting times decay as a power law, the existence of a steady state and a finite first-passage time depend on both the characteristic exponent of the distribution and the properties of the underlying random walk [109, 115, 229, 230, 231, 232]. Along these lines, we previously analyzed the statistical properties of the occupation time in an interval for a Brownian particle with reset times sampled from a power-law PDF [8]. Despite this progress, a comprehensive theory describing the behavior of general stochastic functionals under arbitrary resetting schemes is still lacking.

In this chapter, we investigate how the statistical properties of stochastic functionals are affected when the position of the underlying random walk is reset to the origin after random times drawn from a general PDF. Since the resetting mechanism forms a renewal process, we derive an equation relating the characteristic function of the functional under resetting to two ingredients: the PDF of the resetting times and the characteristic function of the corresponding reset-free functional. We further analyze the temporal behavior of the first two moments, which also provides insight into the ergodic properties. As a concrete application, we specialize our general results to the half occupation time, one of the most widely studied functionals with applications across physics and mathematics [141]. In particular, we obtain its limiting PDF when the resetting times PDF exhibits a power-law tail, considering both normal and subdiffusive underlying random walks.

This chapter is structured as follows. In Sec. 6.2 we derive the characteristic function of a functional under general resetting, obtain expressions for the first two moments, and illustrate how to analyze the ergodic properties. In Sec. 6.3 and 6.4 we prove several general results valid for any stochastic functional. In particular, we show that any stochastic functional becomes ergodic, i.e., deterministic in the long-time limit, when the resetting PDF has finite moments. We also derive the long-time scaling behavior of the first two moments when the resetting PDF decays as a power law. In Sec. 6.5 we apply these results to the case of the half occupation time. Finally, Sec. 6.6 summarizes the main findings.

6.2 Characteristic function

The goal is to compute the characteristic function $Q(p,t|x_0)_r = \mathscr{L}_{Z\to p}[Q(Z,t|x_0)_r]$ of the non-negative functional $Z(t|x_0)_r$ when the underlying random walk is subjected to

resetting the position to $x = x_0$ as denoted by the subscript $_r$. As we had done in [8], we will work with the backward recurrence time B, which will be of great use in the following derivation. In a process of resetting, we can write the observation time t as the sum of the waiting times τ_i drawn from the resetting PDF $\phi(\tau)$ and the backward recurrence time, which is the time elapsed since the last reset. If N resets have occurred in the time interval $(0,t)$, then

$$t = \sum_{l=1}^{N} \tau_l + B. \tag{6.1}$$

Note that B does not have in general the same PDF as the waiting times between resets $\{\tau_1,,...,\tau_N\}$, except when the resetting renewal process is Markovian: when the resets are following a Poisson process with exponentially distributed waiting times between resets (see e.g. Ref. [141, 233] and [205] for discrete reset times).

Next, let us define $F(Z^{'},\tau)$ as the joint probability of the time between consecutive resets τ and the value of the functional is $Z^{'}$ in the same interval. Since the reset distribution and the value of the functional are statistically independent

$$F(Z^{'},\tau|x_0) = \phi(\tau)Q(Z^{'},\tau|x_0)_0 \tag{6.2}$$

where $Q(Z^{'},\tau|x_0)_0$ is the PDF of the functional of the reset-free random walk. Its complementary, $F^*(Z_B,B)$, is the joint probability that no reset has occurred in an interval B and the value of the functional is Z_B in the same interval

$$F^*(Z_B,B|x_0) = \phi^*(B)Q(Z_B,B|x_0)_0 \tag{6.3}$$

where now $\phi^*(B) = \int_B^\infty \phi(\tau)d\tau$. Let $Q_N(Z,t|x_0)dZdt$ be the probability that the N-th resetting event takes place in the time interval $(t,t+dt)$ when the value of the functional is within $(Z,Z+dZ)$. With the above definitions, we can then write the PDF for $N+1$ resettings as the convolution of $Q_N(Z,t|x_0)dZdt$ and $F(Z^{'},\tau|x_0)$

$$Q_{N+1}(Z,t|x_0) = Q_N * F\,(Z,t) = \int_0^Z dZ^{'} \int_0^t d\tau Q_N(Z-Z^{'},t-\tau|x_0)F(Z^{'},\tau|x_0) \tag{6.4}$$

where the zero reset probability is given by $Q_0(Z,t|x_0) = \delta(Z)\delta(t)$.

Finally, the complete PDF $Q(Z,t|x_0)_r$ of the process with resets, is given by summing over all the contributions from all number of possible resets in $(0,t)$, and adding the contribution since the last reset, which, using the definitions above reads

$$Q(Z,t|x_0)_r = \sum_{N=0}^{\infty} \int_0^Z dZ_B \int_0^t dB\, Q_N(Z-Z_B,t-B|x_0)F^*(Z_B,B|x_0). \tag{6.5}$$

In Laplace space, from the convolution property of Laplace transforms, we can write Eq. (6.5) as

$$
\begin{aligned}
Q(p,s|x_0)_r &= \mathscr{L}_{t\to s}\mathscr{L}_{Z\to p}\left[Q(p,s|x_0)_r\right] = \sum_{N=0}^{\infty}\left[F(p,s|x_0)\right]^N F^*(p,s|x_0) \\
&= \frac{F^*(p,s|x_0)}{1-F(p,s|x_0)} = \frac{\mathscr{L}_{t\to s}\left[\phi^*(t)Q(p,t|x_0)_0\right]}{1-\mathscr{L}_{t\to s}\left[\phi(t)Q(p,t|x_0)_0\right]},
\end{aligned}
\tag{6.6}
$$

where we can sum the geometric series, since the Laplace transform of a normalized PDF is smaller than 1. With this equation, we can find the characteristic function of a functional of a random walk under resetting in terms of the characteristic function of the functional of a random walk without resetting. Note that in the absence of resetting $\phi \to 0$ and $\phi^* \to 1$, so that $Q(p,s|x_0)_r = Q(p,s|x_0)_0$.

When the resetting mechanism is a Poisson process, the times between resetting events are exponentially distributed with the constant rate r. Then, considering the particular case $\phi(t) = re^{-rt}$, Eq. (6.6) turns out to be

$$
Q(p,s|x_0)_r = \frac{Q(p,s+r|x_0)_0}{1-rQ(p,s+r|x_0)_0}
\tag{6.7}
$$

which is consistent with the results derived previously in Refs. [225, 226].

Note 6.1 As in the previous chapter, the derivation above has been carried out for a non-negative functional Z. Again, one could consider a functional that can take both positive and negative values, as in the case of the area under the trajectory. In this case, the same renewal structure Eq. (6.6) remains valid. However, to derive it, the Laplace transform with respect to Z has to be replaced by a Fourier transform. Therefore, every occurrence of $Q_0(p,t|x_0)$ must be replaced by $Q_0(\omega,t|x_0)$, where ω is the Fourier variable conjugate to Z. Moreover, the convolution over the functional variable is no longer restricted to positive values. Therefore, in Eqs. (6.4) and (6.5), the integration limits must be changed from $(0,Z)$ to $(-\infty,\infty)$.

6.2.1 Moments

Next, we can relate the moments of the functional in the presence of resetting with the moments of the functional without resetting. To do this, we start with Eq. (6.6). Since $Q(p,s|x_0)_r$ is a MGF, we can again obtain its moments from its derivatives like in Eq. (5.27) via,

$$
\langle Z(s|x_0)^n\rangle = (-1)^n \frac{\partial^n Q(p,s|x_0)}{\partial p^n}\bigg|_{p=0}.
\tag{6.8}
$$

Taking the first derivative of Eq. (6.6) with respect to p we find from (6.8)

$$
\begin{aligned}
\langle Z(s|x_0)\rangle_r &= -\frac{\partial Q(p,s|x_0)_r}{\partial p}\bigg|_{p=0} = -\frac{\partial}{\partial p}\left(\frac{F^*(p,s|x_0)}{1-F(p,s|x_0)}\right)_{p=0} \\
&= -\frac{1}{1-F(0,s|x_0)}\frac{\partial F^*(p,s|x_0)}{\partial p}\bigg|_{p=0} - \frac{F^*(0,s|x_0)}{\left[1-F(0,s|x_0)\right]^2}\frac{\partial F(p,s|x_0)}{\partial p}\bigg|_{p=0}
\end{aligned}
\tag{6.9}
$$

where $F(0,\tau)=\phi(\tau)$ and $F^*(0,\tau)=\phi^*(\tau)$. Hence,

$$\langle Z(s|x_0)\rangle_r = \frac{\mathscr{L}_{t\to s}\left[\phi^*(t)\,\langle Z(t|x_0)\rangle_0\right]}{1-\phi(s)} + \frac{\mathscr{L}_{t\to s}\left[\phi(t)\,\langle Z(t|x_0)\rangle_0\right]}{s\left[1-\phi(s)\right]}. \tag{6.10}$$

Analogously, taking the second derivative of Eq. (6.6) with respect to p, we straightforwardly find

$$\begin{aligned}\left\langle Z(s|x_0)^2\right\rangle_r &= \frac{2\mathscr{L}_{t\to s}\left[\phi(t)\,\langle Z(t|x_0)\rangle_0\right]}{1-\phi(s)}\,\langle Z(s|x_0)\rangle_r \\ &+ \frac{1}{1-\phi(s)}\Bigg\{\mathscr{L}_{t\to s}\left[\phi^*(t)\left\langle Z(t|x_0)^2\right\rangle_0\right] \\ &+ \frac{1}{s}\mathscr{L}_{t\to s}\left[\phi(t)\left\langle Z(t|x_0)^2\right\rangle_0\right]\Bigg\}.\end{aligned} \tag{6.11}$$

Following the steps above, we can obtain the corresponding expressions for higher order moments.

6.3 Limiting PDF for a finite moment resetting distribution

Let us first consider a resetting time PDF with finite moments. In this case, the Laplace transform of the PDF is, in the long-time limit ($s\to 0$), $\phi(s)\simeq 1-\langle t\rangle_R s+\ldots$ where $\langle t\rangle_R$ is the mean resetting time. Expressing the term $\exp(-st)$ as a power series we can write

$$\mathscr{L}_{t\to s}\left[\phi(t)\,\langle Z(t|x_0)\rangle_0\right] = \sum_{n=0}^{\infty}\frac{(-s)^n}{n!}\int_0^\infty t^n\phi(t)\,\langle Z(t|x_0)\rangle_0\,dt. \tag{6.12}$$

We now make some assumptions about the time dependence of the functionals. Most functionals fulfill $\langle Z(t|x_0)\rangle_0\sim t^\zeta$ in the long-time limit, where ζ is a positive real number. The specific value of ζ depends on the specific dependence of $U[\cdot]$ on $x(\tau)$ and on the underlying random walk. Then,

$$\int_0^\infty t^n\phi(t)\,\langle Z(t|x_0)\rangle_0\,dt \sim \int_0^\infty t^{n+\zeta}\phi(t)dt = \left\langle t^{n+\zeta}\right\rangle_R < \infty \tag{6.13}$$

where $\left\langle t^{n+\zeta}\right\rangle_R$ is the moment of order $n+\zeta$ of the resetting time PDF which is finite for any n, since we are considering the case of a finite moment resetting distribution. Consequently, we can approximate the expansion (6.12) as

$$\mathscr{L}_{t\to s}\left[\phi(t)\,\langle Z(t|x_0)\rangle_0\right] = \int_0^\infty \phi(t)\,\langle Z(t|x_0)\rangle_0\,dt + O(s). \tag{6.14}$$

Analogously,

$$\mathscr{L}_{t\to s}\left[\phi^*(t)\left\langle Z(t|x_0)\right\rangle_0\right] = \int_0^\infty \phi^*(t)\left\langle Z(t|x_0)\right\rangle_0 dt + O(s). \tag{6.15}$$

Then, taking the limit $s \to 0$ to Eq. (6.10) we find

$$\left\langle Z(s|x_0)\right\rangle_r \simeq \frac{1}{\langle t\rangle_R s^2}\int_0^\infty \phi(\tau)\left\langle Z(\tau|x_0)\right\rangle_0 d\tau \tag{6.16}$$

which, after Laplace inversion, yields

$$\left\langle Z(t|x_0)\right\rangle_r \simeq \frac{t}{\langle t\rangle_R}\int_0^\infty \phi(\tau)\left\langle Z(\tau|x_0)\right\rangle_0 d\tau. \tag{6.17}$$

Proceeding analogously with Eq. (6.11) and considering a power dependence of $\left\langle Z(t|x_0)^2\right\rangle_0$ on time, we obtain

$$\left\langle Z(t|x_0)^2\right\rangle_r \simeq \frac{t^2}{\langle t\rangle_R^2}\left[\int_0^\infty \phi(\tau)\left\langle Z(\tau|x_0)\right\rangle_0 d\tau\right]^2. \tag{6.18}$$

Consequently, by virtue of (2.54), we obtain EB $= 0$ and the observable $\mathscr{O}[x(t)] = U[x(t)]$ is ergodic, which means that in the long-time limit

$$Q(Z,t|x_0)_r = \delta\left(Z - \left\langle Z(t|x_0)\right\rangle_r\right) \tag{6.19}$$

where $\left\langle Z(t|x_0)\right\rangle_r$ is given by Eq. (6.17). Changing the PDF in Eq. (6.19) to the variable $\eta = Z/\left\langle Z(t|x_0)\right\rangle_r$ one has

$$Q(\eta|x_0)_r = \delta(\eta - 1). \tag{6.20}$$

It should be noted that we have been able to find the limiting PDF -that is, the asymptotic probability distribution at long times- given by Eq. (6.20) from the first two moments of Z by means of the ergodicity of the observable $U[x(t)]$ when the resetting PDF has finite moments. However, the same result can be obtained from the characteristic function under resetting times drawn from a PDF with finite moments, which we detail in Appendix C. These derivations constitute the first general result of this chapter.

From the derivation above, we see that any positive functional of a random walk in the presence of stochastic resetting is ergodic, provided that the PDF of resetting times has finite moments. Thus, for sufficiently long times, the PDF of the functional $Q(Z,t|x_0)_r$ tends to a delta centered on the mean value. Here we have proved the results found in Chapter 5, Eqs. (5.84) and (5.86), where we had found that the PDF of the occupation time in an interval and the half occupation time tended to a Dirac delta in the long-time limit when Poissonian resetting is present. In Fig. 6.1 we check the results for the limiting PDF of three observables: i) the occupation time inside the interval $[-a,a]$, $T_a(t) = \int_0^t \Theta(-a < x(\tau) < a)d\tau$, ii) the area under the square position $A(t) = \int_0^t x^2(\tau)d\tau$ (this functional has been studied when the underlying

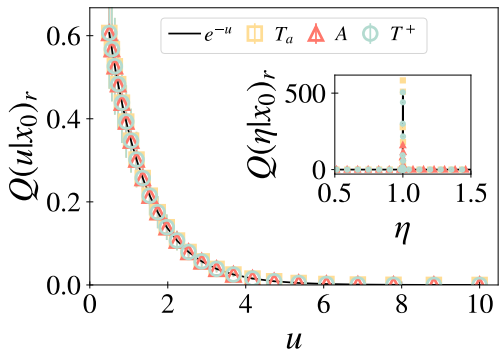


Figure 6.1: **Limiting PDF of Z for exponentially distributed resetting in Laplace space.** The black line represents the Laplace transform of Eq. (6.20) and the symbols are obtained from numerical simulations. In squares $Z = T_a$ with $a = 1$; in triangles $Z = A$, and in circles $Z = T_+$. In the inset, we represent the same data in η space. For all simulations: $x_0 = 0$, $D = 1$, $\langle t \rangle_R = 1.2$. All simulations are run for $N = 10^5$ particles for a total simulation time of $t = 10^7$ with a time discretization of $dt = 0.1$.

motion is subdiffusive and without resetting [122]) and iii) the half occupation time $T_+(t) = \int_0^t \Theta(x(\tau))d\tau$, for exponentially distributed resets. To ease the visualization of the Dirac delta function, we compare the data with the theoretical prediction in the Laplace space, in which $Q(u|x_0)_r = \int_0^\infty e^{-u\eta} Q(\eta|x_0)_r d\eta = e^{-u}$. To do this, we do the simulations in the observable domain, and then we transform the resulting data to the Laplace space by performing a numerical Laplace transform. Since $Q(\eta|x_0)_r$ is a PDF, we compute the numerical Laplace transform as $Q(u|x_0)_r = \langle e^{-u\eta} \rangle$, where we simply average over the ensemble. As can be seen in the figure, the three functionals T_a, A, and T_+ collapse on the theoretical line.

6.4 Moments in the long-time limit

We can obtain the temporal dependence of the first two moments $\langle Z(t|x_0) \rangle_r$ and $\langle Z(t|x_0)^2 \rangle_r$ in the long-time limit. To this end, we again assume that the moments of functional without resetting are finite and behave as $\langle Z(t|x_0) \rangle_0 \sim t^\zeta$ with $\zeta > 0$, as $t \to \infty$, considering now that resetting times are drawn from a fat-tailed PDF $\phi(t) \sim t^{-1-\gamma}$ with $0 < \gamma \leq 2$. As discussed before, the moments of this PDF are diverging if $0 < \gamma < 1$, but the first moment is finite if $1 < \gamma < 2$. In particular, let us consider that the resetting time PDF follows the fat-tailed density

$$\phi(t) = \frac{\gamma t_0^\gamma}{t^{1+\gamma}}, \quad t > t_0 \tag{6.21}$$

and 0 otherwise, which is the same PDF as Eq. (5.12). Note that the limit $\gamma \to 0$ here corresponds to the absence of resetting because in this limit $\phi \to 0$ and $\phi^* \to 1$. To compute the long-time limit we need to consider $s \to 0$ in Eqs. (6.10) and (6.11), which read, see note 6.2 for details,

$$\mathscr{L}_{t\to s}\left[\phi(t) \langle Z(t|x_0)^n \rangle_0\right] \sim \int_{t_0}^\infty e^{-st} t^{n\zeta-1-\gamma} dt \sim \begin{cases} \text{const}, & \gamma > n\zeta \\ s^{\gamma-n\zeta}, & \gamma < n\zeta. \end{cases} \tag{6.22}$$

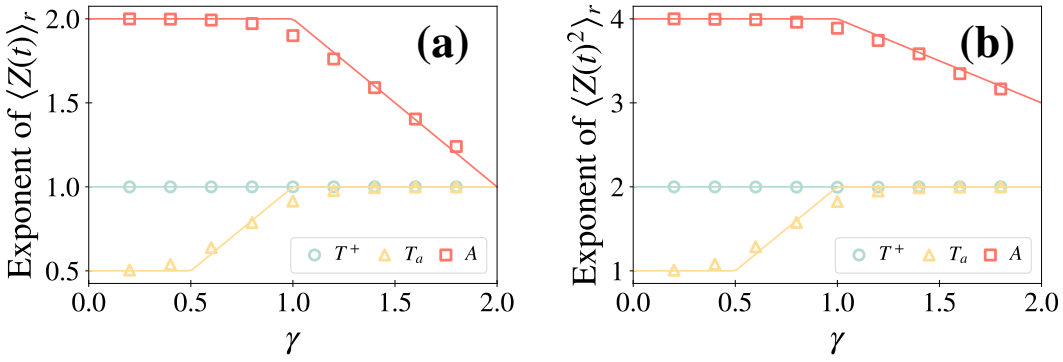


Figure 6.2: **Exponent ω (of $\sim t^{\omega}$) of the first and second moments of the observables for a Brownian Walker with fat-tailed resetting** (Eq. (6.21)) as a function of the resetting exponent γ. For every value of γ, we have computed the values of the observables for the simulation times $t = \{10^3, 10^4, 10^5, 10^6, 10^7\}$. Then, we have performed a least squares fit to $\log_{10}(\langle Z(t)^{1,2}\rangle_r) = \omega \log_{10}(t) + c$, the symbols in the plots represent the obtained values of ω. The solid lines are obtained from Table 6.1. For all simulations, the parameters used are: a time discretization of $dt = 0.1$, $D = 1$, and $t_0 = 1$ for the resetting PDF, the points for $\gamma = 0.2, 1.8$ are run for $N = 10^6$ particles, and all the rest for $N = 10^5$.

and

$$\mathscr{L}_{t\to s}\left[\phi^*(t)\,\langle Z(t|x_0)^n\rangle_0\right] \sim \int_{t_0}^{\infty} e^{-st} t^{n\zeta-\gamma} dt \sim \begin{cases} \text{const}, & \gamma > 1+n\zeta \\ s^{\gamma-n\zeta-1}, & \gamma < 1+n\zeta. \end{cases} \tag{6.23}$$

Keeping only the dominant terms in (6.10) and (6.11), we obtain the results in Table 6.1. Note that the scaling exponent of the moments depends on the values of the resetting exponent γ and the exponent of the functional without resetting ζ. This is the second general result of this chapter, where we find the long-time behavior of the first two moments of a functional with fat-tailed resetting in terms of the temporal scaling of the moments of the functional without resetting.

For example, for the particular case where Z corresponds to the occupation time in an interval T_a, in the absence of resetting, i.e., for free Brownian motion, $\langle T_a(t)\rangle_0 \sim t^{1/2}$ and $\langle T_a^2(t)\rangle_0 \sim t$ and so $\zeta = 1/2$. The results in Table 6.1 predict

$$\langle T_a(t)\rangle_r \sim \begin{cases} t^{1/2}, & 0 < \gamma \le 1/2 \\ t^{\gamma}, & 1/2 \le \gamma < 1 \end{cases}, \quad \langle T_a(t)^2\rangle_r \sim \begin{cases} t, & 0 < \gamma \le 1/2 \\ t^{2\gamma}, & 1/2 \le \gamma < 1 \end{cases} \tag{6.24}$$

γ	$\langle Z(t\|x_0)\rangle_r$	$\langle Z(t\|x_0)^2\rangle_r$
$0 < \gamma \le \zeta$	$\sim t^{\zeta}$	$\sim t^{2\zeta}$
$\zeta < \gamma \le 1$	$\sim t^{\gamma}$	$\sim t^{2\gamma}$
$1 < \gamma \le 2$	$\sim t$	$\sim t^2$

γ	$\langle Z(t\|x_0)\rangle_r$	$\langle Z(t\|x_0)^2\rangle_r$
$0 < \gamma \le 1$	$\sim t^{\zeta}$	$\sim t^{2\zeta}$
$1 < \gamma \le \zeta$	$\sim t^{1+\zeta-\gamma}$	$\sim t^{1+2\zeta-\gamma}$

Table 6.1: Left: long-time limit behavior of the first two moments for $0 \le \zeta \le 1$. Right: long-time limit behavior of the first two moments for $1 < \zeta \le 2$.

In Fig. 6.2 we check the results shown in Table 6.1 for the three different stochastic functionals considered in Fig. 6.1: T_a, T_+, and A. The agreement is excellent.

Note 6.2 In this chapter we need to deal with and approximate integrals of the form of

$$\int_{t_0}^{\infty} e^{-st} t^{\beta} dt = t_0^{\beta+1} e^{-st_0} U(1, 2+\beta, st_0)$$

where $U(a,b,z)$ is the Kummer U function (see chapter 13 of [222]). In the limit $st_0 \ll 1$ this function reads

$$U(1,b,z) = \begin{cases} \frac{1}{1-b} + \frac{z}{b(1-b)} + \ldots, & b < 0, \\ \frac{1}{1-b} - \frac{\Gamma(b)}{1-b} z^{1-b} + \ldots, & 0 < b < 1, \\ \frac{\Gamma(b-1)}{z^{b-1}} + \ldots, & b > 1. \end{cases}$$

Then we can approximate $\int_{t_0}^{\infty} e^{-st} t^{\beta} dt$ as

$$\int_{t_0}^{\infty} e^{-st} t^{\beta} dt \sim \begin{cases} \text{const}, & \beta < -1 \\ s^{-1-\beta}, & \beta > -1. \end{cases}$$

6.5 Application: Half occupation time

In this section, we apply the previous general results to the case of the half occupation time, Eq. (2.34), $T^+(t|x_0) = \int_0^t \Theta[x(\tau)] d\tau$. We will study the case of a Brownian walker, within the framework of general diffusion, and a subdiffusive CTRW one.

6.5.1 The first two moments and EB

In the absence of resetting, the mean and the mean square half occupation time of the Brownian motion are, Eq. (2.36), $\langle T^+(t|x_0)\rangle_0 = t/2$ and $\langle T^+(t|x_0)^2\rangle_0 = 3t^2/8$. If we consider the fat-tailed resetting density in Eq. (6.21) and using (6.2) together with (6.10) and (6.11) we obtain

$$\langle T^+(t|x_0)\rangle_r \simeq \frac{t}{2}, \quad \langle T^+(t|x_0)^2\rangle_r \simeq \begin{cases} \frac{3-\gamma}{8} t^2, & 0 < \gamma < 1 \\ \frac{1}{4} t^2, & 1 < \gamma < 2 \end{cases} \tag{6.25}$$

in the long-time limit. Now, from (2.54) the EB parameter easily follows:

$$\text{EB}_+ = \begin{cases} \frac{1-\gamma}{2}, & 0 < \gamma < 1 \\ 0, & 1 < \gamma < 2 \end{cases}. \tag{6.26}$$

Eqs. (6.25) and (6.26) are the third result of this chapter. Note that this result predicts an ergodic transition between non-ergodic and ergodic phases at $\gamma = 1$. For $1 < \gamma < 2$, the observable $\Theta[x(\tau)]$ is ergodic, thus its limiting PDF converges to a delta function centered on the mean value, Eq. (6.19). Moreover, for the derivation of the limiting PDF we have required that the resetting time PDF has all moments finite, but here we find that for T_+ the condition can be relaxed to only require that the first moment is finite, which is the case for $\gamma > 1$. On the other hand, for $0 < \gamma < 1$ when the resetting times PDF has infinite moments, the observable is non-ergodic, and the limiting PDF converges towards a *generalized arcsine law* as we show below. What is more, for $\gamma = 0$ we get $\mathrm{EB}_+ = 1/2$, which corresponds to the value of EB_+ in the absence of resetting, Eq. (2.55). Then, the presence of resetting reduces the value of EB_+ to such an extent that if the resetting is frequent enough (in particular, if $\gamma > 1$) the observable becomes ergodic. In Fig. 6.3 (a) and (b) we compare (6.25) and (6.26) with numerical simulations showing a very good agreement.

We can further consider the more general case of a subdiffusive walker in the context of the CTRW, to study the competition between the exponents of the resetting mechanism and the waiting times. In Eqs. (5.54), and (5.56) we have computed the first and second moment of the half occupation time, from which we get $\langle T^+(t|x_0)\rangle_0 = t/2$ and $\left\langle T^+(t|x_0)^2\right\rangle_0 = (4-\alpha)t^2/8$, where α is the exponent of the power-law PDF of waiting times of the walker. Considering the fat-tailed resetting PDF given in Eq. (6.21) then, using 6.2, we have

$$\left\langle T^+(t|x_0)\right\rangle_r \simeq \frac{t}{2}, \quad \left\langle T^+(t|x_0)^2\right\rangle_r \simeq \begin{cases} \frac{4-\alpha-\gamma(2-\alpha)}{8} t^2, & 0 < \gamma < 1 \\ \frac{1}{4} t^2, & 1 < \gamma < 2 \end{cases} \tag{6.27}$$

in the long-time limit. And the EB parameter

$$\mathrm{EB}_+ = \begin{cases} \frac{(1-\gamma)(2-\alpha)}{2}, & 0 < \gamma < 1 \\ 0, & 1 < \gamma < 2 \end{cases} . \tag{6.28}$$

Eqs. (6.27), and (6.28) are the fourth result of this chapter. For $\alpha = 1$ the walker moves diffusively and (6.28) reduces to (6.26) as expected. Again, and consistently with the Brownian case, the transition to the ergodic phase is determined by the values of γ for which the resetting PDF has finite first moment, i.e., it occurs again at $\gamma = 1$. Analogously to the diffusive case, in Fig. 6.3 (c) and (d) we compare the predictions from Eqs. (6.27), and (6.28) with simulations. For the subdiffusive walker, we have simulated a CTRW with a jump PDF

$$\Psi(x) = \frac{\delta(x+\sigma)}{2} + \frac{\delta(x-\sigma)}{2} \tag{6.29}$$

and a power-law waiting time PDF of parameter α

$$\varphi(t) = \begin{cases} \alpha t_{\alpha,0}^{\alpha} t^{-1-\alpha}, & t > t_{\alpha,0} \\ 0, & t \leq t_{\alpha,0} \end{cases} . \tag{6.30}$$

where we have taken $t_{\alpha,0} = 1$. Again, we see a good agreement between the analytic predictions and the simulations.

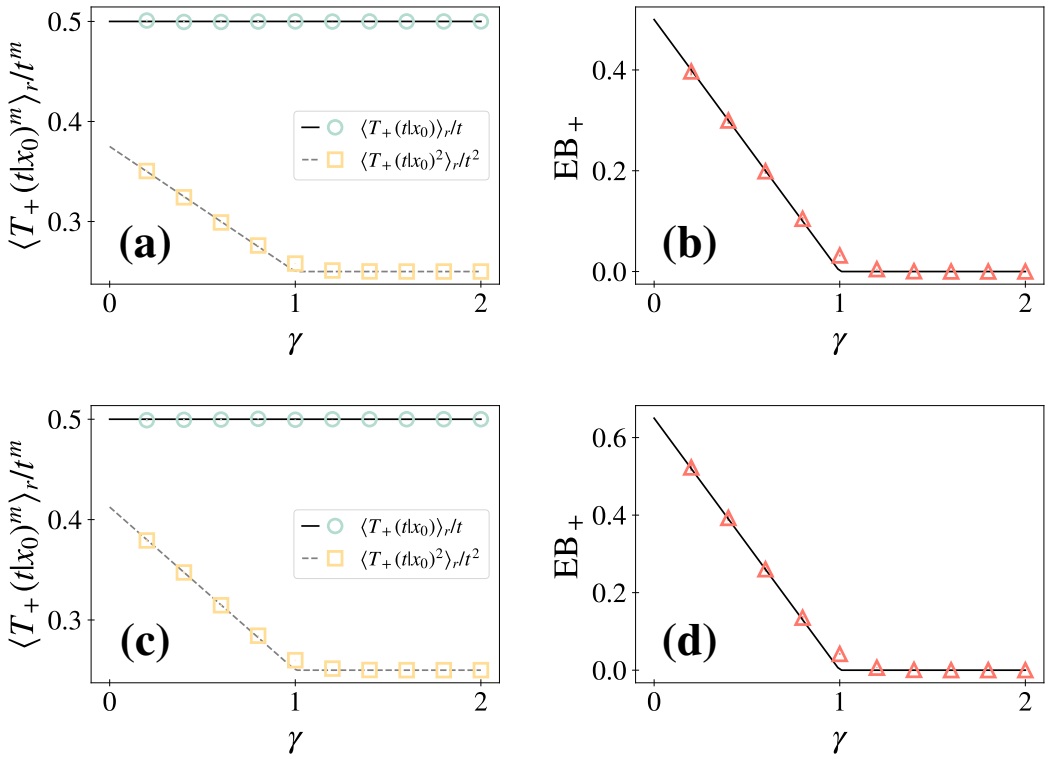


Figure 6.3: **First moment, second moment, and EB parameter of the half occupation time with fat-tailed resetting.** (a) Mean ($m = 1$) and mean square ($m = 2$) half occupation time of a Brownian motion with fat-tailed resetting (Eq. (6.21)) over the m-th power of the total simulation time t as a function of the resetting exponent γ. The solid line and the dashed line represent Eq. (6.25) over t and t^2, respectively. The symbols are obtained from simulations, the circles represent the first moment over t, and the squares represent the second moment over t^2. (b) The EB parameter for T_+ as a function of the resetting exponent γ, where we have computed the numeric results as $\langle T_+(t = 10^7|0)^2\rangle/\langle T_+(t = 10^7|0)\rangle^2 - 1$ from the data. The solid line represents Eq. (6.26) and the triangles are obtained from the same simulations used in panel (a). (c), and (d) represent the same analysis but for a subdiffusive walker with fat-tailed resetting. In these figures the lines correspond to (6.27) in (c), and Eq. (6.28) in (d). The symbols are obtained from simulations of a CTRW. For all simulations, the parameters used are: $x_0 = 0$, and $t_0 = 1$ for the resetting PDF. For (a) and (b) $D = 1$, and $dt = 0.1$ and for (c) and (d) the waiting time PDF has $t_{\alpha,0} = 1$, and $\alpha = 0.7$, and the jump PDF $\sigma = 0.01$. All simulations are run for $N = 10^5$ particles for a total simulation time of $t = 10^7$.

6.5.2 Limiting PDF

We can go beyond the moments and compute the limiting PDF of T_+ in the presence of general resetting. To do so, we start with general considerations on the limiting PDF of a generic functional Z of an isotropic random walk, and its characteristic function $Q(p,s|x_0)_r$, which can be computed from Eq. (6.6). Assume that in general in the long-time limit the PDF $Q(Z,t|x_0)_0$ has a scaling solution

$$\lim_{t\to\infty} Q(Z,t|x_0)_0 = \frac{1}{t^\beta} f\left(\frac{Z}{t^\delta}\right), \tag{6.31}$$

which for the half occupation time $\beta = \delta = 1$, for which the PDF $Q(T_+,t|x_0)_0$ has a limiting density of the form $\lim_{t\to\infty} Q(T_+,t|x_0)_0 = f\left(T_+/t\right)/t$ for $0 < T_+ < t$. Two relevant examples are the Lévy arcsine [138], Eq. (2.35), or the Lamperti [139], Eq. (2.37), distributions which correspond to the case where the underlying random walk is either standard diffusion or subdiffusion, respectively.

Next, for the resettings PDF consider that has a power law tail with index γ

$$\phi(t) \sim t^{-1-\gamma}, \quad 0 < \gamma < 2 \tag{6.32}$$

as $t \to \infty$. This case corresponds to PDFs like the one in Eq. (6.21), but we are not assuming any particular form for the PDF of resetting, just that it has a power-law tail with index γ. Another example of a PDF with this kind of tail is the Mittag-Leffler distribution, eq. (5.16). Regarding the details of the derivation to Appendix D, we find long-time limit of the characteristic function of T_+ under resetting in terms of the scaling function $f(u)$ and the exponent γ of the resetting PDF. On the one hand, when $\phi(t)$ has finite first moment, $1 < \gamma < 2$, we get

$$Q(T_+,t|x_0)_r = \delta\left(T_+ - \langle T_+(t|x_0)\rangle_r\right), \quad 1 \leq \gamma < 2 \tag{6.33}$$

which is in agreement with (6.19), and the results found for the EB parameter.

On the other hand, considering the case $0 < \gamma < 1$ (again we leave the details to Appendix D) we obtain

$$Q(z)_r = \frac{\sin(\gamma\pi)}{\pi} \frac{C_\gamma(z)C_{-1+\gamma}(1-z) + C_{-1+\gamma}(z)C_\gamma(1-z)}{C_\gamma(z)^2 + 2C_\gamma(z)C_\gamma(1-z)\cos(\gamma\pi) + C_\gamma(1-z)^2}, \quad 0 < \gamma < 1 \tag{6.34}$$

with $z = T_+/t$ and $C_\beta(z)$ is given by

$$C_\beta(z) \;=\; \int_0^z f(u)(z-u)^\beta du = z^{\beta+1}\int_0^1 f(zv)(1-v)^\beta dv. \tag{6.35}$$

Eqs. (6.34) and (6.35) are the fifth result of this chapter. Notably, this is the limiting PDF for T_+/t under resetting times sampled from a PDF with a tail that decays as $t^{-1-\gamma}$

with $0 < \gamma < 1$. This expression establishes a link between the characteristic function of T_+ under a resetting with the limiting PDF of T_+ assuming that the resetting PDF decays as $t^{-1-\gamma}$ for $0 < \gamma < 1$ as $t \to \infty$, regardless of the other details and structure of the resetting PDF or the specific random walk. It is a general expression that holds for any underlying isotropic random walk, and can be explicitly found if the limiting PDF of T_+/t without resetting is known. It is important to stress that Eq. (6.34) holds when the resetting time PDF decays as a power law with an exponent such that all moments are divergent, that is, for $\gamma < 1$. For $\gamma \geq 1$, the resetting times PDF has the first moment finite and, as we have shown above, the limiting PDF is not given by (6.34) but by (6.19). It is also worth pointing out that we have derived this result by using the scaling solution of the reset-free process, which is $\lim_{t\to\infty} Q(Z,t|x_0)_0 = f(Z/t)/t$; therefore, Eq. (6.34) also holds for any other functional that has the same scaling as T_+.

In the next pages, we will analyze the shape of the limiting PDF $Q(z)_r$ in terms of the exponent γ and other parameters related to the underlying random walk. As we show below, the limiting PDF $Q(z)_r$ may have a $\cup$ shape, a W shape, or a $\cap$ shape, depending on the values of γ. The transition from the $\cup$ shape to the W shape depends on the existence of a maximum at $T_+ = t/2$ ($z = 1/2$), while the transition from the W shape to the $\cap$ shape depends on the behavior when T_+ is close to 0 ($z \to 0^+$) and when T_+ is close to t ($z \to 1^-$). To get the equation for the value of γ for which $Q(z)_r$ has a local maximum at $z = 1/2$ we compute $(d^2Q(z)_r/dz^2)_{z=1/2} = 0$ using (6.34) and find

$$\begin{aligned} C_\gamma\left(\frac{1}{2}\right)C''_{\gamma-1}\left(\frac{1}{2}\right) &- C''_\gamma\left(\frac{1}{2}\right)C_{\gamma-1}\left(\frac{1}{2}\right) - 2C'_\gamma\left(\frac{1}{2}\right)C'_{\gamma-1}\left(\frac{1}{2}\right) \\ &= 2\frac{C_{\gamma-1}\left(\frac{1}{2}\right)C'_\gamma\left(\frac{1}{2}\right)}{C_\gamma\left(\frac{1}{2}\right)}\tan^2\left(\frac{\gamma\pi}{2}\right) \end{aligned} \tag{6.36}$$

where the primes stand for derivatives with respect to z. This equation has to be numerically solved once the analytic expression for $C_\beta(z)$ is calculated from (6.35). In what follows, we apply the previous general results to a Brownian walker and to a subdiffusive CTRW walker.

A Brownian walker

If, for example, the underlying random walk is a Brownian motion, then the limiting PDF of T_+/t without resetting obeys the Lévy arcsine law [138], Eq. (2.35), which reads

$$f(u) = \frac{1}{\pi\sqrt{u(1-u)}}$$

if $0 < u < 1$ and from (6.35) with (2.35) we obtain

$$C_\beta(z) = \frac{\Gamma(1+\beta)}{\sqrt{\pi}\Gamma\left(\frac{3}{2}+\beta\right)}z^{\frac{1}{2}+\beta}{}_2F_1\left(\frac{1}{2},\frac{1}{2};\frac{3}{2}+\beta;z\right), \tag{6.37}$$

where ${}_2F_1(\cdot)$ is the Gauss's hypergeometric function. In the limit $u \to 0$, $f(u) \sim u^{-1/2}$ and from (6.37) we see that $C_\beta(z) \sim z^{\beta+1/2}$ as $z \to 0$. Hence, from (6.34)

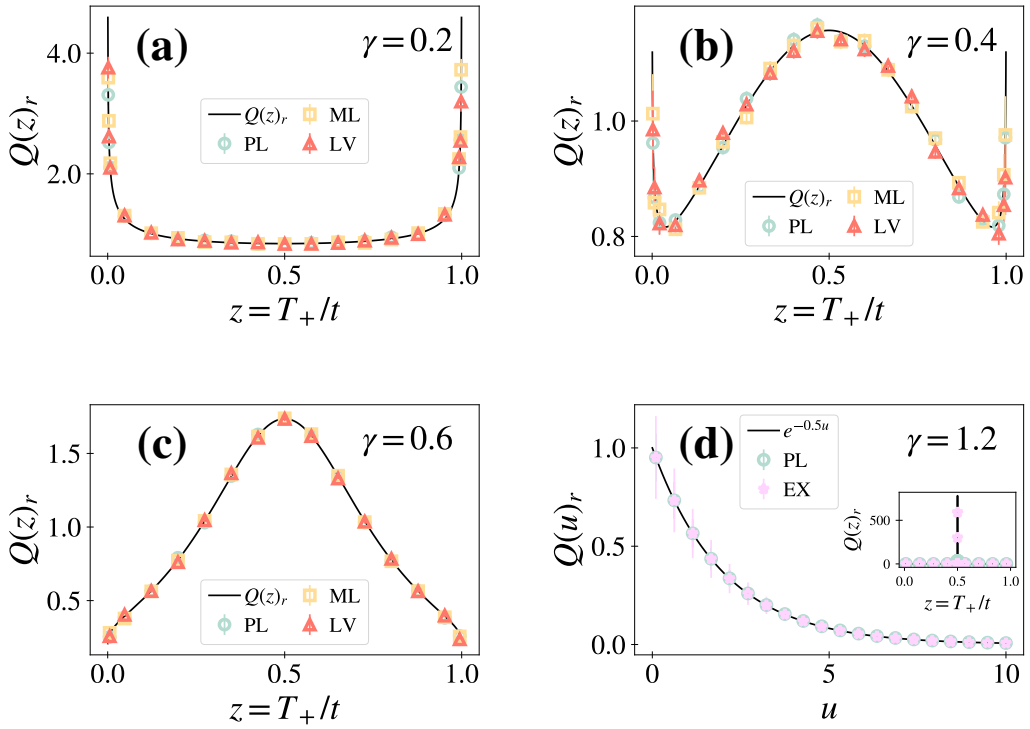


Figure 6.4: **Limiting PDF of the half occupation time of a Brownian motion with resetting for a variety of resetting distributions.** All symbols are obtained from simulations with different resetting PDFs: power-law (PL) in circles with $t_0 = 1$; Mittag-Leffler (ML) in squares; Lévy (LV) in triangles; and exponential (EX) in stars with $\langle t \rangle_R = t_0 \gamma (\gamma - 1)^{-1}$. In panels (a), (b), and (c) the solid black line represents Eq. (6.34) with the $C_\beta(z)$ coefficients obtained from Eq. (6.37). In panel (d) we present the Laplace transform of Eq. (6.33) $Q(u)_r = \mathscr{L}_{z\to u}[Q(z)_r]$. In the inset of panel (d) it is plotted in z space. For all simulations the parameters used are: $x_0 = 0$, $D = 1$, and parameter of the resetting distribution, $\gamma = 0.2, 0.4, 0.6$ and 1.2 for panels (a), (b), (c), and (d) respectively. All simulations are run for $N = 10^5$ particles for a total simulation time of $t = 10^7$ with a time discretization of $dt = 0.1$.

$$\begin{aligned} Q(z)_r &\sim z^{\gamma-1/2}, \quad z \to 0^+ \\ Q(z)_r &\sim (1-z)^{\gamma-1/2}, \quad z \to 1^-. \end{aligned} \tag{6.38}$$

From Eq. (6.38) we see that for $\gamma > 1/2$ the most unlikely values of T_+ are 0 and t, which are given with vanishing probability. In this case, due to the symmetry of the random walk, the most likely value is $T_+ = t/2$, thus giving rise to a $\cap$ shape limiting PDF. Recall that the limiting PDF for the case without resetting is the Lévy's arcsine law Eq. (2.35), where the most probable values of T_+ are 0 and t, implying that a walker is mostly in the positive or negative domain for its entire trajectory. Thus, we see that a sufficiently frequent resetting ($\gamma > 1/2$) dominates the behavior, inducing the walker to spend an equal amount of time in the domain $x > 0$ and $x < 0$, in the long-time limit.

When $\gamma < 1/2$, the resetting is less frequent, and the probability of T_+ at 0 and t does not vanish anymore. In this case, the resetting is not frequent enough to dominate the behavior of the walker. In this regime, we can distinguish two possibilities: for a given value of γ, say γ_c, if $0 < \gamma < \gamma_c$, the limiting PDF has a $\cup$ shape, as in the case without resetting, and the most likely values are $T_+ = 0$ or $T_+ = t$. On the other hand, if $\gamma_c < \gamma < 1/2$, the limiting PDF has the W shape and the most likely values are $T_+ = 0$, $T_+ = t$, and $T_+ = t/2$, as a transition between $\cup$ and $\cap$ shapes. The value of γ_c can be found by solving Eq. (6.36) with (6.37). The resulting nonlinear equation for γ has to be numerically solved. Its solution yields $\gamma_c = 0.269$.

These results are in agreement with what we found in [8] for the occupation time in the interval $[-a, a]$ for a Brownian walker with power-law resetting, where we also found a transition in the ergodic behavior for $\gamma = 1/2$. This transition is due to the competition between the time scale of the resetting and the time scale of the diffusion. The exponent $\gamma = 1/2$ matches that of the first-passage time of a Brownian walker on a line in the absence of resetting $\sim t^{-(1+1/2)}$, Eq. (2.18). In other words, when the resetting is more frequent than the first-passage time of the walker to the origin, then the resetting dominates the behavior and induces a $\cap$ shape limiting PDF. On the other hand, when the resetting is less frequent than the first-passage time of the walker to the origin, then the behavior of the walker is not dominated by resetting, and trajectories spend most of the time either in the positive or negative domain, giving rise to a $\cup$ shape limiting PDF. In the intermediate regime, where the resetting is less frequent than the first-passage time of the walker to the origin but still frequent enough to induce a local maximum at $T_+ = t/2$, gives rise to a W shape PDF as a transition between the $\cup$ and $\cap$ shapes.

In Fig. 6.4 we compare Eq. (6.34) with (6.37) against simulations for three different resetting-time PDFs that decay in time as $t^{-1-\gamma}$ in the long-time limit: power-law (PL) $\phi(t) = \gamma t_0^{\gamma} t^{-1-\gamma}, \quad t > t_0$ and 0 otherwise, $t_0 = 1$; Mittag-Leffler (ML) $\phi(t) = t^{\gamma-1}\tau^{-\gamma}E_{\gamma,\gamma}(-t^{\gamma}\tau^{-\gamma})$ with $E_{\gamma,\beta}(\cdot)$ the two-parametric Mittag-Leffler function [224, 234], $\tau = |\Gamma(1-\gamma)|^{1/\gamma}$; and Lévy (LV), where $\phi(t) = l_{\gamma}(t)$ is the one-sided Lévy stable distribution [235, 236]. As can be seen, the limiting PDF (6.34) agrees with all three cases. This confirms that the limiting PDF depends only on the tail of the resetting times PDF, and not on the particular form of the distribution. In addition, we have included the case of exponentially distributed resetting time together with the power-law PDF

with $\gamma > 1$ (panel (d)), where again we have performed a Laplace transform of the numerical data to better visualize the results. In both cases, the resetting times PDF has a finite first moment, and the limiting PDF under resetting fits Eq. (6.20).

B Subdiffusive walker

When the underlying random walker performs a subdiffusive motion, then the limiting PDF of T_+ in the absence of resetting is given by the Lamperti distribution [139], Eq. (2.37), which reads

$$f(u) = \frac{\sin(\alpha\pi/2)}{\pi} \frac{[u(1-u)]^{\frac{\alpha}{2}-1}}{u^\alpha + (1-u)^\alpha + 2[u(1-u)]^{\frac{\alpha}{2}}\cos(\alpha\pi/2)}.$$

Note that α is the tail exponent of the waiting-time PDF (decaying as $t^{-1-\alpha}$ with $0 < \alpha < 1$). The integral in Eq. (6.35) cannot be done analytically and must be evaluated numerically, but the asymptotics of (6.34) near $z = 0, 1$ can be obtained, in terms of the resetting exponent γ and the CTRW exponent α. Since the Lamperti law (2.37) behaves as $f(u) \sim u^{\alpha/2-1}$ for $u \to 0$, from (6.35) one gets $C_\beta(z) \sim z^{\beta+\alpha/2}$. Hence,

$$\begin{aligned} Q(z)_r &\sim z^{\gamma+\frac{\alpha}{2}-1}, \quad z \to 0^+ \\ Q(z)_r &\sim (1-z)^{\gamma+\frac{\alpha}{2}-1}, \quad z \to 1^- \end{aligned} \tag{6.39}$$

We again find a transition between a $\cup$, $\cap$, and W shapes, but now the transition between the $\cup$ and W shapes depends on both γ and α. If $0 < \gamma < \gamma_c$ the PDF $Q(z)_r$ has the $\cup$ shape, if $\gamma_c < \gamma < \gamma^*$ it has the shape W where $\gamma^* = 1 - \alpha/2$, and for $\gamma^* < \gamma < 1$ it has the $\cap$ shape. The transition between W and $\cup$ shapes is attained at $\gamma = \gamma_c$, which has to be found as in the previous example. The transition at $\gamma^* = 1 - \alpha/2$ can be understood in terms of the first-passage time of the walker to reach the origin. If the FPT has a diverging mean, the walker stays either at $x > 0$ or $x < 0$, and therefore the limiting PDF of T_+ is non-vanishing at 0 and t ($\cup$ or W shapes). On the other hand, when the mean of the FPT is finite, the walker crosses the origin at a finite time, then the probability of the limiting PDF of T_+ vanishes at 0 and t, i.e., it has a maximum ($\cap$ shape). The transition between a finite and diverging mean for a CTRW with resets is known [105] and is precisely at $\gamma = 1 - \alpha/2$. We have applied the same reasoning in the previous section, for the case of the diffusive walker, as in that case $\alpha = 1$. In Ref. [232] the authors find a transition at $\gamma = 1 - \alpha/2$ for the propagator of a subdiffusive walker under a power-law resetting to the initial condition. For sufficiently long times, they find that the propagator changes from being flat near the origin for $\gamma < 1 - \alpha/2$ to having a sharp peak at $x = 0$ with a heavy-tailed decay for larger x. This indicates that resets are frequent enough to create strong localization around the reset point $x = 0$, while still allowing significant excursions away from it. The resulting profile has no characteristic scale, reflecting the interplay between the underlying random walk and the reset dynamics, in agreement with the transition observed in the limiting PDF of the half occupation time. This same reasoning can be applied to the case in the previous section of a Brownian walker with power-law resetting, since we have observed a similar transition at $\gamma = 1/2$ for the infinite densities of the process [8].

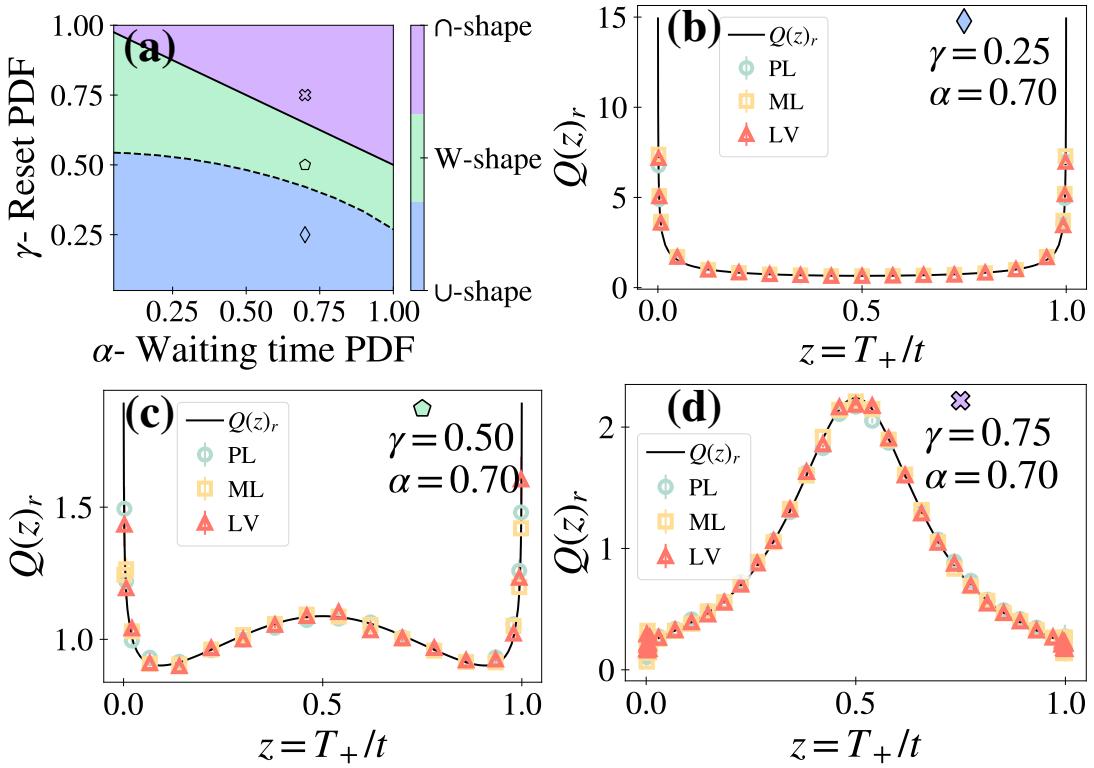


Figure 6.5: **Limiting PDF of the half occupation time of a CTRW with resetting for a variety of resetting distributions.** (a) Phase diagram of the limiting PDF of T_+ of a subdiffusive walker with resetting of exponent γ. The dashed line represents γ_c and the solid line represents $\gamma^* = 1-\alpha/2$. The black symbols mark the corresponding (α,γ) points represented in panels (b), (c), and (d). (b), (c), and (d) limiting PDF of T_+ for a subdiffusive walker with different resetting PDFs: power-law (PL) in circles with $t_0 = 1$; Mittag-Leffler (ML) in squares; Lévy (LV) in triangles. The symbols are obtained from simulations of a CTRW with $\sigma = 0.01$. The black lines are computed by numerical integration of Eq. (6.35) with the $C_\beta(z)$ coefficients obtained from Eq. (2.37). For all simulations, the parameters of the resetting distribution are $\gamma = 0.25, 0.5$, and 0.75 for panels (b), (c), and (d), respectively. The parameters of the waiting time PDF for all cases are $t_{\alpha,0} = 1$, and $\alpha = 0.7$. All simulations are run for $N = 10^5$ particles for a total simulation time of $t = 10^7$, and initial condition $x_0 = 0$.

In Fig. 6.5(a) we present the phase diagram for the shapes of $Q(z)_r$ in terms of the exponents γ and α. We also present the dependence of the curves γ^* and γ_c. In the same figure panels (b), (c), and (d) we show a comparison between the curves obtained by numerically integrating Eq. (6.35) with the $C_\beta(z)$ coefficients obtained from Eq. (2.37) and numerical simulations of the CTRW. In the figure, we show an example for the three different cases: $\cup$ shape, W shape, and $\cap$ shape. In all three cases, we obtain a very good agreement for three resetting distributions: power-law, Mittag-Leffler, and Lévy. This again confirms that the limiting PDF only depends on the tail of the resetting times PDF, also for the subdiffusive case. We want to stress that fine numerical precision is needed, especially as $z \to 0, 1$, to numerically integrate the limiting PDF. This is particularly relevant near the transition values of γ_c and γ^*.

This behavior under resetting is reminiscent of the effects seen when a confining potential is present. Resetting the walker's position to the origin has certain similarities with the presence of a confining potential centered at this point [113, 237]. Both mechanisms can give rise to a non-equilibrium steady state, a finite mean first-passage time -depending on the properties of the resetting times PDF and the underlying random walk [115]. They also share some statistical properties of certain stochastic functionals. For example, as we have seen above, the limiting PDF of T_+ has the $\cup$ shape depending on the value of γ. The same happens when the random walker moves in the presence of a force field [134]. The similarity, however, does not extend to the W shape or $\cap$ shape, which do not appear under a confining potential. Nevertheless, the transition between the shapes $\cup$ and W has also been found when a subdiffusive particle moves in a finite symmetric interval [122] or when a Brownian particle moves in a heterogeneous medium [70].

6.6 Summary of results

In this chapter, we have studied the properties of generic functionals of the trajectory of a random walk under general resetting. We have written an equation for the characteristic function of a functional Z under resetting in terms of the characteristic function of Z without resetting and the PDF of resetting times. Next, we have found that if the PDF has finite moments, the limiting PDF of Z under resetting is a delta function centered at its mean value, which means that the functional is ergodic. For power-law resetting distributions, we have found the scaling with time of the first and second moments of any functional in terms of the exponent of the scaling of the process without resetting and the exponent of the resetting PDF. We have applied these results to the case of the half occupation time T_+ for a Brownian walker and a subdiffusive CTRW walker. We have found its first and second moments, and the EB parameter, which shows that the process is non-ergodic for $\gamma < 1$ and ergodic for $\gamma > 1$, relaxing the condition to only the first moment of the resetting times PDF being finite for the functional to be ergodic. Finally, we have found the limiting PDF of T_+ under resetting in terms of the limiting PDF of T_+/t without resetting. We have found that the shape of the limiting PDF under resetting can be $\cup$, W, or $\cap$ depending on the value of the resetting exponent γ. We have also found the transition values of γ for which the shape changes. These scaling results are general and hold for any functional with a scaling solution of the form $Q(Z,t|x_0)_0 = f(Z/t)/t$ and any underlying isotropic random walk.

7

OCCUPATION TIMES IN HETEROGENEOUS MEDIA

In this chapter, we study the ergodic properties of Brownian motion in heterogeneous media through its occupation-time statistics. Using the Feynman-Kac formalism, we obtain analytical expressions for the distributions, moments, and ergodicity-breaking parameters of the half occupation time and the occupation time in an interval for two classes of space-dependent diffusivity: a piecewise-constant profile and a power-law profile. For the power-law profile, we identify a transition from non-ergodic to ergodic behavior as the heterogeneity exponent is varied.

7.1 Introduction . . . 125
7.2 Generating function and $D(x)$ . . . 126
7.3 Half occupation time . . . 128
7.3.1 Piecewise heterogeneity . . . 128
7.3.2 Power law heterogeneity . . . 131
7.4 Occupation time in an interval . . . 134
7.4.1 Piecewise heterogeneity . . . 135
7.4.2 Power law heterogeneity . . . 136
7.5 Summary of results . . . 139

7.1 Introduction

In the previous chapters we studied how non-Markovianity and general resetting protocols modify the statistical and ergodic properties of stochastic functionals, in particular residence-time functionals. In this chapter, we study a different source of

complexity: spatial heterogeneity in the underlying medium. Such situations arise in a broad range of systems, including transport in porous materials, colloidal suspensions, intracellular media, confined geometries, and nanoporous solids [74, 210, 238, 239]. In these settings, spatial variations of the diffusion coefficient have been directly observed, particularly through single-particle tracking experiments [21, 64, 67, 209, 219, 240, 241], and have been reported, for instance, for protein motion in the cell cytoplasm [83, 211].

Models with space-dependent diffusion coefficients have been used to describe Richardson diffusion in turbulence, transport in disordered porous media, and diffusion on random fractal structures [51, 72, 73]. They are known to produce phenomena like non-Gaussian propagators, anomalous mean-squared-displacement scaling, and weak ergodicity breaking between ensemble- and time-averaged MSDs [67, 71, 219, 242]. Following the analysis on occupation-time statistics developed in the previous chapters, we use these observables to characterize diffusion in heterogeneous media. They provide a direct measure of how the particle explores different regions of space and therefore probe ergodic properties beyond MSD-based analysis.

By means of the Feynman-Kac formalism, we derive exact and asymptotic results for their distributions, moments, and ergodicity-breaking parameter in two representative models with space-dependent diffusion coefficient: a piecewise-constant profile and a power-law profile, as introduced in Chapter 2. These results show how spatial heterogeneity alone modifies occupation-time statistics and can induce nontrivial ergodic behavior.

The chapter is organized as follows. In Sec. 7.2, we introduce the Feynman-Kac equation for a Brownian functional with space-dependent diffusivity and the two heterogeneous models considered. Sections 7.3 and 7.4 contain the results for the half occupation time and the occupation time in an interval, respectively. We summarize our findings in Sec. 7.5.

7.2 Generating function and $D(x)$

Consider again the stochastic functional as defined in Eq. (2.31) $Z(t|x_0) = \int_0^t U[x(\tau)]d\tau$ with $U[x(\tau)]$ a positive function of the stochastic trajectory that starts at x_0. Again, let $Q(Z,t|x_0)$ be the PDF of the functional $Z(t)$ and $Q(p,t|x_0)$ its Laplace transform in Z. Moreover, also consider the Laplace transform conjugate to time as

$$Q(p,s|x_0) = \mathscr{L}_{t\to s}[Q(p,t|x_0)] = \int_0^\infty dt\ e^{-st} Q(p,t|x_0). \tag{7.1}$$

Again, the moments of $Z(t|x_0)$ can be obtained from the derivatives of $Q(p,s|x_0)$ in a systematic manner as

$$\langle Z(s|x_0)^n \rangle = (-1)^n \frac{\partial^n Q(p,s|x_0)}{\partial p^n}\bigg|_{p=0}. \tag{7.2}$$

With the above considerations, we can proceed to derive the generating function for the stochastic functional $Q(p,s|x_0)$, which depends on the details of the underlying

random walk and the specific functional form of $U(x)$. Let $x(t)$ be the position of a Brownian particle moving in a one-dimensional heterogeneous medium, evolving according to the overdamped Langevin equation, Eq. (2.5) with a space dependent coefficient, namely $D(x)$ and $\xi(t)$ a Gaussian white noise with zero mean and autocorrelation $\langle \xi(t)\xi(t')\rangle = \delta(t-t')$. Since in this case we have an space dependence in the noise, in order to proceed we need to specify which stochastic interpretation to use, in this case we adopt the Itô interpretation [243]. Thus, the Langevin equation for the particle's position reads

$$\frac{dx(t)}{dt} = \sqrt{2D(x)}\xi(t) \tag{7.3}$$

When the particle's position evolves according to (7.3), the generating function $Q(p,s|x_0)$ of the functional (2.31) obeys the backward Feynman-Kac equation [244], Eq. (2.32), which in the case of a space-dependent diffusion coefficient reads

$$\frac{\partial Q(p,t|x_0)}{\partial t} = D(x_0)\frac{\partial^2 Q(p,t|x_0)}{\partial x_0^2} - pU(x_0)Q(p,t|x_0). \tag{7.4}$$

Thus, for each explicit expression of $U(x)$, we need to solve Eq. (7.4) for the generating function using suitable boundary conditions, and then use Eq. (7.2) to derive the moments. To do this we need also to specify the explicit expressions for $D(x)$. First we assume the power law dependence [66, 67, 68, 69, 70, 71]

$$D(x) = D_0|x|^\alpha, \quad \alpha < 2, \tag{7.5}$$

As introduced in Sec. 2.1 this model yields subdiffusion for $\alpha < 0$, normal diffusion for $\alpha = 0$, or superdiffusion for $\alpha > 0$. We note that with this dependence, the diffusion coefficient becomes singular at $x = 0$, therefore, in simulations, we need to regularize the diffusion coefficient by considering

$$D(x) = \begin{cases} D_0(|x|^\alpha + \varepsilon), & \alpha > 0 \\ \frac{D_0}{|x|^{-\alpha}+\varepsilon}, & \alpha < 0 \end{cases}$$

with $\varepsilon \ll 1$ to prevent the particles from trapping or divergences at $x = 0$ [22, 219]. Another relevant choice for the spatial dependence of the diffusion coefficient is the piecewise constant spatial form [85, 86, 87]

$$D(x) = \begin{cases} D_-, & x < 0 \\ D_+, & x > 0 \end{cases} \tag{7.6}$$

with $D_\pm > 0$. Once we have introduced the models, we can proceed to solve the Feynman-Kac equation for the two occupation observables of interest: the half occupation time and the occupation time in an interval.

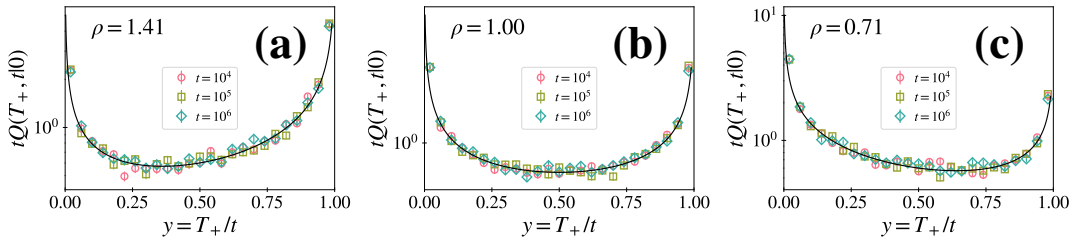


Figure 7.1: **Limiting distribution of the half occupation time for the piecewise heterogeneity.** The different symbols are for trajectories with $t = 10^4, 10^5$, and 10^6. The black solid line corresponds to Eq. (7.10). $D_+ = 0.5, 1.0$, and 2.0 in panels (a), (b), and (c), respectively. In all panels $D_- = 1.0$, $x_0 = 0$, simulation timestep $dt = 0.1$, and $N = 10^4$ trajectories.

7.3 Half occupation time

We consider the occupation time $T_+(t|x_0)$ of the particle above the origin within a time window of size t if it was at $x = x_0$ at $t = 0$, as defined in Eq. (2.34), so that $U(x_0) = \Theta(x_0)$. Performing the Laplace transform of (7.4) with respect to t, the Feynman-Kac equation for the characteristic function $Q(p,s|x_0)$ reads

$$sQ(p,s|x_0) - 1 = D(x_0)\frac{\partial^2 Q(p,s|x_0)}{\partial x_0^2} - p\Theta(x_0)Q(p,s|x_0). \tag{7.7}$$

which has to be solved with the appropriate boundary conditions [129]. If the starting point $x_0 \to +\infty$ the particle will stay on the positive side with $x(t) > 0$ for all finite t implying $T^+(t|x_0 \to +\infty) = t$ and accordingly $Q(T_+,t|x_0 \to +\infty) = \delta(T_+ - t)$, On the other hand, if the starting point $x_0 \to -\infty$ the particle will never reach the positive side and it will stay on the negative half-space implying $T^+(t|x_0 \to -\infty) = 0$ and hence $Q(T_+,t|x_0 \to -\infty) = \delta(T_+)$. In Appendix E we sketch the main steps of the derivation for the different shapes of the diffusion coefficient $D(x)$.

7.3.1 Piecewise heterogeneity

For the piecewise diffusion coefficient (7.6) the solution to (7.7) yields, after inverting the Laplace transforms, the *asymmetric arcsine* PDF

$$Q(T_+,t|0) = \frac{1}{t}F\left(\frac{T_+}{t}\right) = \frac{1}{t}\frac{\rho}{\pi\sqrt{\frac{T_+}{t}\left(1-\frac{T_+}{t}\right)}\left[\frac{T_+}{t} + \rho^2\left(1-\frac{T_+}{t}\right)\right]} \tag{7.8}$$

where

$$\rho = \sqrt{\frac{D_-}{D_+}}, \tag{7.9}$$

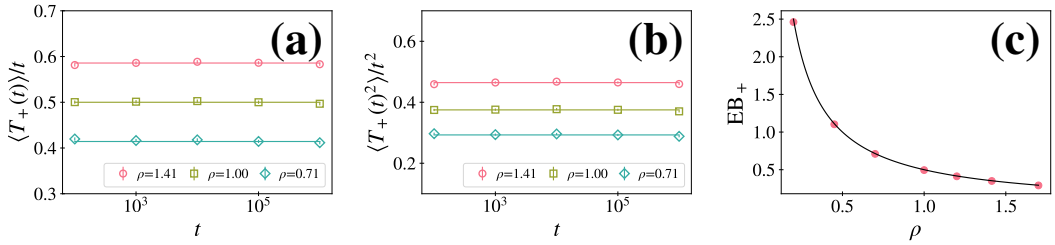


Figure 7.2: **Moments and EB parameter of the half occupation time for the piecewise heterogeneity.** (a) $\langle T^+(t)\rangle$, (b) $\langle T^+(t)^2\rangle$, and (c) EB$_+$. In panels (a), and (b) the solid lines are computed with Eq. (7.12), $D_+ = 0.5, 1.0$, and 2.0; In panel (c) the solid line is Eq. (7.13). In all panels $D_- = 1.0$, $x_0 = 0$, simulation timestep $dt = 0.1$, and $N = 10^4$ trajectories.

can be regarded as the asymmetry parameter. We can write Eq. (7.8) in terms of $y = T_+/t$ to get

$$Q(y|0) = \frac{\rho}{\pi\sqrt{y(1-y)}\,[y+\rho^2(1-y)]} = F(y), \quad 0 < y < 1. \tag{7.10}$$

which is the first result of this chapter. The same limiting distribution has been obtained for a random walk in one dimension under an asymmetric force field acting on a finite region [134]. Although there is no general direct correspondence, this agreement can be understood physically from the fact that, in both problems, the long-time occupation statistics are governed by recurrent returns to the interface separating two dynamically asymmetric regions. In the present case the asymmetry is not produced by a force field but by the different diffusion constants: excursions in the slower region last longer, so the occupation fraction is biased toward that side, with the bias controlled by $\rho = \sqrt{D_-/D_+}$. In Fig. 7.1 we test the result from Eq. (7.10) against numerical simulations. We see that for sufficiently large values of t, $tQ(T_+,t|0)$ converges to the limiting distribution $F(y)$.

For this distribution, unlike for the arcsine case, the minimum of $F(y)$ is not located at $y = 1/2$, as can also be observed in Fig. 7.1. We can find it by computing the derivatives of $F(y)$. We find that it is located at

$$y_{min} = \frac{5\rho^2 - 3 - \sqrt{9\rho^4 - 14\rho^2 + 9}}{8(\rho^2 - 1)}. \tag{7.11}$$

From this expression and also from Fig. 7.1, we see that if $\rho > 1$ then y_{min} moves to the left while if $\rho < 1$ it moves to the right. Meaning that for $\rho < 1$, that is, when $D_+ > D_-$, the particle spends more time on the negative side, while for $\rho > 1$, the particle spends more time on the positive side. This is expected since the particle moves more slowly in the region with a smaller diffusion coefficient, therefore it tends to spend more time there. For $\rho = 1$ the minimum is located at $y_{min} = 1/2$, and the distribution reduces to the *arcsine law* [138], with no distinction between the two sides. The first two moments of $Q(T_+,t|0)$ can be found from (7.2) with $Q(p,s|0)$ as given in (E.3) or from (7.10). In any case we find

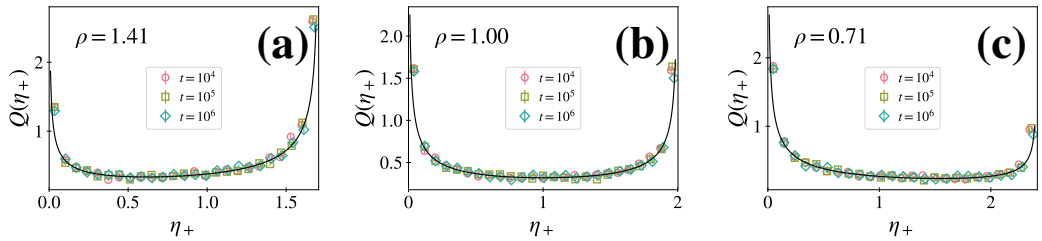


Figure 7.3: **PDF of the time averaged half occupation time for the piecewise heterogeneity.** The different symbols are for trajectories with $t = 10^4, 10^5$, and 10^6. $D_+ = 0.5, 1.0$, and 2.0 in panels (a), (b), and (c), respectively. The solid line is computed with Eq. (7.15) In all panels $D_- = 1.0$, $x_0 = 0$, simulation timestep $dt = 0.1$, and $N = 10^4$ trajectories.

$$\langle T^+(t)\rangle = \frac{\rho}{\rho+1}t, \quad \langle T^+(t)^2\rangle = \frac{\rho(1+2\rho)}{2(\rho+1)^2}t^2. \tag{7.12}$$

Note first that $\langle T^+(t)\rangle > t/2$ (the time spent at $x > 0$) is on average higher than half of the total time if $\rho > 1$, that is, if $D_- > D_+$. This is expected since, as discussed above, in this case the motion of the particle is slower in the region $x > 0$ than in the region $x < 0$. Note also that the coefficient $\rho/(1+\rho)$ in Eq. (7.12) corresponds to the probability that the particle is at $x > 0$. If $D_- = D_+$ one has $\rho = 1$ and the two moments (7.12) reduce to the values corresponding to the BM in a homogeneous medium. Now, we are in a position to compute the ergodicity breaking parameter. From (2.54) and (7.12) we finally find

$$\mathrm{EB}_+ = \frac{\langle T^+(t)^2\rangle}{\langle T^+(t)\rangle^2} - 1 = \frac{1}{2\rho}, \tag{7.13}$$

which predicts a non-ergodic behavior regardless of the values of ρ. Eq. (7.13) together with (7.12), represents the second result of this chapter. We find that the EB_+ parameter increases with decreasing ρ, that is, with increasing D_+ in comparison to D_-. This is expected since the particle moves faster in the region $x > 0$ when D_+ is greater than D_-, therefore it tends to spend less time there, and thus the fluctuations of the time spent at $x > 0$ are greater. Note that $\mathrm{EB}_+ \to 0$ as $\rho \to \infty$, this is, when $D_- \gg D_+$ and the particle is effectively trapped at $x > 0$ for all times, therefore $T_+(t) = t$ for all trajectories and the fluctuations of T_+ vanish for the half occupation time (note that regarding any other observable one still might see ergodicity breaking in this limit). In Fig. 7.2 we compare (7.12) and (7.13) with numerical simulations. The greater D_- is in comparison to D_+, the greater ρ is, therefore the probability that the particle is at $x > 0$ increases, and thus the time spent there also is greater. This is captured by EB_+, which decreases with ρ as expected.

Finally, we can compute the PDF of the time average of the observable $\Theta[x(t)]$, this is, the PDF of the time averaged occupation fraction

$$\eta_+ = \lim_{t\to\infty} \frac{T^+}{\langle T^+(t)\rangle} \tag{7.14}$$

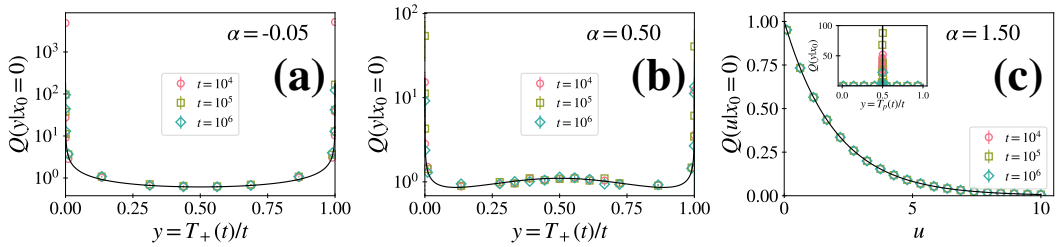


Figure 7.4: **Limiting distribution of the half occupation time for the power-law heterogeneity.** The different symbols are for trajectories with $t = 10^4, 10^5$, and 10^6. In panels (a), and (b) the black solid line corresponds to Eq. (7.16); In panel (c) corresponds to $e^{-0.5u}$, and to $\delta(t-0.5)$ in its inset. $\alpha = -0.05, 0.5$, and 1.5 in panels (a), (b), and (c), respectively. If $\alpha > 0$ $\varepsilon = 10^{-10}$, and $\varepsilon = 10^{-3}$ if $\alpha < 0$. In all panels $D_0 = 1.0$, $x_0 = 0$, simulation timestep $dt = 0.1$, and $N = 10^4$ trajectories.

as defined in Eq. (2.57). It can be obtained from the limiting distribution $Q(y|0)$ by simply accounting for the relation between the variables y and η_+. We find from (7.10) the density

$$Q(\eta_+) = \frac{\rho}{\rho+1} Q\left(\frac{\rho}{\rho+1}\eta_+\right) = \frac{\rho}{\pi(\rho+\eta_+-\rho\eta_+)\sqrt{\rho\eta_+(1+\rho-\rho\eta_+)}} \tag{7.15}$$

where $0 < \eta_+ < (\rho+1)/\rho$. In Fig. 7.3 we compare Eq. (7.15) with numeric simulations.

7.3.2 Power law heterogeneity

For the power-law diffusion coefficient (7.5) the solution to (7.7) yields, after inverting the Laplace transforms, the PDF for $y = T_+/t$ reads

$$Q(y|0) = \frac{\sin\left(\frac{\pi}{2-\alpha}\right)}{\pi} \frac{[y(1-y)]^{\frac{1}{2-\alpha}-1}}{y^{\frac{2}{2-\alpha}} + (1-y)^{\frac{2}{2-\alpha}} + 2\cos\left(\frac{\pi}{2-\alpha}\right)[y(1-y)]^{\frac{1}{2-\alpha}}} \tag{7.16}$$

for $0 < y < 1$. Note that Eq. (7.16) is the Lamperti PDF, Eq. (2.37), with index $2/(2-\alpha)$ which has been obtained in Refs [122, 139] for a particle moving subdiffusively, and which we found for the half occupation time of the subdiffusive CTRW in Chapter 5. When $\alpha \to 1^-$ we get

$$Q(y|0) = \delta\left(y - \frac{1}{2}\right), \tag{7.17}$$

meaning that when $\alpha \to 1^-$, the half occupation time is always $t/2$, coinciding with its mean value, as shown below. Both Eq. (7.16) and (7.17) have been found in [70] for the power-law heterogeneity by other means, but we included them here for completeness. However, the ergodic properties have not been explored in [70]. First note that Eq. (7.16) holds both when the underlying random walk is subdiffusive ($\alpha < 0$) or superdiffusive ($0 < \alpha < 1$). Note also that in the limit $\alpha \to 0$ (homogeneous case) Eq. (7.16) reduces to the arcsine law. Moreover, it can be shown that Eq. (7.16)

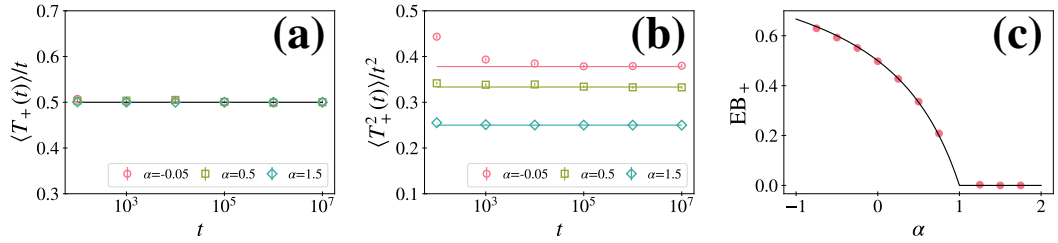


Figure 7.5: **Moments and EB parameter of the half occupation time for the power-law heterogeneity.** (a) $\langle T^+(t)\rangle$, (b) $\langle T^+(t)^2\rangle$, and (c) EB$_+$. In panels (a), and (b) the solid lines are computed with Eq. (7.19) and $\alpha = -0.05, 0.5$, and 1.5; In panel (c) the solid line is Eq. (7.20). If $\alpha > 0$ $\varepsilon = 10^{-10}$, and $\varepsilon = 10^{-3}$ if $\alpha < 0$. In all panels $D_0 = 1.0$, $x_0 = 0$, simulation timestep $dt = 0.1$, and $N = 10^4$ trajectories.

possesses a local maximum at $y = 1/2$ when the heterogeneity is strong enough, that is, when the exponent α is high enough. The heterogeneity introduced through the spatial dependence given in Eq. (7.5) induces the particle to move in a region close to the origin, where the diffusion coefficient attains its minimum value. As α increases, this region shrinks. This effect prevents the particle from performing excursions of long duration and forces the particle to revisit the origin more frequently. Thus, if $\alpha > \alpha_c$ a maximum of $Q(y|0)$ appears at $y = 1/2$ ($T_+ = t/2$). When $\alpha < \alpha_c$ this peak disappears and $Q(y|0)$ attains a $\cup$ shape, indicating that the particle spends almost its entire time in one side ($x < 0$ or $x > 0$) only.

To find α_c we impose that at $y = 1/2$ the first derivative of $Q(y|0)$ with respect to y vanish for the PDF given in Eq. (7.16). Thus, α_c is the solution to the nonlinear equation

$$\cos\left(\frac{\pi}{2-\alpha_c}\right) = \frac{4\alpha_c - 2 - \alpha_c^2}{(2-\alpha_c)^2} \tag{7.18}$$

whose numerical solution is $\alpha_c \simeq 0.318$, in agreement with the results in [70]. It is easy to show that $Q(y|0) \sim y^{-\frac{1-\alpha}{2-\alpha}}$ and

$$Q(y|0) \sim (1-y)^{-\frac{1-\alpha}{2-\alpha}}$$

when y is close to 0 and 1, respectively. Then, $Q(y|0)$ diverges at $y = 0$ and at $y = 1$. Consequently, (7.16) has two possible shapes, a $\cup$ shape if $\alpha < 0.318$ or a W shape if $\alpha > 0.318$; both cases are shown in Fig. 7.4 (panels (a) and (b)). If $\alpha \to 1^-$ the heterogeneity is strong enough to localize the particle near the origin, preventing large excursions, and thus $Q(y|0)$ converges to a delta function at $y = 1/2$ as given by Eq. (7.17). In panel (c) we compare the limiting distribution obtained from simulations for $\alpha = 1.5$ with (7.17) in the Laplace space, this is, with $Q(u|0) = \mathscr{L}_{y\to u}[Q(y|0)] = \mathscr{L}_{y\to u}[\delta(y-1/2)] = e^{-0.5u}$. In the inset, we show the plot in real space. In all panels, we plot data for different t to illustrate the convergence to the limiting distribution. This transition in the shape of the limiting PDF of T_+ is consistent with the results found in Chapter 6, where stronger localization induced by resetting changes the limiting

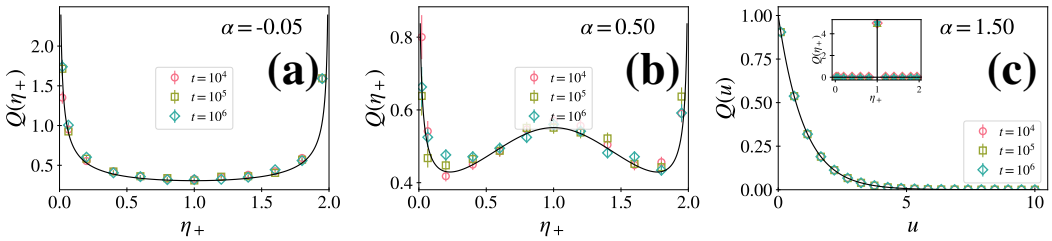


Figure 7.6: **PDF of the time averaged half occupation time for the power-law heterogeneity.** The different symbols are for trajectories with $t = 10^4, 10^5$, and 10^6. The black solid line corresponds to Eq. (7.21) in panels (a), and (b); to e^{-u} in panel (c), and to $\delta(t-1)$ in its inset. $\alpha = -0.05, 0.5$, and 1.5 in panels (a), (b), and (c), respectively. If $\alpha > 0$ we take $\varepsilon = 10^{-10}$, and $\varepsilon = 10^{-3}$ if $\alpha < 0$. In all panels $D_0 = 1.0$, $x_0 = 0$, simulation timestep $dt = 0.1$, and $N = 10^4$ trajectories.

distribution from a $\cup$-shaped law to a delta function at $y = 1/2$ when the resetting-time distribution has a finite first moment.

The mean half occupation time and the mean squared half occupation time can be obtained from the moments equation (7.2) and the expression of $Q(p,s|0)$ as given in (E.11)

$$\left\langle T^+(t)\right\rangle = \frac{t}{2}, \quad \left\langle T^+(t)^2\right\rangle = \frac{3-2\alpha}{4(2-\alpha)}t^2. \tag{7.19}$$

Note that now the first moment is independent of α and equal to $1/2$, since in this case the left-right symmetry is preserved. The ergodicity breaking parameter can be straightforwardly found from (2.54) and (7.19) as

$$\mathrm{EB}_+ = \frac{1-\alpha}{2-\alpha}, \quad \alpha \leq 1. \tag{7.20}$$

For this process, we find that EB_+ decreases with α and vanishes at $\alpha = 1$, where there is an ergodic transition. This transition can be understood by the effect of the heterogeneity, which, for $\alpha \geq 1$ is strong enough to localize the particles near the origin, preventing large excursions. On the other hand, for $\alpha < 0$, $D(x)$ decreases with x and is maximum at $x = 0$, therefore the walker escapes fast from the origin and as x increases gets progressively slowed, acting as an effective binding potential. Indeed, the PDF $Q(x,t)$ in the subdiffusive regime, $\alpha < 0$, is zero at $x = 0$ and decays as $Q(x,t) \sim |x|^{|\alpha|/2} \exp\left(-A|x|^{2+|\alpha|}/t\right)$, where $A > 0$ is a parameter (see Eq. (2.15) and reference [71]). Thus, as $|x| \to \infty$, the diffusion coefficient vanishes and trajectories become effectively trapped at the system boundaries. The more negative α is, the fewer steps are required to reach this limiting regime, increasing the differences of T_+ value between trajectories and thus the EB_+ parameter. Fig. 7.5 compares Eqs. (7.19) and (7.20) with numerical simulations. The ergodic transition can be noticed at $\alpha = 1$ in panel 7.5(c). The ergodicity breaking parameter and its discussion are the second result of this chapter.

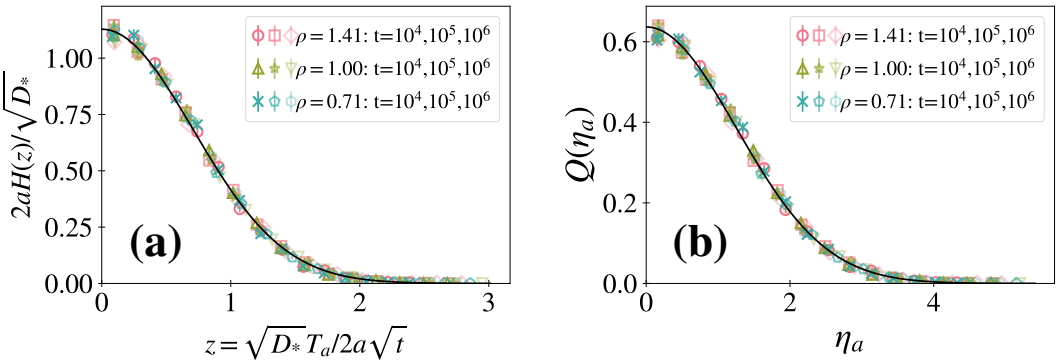


Figure 7.7: **Distribution of the occupation time in the interval for the piecewise heterogeneity.** (a) Limiting distribution of the occupation time in an interval. The black solid line corresponds to Eq. (7.23). (b) PDF of the time averaged occupation time in an interval. The black solid line corresponds to Eq. (7.27). In all panels, the symbols of the same color are for $D_+ = 0.5, 1.0$, and 2.0 salmon, green, and blue, respectively. The different symbol shapes are for trajectories with $t = 10^4, 10^5$, and 10^6. $D_- = 1.0$, $x_0 = 0$, interval $[-3,3]$, simulation timestep $dt = 0.1$, and $N = 10^4$ trajectories.

Finally, The PDF for the time averaged observable $\Theta[x(t)]$ (this is η_+ defined in (7.14)) can be obtained from (7.16) noting that $\eta_+ = 2y$ to get

$$Q(\eta_+) = \frac{\sin\left(\frac{\pi}{2-\alpha}\right)}{\pi} \frac{2\left[\eta_+(2-\eta_+)\right]^{\frac{-1+\alpha}{2-\alpha}}}{\eta_+^{\frac{2}{2-\alpha}} + (2-\eta_+)^{\frac{2}{2-\alpha}} + 2\cos\left(\frac{\pi}{2-\alpha}\right)\left[\eta_+(2-\eta_+)\right]^{\frac{1}{2-\alpha}}} \tag{7.21}$$

for $0 < \eta_+ < 2$. In Fig. 7.6 we compare Eq. (7.21) to numerical simulations.

7.4 Occupation time in an interval

We consider now the occupation time $T_a(t|x_0)$ of the random particle in an interval $[-a,a]$ up to time t if starting initially from x_0, as defined in Eq. (2.39). The corresponding Feynman-Kac Eq. (7.4) is in this case

$$sQ(p,s|x_0) - 1 = D(x_0)\frac{\partial^2 Q(p,s|x_0)}{\partial x_0^2} - p\Theta(-a < x_0 < a)Q(p,s|x_0) \tag{7.22}$$

which again needs to be solved under suitable boundary conditions. Note that it must be explicitly found in the regions I ($x_0 < -a$), II ($-a < x_0 < 0$), III ($0 < x_0 < a$), and IV ($x_0 > a$). For instance, if the starting point is at infinity i.e., $x_0 \to \pm\infty$ the particle will never reach the interval so that $Q(T_a,t|x_0 \to \pm\infty) = \delta(T_a)$, i.e., $Q(p,s|x_0 \to \pm\infty) = 1/s$. The initial condition is such that $T_a(t=0|x_0) = 0$ so that $Q(p,t=0|x_0) = 1$. Therefore, we must explicitly find the solution in the regions I ($x_0 < -a$), II ($-a < x_0 < 0$), III ($0 < x_0 < a$), and IV ($x_0 > a$). In Appendix E we again detail the derivation.

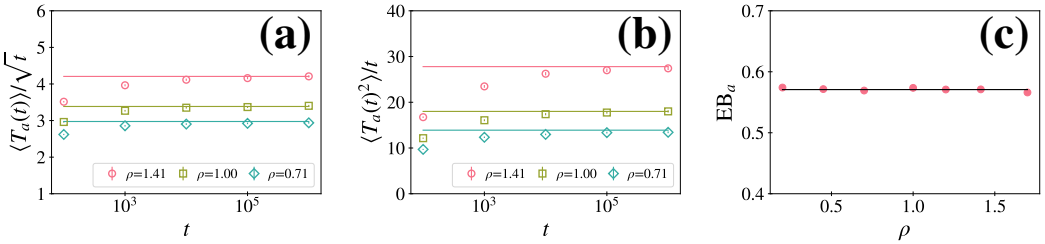


Figure 7.8: **Moments and EB parameter of the half occupation time for the piecewise heterogeneity.** (a) $\langle T_a(t)\rangle$, (b) $\langle T_a(t)^2\rangle$, and (c) EB$_a$. In panels (a), and (b) the solid lines are computed with Eq. (7.24), $D_+ = 0.5, 1.0$, and 2.0; In panel (c) the solid line is Eq. (7.25). In all panels $D_- = 1.0$, $x_0 = 0$, simulation timestep $dt = 0.1$, and $N = 10^4$ trajectories. In panels (a), and (b) the interval is $[-3,3]$ and in panel (c) the interval is $[-0.5,0.5]$.

7.4.1 Piecewise heterogeneity

The solution to (7.22) for the piecewise heterogeneity can be found in Appendix E, which we have to find it in the long-time limit, since we are not able to invert the Laplace transform in the general case. The resulting PDF is

$$Q(T_a,t|0) \simeq \sqrt{\frac{D_*}{\pi a^2 t}} \exp\left[-\frac{D_* T_a^2}{4a^2 t}\right], \quad D_* = \left(\frac{D_+\sqrt{D_-}+D_-\sqrt{D_+}}{D_+ + D_-}\right)^2, \tag{7.23}$$

which is nothing but the half-Gaussian shape as given in Eq. (2.40), with diffusion coefficient D_*. Thus, we conclude that at long times the PDF behaves like that of Brownian motion also. In panel (a) of Fig. 7.7 we check (7.23) against numerical solutions for different values of ρ. We also add data computed for different large values of t to show that when t is sufficiently large, the numerical results fall on the theoretical curve.

Next, the mean and mean square occupation time can be again computed from the expression of $Q(p,s|0)$ (E.16) and (7.2), yielding

$$\langle T_a(t)\rangle \simeq \frac{2a\sqrt{t}}{\sqrt{\pi D_*}}, \quad \langle T_a(t)^2\rangle \simeq \frac{2a^2}{D_*}t, \tag{7.24}$$

which not surprisingly agree with the results for the Brownian motion in a homogeneous medium with diffusion coefficient D_*, Eq. (2.41), as expected from the form of the PDF given in (7.23).

The ergodicity breaking parameter can be found from (2.54) and (7.24) to get

$$\mathrm{EB}_a = \frac{\langle T_a(t)^2\rangle}{\langle T_a(t)\rangle^2} - 1 = \frac{\pi}{2} - 1 \tag{7.25}$$

which again is the same as the EB parameter for the Brownian motion in homogeneous media. This means that in the long-time limit, the ergodic properties in terms of the

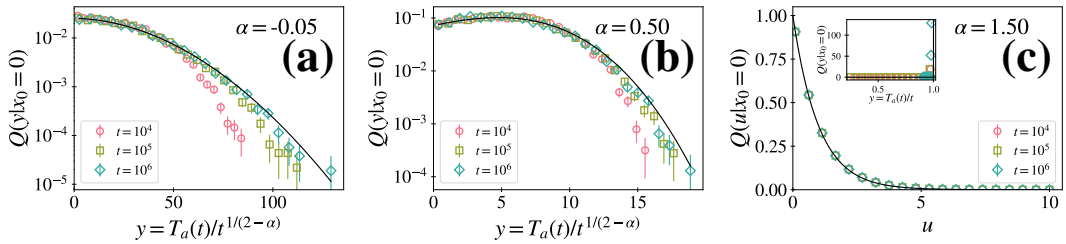


Figure 7.9: **Limiting distribution of the occupation time in an interval for the power-law heterogeneity.** The different symbols are for trajectories with $t = 10^4, 10^5$, and 10^6. The black solid line corresponds to Eq. (7.28) in panels (a), and (b); to e^{-u} in panel (c), and to Eq. (7.29) in its inset. $\alpha = -0.05, 0.5$, and 1.5 in panels (a), (b), and (c), respectively. If $\alpha > 0$ $\varepsilon = 10^{-10}$, and $\varepsilon = 10^{-3}$ if $\alpha < 0$. In all panels $D_0 = 1.0$, $x_0 = 0$, the interval is $[-20, 20]$, simulation timestep $dt = 0.1$, and $N = 10^4$ trajectories.

occupation time in an interval for a Brownian particle are not altered by the piecewise heterogeneity. In Fig. 7.8 we compare (7.24) and (7.25) with numerical simulations.

As before, we find the PDF of the time average of the observable $\Theta[-a < x(t) < a]$ in the long-time limit, as defined in Eq. (2.57), this is, the PDF of

$$\eta_a = \lim_{t\to\infty} \frac{T_a}{\langle T_a(t)\rangle} = \frac{T_a}{2a}\sqrt{\frac{\pi D_*}{t}}, \tag{7.26}$$

for the piecewise diffusion coefficient. Then its PDF follows from Eqs. (2.58) and (7.23). In this case we find that the PDF of η_a is given by the Mittag-Leffler distribution with index $1/2$ as defined in (2.59), that is

$$Q(\eta_a) = \mathscr{M}_{1/2}(\eta_a) = \frac{2}{\pi} e^{-\frac{\eta_a^2}{\pi}}, \tag{7.27}$$

which is the same result as for BM in a homogeneous medium. In panel (b) of Fig. 7.7, we compare Eq. (7.27) with numerical simulations. We note that the PDF $Q(\eta_a)$ computed for different values of the asymmetry parameter ρ collapse on the same curve, which confirms that $Q(\eta_a)$ does not depend on ρ. In addition, it can be observed how the distribution converges to the theoretical result Eq. (7.27) in the long-time limit. The above results for the occupation time in an interval are the third result of this chapter.

7.4.2 Power law heterogeneity

The $Q(T_a, t|0)$ in this case also needs to be found in the long-time limit. In this limit, it also admits a scaling form given by

$$Q(T_a, t|0) \sim \frac{1}{t^{\frac{1}{2-\alpha}}} N_\alpha\left(\frac{T_a}{\lambda_\alpha t^{\frac{1}{2-\alpha}}}\right), \quad N_\alpha(z) = \frac{2-\alpha}{\lambda_\alpha z^{3-\alpha}} l_{\frac{1}{2-\alpha}}\left(\frac{1}{z^{2-\alpha}}\right) \tag{7.28}$$

for $\alpha < 1$. Here $l_\beta(z)$ is the one-sided Lévy stable distribution with index β, and λ_α is defined in Eq. (E.19) and it depends on D_0, a, and α.

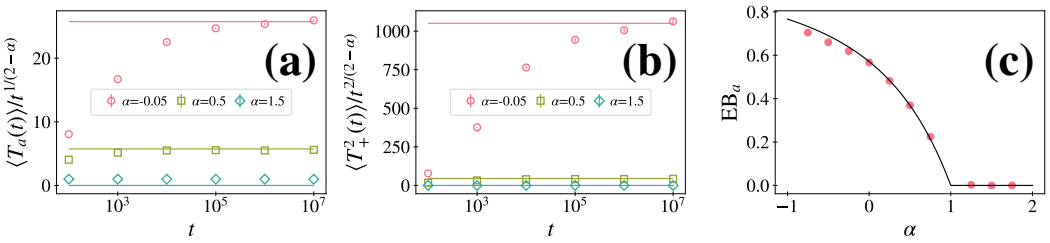


Figure 7.10: **Moments and EB parameter of the occupation time in an interval for the power-law heterogeneity.** (a) $\langle T_a(t)\rangle$, (b) $\langle T_a(t)^2\rangle$, and (c) EB_a. In panels (a), and (b) the solid lines are computed with Eq. (7.30) and $\alpha = -0.05, 0.5$, and 1.5; In panel (c) the solid line is Eq. (7.31). We take $\alpha > 0$ if $\varepsilon = 10^{-10}$, and $\varepsilon = 10^{-3}$ if $\alpha < 0$. In all panels $D_0 = 1.0$, $x_0 = 0$, the interval is $[-20, 20]$, simulation timestep $dt = 0.1$, and $N = 10^4$ trajectories.

We find that in the limit $\alpha \to 1^-$ the heterogeneity is strong enough to localize the particle near the origin, preventing large excursions, since we find (see Appendix E)

$$Q(T_a, t|0) \simeq \delta(T_a - t), \quad \alpha \to 1^-, \tag{7.29}$$

in this case, the particle will be in the interval for all time t. Note that at $\alpha = 1$ there is a transition in the behavior of the PDF $Q(T_a, t|0)$. For $1 \leq \alpha < 2$ the heterogeneity is so strong that the particle cannot escape the interval $[-a, a]$ for any a, which is reflected in the fact that T_a is equal to t. The comparison of the limiting distributions given in Eqs. (7.28) and (7.29) with numerical simulations is shown in Fig. 7.9. We note that the PDFs converge to the theoretical results in the long-time limit in panels (a) and (b). In panel (c) we show the limiting distribution for a value of $\alpha > 1$ in the Laplace space, to again better visualize the Dirac delta function, Eq. (7.29). The inset shows the limiting distribution in real space.

Next, we can compute the first two moments by means of (E.19). The mean and mean square occupation time are

$$\langle T_a(t)\rangle \simeq \frac{\lambda_\alpha}{\Gamma\left(\frac{3-\alpha}{2-\alpha}\right)} t^{\frac{1}{2-\alpha}}, \quad \langle T_a(t)^2\rangle \simeq \frac{2\lambda_\alpha^2}{\Gamma\left(\frac{4-\alpha}{2-\alpha}\right)} t^{\frac{2}{2-\alpha}}. \tag{7.30}$$

Likewise, the ergodicity breaking parameter can be found from (2.54) and (7.30) to get

$$\mathrm{EB}_a = \frac{\langle T_a(t)^2\rangle}{\langle T_a(t)\rangle^2} - 1 = \begin{cases} \frac{2\Gamma\left(\frac{3-\alpha}{2-\alpha}\right)^2}{\Gamma\left(\frac{4-\alpha}{2-\alpha}\right)} - 1, & \alpha < 1 \\ 0, & 1 < \alpha < 2 \end{cases} \tag{7.31}$$

Note that at $\alpha = 1$ there is an ergodic transition between non-ergodic phase $\alpha < 1$ and ergodic phases $\alpha > 1$, like for the half occupation time. The results given in (7.28) and (7.31) have been previously obtained in Ref. [68] by assuming that the PDF of T_a can be given by the PDF of the number of returns to the interval $[-a, a]$. This assumption

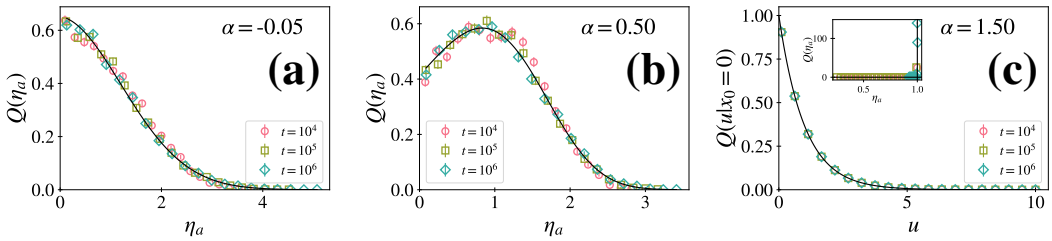


Figure 7.11: **PDF of the time averaged occupation time in the interval for the power-law heterogeneity.** The different symbols are for trajectories with $t = 10^4, 10^5$, and 10^6. The black solid line corresponds to Eq. (7.32) in panels (a), and (b); to e^{-u} in panel (c), and to $\delta(\eta_a - 1)$ in its inset. $\alpha = -0.05, 0.5$, and 1.5 in panels (a), (b), and (c), respectively. If $\alpha > 0$ $\varepsilon = 10^{-10}$, and $\varepsilon = 10^{-3}$ if $\alpha < 0$. In all panels $D_0 = 1.0$, $x_0 = 0$, the interval is $[-20, 20]$, simulation timestep $dt = 0.1$, and $N = 10^4$ trajectories.

requires that the returns constitute a renewal process [134], i.e., the times between successive returns are uncorrelated, which is not true for any general process, as we will see in the next chapter. However, we have obtained the same results without making any further assumption, but by directly solving the corresponding Feynman-Kac equation.

In Fig. 7.10 we compare the theoretical results for the first two moments given in Eqs. (7.30) and (7.31) with numerical simulations. We note that for $\alpha < 0$ the convergence to the analytic result is slower the smaller α is. Note also that EB_a and EB_+ vs α in panels 7.5(c) and 7.10(c) look qualitatively very similar and can be regarded as phase diagrams of the ergodic properties.

Finally, we compute the PDF for the time average of the observable $\Theta[-a < x(t) < a]$ in the long-time limit. From (7.26) and (7.24)

$$\eta_a = \frac{T_a}{\lambda_\alpha t^{\frac{1}{2-\alpha}}} \Gamma\left(\frac{3-\alpha}{2-\alpha}\right)$$

and from (7.28), we find that in the long-time limit $Q(\eta_a)$ is given by the ML distribution of order β:

$$Q(\eta_a) = \mathscr{M}_\beta(\eta_a) = \frac{\Gamma(1+\beta)^{\frac{1}{\beta}}}{\beta \eta_a^{1+\frac{1}{\beta}}} l_\beta \left[\frac{\Gamma(1+\beta)^{\frac{1}{\beta}}}{\eta_a^{\frac{1}{\beta}}}\right], \quad \beta = \frac{1}{2-\alpha} \tag{7.32}$$

for $\alpha < 1$. The PDF given in (7.32) depends on neither D_0 nor a but only on α. This result is checked with numerical simulations as shown in Fig. 7.11. For $\alpha > 1$ the PDF of time averaged occupation time in the interval is $Q(\eta_a) = \delta(\eta_a - 1)$, according to (7.29). In panels (a) and (b) we show two cases for $\alpha < 1$, while in panel (c) we show a case for $\alpha > 1$ in the Laplace space. In the inset of panel (c) we show the same PDF but in the real space.

7.5 Summary of results

In this chapter, we have analyzed the ergodic properties of Brownian motion in heterogeneous media through the statistics of the occupation time. By solving the Feynman-Kac equation associated with the characteristic function of the occupation times, we obtained analytical results for two relevant forms of spatially varying diffusion coefficient: a piecewise-constant model and a power-law dependence. From these solutions, we derived the limiting distributions of the occupation times, their first two moments, and the corresponding ergodicity breaking parameters, finding agreement with numerical simulations.

For the piecewise diffusion coefficient, we showed that the probability density of the half occupation time follows an asymmetric arcsine law, with a strictly positive EB parameter. The distribution of the occupation time within an interval is half-Gaussian—analogous to the homogeneous case but with an effective diffusion coefficient—and the EB parameter matches that of standard Brownian motion, confirming non-ergodic behavior in terms of both occupation times.

For the power-law diffusion coefficient, our results reproduce the occupation-time distributions previously obtained in Refs. [68, 70], but reveal a transition between non-ergodic and ergodic phases. As the exponent α increases, the system evolves from a non-ergodic regime for $\alpha < 1$ to an ergodic regime for $\alpha > 1$.

Overall, in this chapter, we have illustrated how the Feynman-Kac formalism provides a powerful framework to characterize ergodic properties of diffusion processes in heterogeneous media. While we focused on two specific spatial dependencies of the diffusion coefficient, the approach can be extended to more general forms [219].

8

OCCUPATION AND AREA OBSERVABLES IN GAUSSIAN ANOMALOUS DIFFUSION

In this chapter, we study stochastic functionals of anomalous random walks through their first two moments, obtained directly from the one-time and two-time probability density functions of the underlying process. We use this framework to analyze occupation-time and area observables, with explicit study cases to scaled Brownian motion and fractional Brownian motion. In particular, we investigate the half occupation time, the occupation time in an interval, the area, and the absolute area under the trajectory. From these results, we study the corresponding ergodic properties through the EB parameter and derive the long-time scaling forms of the associated PDFs.

8.1 Introduction . . . 142
8.2 The first two moments . . . 142
8.2.1 Gaussian processes . . . 145
8.3 Stationary processes . . . 146
8.4 Occupation-time statistics . . . 147
8.4.1 Half occupation time . . . 150
8.4.2 Occupation time in an interval . . . 153
8.4.3 Scaling of the PDF . . . 156
8.5 Area observables . . . 158
8.5.1 Area . . . 159
8.5.2 Absolute Area . . . 160
8.5.3 Scaling of the PDF . . . 163
8.6 Summary of results . . . 165

8.1 Introduction

In chapters 5 to 7, we studied stochastic functionals for non-Markovian random walks, resetting processes, and heterogeneous diffusion processes using a combination of Feynman-Kac and renewal methods. Although these approaches are powerful, the resulting equations are not always solvable, nor can they always be inverted from Laplace or Fourier spaces. In this chapter, we therefore adopt a different approach: instead of solving a Feynman-Kac equation for each functional separately, we derive the first two moments directly from the one-time and two-time probability density functions of the underlying process. This provides a general moment-based framework for the analysis of stochastic functionals. We further simplify the computation by focusing on Gaussian dynamics, for which the resulting expressions can be written in terms of the mean and autocorrelation function [245].

We then apply this framework to two Gaussian models of anomalous diffusion, the Scaled Brownian motion and fractional Brownian motion. In the former, anomalous diffusion is generated by a time-dependent diffusivity, whereas in the latter it originates from long-range temporal correlations [22, 246, 247]. These two models provide useful examples to investigate how stochastic functionals reflect different microscopic mechanisms of anomalous transport.

The first part of the chapter is devoted to occupation-time statistics. We derive general expressions for the first two moments of the half occupation time and the occupation time in an interval, and then apply them to scaled Brownian motion and fractional Brownian motion. These results allow us to compare the ergodic properties of different anomalous diffusion models through the corresponding ergodicity-breaking parameters and the long-time scaling of their probability density functions.

In the second part, we extend the analysis to area observables, namely the area and the absolute area under the trajectory. For the models considered in this chapter, we obtain explicit expressions for their moments, fluctuations, ergodicity-breaking properties, and scaling forms. In the case of Gaussian processes, the area distribution can moreover be obtained exactly.

This chapter is organized as follows. In Sec. 8.2 we derive the first two moments of a stochastic functional in terms of the one-time and two-time probability density functions of the underlying random walk. In Sec. 8.3 we show that functionals of stationary processes are ergodic in the long-time limit. In Sec. 8.4 we present the occupation-time statistics and apply the general results to scaled Brownian motion and fractional Brownian motion. In Sec. 8.5 we study the area and the absolute area under anomalous trajectories, focusing on the same two models. Finally, in Sec. 8.6 we summarize the main results of the chapter.

8.2 The first two moments

In what follows, instead of solving the Feynman-Kac equation, we derive the moments of the functionals directly from the one-time and two-time PDFs of the underlying process, by using Kac's formalism to study additive functionals of stochastic trajectories [125]. Proceeding in this way will allow us to derive general moment formulas without

the need to solve the Feynman-Kac equation, which, as we have seen in the previous chapters, can be cumbersome to solve and to invert. Unlike in [125], we do not require the functional to be positively defined, but we consider a generic stochastic functional, Eq. (2.31), $Z(t) = \int_0^t U[x(\tau)]d\tau$ that can take both positive and negative values. Next, if $P(x,t)$ is the probability of finding the walker at position x at time t that was initially at x_0, we can write the first moment of the stochastic functional as

$$\langle Z(t)\rangle = \left\langle \int_0^t U[x(\tau)]d\tau \right\rangle = \int_0^t d\tau \int_{-\infty}^{\infty} dx U(x) P(x,\tau), \tag{8.1}$$

In the same way, the $\langle Z(t)^2\rangle$ can be written as

$$\begin{aligned}\langle Z(t)^2\rangle &= \left\langle \left(\int_0^t U[x(\tau)]d\tau \right)^2 \right\rangle = \int_0^t d\tau_2 \int_0^t d\tau_1 \langle U[x(\tau_1)]U[x(\tau_2)]\rangle \\ &= 2! \int_0^t d\tau_2 \int_0^{\tau_2} d\tau_1 \int_{-\infty}^{\infty} dx_2 \int_{-\infty}^{\infty} dx_1 U(x_1)U(x_2)P(x_2,\tau_2;x_1,\tau_1)\end{aligned} \tag{8.2}$$

where now $P(x_2,\tau_2;x_1,\tau_1)$ is the two-time PDF. Eqs. (8.1) and (8.2) are general expressions for the first two moments of any stochastic functional in terms of the one-time and two-time PDFs of a generic random walk, where we haven't introduced any assumptions about the underlying process.

Sometimes, it can be more convenient, depending on the specific case, to work with the characteristic functions instead. Since the one- and two-time PDFs can be written as

$$P(x,t) = \frac{1}{2\pi} \int_{-\infty}^{\infty} e^{-ikx} P(k,t) dk \tag{8.3}$$

and

$$P(x_2,t_2;x_1,t_1) = \frac{1}{(2\pi)^2} \int_{-\infty}^{\infty} dk_1 \int_{-\infty}^{\infty} dk_2 P(k_2,t_2;k_1,t_1) e^{-i(k_1x_1+k_2x_2)}, \tag{8.4}$$

respectively, Eq. (8.1) becomes

$$\langle Z(t)\rangle = \frac{1}{2\pi} \int_0^t d\tau_1 \int_{-\infty}^{\infty} dk_1 P(k_1,\tau_1)\tilde{U}(-k_1) \tag{8.5}$$

where

$$\tilde{U}(-k_i) = \int_{-\infty}^{\infty} e^{-ik_ix_i} U(x_i) dx_i \tag{8.6}$$

and $i = 1,2$. Analogously, Eq. (8.2) can be written as

$$\left\langle Z(t)^2 \right\rangle = \frac{2}{(2\pi)^2} \int_0^t d\tau_2 \int_0^{\tau_2} d\tau_1 \int_{-\infty}^{\infty} dk_1 \int_{-\infty}^{\infty} dk_2 P(k_2,\tau_2;k_1,\tau_1)\tilde{U}(-k_1)\tilde{U}(-k_2). \quad (8.7)$$

Again, Eqs. (8.5) and (8.7) are general expressions, equivalent to those in (8.1) and (8.2), but expressed in terms of the characteristic functions of the one-time and two-time PDFs. Depending on the particular functional and the random walk, it can be more convenient to use one or the other. For example, if the random walk is a Gaussian process, as we will soon see, then the characteristic functions of the one-time and two-time PDFs can be expressed in terms of the autocorrelation function only, which simplifies the calculation of the first two moments. In any case, Eqs. (8.1), (8.2), (8.5), and (8.7) are general expressions, not necessarily restricted to Gaussian processes.

It is clear from the derivation above that, proceeding analogously, we can get the expression for the n-th moment in terms of the n-time PDFs of the underlying random walk. We can write them in an iterative manner [125]

$$\left\langle Z(t)^n \right\rangle = n! \int_{-\infty}^{\infty} F_n(x,t)dx \quad (8.8)$$

where to construct the functions $F_n(x,t)$ with $n \in \mathbb{N}$, one has to take into account the definition of the conditional probability $P(x,\tau;x_1,\tau_1) = P(x,\tau|x_1,\tau_1)P(x_1,\tau_1)$. Moreover, the $F_n(x,t)$ functions satisfy the following renewal iterative equation

$$F_{n+1}(x,t) = \int_0^t d\tau_1 \int_{-\infty}^{\infty} dx_1 U(x_1) F_n(x_1,\tau_1) P(x,t|x_1,\tau_1) \quad (8.9)$$

with $P(x,t|x_1,\tau_1)$ the propagator of the process $x(t)$ (the probability density for the process $x(t)$ to take the value x at time t given that its value at time τ_1 is x_1) and $F_0(x,t) \equiv P(x,t)$. In this way, we can obtain all the moments of the functionals without solving the FK equation.

Note 8.1 In principle, since we have an expression to compute all moments, we could use them to write the equation for the PDF $Q(Z,t)$ of the functional, by means of the moment generating function

$$Q(\omega,t) \quad = \quad \int_{-\infty}^{\infty} e^{-i\omega Z} Q(Z,t)dZ = \left\langle e^{-i\omega Z(t)} \right\rangle,$$

where, when expanding the exponential in a power series, it can be written as

$$Q(\omega,t) = \left\langle \sum_{n=0}^{\infty} \frac{(-i\omega)^n}{n!} Z(t)^n \right\rangle = \sum_{n=0}^{\infty} \frac{(-i\omega)^n}{n!} \left\langle Z(t)^n \right\rangle.$$

Inserting (8.8) into the above equation we get

$$Q(\omega,t) = \sum_{n=0}^{\infty} (-i\omega)^n \int_{-\infty}^{\infty} F_n(x,t)dx.$$

By defining

$$Q(x,\omega,t) = \sum_{n=0}^{\infty} (-i\omega)^n F_n(x,t),$$

and then multiplying (8.9) by $(-i\omega)^n$ and summing over n we can obtain the integral equation for $Q(x,\omega,t)$:

$$Q(x,\omega,t) = P(x,t) - i\omega \int_0^t d\tau_1 \int_{-\infty}^{\infty} dx_1 U(x_1) P(x,t|x_1,\tau_1) Q(x_1,\omega,\tau_1).$$

Once the above equation is solved for $Q(x,\omega,t)$, then $Q(\omega,t)$ follows from

$$Q(\omega,t) = \int_{-\infty}^{\infty} Q(x,\omega,t)dx.$$

However, this is usually a very difficult task. Luckily, in many cases of interest, the first two moments are enough to characterize the ergodic properties of the functional and to obtain the long-time scaling form of its PDF, as we will see in the next sections.

8.2.1 Gaussian processes

If the position of the random walker $x(t)$ is a Gaussian process, then we can show that the one-time and two-time PDFs can be expressed in terms of the autocorrelation function only. Let $x(t)$ be a Gaussian process with mean $\langle x(t)\rangle$ and autocorrelation $C(t_1,t_2) \equiv \langle x(t_1)x(t_2)\rangle - \langle x(t_1)\rangle \langle x(t_2)\rangle$. Then, the characteristic functional of $x(t)$ is the characteristic function of the functional $\int_{-\infty}^{\infty} f(t)x(t)dt$ and is given by [245]

$$\left\langle e^{i\int_{-\infty}^{\infty} f(t)x(t)dt} \right\rangle = \exp\left[i\int_{-\infty}^{\infty} f(t)\langle x(t)\rangle dt \quad - \right. \tag{8.10}$$
$$\left. \frac{1}{2}\int_{-\infty}^{\infty} dt_1 \int_{-\infty}^{\infty} dt_2 f(t_1) f(t_2) C(t_1,t_2) \right]$$

where $f(t)$ is an arbitrary function. In particular, to find the expression for the one-time and two-time PDFs we consider $f(\tau) = k\delta(\tau - t)$ and $f(\tau) = k_1\delta(\tau - t_1) + k_2\delta(\tau - t_2)$ respectively. Thus, the one-time PDF reads

$$P(k,t) = \left\langle e^{ikx(t)} \right\rangle = \exp\left[ik\langle x(t)\rangle - \frac{k^2}{2} C(t,t) \right], \tag{8.11}$$

and the two-time PDF is given by

$$P(k_2,t_2;k_1,t_1) = \left\langle e^{ik_1x(t_1)+ik_2x(t_2)} \right\rangle = \exp\left[ik_1 \langle x(t_1)\rangle + ik_2 \langle x(t_2)\rangle - \frac{k_1^2}{2}C(t_1,t_1) - \frac{k_2^2}{2}C(t_2,t_2) - k_1k_2C(t_1,t_2)\right]. \tag{8.12}$$

If the Gaussian process is isotropic, we can simplify even further the above expressions by taking $\langle x(t)\rangle = 0$ for all t. In this case, the one-time PDF is given by $P(k,t) = \exp[-k^2C(t,t)/2]$ which after Fourier inversion yields

$$P(x,t) = \frac{e^{-\frac{x^2}{2C(t,t)}}}{\sqrt{2\pi C(t,t)}}. \tag{8.13}$$

Analogously, the two-time PDF reads $P(k_2,t_2;k_1,t_1) = \exp\left[-\frac{k_1^2}{2}C(t_1,t_1) - \frac{k_2^2}{2}C(t_2,t_2) - k_1k_2C(t_1,t_2)\right]$ which after a double Fourier inversion yields

$$P(x_2,t_2;x_1,t_1) = \frac{\exp\left[-\frac{C(t_1,t_1)x_2^2+C(t_2,t_2)x_1^2-2C(t_1,t_2)x_1x_2}{2\Phi(t_1,t_2)}\right]}{2\pi\sqrt{\Phi(t_1,t_2)}} \tag{8.14}$$

where

$$\Phi(t_1,t_2) = C(t_1,t_1)C(t_2,t_2) - C(t_1,t_2)^2.$$

With this, we have seen that for Gaussian processes, the computation of the moments of a stochastic functional can be reduced to the computation of the mean and autocorrelation function of the underlying process, which is a great simplification, but not a requirement for the applicability of Eqs. (8.1) and (8.2).

8.3 Stationary processes

Before applying the above framework to specific cases, we study of the long-time behavior of the moments of a stochastic functional when the underlying process is stationary, meaning that there exists a time-independent stationary PDF defined as $P_s(x) = \lim_{t\to\infty} P(x,t) = \lim_{t-t'\to\infty} P(x,t|x',t')$ independently of the initial position x'. An example of this is the NESS induced by Poissonian resetting, since the PDF of the position of the Brownian particle converges to a time-independent distribution, Eq. (2.23), or the NESS found in Eqs. (3.33) and (3.34). A stationary process also arises when Brownian particles are confined in a finite domain; after a sufficiently long time, their concentration becomes uniform (for reflecting boundary conditions) and thus time invariant. Another example is the case of a Brownian particle under the effect of an external confining potential [122, 133, 134], or in heterogeneous media that effectively confine the dynamics [68]. In the long-time limit (8.9) reduces to

$$F_{n+1}(x,t) \simeq P_s(x) \int_0^t d\tau_1 \int_{-\infty}^{\infty} dx_1 U(x_1) F_n(x_1,\tau_1). \tag{8.15}$$

By Laplace transforming with respect to time, the above equation becomes

$$F_{n+1}(x,s) \simeq \frac{P_s(x)}{s} \int_{-\infty}^{\infty} dx_1 U(x_1) F_n(x_1,s). \tag{8.16}$$

From Eqs. (8.8) and (8.16) it can be shown that the n-th moment in the long-time limit is given by

$$\langle Z(s)^n \rangle \simeq \frac{n!}{s^{n+1}} \langle U \rangle_s^n \tag{8.17}$$

where $\langle U \rangle_s = \int_{-\infty}^{\infty} U(x) P_s(x) dx$. After Laplace inversion

$$\langle Z(t)^n \rangle \simeq (t \langle U \rangle_s)^n \tag{8.18}$$

as $t \to \infty$. This result is general, for a stationary process, and independent of the functional form and the details of the random walk. In addition, using the expansion of $Q(\omega,t)$ in Note 8.1, with the above equation Eq. (8.18) one has $Q(\omega,t) \simeq e^{-i\omega t \langle U \rangle_s}$ and Fourier inverting with respect to the variable ω we get that

$$Q(Z,t) \simeq \delta(Z - t\langle U \rangle_s) = \delta(Z - \langle Z(t) \rangle) \quad \text{as} \quad t \to \infty, \tag{8.19}$$

This result is in agreement with Eq. (6.19), where we found that in the long-time limit the PDF of a functional approaches a delta function when there is stochastic resetting from a finite-moment resetting distribution. The result in Eq. (8.19) is more general, since it is valid for any other mechanism that induces a stationary process, not only resetting. Thus, Eq. (6.19) is a particular case of the more general result in (8.19). We can further say that in this case the ergodicity breaking parameter is $\mathrm{EB} = \langle Z(t)^2 \rangle / \langle Z(t) \rangle^2 - 1 = t^2 \langle U \rangle_s^2 / (t \langle U \rangle_s)^2 - 1 = 0$, in agreement with Khinchin's theorem [248], which provides the condition that a stationary process is ergodic.

8.4 Occupation-time statistics

We have studied occupation-time statistics for the CTRW in Chapter 5 and for heterogeneous diffusion processes in Chapter 7. In this section, we present the first two moments for the occupation-time statistics of Gaussian processes, and apply these results to the cases of the SBM and fBM. We consider first the half occupation time $T_+(t)$ as defined in Eq. (2.34), $T_+(t) = \int_0^t \Theta[x(\tau)] d\tau$. Thus, as before, for this functional $U(x) = \Theta(x)$, where $\Theta(x)$ is the Heaviside step function. Using Eq. (8.6) we find that the Fourier transform of $U(x)$ is given by

$$\tilde{U}(-k) = -\frac{i}{k} + \pi\delta(k). \tag{8.20}$$

Thus, the mean half occupation time follows from Eq. (8.5) and (8.11)

$$\langle T_+(t)\rangle = \frac{t}{2} + \frac{1}{2}\int_0^t \mathrm{erf}\left(\frac{\langle x(\tau)\rangle}{\sqrt{2C(\tau,\tau)}}\right) d\tau, \tag{8.21}$$

The above expression is a general expression for the mean half occupation time of a Gaussian random walk in terms of $\langle x(t)\rangle$ and $\langle x(t)^2\rangle = C(t,t)$. The mean square occupation time follows from (8.7) and (8.20), we get

$$\begin{aligned}\langle T_+(t)^2\rangle &= \langle T_+(t)\rangle^2 \\ &+ \frac{1}{\pi}\int_0^t d\tau_2 \int_0^{\tau_2} d\tau_1 \int_0^{\frac{C(\tau_1,\tau_2)}{\sqrt{C(\tau_1,\tau_1)C(\tau_2,\tau_2)}}} \frac{dz}{\sqrt{1-z^2}} \exp\left[-\frac{\xi_1^2+\xi_2^2-2z\xi_1\xi_2}{2(1-z^2)}\right]\end{aligned} \tag{8.22}$$

where

$$\xi_i = \frac{\langle x(\tau_i)\rangle}{\sqrt{C(\tau_i,\tau_i)}}, \quad i = 1,2. \tag{8.23}$$

Next, we consider the occupation time $T_a(t)$ in the interval $[-a,a]$, as defined in Eq. (2.39) $T_a(t) = \int_0^t \mathbb{1}_{[-a,a]}(x(\tau))d\tau$. In this case, $U(x) = \mathbb{1}_{[-a,a]}(x)$, being $\mathbb{1}_{[-a,a]}$ the indicator function of $[-a,a]$. Hence, using Eq. (8.6) we obtain the expression

$$\tilde{U}(-k) = \frac{2\sin(ka)}{k} \tag{8.24}$$

which after being introduced into Eq. (8.5) and using (8.11) and integrating over k, we obtain the general expression for $\langle T_a(t)\rangle$ in terms of $\langle x(t)\rangle$ and autocorrelation of the Gaussian process:

$$\langle T_a(t)\rangle = \frac{1}{2}\int_0^t \left[\mathrm{erf}\left(\frac{a-\langle x(\tau)\rangle}{\sqrt{2C(\tau,\tau)}}\right) + \mathrm{erf}\left(\frac{a+\langle x(\tau)\rangle}{\sqrt{2C(\tau,\tau)}}\right)\right] d\tau. \tag{8.25}$$

Now, the second moment $\langle T_a(t)^2\rangle$ is found from (8.7) and integrating over k_2, we arrive at the expression

$$\begin{aligned}\langle T_a(t)^2\rangle = \frac{2}{\pi^2}\int_0^t d\tau_2 \int_0^{\tau_2} d\tau_1 \int_{-\infty}^{\infty} dk_1 \frac{\sin(k_1 a)}{k_1} \\ \times e^{ik_1\langle x(\tau_1)\rangle - \frac{k_1^2}{2}C(\tau_1,\tau_1)} I_2(a,k_1,\tau_1,\tau_2)\end{aligned} \tag{8.26}$$

where $I_2(a,K_1,\tau_1,\tau_2)$ is defined as

$$I_2(a,k_1,\tau_1,\tau_2) = \frac{\pi}{2}\left[\mathrm{erf}\left(\frac{a-\langle x(\tau_2)\rangle - ik_1C(\tau_1,\tau_2)}{\sqrt{2C(\tau_2,\tau_2)}}\right) + \mathrm{erf}\left(\frac{a+\langle x(\tau_2)\rangle + ik_1C(\tau_1,\tau_2)}{\sqrt{2C(\tau_2,\tau_2)}}\right)\right]. \tag{8.27}$$

In the case that the random walk is isotropic, so that $\langle x(\tau_i)\rangle = 0$ with $i = 1,2$, we can further simplify the above expressions. In this case, Eqs. (8.21) and (8.23) read

$$\begin{aligned}\langle T_+(t)\rangle &= \frac{t}{2},\\ \left\langle T_+(t)^2\right\rangle &= \frac{t^2}{2} - \frac{1}{\pi}\int_0^t d\tau_2\int_0^{\tau_2} d\tau_1 \arctan\left(\sqrt{\frac{C(\tau_2,\tau_2)C(\tau_1,\tau_1)}{C(\tau_1,\tau_2)^2}-1}\right).\end{aligned} \tag{8.28}$$

The above results, Eq. (8.28), are exact general results for the first two moments of the half occupation time of a Gaussian isotropic process and can be explicitly found from the autocorrelation functions of the underlying random walk. Analogously, for the occupation time in an interval, Eqs. (8.25) and (8.26) become

$$\langle T_a(t)\rangle = \int_0^t \mathrm{erf}\left(\frac{a}{\sqrt{2C(\tau,\tau)}}\right) d\tau \tag{8.29}$$

and the second moment reads

$$\begin{aligned}\left\langle T_a(t)^2\right\rangle &= \frac{1}{\pi}\int_0^t d\tau_2\int_0^{\tau_2} d\tau_1\int_{-\infty}^{\infty} dk \frac{\sin(ka)}{k} e^{-\frac{k^2}{2}C(\tau_1,\tau_1)}\\ &\times \left[\mathrm{erf}\left(\frac{a-ikC(\tau_1,\tau_2)}{\sqrt{2C(\tau_2,\tau_2)}}\right) + \mathrm{erf}\left(\frac{a+ikC(\tau_1,\tau_2)}{\sqrt{2C(\tau_2,\tau_2)}}\right)\right].\end{aligned} \tag{8.30}$$

We can derive a simpler expression if we consider the long-time limit. Note that, in most cases, the one-time autocorrelation (i.e., the mean square displacement of the random walk) $C(\tau,\tau) = \left\langle x(\tau)^2\right\rangle$ at large times depends on time as $\left\langle x(\tau)^2\right\rangle \sim t^p$. Then, the argument of the error function in Eq. (8.29) defines the dimensionless quantity $a/\sqrt{2C(\tau,\tau)}$ (of order $t^{-p/2}$) which is very small when $t\to\infty$. When the argument is small, the error function can be approximated as $\mathrm{erf}(z) \simeq 2z/\sqrt{\pi}$. Then, Eq. (8.29) is

$$\langle T_a(t)\rangle \simeq a\sqrt{\frac{2}{\pi}}\int_0^t \frac{d\tau}{\sqrt{C(\tau,\tau)}} \tag{8.31}$$

in the long-time limit. Proceeding analogously with Eq. (8.28), we consider the term $a/\sqrt{2C(\tau_2,\tau_2)}$ to be much smaller than $kC(\tau_1,\tau_2)/\sqrt{2C(\tau_2,\tau_2)}$ in the long-time limit. In this case we can approximate the error functions in Eq. (8.30) taking

into account that $\mathrm{erf}(\varepsilon+iy)+\mathrm{erf}(\varepsilon-iy)\simeq 4\varepsilon e^{y^2}/\sqrt{\pi}+O(\varepsilon^2)$, and provided that $C(\tau_1,\tau_1)C(\tau_2,\tau_2)-C(\tau_1,\tau_2)^2>0$ we find that the second moment of the occupation time in an interval is given by

$$\left\langle T_a(t)^2\right\rangle \simeq \frac{4a^2}{\pi}\int_0^t d\tau_2\int_0^{\tau_2}\frac{d\tau_1}{\sqrt{C(\tau_1,\tau_1)C(\tau_2,\tau_2)-C(\tau_1,\tau_2)^2}}. \tag{8.32}$$

Likewise, the results (8.31) and (8.32) correspond to the first and second moments of the occupation time in an interval for a Gaussian isotropic process in the long-time limit, and like the half occupation time, they depend solely on the autocorrelation function of the process.

Now, we can apply the above results to specific examples of Gaussian processes of physical interest. We first analyze the half occupation time and then the occupation time in an interval, considering in each case the scaled Brownian motion (SBM) and the fractional Brownian motion (fBM).

8.4.1 Half occupation time

A Time dependent diffusivity and Scaled Brownian motion

We start with the general case of an isotropic process $x(t)$ with a diffusion coefficient that depends on time, $D(t)$. For such processes we can compute their autocorrelation function, which reads

$$\begin{aligned} C(t_1,t_2) &= 2\int_0^{t_1}\sqrt{D(\tau_1)}d\tau_1\int_0^{t_2}\sqrt{D(\tau_2)}\left\langle\xi(\tau_1)\xi(\tau_2)\right\rangle d\tau_2 \\ &= 2\int_0^{\min(t_1,t_2)}D(\tau)d\tau, \end{aligned} \tag{8.33}$$

Since the random walk is isotropic, the mean half occupation time $\langle T_+(t)\rangle = t/2$ as in Eq. (8.28). The mean square half occupation time follows from Eq. (8.28) using Eq. (8.33). Then,

$$\left\langle T_+(t)^2\right\rangle = \frac{t^2}{2}\left[1-\frac{2}{\pi}\int_0^1 vdv\int_0^1 \arctan\left(\sqrt{\frac{\int_0^{vt}D(\tau)d\tau}{\int_0^{uvt}D(\tau)d\tau}-1}\right)du\right], \tag{8.34}$$

where we introduced the dimensionless variables $u=\tau_1/\tau_2$ and $v=\tau_2/t$. Eq. (8.34) is general for a time-dependent diffusivity $D(t)$. Different temporal dependencies of the diffusion coefficient have been considered in the physical literature [249, 250, 251], in our case, we focus on the SBM, Eq. (2.8), which is defined by a power-law time-dependent diffusivity of the form

$$D(t)=\alpha K t^{\alpha-1}$$

with $\alpha\in(0,2)$. In this case, the two-time autocorrelation function reads

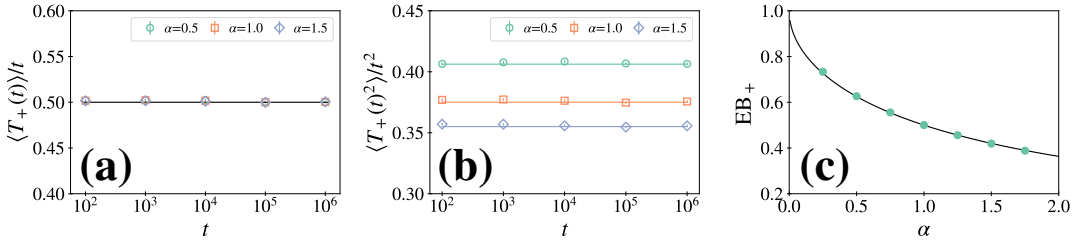


Figure 8.1: **First -(a)- and second -(b)- moments, and -(c)- EB parameter of the half occupation time for the SBM**. The symbols are obtained from numerical simulations for $\alpha = 0.5, 1.0$, and 1.5 in panels (a) and (b), and for a final simulation time $t = 10^6$ in panel (c). The solid lines are given by Eq. (8.28) in panel (a), by Eq. (8.36) in panel (b), and by Eq. (8.37) in panel (c). All simulations are performed with parameters: $x_0 = 0$, $K = 1$, time discretization of $dt = 0.1$, and $N = 10^5$ trajectories.

$$C(t_1,t_2) = 2K\left[\min(t_1,t_2)\right]^{\alpha} \tag{8.35}$$

which can be derived by means of (8.33) and (2.8).

Then, the half occupation time $T_+(t)$ for the SBM can be derived from (8.28) and (8.35), from which we get

$$\left\langle T_+(t)^2 \right\rangle = \frac{t^2}{2}\left[1 - \frac{1}{2\sqrt{\pi}}\frac{\Gamma\left(\frac{1}{2}+\frac{1}{\alpha}\right)}{\Gamma\left(1+\frac{1}{\alpha}\right)}\right]. \tag{8.36}$$

We can recover the standard Brownian motion result by setting $\alpha = 1$ in the above expression, indeed we obtain $\left\langle T_+(t)^2 \right\rangle = 3t^2/8$ which is the result that corresponds to the standard Brownian motion, Eq. (2.36). Since we have the first and second moment, we can characterize the ergodic properties of the half occupation time using Eq. (2.54), in this case the EB parameter is given by

$$\mathrm{EB}_+ = \frac{\left\langle T_+(t)^2 \right\rangle}{\left\langle T_+(t) \right\rangle^2} - 1 = 1 - \frac{1}{\sqrt{\pi}}\frac{\Gamma\left(\frac{1}{2}+\frac{1}{\alpha}\right)}{\Gamma\left(1+\frac{1}{\alpha}\right)} \tag{8.37}$$

which is monotonically decreasing with α. Again, for $\alpha = 1$ one has $\mathrm{EB}_+ = 1/2$ corresponding to the standard Brownian motion, as we have discussed in Chapter 5. In panels (a) and (b) of Fig. 8.1, we compare numerical simulations of SBM, with the results of the first and second moments of the half occupation time as a function of time, for three different values of the exponent α. In all cases, there is a good agreement between the simulations and the analytical results. In panel (c) of Fig. 8.1, we present the EB parameter for this observable as a function of the exponent α, where we see that the EB parameter decreases monotonically with α. Because EB measures trajectory-to-trajectory variability in the observable $\mathscr{O}$, this implies greater trajectory dispersion at low α. For $\alpha \in (0,1)$, the decreasing diffusion coefficient $D(t)$ makes escaping from a given region progressively harder, enhancing trajectory differences with respect to T_+. Conversely, for $\alpha \in (1,2)$, $D(t)$ increases with time, reducing trajectory persistence and thus lowering EB.

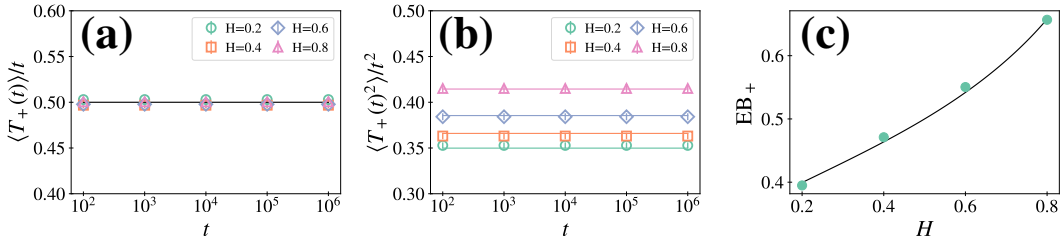


Figure 8.2: **First -(a)- and second -(b)- moments, and -(c)- EB parameter of the half occupation time for the fBM**. The symbols are obtained from numerical simulations for $H = 0.2, 0.4, 0.6$, and 0.8 in panels (a) and (b), and for a final simulation time $t = 10^6$ in panel (c). The solid lines are given by Eq. (8.28) in panel (a), Eq. (8.38) in panel (b), and Eq. (8.40) in panel (c), where the integral has been computed numerically. All simulations are performed with parameters: $x_0 = 0$, $D_H = 1/2$, number of time points $M = 2^{23}$, and $N = 10^4$ trajectories.

B Fractional Brownian motion

We next consider the same observable for the fBM. The fBM is a self-similar Gaussian process with zero mean and autocorrelation as defined in Eq. (2.10), $C(t_1,t_2) = D_H\left(t_1^{2H} + t_2^{2H} - |t_1 - t_2|^{2H}\right)$ with $H \in (0,1)$. Numerous works have studied the statistical properties of fBM. They include ergodicity breaking, using the time-average square displacement, [246, 247], the generalization of the arcsine laws [213], and the PDF in confined geometries [247, 252, 253].

We start by computing the moments. The mean half occupation time is again given in Eq. (8.28) while the mean square half occupation time follows from (8.28) and (2.10), for which we find

$$\left\langle T_+(t)^2 \right\rangle = \frac{t^2}{2}\left(1 - \frac{\mathscr{B}_H}{\pi}\right) \tag{8.38}$$

where

$$\mathscr{B}_H = \int_0^1 \arctan\left(\frac{\sqrt{4u^{2H} - \left[1 + u^{2H} - (1-u)^{2H}\right]^2}}{1 + u^{2H} - (1-u)^{2H}}\right) du. \tag{8.39}$$

Consequently, the ergodicity breaking parameter EB_+ is computed from (2.54) to get

$$\mathrm{EB}_+ = 1 - \frac{2}{\pi}\mathscr{B}_H \tag{8.40}$$

Note that on setting $H = 1/2$ into (8.40) we recover $\mathrm{EB}_+ = 1/2$. In Fig. 8.2 panels (a) and (b) we compare numerical simulations of fBM, with the results of the first and second moments of the half occupation time as a function of time, for distinct values of the exponent H. In panel (c) of Fig. 8.2 we present the EB for this observable, as a function of the exponent H. In this case, we find that EB increases with H for the fBM,

which is consistent with the results for the SBM previously discussed, where greater persistence led to larger EB values. Since for $H > 1/2$ the fBM has positively correlated increments, the process is more persistent in this regime, leading to correspondingly higher values of EB.

8.4.2 Occupation time in an interval

We now turn to the occupation time in an interval and again analyze the cases of the SBM and the fBM. From previous results, it is known that when the return times to the interval are a renewal process, they are i.i.d. random variables, the PDF of $T_a(t)/t$ follows the ML distribution of order β Eq. (2.59) [68, 141, 158, 214, 254]. The parameter β of the ML distribution is obtained from the long-time limit of the first-passage time PDF $\sim t^{-1-\beta}$. Then, it follows that, in this case, the ergodicity breaking parameter for T_a corresponds to Eq. (2.61)

$$\mathrm{EB}_a^* = \frac{2\Gamma^2(1+\beta)}{\Gamma(1+2\beta)} - 1,$$

which, in the case of the SBM, $\beta = \alpha/2$ [255], and in the case of the fBM, $\beta = 1-H$ [214]. Indeed, we have seen this result in Eq. (7.31) of Chapter 7, where for the power-law spatial heterogeneous diffusion process, the PDF of the occupation time in an interval follows a ML distribution with $\beta = 1/(2-\alpha)$. In that case, the return times to the interval are a renewal process, and therefore, Eq. (2.61) holds. However, this is not the case for the fBM or the SBM.

These properties above have been recently used to study the ergodic properties for the occupation time of fBM [214]. However, since the return times to the interval are not a renewal process for the fBM, the EB parameter obtained from the ML distribution is not exact for this process. Then, the ML limit is valid solely near the Brownian limit $H = 1/2$, which the authors acknowledge in their analysis [214]. Below we find the exact expression for the EB valid for any H in the case of the fBM and α in the case of the SBM and compare it to the ML result.

A Time-dependent diffusivity and Scaled Brownian motion

In the derivation of the half occupation time, we have written the autocorrelation function for the general case of time-dependent diffusivity, Eq. (8.35). From this, the first two moments for T_a can be derived from (8.31) and (8.32). We thus find,

$$\langle T_a(t)\rangle \simeq \frac{at}{\sqrt{\pi}} \int_0^1 \left[\int_0^{zt} D(\tau)d\tau\right]^{-1/2} dz \tag{8.41}$$

and

$$\left\langle T_a(t)^2\right\rangle \simeq \frac{2a^2t^2}{\pi} \int_0^1 v dv \int_0^1 du \left[\int_0^{uvt} D(\tau)d\tau\right]^{-1/2} \left[\int_{uvt}^{vt} D(\tau)d\tau\right]^{-1/2}. \tag{8.42}$$

Both Eqs. (8.41) and (8.42) hold in the long-time limit and are valid for any time-dependent diffusivity $D(t)$, provided that the integrals converge. From them, we can

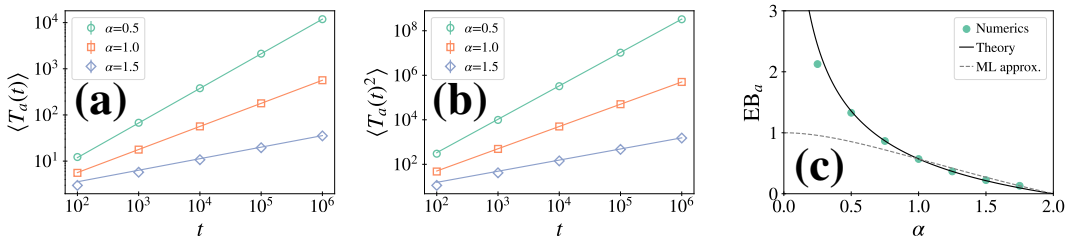


Figure 8.3: **First -(a)- second -(b)- moments, and -(c)- EB of the occupation time in an interval for the SBM**. The symbols are obtained from numerical simulations for $\alpha = 0.5, 1.0$, and 1.5 in panels (a) and (b), and for a final simulation time $t = 10^6$ in panel (c). The solid lines are given by Eq. (8.43) in panel (a), by Eq. (8.44) in panel (b), and by Eq. (8.45) in panel (c). The dashed line in panel (c) corresponds to Eq. (2.61) with $\beta = \alpha/2$.. All simulations are performed with parameters: $a = 0.5$, $x_0 = 0$, $K = 1$, time discretization of $dt = 0.1$, and $N = 10^5$ trajectories.

obtain the mean occupation time in an interval for a SBM. Using (8.35) and (8.41) we readily find

$$\langle T_a(t)\rangle \simeq \frac{2at^{1-\frac{\alpha}{2}}}{(2-\alpha)\sqrt{\pi K}} \quad \text{as} \quad t \to \infty. \tag{8.43}$$

The mean square occupation time in an interval follows from Eqs. (8.42) and (8.35), which yields

$$\left\langle T_a(t)^2\right\rangle \simeq \frac{2a^2}{K\sqrt{\pi}} \frac{\Gamma\left(\frac{1}{\alpha}-\frac{1}{2}\right)}{\alpha(2-\alpha)\Gamma(1/\alpha)} t^{2-\alpha} \quad \text{as} \quad t \to \infty. \tag{8.44}$$

Note that for $\alpha = 1$ both the first and the second moments match with the standard Brownian motion result, given by Eq. (2.41), derived in [8]. For the first moment we get $\langle T_a(t)\rangle \simeq 2a\sqrt{t}/\sqrt{\pi D}$, and for the second moment $\left\langle T_a(t)^2\right\rangle \simeq 2a^2 t/D$. The EB parameter is from (2.54) given by

$$\mathrm{EB}_a = \frac{\left\langle T_a(t)^2\right\rangle}{\langle T_a(t)\rangle^2} - 1 = \frac{\sqrt{\pi}\Gamma\left(\frac{1}{\alpha}-\frac{1}{2}\right)(2-\alpha)}{2\alpha\Gamma(1/\alpha)} - 1 \tag{8.45}$$

which is monotonically decreasing with α, in line with the results of the half occupation time for this model.

Comparing Eq. (2.61), the ML result, to Eq. (8.45), we see that the two expressions do not yield the same predictions for EB_a. Indeed, in [255], the authors find that aging changes the first-passage statistics of the SBM. Aging in this case is related to the time of the last exit time from the interval $[-a, a]$. Since the return times are linked to the first-passage PDF, it follows that the return times cannot in general be assumed to be independent and, therefore, Eq. (2.61) is not valid for the SBM, except for the Brownian case $\alpha = 1$.

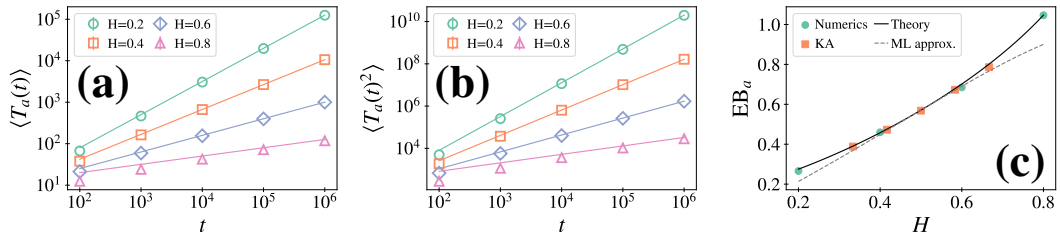


Figure 8.4: **First -(a)- second -(b)- moments, and -(c)- EB of the occupation time in an interval for the fBM**. The symbols are obtained from numerical simulations for $H = 0.2, 0.4, 0.6$, and 0.8 in panels (a) and (b), and for a final time $t = 10^6$ in panel (c). The solid lines are given by Eq. (8.46) in panel (a), by Eq. (8.47) in panel (b), and by Eq. (8.49) in panel (c). In both cases, the integrals have been numerically computed. The dashed line in panel (c) corresponds to the ML approximation (2.61) and the orange squares to data from [214]. where the integral has been computed numerically. All simulations are performed with parameters: $a = 2$, $x_0 = 0$, $D_H = 1/2$, number of time points $M = 2^{23}$, and $N = 10^4$ trajectories.

In Fig. 8.3 we compare the results of this section with numerical simulations. In the first two panels, we plot the first and second moments of the occupation time in the interval $[-0.5, 0.5]$ as a function of time, for distinct values of the exponent α, and in the third, the EB parameter. We find a good agreement between the analytic results and the numerical data. We also observe that the total trajectory time required for the simulation and the data to converge is smaller for $\alpha \to 1$, and increases for $\alpha \to 0$ and $\alpha \to 2$. This can also be seen in panel (c) where the agreement is better for $\alpha \to 1$ for a given time t. We have also included in panel (c) the prediction from Eq. (2.61), and we can see that for values of $1 < \alpha < 2$ the results provided by the ML distribution are quite similar to the exact theoretical prediction given by Eq. (8.45), being equal for $\alpha = 1$, as expected. However, the approximation breaks for $0 < \alpha < 1$, and the numerical simulations, in agreement with (8.45), confirm the deviation as $\alpha \to 0$.

B fractional Brownian motion

Finally, we analyze the occupation time in an interval for the fBM. Even if the stochastic dynamics of the SBM is not equivalent to that of the fBM, the mean occupation time is as in Eq. (8.43) but replacing α and K by $2H$ and D_H respectively. Thus,

$$\langle T_a(t)\rangle \simeq \frac{a t^{1-H}}{(1-H)\sqrt{\pi D_H}} \quad \text{as} \quad t \to \infty. \tag{8.46}$$

The mean square occupation time in the long-time limit is obtained after introducing Eq. (2.10) in (8.32) and considering the changes of variables $\tau_2 = st$ ($s \in [0,1]$) and $\tau_1 = u\tau_2$ ($u \in [0,1]$). We finally get

$$\langle T_a(t)^2\rangle \simeq \frac{2a^2 \mathscr{B}_H}{\pi D_H (1-H)} t^{2-2H} \tag{8.47}$$

with

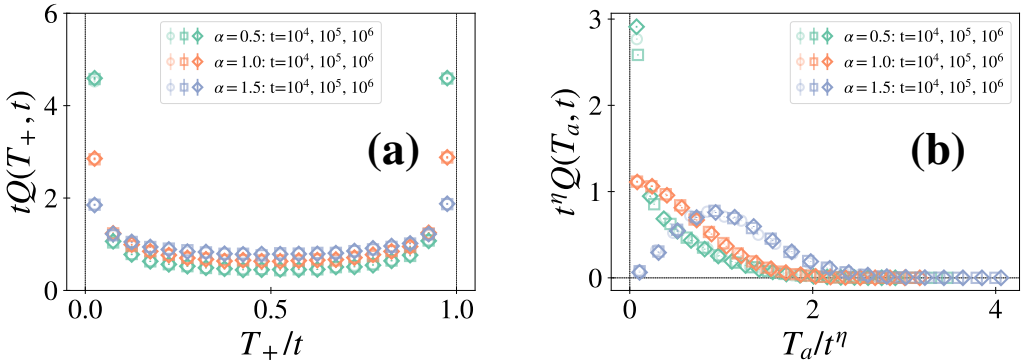


Figure 8.5: **Scaling form for T_+ -(a)- and T_a -(b)- for the SBM** for three values of $\alpha = 0.5, 1$, and 1.5 in green, orange and blue symbols respectively. For each parameter value, we show three trajectory final times: $t = 10^4, 10^5$, and 10^6 in circles, squares, and diamonds, respectively. In panel (b) $\eta = 1-\alpha/2$. The other simulation parameters are $a = 0.5$, $x_0 = 0$, $K = 1$, time discretization of $dt = 0.1$, and $N = 10^5$ trajectories.

$$\mathscr{B}_H = \int_0^1 \frac{du}{\sqrt{4u^{2H} - [1+u^{2H}-(1-u)^{2H}]^2}}. \tag{8.48}$$

The EB_a follows easily from Eq. (2.54) together with Eqs. (8.46) and (8.47)

$$\mathrm{EB}_a = 2(1-H)\mathscr{B}_H - 1. \tag{8.49}$$

Note that for $H = 1/2$ we find $\mathrm{EB}_a = \pi/2 - 1$ as it should for the Brownian motion [8].

In panels (a) and (b) of Fig. 8.4, we compare numerical simulations of fBM with the results of the first and second moments of the occupation time in the interval $[-2,2]$ as a function of time, for different values of the exponent H. We find a good agreement between the analytic results and the numerical data. We also see that the convergence to the prediction is slower for higher values of H. We plot the EB_a parameter in panel (c) of Fig. 8.4. We find a good agreement between Eq. (8.49) and the numerical data. We observe that, as expected from the results and discussion in [214] (which we include in the plot as orange squares with the label KA), the EB_a computed from the ML distribution is valid solely in the region near $H = 1/2$, where Eq. (8.49) and (2.61) provide similar results. For values of $H \to 0$ and $H \to 1$ we find that (2.61) is no longer valid. However, our result (8.49) is exact and holds for the whole range of values of H.

8.4.3 Scaling of the PDF

Since we have obtained the first and second moments of T_+ and T_a, we can then derive the scaling form of the PDFs of these observables for the SBM and fBM in the long-time limit since $\langle T_+(t)^2\rangle \sim \langle T_+(t)\rangle^2$ and $\langle T_a(t)^2\rangle \sim \langle T_a(t)\rangle^2$. Assume that in the long-time limit the PDF of T_+ has the scaling form $Q(T_+,t) \sim g_+(T_+/t^\kappa)/t^\eta$. Then,

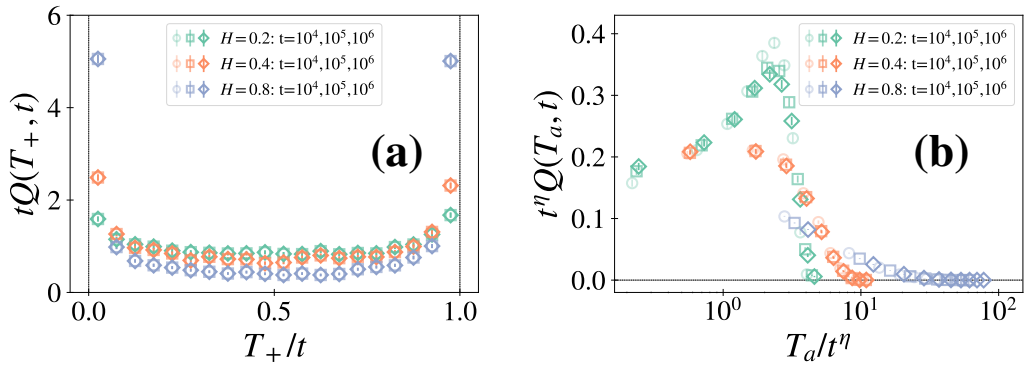


Figure 8.6: **Scaling form for T_+ -(a)- and T_a -(b)- for the fBM** for three values of $H = 0.2, 0.4$ and 0.8 in green, orange, and blue symbols respectively. For each parameter value, we show three trajectory final times: $t = 10^4, 10^5$, and 10^6 in circles, squares, and diamonds, respectively. In panel (b) $\eta = 1 - H$. The other simulation parameters are $a = 2$, $x_0 = 0$, $D_H = 1/2$, number of time points $M = 2^{23}$, and $N = 10^4$ trajectories.

$$\langle T_+(t)\rangle \sim \int_0^\infty T_+ Q(T_+,t)dT_+ = t^{2\kappa-\eta}\int_0^\infty u g_+(u)du \tag{8.50}$$

and

$$\langle T_+(t)^2\rangle \sim \int_0^\infty T^{+2} Q(T_+,t)dT_+ = t^{3\kappa-\eta}\int_0^\infty u^2 g_+(u)du. \tag{8.51}$$

Since $\langle T_+(t)\rangle \sim t$ and $\langle T_+(t)^2\rangle \sim t^2$ we have $\kappa = \eta = 1$ and the scaling is

$$Q(T_+,t) \sim \frac{1}{t} g_+\left(\frac{T_+}{t}\right), \tag{8.52}$$

for both SBM and fBM. Note that arcsine law, Eq. (2.35), and the Lamperti distribution, Eq. (2.37), obey this scaling. Proceeding analogously with T_a we get

$$Q(T_a,t) \sim \frac{1}{t^\eta} g_\eta\left(\frac{T_a}{t^\eta}\right) \tag{8.53}$$

where $\eta = 1 - \alpha/2$ for SBM and $\eta = 1 - H$ for fBM. Note also that in the Brownian limit ($\alpha = 1$ and $H = 1/2$) this scaling is in agreement with the half-Gaussian distribution.

In Figs. 8.5 and 8.6 we check the scalings (8.52) (panels (a)) and (8.53) (panels (b)) with simulations for SBM and fBM respectively. Note that the scaling functions $g_+(\cdot)$ and $g_\eta(\cdot)$ depend on the values of parameters α and H. We show that for fixed values of the parameters and different values of t, the data collapse on the same curve, proving the scalings.

8.5 Area observables

In this section, we go beyond occupation-time functionals and study the statistical properties of the area and the absolute area underneath a random walk. For the area, we compute the PDF and the first two moments, while for the absolute area, we compute the first two moments, the ergodicity breaking parameter, and the scaling form of the PDF. We will apply the results to the SBM, and fBM.

We consider the area functional as defined in Eq. (2.42) with $U(x) = x$. By considering isotropic random walks, so that $\langle x(\tau)\rangle = 0$, the first moment of the area can be written as

$$\langle A(t)\rangle = 0. \tag{8.54}$$

The second moment of the area can be written in general, from Eq. (8.2), as

$$\left\langle A(t)^2\right\rangle = \int_0^t dt_1 \int_0^t dt_2 \left\langle x(t_1)x(t_2)\right\rangle = 2\int_0^t dt_1 \int_0^{t_1} dt_2 C(t_1,t_2) \tag{8.55}$$

where $C(t_1,t_2) \equiv \langle x(t_1)x(t_2)\rangle$. We thus see that the second moment can be found from the autocorrelation function of the particle's position $C(t_1,t_2)$. For this observable, since in this case the mean value of the area is zero, it does not make sense to compute the ergodicity breaking here. This does not mean that the underlying process has no ergodicity properties, but only that the EB parameter is an observable-dependent quantity, and for the area is not defined.

Moreover, we also consider the absolute area observable. It is defined as the area below the absolute value of the trajectory with $U(x) = |x|$, as written in Eq. (2.43). In this case, our method for computing the first two moments from Eqs. (8.1) and (8.2) is especially useful since the solution of the corresponding FK equation is extremely difficult, and one cannot get a closed form equation for the moments from it. To compute the mean value of $\mathscr{A}(t)$, we need the expression for $P(x,t)$. From Eq. (8.1) and Eq. (2.43), since the underlying random walk is isotropic,

$$\langle \mathscr{A}(t)\rangle = \int_0^t \langle |x(\tau)|\rangle \, d\tau = \int_0^t d\tau \int_{-\infty}^{\infty} |x| P(x,\tau) dx = 2\int_0^t d\tau \int_0^{\infty} x P(x,\tau) dx. \tag{8.56}$$

For the second moment, from (8.2) and (2.43) it follows that

$$\left\langle \mathscr{A}(t)^2\right\rangle = 8\int_0^t d\tau_2 \int_0^{\tau_2} d\tau_1 \int_0^{\infty} x_2 dx_2 \int_0^{\infty} x_1 dx_1 P(x_2,\tau_2;x_1,\tau_1). \tag{8.57}$$

As we have done for the occupation-time statistics, the expression of the first two moments of the absolute area, can be further simplified when the underlying random walk is Gaussian. By inserting Eq. (8.13) into Eq. (8.56) and integrating over x we get

$$\langle \mathscr{A}(t)\rangle = \sqrt{\frac{2}{\pi}} \int_0^t \sqrt{C(\tau,\tau)} d\tau = \sqrt{\frac{2}{\pi}} \int_0^t \sqrt{\langle x^2(\tau)\rangle} d\tau. \tag{8.58}$$

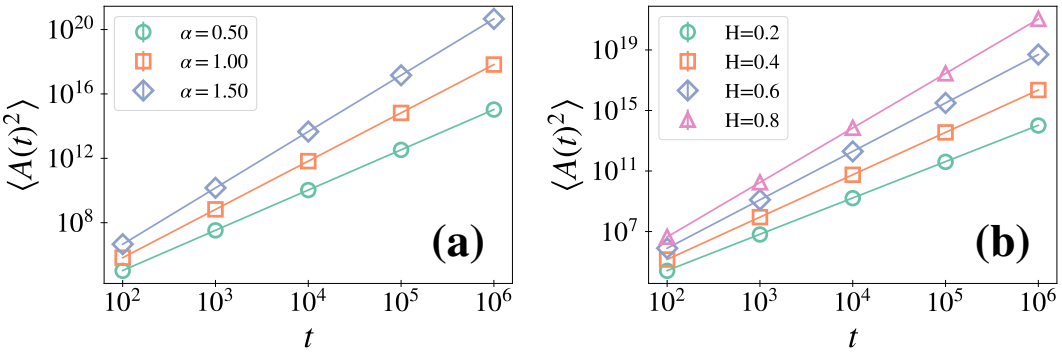


Figure 8.7: **Second moment of the area for the SBM -(a)- and fBM -(b)-.** In panel (a), SBM, the symbols are obtained from numerical simulations for $\alpha = 0.5, 1.0$, and 1.5; The solid lines are given by Eq. (8.60); the simulation parameters are: $x_0 = 0$, $K = 1$, time discretization of $dt = 0.1$, and $N = 10^5$ trajectories. In panel (b), fBM, the symbols are obtained from numerical simulations for $H = 0.2, 0.4, 0.6$, and 0.8; the solid lines are given by Eq. (8.61); the simulation parameters are: $x_0 = 0$, $D_H = 1/2$, number of time points $M = 2^{23}$, and $N = 10^5$ trajectories.

Thus, we can find the mean absolute area in terms of the MSD of the random walk. Doing the same for the second moment from Eqs. (8.14) and (8.57), and performing the integrals over x_2 and x_1 we find

$$\langle \mathscr{A}(t)^2 \rangle = \frac{2}{\pi} \int_0^t dt_2 \int_0^{t_2} dt_1 C(t_2,t_1) \Psi(t_2,t_1) \tag{8.59}$$

where

$$\Psi(t_2,t_1) = \pi - 2\arctan\left[\sqrt{\frac{C(t_2,t_2)C(t_1,t_1)}{C(t_2,t_1)^2} - 1}\right] + 2\sqrt{\frac{C(t_2,t_2)C(t_1,t_1)}{C(t_2,t_1)^2} - 1}.$$

Therefore, we have found an expression for the mean square absolute area under a Gaussian process in terms of its autocorrelation function. Note that while Eqs. (8.56) and (8.57) hold for any random walk, Eqs. (8.58) and (8.59) are valid only for Gaussian processes.

8.5.1 Area

A Scaled Brownian motion

Combining Eqs. (8.35) and (8.55), we find for the SBM

$$\langle A(t)^2 \rangle = 2\alpha K \int_0^t (t-t')^2 (t')^{\alpha-1} dt' = \frac{4Kt^{\alpha+2}}{(\alpha+1)(\alpha+2)}. \tag{8.60}$$

Note that for $\alpha = 1$ Eq. (8.60) reduces to (2.44) as expected. In Fig. 8.7(a) we verify the analytical results for $\langle A^2(t) \rangle$ with numerical simulations. These results show

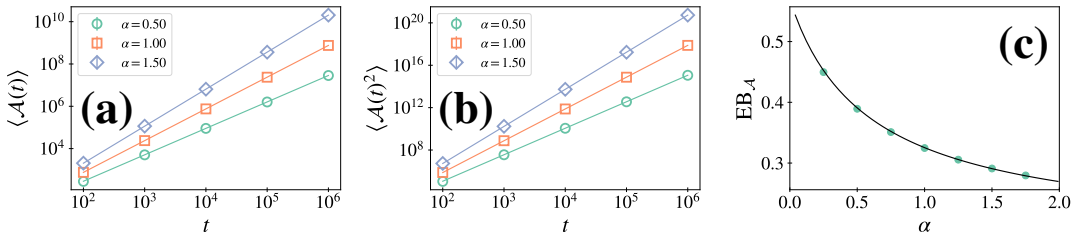


Figure 8.8: **First -(a)- and second -(b)- moments, and -(c)- EB parameter of the absolute area for the SBM** The symbols are obtained from numerical simulations for $\alpha = 0.5, 1.0$, and 1.5 in panels (a) and (b), and for a final simulation time $t = 10^6$ in panel (c). The solid lines are given by Eq. (8.62) in panel (a), by Eq. (8.63) in panel (b), and by Eq. (8.64) in panel (c). All simulations are performed with parameters: $x_0 = 0$, $K = 1$, time discretization of $dt = 0.1$, and $N = 10^5$ trajectories.

that subdiffusive SBM ($\alpha < 1$) leads to a slower growth in the variance of the area, while superdiffusive SBM ($\alpha > 1$) leads to a faster growth in the variance of the area, compared to the Brownian case ($\alpha = 1$).

B fractional Brownian motion

Next we consider the fBM, as before, its autocorrelation is given by Eq. (2.10), which, together with Eq. (8.55), the second moment of the area is

$$\begin{aligned} \langle A(t)^2 \rangle &= \int_0^t dt_1 \int_0^t dt_2 D_H \left(t_1^{2H} + t_2^{2H} - |t_1 - t_2|^{2H} \right) \\ &= \frac{2D_H}{2H+1} t^{2H+2} - 2D_H \int_0^t dt_1 \int_0^{t_1} dt_2 (t_1 - t_2)^{2H} = \frac{D_H t^{2H+2}}{H+1}. \end{aligned} \tag{8.61}$$

In Fig. 8.7(b) we verify the analytical results for $\langle A^2(t) \rangle$ with numerical simulations. In this case, we also find that subdiffusive fBM ($H < 1/2$) leads to a slower growth in the variance of the area, while superdiffusive fBM ($H > 1/2$) leads to a faster one, compared to the Brownian case ($H = 1/2$). Thus, the area provides a useful observable to distinguish persistent and antipersistent dynamics through their accumulated effect over time.

8.5.2 Absolute Area

A Absolute area under SBM

To compute the first two moments of the absolute area, we employ the formulas provided by Eqs. (8.58) and (8.59). The first moment can be readily found from Eq. (8.35), which yields

$$\langle \mathscr{A}(t) \rangle = \frac{4}{2+\alpha} \sqrt{\frac{K}{\pi}} t^{1+\frac{\alpha}{2}} \tag{8.62}$$

but the second moment needs some care, where we detail the calculation in Appendix F where we find that

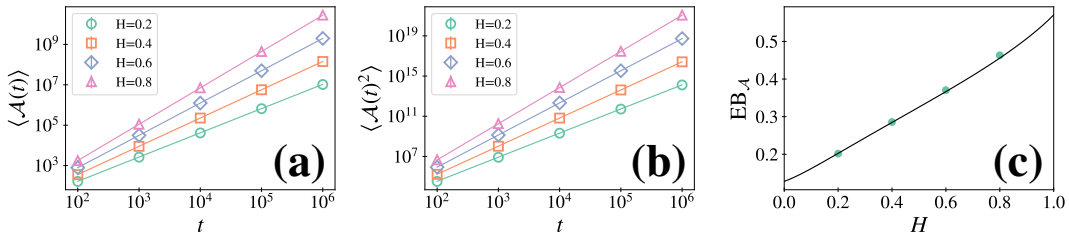


Figure 8.9: **First -(a)- and second -(b)- moments, and -(c)- EB parameter of the absolute area for the fBM.** The symbols are obtained from numerical simulations for $H = 0.2, 0.4, 0.6$ and 0.8 in panels (a) and (b), and for a final simulation time $t = 10^6$ in panel (c). The solid lines are given by Eq. (8.65) in panel (a), by Eq. (8.65) in panel (b), and by Eq. (8.66) in panel (c), where the integral has been computed numerically. All simulations are performed with parameters: $x_0 = 0$, $D_H = 1/2$, number of time points $M = 2^{23}$, and $N = 10^5$ trajectories.

$$\left\langle \mathscr{A}(t)^2 \right\rangle = \frac{4Kt^{\alpha+2}}{(\alpha+1)(\alpha+2)} \left[1 + \frac{1}{2\sqrt{\pi}} \frac{\Gamma\left(\frac{1}{2}+\frac{1}{\alpha}\right)}{\Gamma\left(2+\frac{1}{\alpha}\right)} \right]. \tag{8.63}$$

The EB parameter follows easily from (2.54) as

$$\mathrm{EB}_{\mathscr{A}} = \frac{\pi(\alpha+2)}{4(\alpha+1)} \left[1 + \frac{1}{2\sqrt{\pi}} \frac{\Gamma\left(\frac{1}{2}+\frac{1}{\alpha}\right)}{\Gamma\left(2+\frac{1}{\alpha}\right)} \right] - 1. \tag{8.64}$$

Note that by setting $\alpha = 1$, Eq. (8.64) reduces to (2.55). EB decreases monotonically as α increases from 0 to 2, which is the same behavior as the EB parameter for the half occupation time and the occupation time in an interval. In Fig. 8.8 we show a comparison between the theoretical values. In the numerical calculation of EB, we can see that convergence towards the asymptotic value in the long-time limit is rapid.

B Absolute area under fBM

The mean value of the absolute area for a fBM follows easily from introducing the autocorrelation (2.10) into (8.58). To obtain the second moment, we insert (2.10) into (8.59), and using again the variables $u = \tau_1/\tau_2$ and $v = \tau_2/t$ we write, after integrating over v,

$$\left\langle \mathscr{A}(t) \right\rangle = \frac{2}{1+H}\sqrt{\frac{D_H}{\pi}}t^{1+H}, \quad \left\langle \mathscr{A}(t)^2 \right\rangle = \frac{D_H \lambda_H}{(H+1)\pi}t^{2+2H} \tag{8.65}$$

where the constant λ_H is

$$\lambda_H = \pi - 2\int_0^1 \psi(u) \arctan\left[\frac{\Phi(u)}{\psi(u)}\right] du + 2\int_0^1 \Phi(u) du$$

with

$$\psi(u) = 1 + u^{2H} - (1-u)^{2H}, \quad \Phi(u) = \sqrt{4u^{2H} - \psi(u)^2}.$$

The ergodicity breaking parameter is obtained from (8.65)

$$\mathrm{EB}_{\mathscr{A}} = \frac{1+H}{4}\lambda_H - 1. \tag{8.66}$$

In Fig. 8.9, we compare the above results with numerical simulations, showing excellent agreement. We see that in this case, in agreement with the EB of the half occupation time and the occupation time in an interval, the ergodicity breaking parameter of the absolute area increases with H. Again, this is because the persistence of the fBM increases with H, and thus the fluctuations between trajectories regarding $\mathscr{A}$ are enhanced.

C EB parameter discussion

It is worthy to compare the behavior of the EB parameter for $\mathscr{A}$ across the models presented in this chapter. In Fig. 8.8(c), we can see that for the SBM the EB parameter decreases with α. Since EB is a measure of the variability between trajectories regarding a certain observable this means that the lower the α the higher fluctuations of $\mathscr{A}$ for each trajectory. For the SBM, since $\alpha \in (0,1)$, $D(t)$ decreases with time, making escaping from a given region progressively harder, and thus enhancing differences in $\mathscr{A}$ between trajectories. This effect is more pronounced at lower values of α, and hence the increase in EB. Moreover, for the fBM we can see in Fig. 8.9(c) that the EB of $\mathscr{A}$ increases with H. This result is in line with the previous two, since the persistence of the fBM increases with H, and thus EB increases too.

Note that an increase of the EB parameter means that the value of the functional is less reproducible from one trajectory to another. In the case of $\mathscr{A}$, this means that different particles accumulate very different values of the total distance from the origin. On the other hand, a decrease of EB means that the observable becomes more self-averaging, in the sense that the trajectory-to-trajectory fluctuations of $\mathscr{A}$ become smaller. Therefore, EB gives information on how reliable a given time-integrated observable is when measured from single trajectories. Since the EB parameter is a measure that depends on the observable, thus depending on what is being measured, as we have seen, the same underlying random walk can give rise to different EB behaviors. This means that the choice of observable can be crucial in order to obtain and analyze data.

In this sense, we can further compare these results to the EB parameter previously obtained for the other functionals of the random walk, the half occupation time T_+, or the occupation time in an interval T_a. We can see that for the SBM, and fBM, the EB of the three functionals has the same qualitative behavior with α (or H). This, however, is not a universal result. In [7] we show that for the case of spatial heterogeneity the EB of the absolute area $\mathscr{A}$ increases with the heterogeneity parameter α, while in Chapter 7 we have seen that it decreases with α for T_+ and T_a. This comparison highlights the role of the functional of study, and how the same underlying random walk gives rise to different ergodic behaviors depending on the observable.

From a physical point of view, different microscopic mechanisms can lead to different behaviors of EB. This is useful in applications because two processes can have

similar MSD scaling but different fluctuations of time-integrated observables. Thus, quantities such as $\mathscr{A}$ and the occupation times and their related EB parameter can help distinguish between different mechanisms of anomalous transport in single-particle tracking experiments, for instance in crowded biological media, gels, or heterogeneous porous materials.

8.5.3 Scaling of the PDF

In Sec. 8.5.1 and Sec. 8.5.2, we have derived the first two moments of A and $\mathscr{A}$ for two Gaussian processes, the SBM and the fBM. As we have done for the occupation time functionals, we can study the general properties of the PDFs of A and $\mathscr{A}$ in both models. To do so we begin by connecting the MSD of the random walk with the second moment of A and $\mathscr{A}$. Suppose that ν is the exponent of the MSD: $\langle x(t)^2 \rangle \sim t^{\nu}$. Rewriting the second moment of the area (or absolute area), for all processes studied in this work, in terms of their corresponding ν we find that the scaling is as

$$\langle Z(t)^2 \rangle \sim t^{2+\nu}, \tag{8.67}$$

where Z is either A or $\mathscr{A}$. To understand this result, recall that by the definition of ν we have $x \sim t^{\nu/2}$, and then $Z \sim \int^t \tau^{\nu/2} d\tau \sim t^{1+\nu/2}$, yielding the $t^{2+\nu}$ scaling for the second moment. Note that the second moment of both the area and the absolute area has the same temporal scaling. In the case of the absolute area, we can follow the same reasoning to find that the scaling of the first moment goes as $\langle \mathscr{A}(t) \rangle \sim t^{1+\nu/2}$. Then, we see that for the absolute area the first two moments obey the simple scaling $\langle \mathscr{A}(t)^2 \rangle \sim \langle \mathscr{A}(t) \rangle^2$.

Once we have found a general scaling for the moments of A and $\mathscr{A}$, we can compute the scaling of the $Q(Z,t)$. Assume that in the long-time limit the PDF of $Z(t)$ has the scaling form $Q(Z,t) \sim t^{-\eta} g(Z/t^{\rho})$ where $g(\cdot)$ is the scaling function and the exponents η and ρ have to be found. Since the integral $\int_{-\infty}^{\infty} Q(Z,t) dZ = t^{\rho-\eta} \int_{-\infty}^{\infty} h(u) du$ must be time-independent (and equal to 1), both exponents must be equal, and therefore $\rho = \eta$. We can determine the remaining exponent through the scaling of the second moment, which we know. The second moment is $\langle Z(t)^2 \rangle = \int_{-\infty}^{\infty} Z^2 Q(Z,t) dZ \sim t^{2\eta} \int_{-\infty}^{\infty} u^2 h(u) du$. Comparing this scaling with Eq. (8.67) we have $\eta = 1 + \nu/2$. Thus, we have obtained a general scaling for both the PDF of A and $\mathscr{A}$,

$$Q(Z,t) \sim \frac{1}{t^{1+\frac{\nu}{2}}} g_{\nu}\left(\frac{Z}{t^{1+\frac{\nu}{2}}} \right) \tag{8.68}$$

in terms of the scaling exponent of the MSD of the random walk ν. Note that $g_{\nu}(\cdot)$ is different for the different models as well as observables, and, in general, depends on ν. The specific values of ν for the models discussed in this work are: $\nu_{BM} = 1$, $\nu_{SBM} = \alpha$, $\nu_{fBM} = 2H$.

For the area A under a Gaussian process, we can go beyond the scaling and derive a closed form expression for $Q(A,t)$. If $x(t)$ follows a Gaussian process with zero mean and autocorrelation $C(t_1,t_2)$, the characteristic functional of $x(t)$ is given by [245] and is written in Eq. (8.11). On the other hand, the characteristic function of $A(t)$ is its Fourier transform

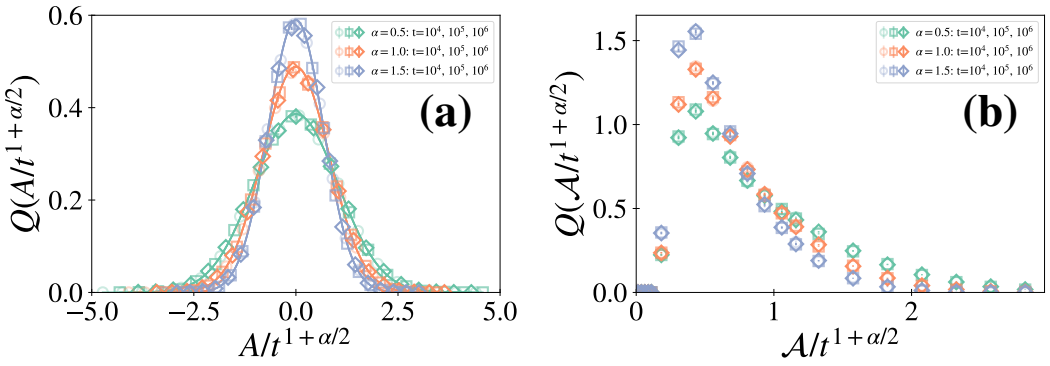


Figure 8.10: **Scaling form for A -(a)- and $\mathscr{A}$ for the SBM.** for three values of $\alpha = 0.5, 1$, and 1.5 in green, orange and blue symbols respectively. For each parameter value, we show three trajectory final times: $t = 10^4, 10^5$, and 10^6 in circles, squares, and diamonds, respectively. In panel (a) the solid lines correspond to Eq. (8.73). The other simulation parameters are $x_0 = 0$, $K = 1$, time discretization of $dt = 0.1$, and $N = 10^5$ trajectories.

$$Q(k,t) = \mathscr{F}_{Z\to k}[Q(A,t)] = \int_{-\infty}^{\infty} e^{ikA} Q(A,t) dA = \left\langle e^{ikA(t)} \right\rangle. \tag{8.69}$$

Eq. (8.69) can be linked to the characteristic functional of $x(t)$ by considering $f(\tau) = k\mathbb{1}_{[0,t]}(\tau)$ in (8.11), where $\mathbb{1}_{[a,b]}(x)$ is the indicator function,

$$Q(k,t) = \left\langle e^{ikA(t)} \right\rangle = \left\langle e^{ik\int_0^t x(\tau)d\tau} \right\rangle = e^{-\frac{k^2}{2}\langle A(t)^2\rangle}. \tag{8.70}$$

Performing the inverse Fourier transform, we finally find

$$Q(A,t) = \frac{1}{\sqrt{2\pi\langle A(t)^2\rangle}} e^{-\frac{A^2}{2\langle A(t)^2\rangle}}. \tag{8.71}$$

This result is expected: since $A(t)$ is the sum of Gaussian processes $x(t)$, then $A(t)$ is also a Gaussian process. Consequently, the PDF of A must be a Gaussian distribution. Notice that indeed Eq. (8.71) fulfills the scaling derived in Eq. (8.68). For the models discussed in this work, we get

$$Q(A,t)_{\text{BM}} = \frac{1}{\sqrt{4\pi D t^3/3}} e^{-\frac{3A^2}{4Dt^3}}, \tag{8.72}$$

$$Q(A,t)_{\text{SBM}} = \sqrt{\frac{(\alpha+1)(\alpha+2)}{8\pi K t^{\alpha+2}}} \exp\left[-\frac{(\alpha+1)(\alpha+2)}{8Kt^{\alpha+2}}A^2\right], \tag{8.73}$$

$$Q(A,t)_{\text{fBM}} = \sqrt{\frac{H+1}{2\pi D_H t^{2H+2}}} \exp\left[-\frac{(H+1)A^2}{2D_H t^{2H+2}}\right]. \tag{8.74}$$

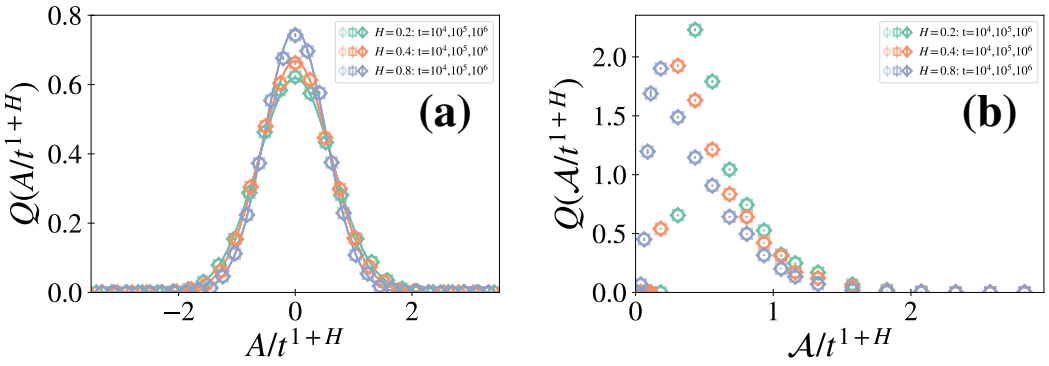


Figure 8.11: **Scaling form for A -(a)- and $\mathscr{A}$ -(b)- for the fBM.** for three values of $H = 0.2, 0.4$ and 0.8 in green, orange, and blue symbols respectively. For each parameter value, we show three trajectory final times: $t = 10^4, 10^5$, and 10^6 in circles, squares, and diamonds, respectively. In panel (a) the solid lines correspond to Eq. (8.74). The other simulation parameters are $x_0 = 0$, $D_H = 1/2$, number of time points $M = 2^{23}$, and $N = 10^5$ trajectories.

We have included the results for the BM for comparison. The results for the area under a BM connect to the random acceleration process (when the particle's velocity is a Wiener process or the acceleration is a white Gaussian noise) [150], where the particle position follows the same distribution as (8.72). In Fig. 8.10(a), we study the scaling of the $Q(A,t)$ at different simulation times for the SBM, and in Fig. 8.11(a) for the fBM. In both cases, we see that the scaling derived in Eq. (8.68) is satisfied. Moreover, in both panels we compare the data to a corresponding Gaussian PDF, Eq. (8.71). Finally, in Figs.8.10(b), and 8.11(b) we plot the PDF for the absolute area $\mathscr{A}$, and again we can see that the scaling predicted by Eq. (8.68) is fulfilled.

8.6 Summary of results

In this chapter, we have made use of the Kac formalism to derive the first two moments of positive stochastic functionals in terms of the one-time and two-time PDFs of the underlying random walk. This formalism also allows us to show that observables of stationary random walks are ergodic, i.e., their PDFs converge to a Dirac delta function in the long-time limit. We have explicitly considered some relevant examples of Gaussian random walks, the SBM and the fBM, by applying the general expressions for the first two moments to study the half occupation time, the occupation time in an interval, the area, and the absolute area. We have found that the temporal scaling of the area functionals is universal for the models studied, with different prefactors of the moments and EB parameter.

We have further compared the results for the EB_a parameter for SBM and fBM with those from the ML distribution for occupation time in an interval. We have seen that the ML distribution is not in general the PDF of the occupation time in an interval for the SBM and fBM, but only for specific values of the exponents α and H.

Finally, since the occupation times and area observables are such that the second

moment scales as the square of the first moment, we can infer a simple scaling form of their corresponding PDFs in the long-time limit. We have found that for the area under a Gaussian process, we can derive an exact expression for the PDF, which is a Gaussian distribution with zero mean and variance given by the second moment of A.

IV Concluding statements

9 **Conclusions** 169

A **Numerical simulation methods** 173
- A.1 Trajectory generation 174
- A.2 Numerical evaluation of functionals 177
- A.3 Ensemble statistics 178

B **PDF of the occupation time in an interval** 179
- B.1 Left edge regime 180
- B.2 Right edge regime 182
- B.3 Central bulk regime 183

C **Limiting PDF for a finite moment resetting distribution** 185

D **Limiting PDF of the half occupation time under general resetting** ... 187

E **Probability density functions of occupation times in heterogeneous media** 191
- E.1 Derivation of the half occupation time distribution 191
- E.2 Derivation of the distribution of the occupation time in an interval 194

F **Second moment of the absolute area under a SBM** 197

Bibliography 219

9

CONCLUSIONS

In this thesis, we have characterized diffusion and anomalous diffusion random walks in different contexts, with a particular focus on the effects of stochastic resetting and the ergodic properties of the occupation time statistics of such processes. On the one hand, we have studied the effects of resetting on the efficiency of search processes, characterized by the mean first-passage time to a target. We have also provided general results for stochastic functionals for random walks undergoing stochastic resetting, which can be applied to a wide variety of observables and underlying dynamics. We have studied several models that give rise to anomalous diffusion in the macroscopic limit, but with a different microscopic dynamics, and we have analyzed the differences between them in terms of the occupation times and area observables.

Globally, we have seen that stochastic functionals provide a powerful way to distinguish between random-walk models that may look similar if one only considers standard transport observables. The MSD and the propagator are fundamental quantities, but they do not always reveal how a trajectory explores space in time. This is particularly relevant in anomalous diffusion, where different microscopic mechanisms can lead to similar scaling laws at the ensemble level. Throughout the thesis we have seen that occupation times, first-passage observables, and area functionals give complementary information: they quantify how long the particle remains in a region, how efficiently it reaches a target, how much it accumulates along its trajectory, and whether time-averaged quantities remain random in the long-time limit. In this sense, the results of the thesis contribute to the broader problem of using trajectory-level observables to distinguish anomalous diffusion mechanisms that would otherwise appear similar at the level of the MSD or the propagator, potentially helping to identify the underlying dynamics from experimental data.

By focusing on different models and observables we are able to compare different

mechanisms that modify standard diffusion: intermittent random walks, stochastic resetting, non-Markovian waiting times, spatial heterogeneity, time-dependent diffusivity, or temporal correlations. In some cases, these mechanisms produce similar qualitative effects, such as transitions between ergodic and non-ergodic regimes. In other cases, the behavior depends strongly on the observable considered. For example, the same underlying random walk can give different values and even different trends of the EB parameter depending on whether one studies the half occupation time, the occupation time in an interval, or the absolute area, showing the importance of the choice of observable in the analysis of stochastic trajectories. As a particular example, in Chapter 8 we have seen that the ergodic properties of two Gaussian processes, the SBM and fBM, have opposite trends of the EB parameter in terms of the anomalous diffusion exponent of each of the models, showing how stochastic functionals capture relevant information of the underlying dynamics.

This comparison provides a useful way to interpret the results of the thesis. First-passage times, occupation times, and area observables are all functionals of the trajectory, but they do not answer the same physical question. The first-passage time is naturally related to search efficiency, while occupation times describe residence properties and area observables quantify accumulated displacement along the path. Therefore, the role of these functionals is not only to provide additional observations, but to reveal different aspects of the same dynamics. This perspective is also relevant beyond the theoretical physical models considered here, for example in movement ecology, where animal trajectories may encode information about search strategies, residence patterns, home ranges, or changes in behavioral state. In that context, trajectory observables such as first-passage times, occupation times, or related residence measures provide a way to quantify behavioral information that is not captured by displacement statistics alone. For example, Chapters 3 and 4 show how resetting changes search properties through the reset state or reset position, while Chapters 5, 7, and 8 show that occupation and area statistics can distinguish mechanisms that may have similar transport scaling. In this light, we can see that the EB parameter should not be understood as a label of the process alone, but as a property of a given functional of the trajectory. A process may show weak ergodicity breaking for one observable and a different degree of self-averaging for another one. Thus, the conclusions about ergodicity obtained here are linked to the particular stochastic functional being studied, which is also why computing several functionals is useful.

Throughout this work, we have employed different formalisms, which are complementary to one another, with the choice between them being the tractability of the problem at hand. The Feynman-Kac formalism is a powerful tool to derive the distribution of stochastic functionals, and it can be applied to a wide variety of processes and observables, however, as we have seen in Chapters 5 and 7, it can be difficult to solve the resulting equations. In particular, note that the first-passage time studied in Chapters 3 and 4 can be formulated as a stochastic functional, and thus the Feynman-Kac formalism can be used to study it. However, in practice, the first-passage problem is often more easily solved by other methods, such as renewal theory. In this sense, the Feynman-Kac formalism is a general framework that can be applied to a wide variety of problems, but it is not always the most efficient method to solve them. Knowing the full distribution of a stochastic functional is often more information than needed, and

in many cases, it is enough to know some moments of the distribution. In this sense, in Chapter 8 we have seen that the n-th moment of the stochastic functional can be obtained by means of the n-th time PDF of the underlying process. In this work, we have applied this procedure to Gaussian processes, but the method can be applied in general to any process for which the n-th time PDF is known.

On top of studying the behavior of different microscopic mechanisms, we have also investigated how stochastic resetting modifies the properties of the underlying process, be its first-passage properties, occupation times, or other observables. In particular, in Chapters 3 and 4 we have seen how the state at which the walker resets, be its position or its movement mode, have a strong influence on the first-passage properties of the process. On the other hand, in Chapters 5 and 6 we have seen how stochastic resetting can induce transitions between ergodic and non-ergodic regimes, and how the tails of the resetting time distribution affect the long-time behavior of the moments and limiting distributions of the stochastic functionals. In this sense, stochastic resetting appears as a powerful mechanism to modify the properties of the underlying process, and it can be used to optimize search processes or to induce transitions in the ergodic properties of the system.

Throughout this work, we have tried to provide general results before particularizing to specific models and observables, with the aim of giving the most general framework possible. At the same time however, this work has a limited scope. While all frameworks discussed here are general and can potentially be extended to $n-$dimensions, the analysis has been restricted to one-dimensional models. Moreover, the processes studied are idealized stochastic processes that are tractable analytically. This is a simplification with respect to many experimental systems, where trajectories may be finite, missing data points, or affected by several mechanisms at the same time. Many of the results also concern long-time limiting distributions or asymptotic values, and finite-time corrections may be relevant in applications. Moreover, the ergodic properties have been quantified mainly through the EB parameter and through limiting distributions of normalized functionals. These quantities are useful because they are explicit and comparable between models, but we recognize that they do not exhaust all possible measures of ergodicity nor all relevant trajectory observables. These limitations also point to several open problems that could be addressed with the methods developed here, such as extending the results to higher-dimensional geometries, or studying other observables of interest. From a more applied perspective, it would be interesting to use this formalism to analyze single particle trajectories for example of particles in crowded cells, porous or heterogeneous materials, or animal movement data, where residence and first-passage statistics may reveal trapping, spatial heterogeneity, or changes in search behavior.

A recurring theme of this work has been that the characterization of stochastic trajectories depends strongly on what is used to analyze them. Then, we have seen that a process is not completely described by labeling it as subdiffusive, superdiffusive, Gaussian, non-Gaussian, Markovian, or non-Markovian. These labels certainly contain relevant aspects of the dynamics, but they do not fully inform how a single trajectory explores space, how long it remains in a given region, or whether a time average is representative of the ensemble. Overall, the results and frameworks presented in this work underscore that stochastic functionals, including first-passage times, occupation-time

statistics, area observables, and related quantities, are powerful tools for characterizing random walks beyond transport properties and giving a more complete picture of the underlying dynamics.

A

NUMERICAL SIMULATION METHODS

A.1 Trajectory generation 174
A.1.1 Chapter 3: Intermittent random walks under stochastic resetting 174
A.1.2 Chapter 4: Stochastic resetting to random positions 174
A.1.3 Chapter 5: Occupation time statistics for non-Markovian random walks 175
A.1.4 Chapter 6: Stochastic functionals under general resetting 176
A.1.5 Chapter 7: Occupation times in heterogeneous media 176
A.1.6 Chapter 8: Occupation and area observables in Gaussian anomalous diffusion 177
A.2 Numerical evaluation of functionals 177
A.3 Ensemble statistics 178

The numerical results presented in this thesis were obtained by Monte Carlo simulation of stochastic trajectories. Although the specific dynamics varies from chapter to chapter, the numerical procedure is always the same at a general level: an ensemble of trajectories is generated up to prescribed observation times, the relevant observables are evaluated along each trajectory, and the reported quantities are then obtained from ensemble averages, moments, and normalized histograms. In this way, there are three conceptually distinct steps: trajectory generation, evaluation of path functionals, and ensemble postprocessing. This structure is common to all the stochastic models considered in the thesis.

Below, we describe the numerical methods used for each of these steps. In all cases, N denotes the number of simulated trajectories, M the number of time steps, t the observation time, ξ a Gaussian random variable with zero mean and unit variance, and when time discretization is required, Δ_t denotes the numerical time step. We will

also denote by x_j the position of the particle at time $t_j = j\Delta_t$.

A.1 Trajectory generation

A.1.1 Chapter 3: Intermittent random walks under stochastic resetting

In Chapter 3, the particle alternates between a diffusive phase and a ballistic relocation phase. During the diffusive phase, the position evolves through a diffusive process with diffusivity D. On the other hand, during the relocation phase, the particle moves at constant speed v in the positive or negative direction chosen with equal probability. The durations of both phases are exponentially distributed, with mean times τ_D and τ_v, respectively. Moreover, the process may also be interrupted by Poissonian resetting to the initial position.

Numerically, we first sample a duration of the initial phase from the exponential distribution with parameter τ_i ($i = D$ for the diffusive phase and $i = v$ for the ballistic phase). Then, we generate the corresponding segment of the trajectory according to the chosen phase. When the end of the segment is reached, a new phase duration is sampled for the complementary phase, and the process is repeated until the final observation time is reached. In the presence of resetting, reset times are sampled from an exponential distribution with rate r, and whenever a reset occurs, the current phase is interrupted and the particle is instantaneously returned to the resetting position x_0, and a new phase duration is sampled from the distribution corresponding to the initial condition of the trajectory. In the diffusive phase, the motion is updated by the Euler-Maruyama scheme

$$x_{j+1} = x_j + \sqrt{2D\Delta_t}\,\xi_{j+1}. \tag{A.1}$$

In the ballistic phase, the particle evolves deterministically as

$$x_{j+1} = x_j + \mathrm{sign}(u)v\Delta_t, \tag{A.2}$$

where $\mathrm{sign}(u) = \pm 1$ is the direction of the ballistic motion, which we generate by sampling a uniform random variable $u \sim U(-1,1)$ from a uniform distribution over $(-1,1)$ at the beginning of each ballistic phase, when the phase duration is sampled. First-passage observables are obtained by monitoring the first crossing of the target position. In practice, the first-passage time is recorded when a position lies on top or on the opposite side of the target when the walker is in the diffusive phase. Then the trajectory is interrupted.

A.1.2 Chapter 4: Stochastic resetting to random positions

In Chapter 4, the underlying motion is Brownian with diffusion constant D, while resetting takes place at Poissonian times with rate r to positions sampled from a given spatial distribution $f(x_0)$. For each trajectory, the particle starts at a given initial position x_0, which is fixed. Then, we sample a reset time according to an exponential distribution with rate r. The particle then evolves until the next reset time, when it is instantaneously returned to a new position sampled from $f(x_0)$, and the process is

repeated until the final observation time is reached. As before, the Brownian evolution is implemented by the Euler-Maruyama scheme

$$x_{j+1} = x_j + \sqrt{2D\Delta_t}\,\xi_{j+1}. \tag{A.3}$$

Again, the first-passage time is determined from the first crossing of the target position, and the trajectory is interrupted at that time.

A.1.3 Chapter 5: Occupation time statistics for non-Markovian random walks

In Chapter 5, we simulate a CTRW with different waiting time distributions. Moreover, the trajectory may be subjected to exponential resetting, with resetting times sampled from an exponential distribution with reset rate r. To simulate a single step of the CTRW process for a given particle, we compute the time increment t_i based on the waiting time PDF $\varphi(t)$:

$$t_i = -\langle\tau\rangle \ln u_i \qquad \text{if} \quad \varphi(t) = e^{-t/\langle\tau\rangle}/\langle\tau\rangle \tag{A.4}$$

$$t_i = \frac{t_0}{(1-u_i)^{1/\alpha}} \qquad \text{if} \quad \varphi(t) = \begin{cases} 0, & t < t_0 \\ \frac{\alpha t_0^\alpha}{t^{1+\alpha}}, & t > t_0 \end{cases} \tag{A.5}$$

$$t_i = \tau^* z_i w_i^{\frac{1}{\alpha}} \qquad \text{if} \quad \varphi(t) = \frac{t^{\alpha-1}}{\tau^{*\alpha}} E_{\alpha,\alpha}\left(-\frac{t^\alpha}{\tau^{*\alpha}}\right) \tag{A.6}$$

where $u_i \sim U(0,1)$ is a random variable drawn from a uniform distribution over $(0,1)$, $z_i = -\ln(u_1)$, and $w_i = \frac{\sin(\pi\alpha)}{\tan(\pi\alpha u_2)} - \cos(\pi\alpha)$. The indices u_1 and u_2 indicate the need for two independent uniform random variables to compute w_i and z_i at each time step. The generation of random numbers from the exponential and fat-tailed distributions is based on the cumulative distribution function. For details on the Mittag-Leffler random number generation, see [234]. Once the waiting time is computed, we ensure that it does not exceed the maximum simulation time so that all trajectories are evaluated at the same temporal point. The particle then takes a step of size σ with equal probability (1/2) to the left or right, determined by a uniform random variable.

To compute the time evolution of a single particle, we initialize its position at x_0 and iteratively perform CTRW steps until the maximum simulation time t_{max} is reached. For each trajectory, we track the desired observables, T_a and T_+, repeating this process over N realizations.

For the CTRW model with exponential resetting, the procedure remains the same, except that we sample the resetting times, after which the particle is returned to its initial position x_0, before resuming its evolution, computing a new waiting time and step size. We note that whenever the waiting time of the particle exceeds the time remaining until the next reset, the particle is returned to its initial position at the reset time, and a new waiting time is sampled. The same procedure is applied if the waiting time exceeds the maximum simulation time, in which case the trajectory is interrupted. We do it in this way because after a reset the process starts anew.

A.1.4 Chapter 6: Stochastic functionals under general resetting

In Chapter 6, the underlying walk is either Brownian or subdiffusive, with resetting times that are drawn from a general distribution. For the diffusive case, the trajectory is generated by the Euler-Maruyama scheme, as described in A.1.1 and A.1.2. For the CTRW case, the trajectory is generated by iteratively sampling waiting times and jump lengths until the maximum simulation time is reached, as described in A.1.3.

For the resetting times, the exponential and power-law distributions are generated from the cumulative distribution function; for random number generation of Mittag-Leffler-type random variables, see [234], and for one-sided Lévy stable random numbers, see [236].

A.1.5 Chapter 7: Occupation times in heterogeneous media

In Chapter 7, we considered two types of heterogeneous diffusion processes: one with piecewise constant diffusivity and another with power-law diffusivity. In both cases, the trajectories are generated by a Brownian increment whose variance depends on the current position of the particle.

A Piecewise diffusivity

For heterogeneous diffusion with piecewise diffusivity, we have considered a diffusion coefficient that takes two different values on the positive and negative sides of the real line, respectively, Eq. (7.6), which reads

$$D(x) = \begin{cases} D_+, & x > 0, \\ D_-, & x < 0. \end{cases}$$

Numerically, we implement the same algorithm as for standard Brownian motion, namely

$$x_{j+1} = x_j + \sqrt{2D(x_j)\Delta_t}\,\xi_{j+1}. \tag{A.7}$$

In the particular case where $x_j = 0$, which only occurs at the initial condition, since numerically $x_j = 0$ will not occur again, we choose $D = 0.5(D_+ + D_-)$, but one can take either D_+ or D_- without affecting the results.

B Power-law diffusivity

For the power-law case, Eq. (7.5), the diffusivity is taken as

$$D(x) = D_0|x|^\alpha, \quad \alpha < 2.$$

In the Itô interpretation, in order to prevent trapping of the particles at $x = 0$ or divergences in the numerical implementation, we regularize the diffusion coefficient near the origin [22, 219] by taking

$$D(x) = \begin{cases} D_0(|x|^\alpha + \varepsilon), & \alpha > 0 \\ \frac{D_0}{|x|^{-\alpha}+\varepsilon}, & \alpha < 0 \end{cases} \tag{A.8}$$

with $\varepsilon \ll 1$. Since we are working in the Itô interpretation, the trajectory is then generated by the corresponding Euler-Maruyama scheme, as described in Eq. (A.7).

A.1.6 Chapter 8: Occupation and area observables in Gaussian anomalous diffusion

In Chapter 8 we have considered two types of anomalous diffusion processes: SBM and fBM.

A Scaled Brownian motion

The diffusion coefficient for SBM is given by Eq. (2.8), which reads

$$D(t) = \alpha K t^{\alpha-1}, \quad \alpha \in (0,2).$$

Numerically, we generate the trajectories by means of the Euler-Maruyama scheme, which for this process reads

$$x_{j+1} = x_j + \sqrt{2D(t_{j+1})\Delta_t}\,\xi_{j+1}. \tag{A.9}$$

B Fractional Brownian motion

For fBM, we obtain trajectories using the circulant embedding method (see, for example, [256]). For a discretization with M time steps and $\Delta_t = t/M$, the covariance of the fractional Gaussian noise is

$$c_H(k) = \frac{1}{2}\left(|k+1|^{2H} - 2|k|^{2H} + |k-1|^{2H}\right), \qquad k \geq 0, \tag{A.10}$$

where $H \in (0,1)$ is the Hurst exponent. Numerically, we construct the circulant embedding associated with this covariance, diagonalize it by discrete Fourier transform, and generate a single realization of correlated Gaussian increments in Fourier space. After inverse transforming, the fractional Gaussian noise increments are cumulatively summed to obtain a single trajectory.

A.2 Numerical evaluation of functionals

Once a trajectory is generated as described in the previous section, we evaluate the relevant observables along its path.

A Half occupation time and occupation time in an interval

Whenever the observables are occupation times, we obtain them at every time step of the simulated trajectory. For dynamics generated in discrete time, such as Brownian motion, scaled Brownian motion, fractional Brownian motion, or heterogeneous diffusion, these functionals are approximated by Riemann sums along the simulated path $\{x_j\}_{j=0}^{M-1}$:

$$T_+(t) \approx \Delta_t \sum_{j=0}^{M-1} \Theta(x_j), \qquad T_a(t) \approx \Delta_t \sum_{j=0}^{M-1} \Theta\big(a - |x_j|\big), \tag{A.11}$$

with $\Delta_t = t/M$. Numerically, the Θ function is evaluated at each time step, using an if condition to determine whether the current position is positive or whether it lies inside the interval $[-a,a]$. The corresponding contribution Δ_t is then added to the accumulated occupation time.

For the CTRW, the occupation times are computed by summing the residence times associated with each waiting period. If the walker remains at position x during a time interval of length τ, then this interval contributes τ to the occupation time if x satisfies the corresponding condition. Thus, if the particle is located at x during a waiting time τ, we add $\tau\,\Theta(x)$ to the half occupation time and $\tau\,\Theta\big(a-|x|\big)$ to the occupation time in the interval. In the presence of a finite observation time or resetting, the last residence interval is truncated, and only the effective elapsed time is added.

B Area and absolute area

The area and absolute area under the trajectory are obtained similarly: we evaluate them numerically from the simulated path $\{x_j\}$ as

$$A(t) \approx \Delta_t \sum_{j=0}^{M-1} x_j, \qquad \mathscr{A}(t) \approx \Delta_t \sum_{j=0}^{M-1} |x_j|. \tag{A.12}$$

A.3 Ensemble statistics

After generating the ensemble of trajectories, all reported numerical quantities are obtained from standard sample estimators. For a trajectory-dependent observable $Z(t)$ measured at time t, the first two moments are estimated as

$$\langle Z(t)\rangle = \frac{1}{N}\sum_{i=1}^{N} Z_i(t), \qquad \langle Z(t)^2\rangle = \frac{1}{N}\sum_{i=1}^{N} Z_i^2(t). \tag{A.13}$$

Probability density functions are estimated from normalized histograms of the corresponding rescaled observables.

B

PDF OF THE OCCUPATION TIME IN AN INTERVAL

B.1 Left edge regime 180

B.2 Right edge regime 182

B.3 Central bulk regime 183

In this Appendix we schematize the inversion of the double Laplace transform of the occupation time distribution $Q(p,s)$, given by Eq. (5.28), to obtain the behavior of the PDF of the occupation time, $Q(T_a,t)$ for non-Markovian random walks. As mentioned in the main text, in Section 5.4.2, in order to invert the double Laplace transform $Q(p,s)$ we need to consider some limits. In particular, we will consider the long-time limit $t \to \infty$, which in Laplace space corresponds to $s \to 0$. Still, we need further approximations. For this, we consider three regimes: left edge, when the occupation time is much shorter than the measurement time $T_a \ll t$, bulk, when the occupation time is comparable to the measurement time, and right edge, when the occupation time is close to the measurement time $t - T_a \ll 1$.

In the following, we will consider the three regimes separately and we will also consider two different types of waiting time PDF: the finite moments (FM) Eq. (5.8) and the fat-tailed (FT), Eq. (5.12). In what follows, we will not detail the computation of the Mittag-Leffler (ML) waiting times, Eq. (5.16), since in the long time limit we obtain the same results as for the FT (after replacing b_α by τ^α, and which hold for $0 < \alpha < 1$).

B.1 Left edge regime

First we consider $T_a \ll t$ (i.e., $s \ll p$) with T_a small (corresponding to large p). Then, $s+p \approx p$ and $\lambda(s+p) \approx \lambda(p)$ and Eq. (5.28) turns into

$$Q(p,s) \approx \frac{1}{p} + \frac{s^{-1}}{\cosh(\lambda(p)) + \frac{\lambda(p)}{\lambda(s)}\sinh(\lambda(p))}. \tag{B.1}$$

In addition, since $s \ll p$ we have $\lambda(s) \ll \lambda(p)$, so that Eq. (B.1) reduces to

$$Q(p,s) \approx \frac{1}{p} + \frac{2}{s}\frac{\lambda(s)e^{-\lambda(p)}}{\lambda(p)}. \tag{B.2}$$

To proceed further, we need to specify explicit expressions for the memory kernel or the waiting time PDF.

We start by considering the case of a waiting time PDF with finite moments. Recalling expressions from Eqs (5.9) and (5.30), we have $\lambda(s) \approx a\sqrt{2s\langle\tau\rangle/\sigma^2}$ as $s \to 0$, so that Eq. (B.2) turns into

$$Q(p,s) \approx \frac{1}{p} + \frac{2}{\sqrt{sp}}e^{-\frac{a}{\sqrt{D}}\sqrt{p}}. \tag{B.3}$$

To invert this expression in Laplace with respect to s we use

$$\mathscr{L}^{-1}_{s\to t}\left(\frac{1}{\sqrt{s}}\right) = \frac{1}{\sqrt{\pi t}},$$

so that

$$Q(p,t) \approx \frac{\delta(t)}{p} + \frac{2}{\sqrt{\pi pt}}e^{-\frac{a}{\sqrt{D}}\sqrt{p}}. \tag{B.4}$$

Next, we invert the above expression with respect to p using

$$\mathscr{L}^{-1}_{p\to T_a}\left(\frac{e^{-\frac{a}{\sqrt{D}}\sqrt{p}}}{\sqrt{p}}\right) = \frac{e^{-\frac{a^2}{4DT_a}}}{\sqrt{\pi T_a}},$$

and find

$$Q(T_a,t)_{\mathrm{FM}} \approx \frac{2}{\pi\sqrt{tT_a}}e^{-\frac{a^2}{4DT_a}}. \tag{B.5}$$

which is Eq. (5.45).

Next, consider we consider a fat-tailed waiting time PDF with $0 < \alpha < 1$. In this case, we can approximate Eq. (5.30) as $\lambda(s) = as^{\alpha/2}/\sqrt{K_\alpha}$ where $K_\alpha = \sigma^2/2b_\alpha$, plugging the same into Eq. (B.2) we find

$$Q(p,s) \approx \frac{1}{p} + \frac{2e^{-\frac{ap^{\alpha/2}}{\sqrt{K_\alpha}}}}{s^{1-\frac{\alpha}{2}} p^{\alpha/2}}. \tag{B.6}$$

Inverting this expression with respect to s using

$$\mathscr{L}^{-1}_{s\to t}\left(\frac{1}{s^{1-\frac{\alpha}{2}}}\right) = \frac{t^{-\alpha/2}}{\Gamma\left(1-\frac{\alpha}{2}\right)},$$

we find

$$Q(p,t) \approx \frac{\delta(t)}{p} + \frac{2e^{-\frac{ap^{\alpha/2}}{\sqrt{K_\alpha}}}}{\Gamma\left(1-\frac{\alpha}{2}\right)(pt)^{\alpha/2}}. \tag{B.7}$$

Now, we invert with respect to p by noticing that the one-sided Lévy density has the characteristic function given by Eq. (2.60), and so

$$\mathscr{L}^{-1}_{p\to T_a}\left(e^{-\frac{ap^{\alpha/2}}{\sqrt{K_\alpha}}}\right) = \left(\frac{\sqrt{K_\alpha}}{a}\right)^{\frac{2}{\alpha}} l_{\alpha/2}\left[\left(\frac{\sqrt{K_\alpha}}{a}\right)^{\frac{2}{\alpha}} T_a\right].$$

Hence,

$$\mathscr{L}^{-1}_{p\to T_a}\left[\frac{e^{-\frac{ap^{\alpha/2}}{\sqrt{K_\alpha}}}}{p^{\alpha/2}}\right] = \frac{\left(\sqrt{K_\alpha}/a\right)^{\frac{2}{\alpha}}}{\Gamma(\alpha/2)} \int_0^{T_a} \frac{l_{\alpha/2}\left[\left(\frac{\sqrt{K_\alpha}}{a}\right)^{\frac{2}{\alpha}} t'\right]}{(T_a-t')^{1-\frac{\alpha}{2}}} dt'.$$

Using the above result, the inverse Laplace transform of Eq. (B.7)

$$Q(T_a,t)_{\mathrm{FT}} \approx \frac{2\sin\left(\frac{\pi\alpha}{2}\right)}{\pi} \frac{(T_a/t)^{\frac{\alpha}{2}}}{\left(a/\sqrt{K_\alpha}\right)^{\frac{2}{\alpha}}} \int_0^1 \frac{l_{\alpha/2}\left[\frac{T_a z}{\left(a/\sqrt{K_\alpha}\right)^{\frac{2}{\alpha}}}\right]}{(1-z)^{1-\frac{\alpha}{2}}} dz, \tag{B.8}$$

which is precisely Eq. (5.48). A series expansion can be done in the following way, which might be useful to evaluate the expression

$$Q(T_a,t)_{\mathrm{FT}} \approx \frac{2}{\Gamma\left(1-\frac{\alpha}{2}\right) t^{\frac{\alpha}{2}} T_a^{1-\frac{\alpha}{2}}} \sum_{n=0}^{\infty} \frac{\left(-\frac{aT_a^{-\frac{\alpha}{2}}}{\sqrt{K_\alpha}}\right)^n}{n!\Gamma\left(\frac{\alpha}{2}-\frac{\alpha n}{2}\right)}. \tag{B.9}$$

The case of a fat-tailed waiting time PDF with $1<\alpha<2$ can be treated in the same way, and we get the same result as for the finite moments case, Eq. (B.5).

B.2 Right edge regime

This regime corresponds to the large time limit but $T_a \to t$. To deal with it, we define the new random variable $\varepsilon = t - T_a$. Let $Q_\varepsilon(\varepsilon,t)$ be the PDF of ε and consider its double Laplace transform $Q_\varepsilon(p_\varepsilon,s) = \mathscr{L}_{\varepsilon\to p_\varepsilon}\mathscr{L}_{t\to s}[Q(\varepsilon,t)]$. In Laplace space, $Q_\varepsilon(p_\varepsilon,s) = Q(-p_\varepsilon, s+p_\varepsilon)$ where $Q(-p_\varepsilon,s+p_\varepsilon)$ is obtained by replacing p by $-p_\varepsilon$ and s by $s+p_\varepsilon$ in $Q(p,s)$. Thus,

$$Q_\varepsilon(p_\varepsilon,s) = \frac{1}{s}\left[1 - \frac{p_\varepsilon}{(s+p_\varepsilon)F(s+p_\varepsilon,-p_\varepsilon)}\right]. \tag{B.10}$$

In the large time limit and $\varepsilon \to 0$ (this is, $s \ll p_\varepsilon$)

$$Q_\varepsilon(p_\varepsilon,s) \approx \frac{1}{s} - \frac{\lambda(p_\varepsilon)}{\lambda(p_\varepsilon)+\lambda(s)\tanh(\lambda(s))}\frac{1}{s\cosh(\lambda(s))}, \tag{B.11}$$

where we have taken into account the expression of $F(s,p)$ in Eqs. (5.29) and (B.10). Taking the large time limit (correspondingly, $s \to 0$) and since $\lambda(s) \to 0$ as $s \to 0$ we have $\cosh(\lambda(s)) \approx 1$ and $\sinh(\lambda(s)) \approx \lambda(s)$, so that

$$Q_\varepsilon(p_\varepsilon,s) \approx \frac{1}{s}\frac{\lambda(s)^2}{\lambda(p_\varepsilon)+\lambda(s)^2}. \tag{B.12}$$

This is a general expression for the characteristic function of $t - T_a$ in the large time limit and when $t - T_a \ll 1$, which again can be found for different expressions of the waiting time PDF. As before, we need to specify the waiting time PDF.

Again, we start with the case of a waiting time PDF with finite moments. Then $\lambda(s) \approx a\sqrt{2s\langle\tau\rangle/\sigma^2}$ as $s \to 0$ and from Eq. (B.12)

$$Q_\varepsilon(p_\varepsilon,s) \approx \frac{1}{s}\frac{\frac{as}{\sqrt{D}}}{\sqrt{p_\varepsilon}+\frac{as}{\sqrt{D}}}. \tag{B.13}$$

Performing the double Laplace inversion

$$Q(T_a,t)_{\mathrm{FM}} \approx \sqrt{\frac{D}{4a^2\pi}}\frac{t}{(t-T_a)^{\frac{3}{2}}}e^{-\frac{t^2 D}{4a^2(t-T_a)}}. \tag{B.14}$$

which corresponds to Eq. (5.46).

Next, consider when the waiting time PDF is a fat-tailed. Note that in the right edge regime, T_a and t are very large compared to t_0 so that $p_\varepsilon t_0 \ll 1$ and $st_0 \ll 1$. The memory kernel in this regime is then given by Eq. (5.15), so that

$$\lambda(s) \approx \begin{cases} a\sqrt{\frac{2b_\alpha s^\alpha}{\sigma^2}}, & 0<\alpha<1 \\ a\sqrt{\frac{2\langle\tau\rangle s}{\sigma^2}}\left(1-\frac{b_\alpha}{2\langle\tau\rangle}s^{\alpha-1}\right), & 1<\alpha<2 \end{cases} \tag{B.15}$$

Substituting Eq. (B.15) into (B.12) we find

$$Q(T_a,t)_{\rm PL} \approx \frac{\mathscr{B}_\alpha}{t^\alpha (t-T_a)^{1-\frac{\alpha}{2}}}, \quad 0<\alpha<1 \tag{B.16}$$

where

$$\mathscr{B}_\alpha = \frac{a}{\sqrt{K_\alpha}\Gamma(\frac{\alpha}{2})\Gamma(1-\alpha)}, \tag{B.17}$$

after the double Laplace inversion. Note that this equation, Eq. (B.16), can be expressed in a scaling form by defining $y = T_a/t$ then

$$t^{\alpha/2} Q(y,t)_{\rm PL} = \frac{\mathscr{B}_\alpha}{(1-y)^{1-\frac{\alpha}{2}}}. \tag{B.18}$$

B.3 Central bulk regime

Finally, we consider the regime where t and T_a are both large or s and p are small. Then, it is expected that this solution agrees with the limit $T_a \to t$ but does not fit with the limit $T_a \to 0$, therefore we assume $O(s) \sim O(p)$. Since both s and p are small, $\lambda(s+p)$ is also small, since $d\lambda(s)/ds > 0$. Then, $\cosh(\lambda(s+p)) \approx 1$ and $\sinh(\lambda(s+p)) \approx \lambda(s+p)$ so that

$$Q(p,s) \approx \frac{1}{s+p}\left[1+\frac{p}{s}\frac{1}{1+\frac{\lambda(s+p)^2}{\lambda(s)}}\right]. \tag{B.19}$$

As we have done above, consider a waiting time PDF with finite moments Eq. (B.19) reads

$$Q(p,s) \approx \frac{1}{s+p}\left[1+\frac{ps^{-1/2}}{s^{1/2}+a\sqrt{\frac{2\tau}{\sigma^2}}(s+p)}\right]. \tag{B.20}$$

Laplace inverting Eq. (B.20) with respect to p and s we find that the PDF for T_a follows the half-Gaussian

$$Q(T_a,t)_{\rm FM} \approx \sqrt{\frac{D}{a^2\pi(t-T_a)}}\, e^{-\frac{T_a^2 D}{4a^2(t-T_a)}}. \tag{B.21}$$

Finally, consider the waiting time PDF is FT given in Eq. (5.14) for $0<\alpha<1$. To get the asymptotic expression for the PDF of occupation time in the right edge regime, we insert $K(s)$ given in Eq. (5.15) for $0<\alpha<1$ into Eq. (B.12). This yields

$$Q_\varepsilon(p_\varepsilon,s) \sim \frac{1}{s} - \frac{1}{s}\frac{p_\varepsilon^{\alpha/2}}{p_\varepsilon^{\alpha/2} + \frac{as^\alpha}{\sqrt{K_\alpha}}}, \tag{B.22}$$

which gives

$$Q_\varepsilon(p_\varepsilon,s) \sim \frac{\delta(\varepsilon)}{s} - \frac{1}{s\varepsilon}E_{\frac{\alpha}{2},0}\left(-\frac{as^\alpha\varepsilon^{\alpha/2}}{\sqrt{K_\alpha}}\right), \tag{B.23}$$

after the Laplace inversion with respect to p_ε. Here, $E_{a,b}(z)$ is two-parametric Mittag-Leffler function [224]. Since we are interested in the small s and ε limits, we use the small argument expansion of the Mittag-Leffler function (see Eq. (4.1.1) in Ref. [224]). This leads to

$$Q_\varepsilon(\varepsilon,s) \sim \frac{\delta(\varepsilon)}{s} + \frac{as^{\alpha-1}\varepsilon^{\frac{\alpha}{2}-1}}{\sqrt{K_\alpha}\Gamma(\alpha/2)}. \tag{B.24}$$

The Laplace inversion of the above expression to real time leads to

$$Q(T_a,t)_{\mathrm{FT}} \approx \mathscr{B}_\alpha \frac{(t-T_a)^{\frac{\alpha}{2}}}{T_a^{1+\alpha}}\left(2+\frac{T_a}{t-T_a}\right) \tag{B.25}$$

which is Eq. (B.16) in the main text. Note that if $T_a \sim t$ Eq. (B.25) reduces to Eq. (B.16). For the fat-tailed PDF with $1<\alpha<2$, using Eq. (B.15), we get exactly the same result as for the finite moments PDF, in Eq. (B.21). which is Eq. (B.16) in the main text. Note that if $T_a \sim t$ Eq. (B.25) reduces to Eq. (B.16). For the fat-tailed PDF with $1<\alpha<2$, using Eq. (B.15), we get exactly the same result as for the finite moments PDF, in Eq. (B.21).

Again, Eq. (B.25) can also be written in scaling form as

$$t^{\alpha/2}Q(y,t) = \mathscr{B}_\alpha \frac{2-y}{y^{1+\alpha}(1-y)^{1-\frac{\alpha}{2}}}. \tag{B.26}$$

C

LIMITING PDF FOR A FINITE MOMENT RESETTING DISTRIBUTION

In Chapter 6, we have found the limiting PDF given by Eq. (6.20) from the first two moments of Z by means of the ergodicity of the observable $U[x(t)]$ when the resetting PDF has finite moments. Here we derive the same result from the characteristic function under resetting times drawn from a PDF with finite moments. To do this, we need to consider the long-time limit. Since the functionals we are considering here are additive, Z grows with t, so we can expect Z to be of the order of t, which means that s and p are comparable. Therefore, the long-time limit corresponds to assuming that s and p are both small and comparable. Writing $Q(p,t|x_0)_0$ as a moment-generating function

$$Q(p,t|x_0)_0 = \sum_{n=0}^{\infty} \frac{(-p)^n}{n!} \langle Z(t|x_0)^n \rangle_0 \tag{C.1}$$

one can see that

$$\mathscr{L}_{t\to s}\left[\phi(t)Q(p,t|x_0)_0\right] = \sum_{n=0}^{\infty} \frac{(-p)^n}{n!} \int_0^{\infty} e^{-st}\phi(t)\,\langle Z(t|x_0)^n \rangle_0\, dt \tag{C.2}$$

and analogously $\mathscr{L}_{t\to s}\left[\phi^*(t)Q(p,t|x_0)_0\right]$.

Considering the limit $p \to 0$ to the above expression, the approximations

$$\mathscr{L}_{t\to s}\left[\phi(t)Q(p,t|x_0)_0\right] = \phi(s) - p\int_0^\infty e^{-st}\phi(t)\left\langle Z(t|x_0)\right\rangle_0 dt + O(p^2) \tag{C.3}$$

and

$$\mathscr{L}_{t\to s}\left[\phi(t)^* Q(p,t|x_0)_0\right] = \phi^*(s) - p\int_0^\infty e^{-st}\phi^*(t)\left\langle Z(t|x_0)\right\rangle_0 dt + O(p^2) \tag{C.4}$$

holds if

$$\lim_{s\to 0}\int_0^\infty e^{-s\tau}\phi(\tau)\left\langle Z(\tau|x_0)^n\right\rangle_0 d\tau < \infty \tag{C.5}$$

for any $n \in \mathbb{N}$. This condition is necessary to guarantee that all the coefficients of the expansion in powers of p are finite when taking the limit $s \to 0$. Thus, from Eq. (6.6)

$$Q(p,s|x_0)_r \simeq \frac{\phi^*(s)}{1-\phi(s)+p\int_0^\infty e^{-st}\phi(t)\left\langle Z(t|x_0)\right\rangle_0 dt} = \frac{1}{s+p\mathscr{I}(s)} \tag{C.6}$$

as $p \to 0$, where

$$\mathscr{I}(s) = \frac{s}{1-\phi(s)}\int_0^\infty e^{-st}\phi(t)\left\langle Z(t|x_0)\right\rangle_0 dt. \tag{C.7}$$

If the resetting times PDF has finite moments, then $\phi(s) \simeq 1 - \langle t\rangle_R s + \ldots$ as $s \to 0$, then condition (C.5) is

$$\mathscr{I} = \frac{1}{\langle t\rangle_R}\int_0^\infty \phi(\tau)\left\langle Z(\tau|x_0)\right\rangle_0 d\tau. \tag{C.8}$$

Finally, performing the double Laplace inversion of (C.6) with respect to p and s we get

$$Q(Z,t|x_0)_r = \delta(Z - \mathscr{I}t) \tag{C.9}$$

which is exactly (6.19) provided that $\left\langle Z(t|x_0)\right\rangle_r \simeq \mathscr{I}t$ from (6.17). In terms of the variable $\eta = Z/\mathscr{I}t$ it reads $Q(\eta|x_0)_r = \delta(\eta - 1)$ as we have found in Eq. (6.20).

D

LIMITING PDF OF THE HALF OCCUPATION TIME UNDER GENERAL RESETTING

In this Appendix, we detail the derivation of the limiting PDF of T_+ under general resetting from Chapter 6. As we have seen, we start by considering the limiting PDF of a generic functional Z, and its characteristic function $Q(p,s|x_0)_r$, which can be computed from Eq. (6.6). Assume that in the long-time limit the PDF $Q(Z,t|x_0)_0$ has a scaling solution

$$\lim_{t\to\infty} Q(Z,t|x_0)_0 = \frac{1}{t^\beta} f\left(\frac{Z}{t^\delta}\right). \tag{D.1}$$

Then, the Laplace transform in the numerator of Eq. (6.6) can be written as

$$\begin{aligned} \mathscr{L}_{t\to s}[\phi(t)Q(p,t|x_0)] &= \int_0^\infty dt\, e^{-st}\phi(t) \int_0^\infty e^{-pZ} \frac{1}{t^\beta} f\left(\frac{Z}{t^\delta}\right) dZ \\ &= \int_0^\infty du\, f(u) \int_0^\infty e^{-st-put^\delta} t^{\delta-\beta}\phi(t)dt \end{aligned} \tag{D.2}$$

where we have introduced the new variable $u = Z/t^\delta$. Note that the integral over time can be expressed as the Laplace transform of $\phi(t)$ when $\delta = \beta = 1$. In this case, $u = T_+/t$ and the Laplace transforms in Eq. (6.6) read

$$\begin{aligned}\mathscr{L}_{t\to s}\left[\phi(t)Q(p,t|x_0)\right] &= \int_0^1 f(u)\phi(s+pu)du \\ \mathscr{L}_{t\to s}\left[\phi^*(t)Q(p,t|x_0)\right] &= \int_0^1 f(u)\phi^*(s+pu)du. \end{aligned} \tag{D.3}$$

Next, consider the long-time limit where both s and p are small and comparable. Since $u \in [0,1]$, the argument $s+pu$ is always small. Moreover, consider also a PDF of resettings that has a power law tail with index γ

$$\phi(t) \sim t^{-1-\gamma}, \quad 0<\gamma<2 \tag{D.4}$$

as $t \to \infty$. This case corresponds to PDFs like the one in Eq. (6.21), but we are not assuming any particular form for the PDF of resetting, just that it has a power-law tail with index γ. Another example of a PDF with this kind of tail is the Mittag-Leffler distribution, eq. (5.16). As we have seen in Chapter 5, using the Tauberian theorem [223], Eq. (D.4) admits the following expansion in Laplace space for small s

$$\phi(s) = \begin{cases} 1-b_\gamma s^\gamma + ..., & 0<\gamma<1 \\ 1-\langle t_R\rangle s + ..., & 1<\gamma<2 \end{cases} \tag{D.5}$$

where b_γ depends on the details of the specific expression for $\phi(t)$. With the help of (D.5), Eqs. (D.3) can be approximated as

$$\begin{aligned}\mathscr{L}_{t\to s}\left[\phi(t)Q(p,t|x_0)\right] &\approx \begin{cases} 1-b_\gamma \int_0^1 f(u)(s+pu)^\gamma du, & 0<\gamma<1 \\ 1-\langle t_R\rangle \int_0^1 f(u)(s+pu)du, & 1<\gamma<2 \end{cases} \\ \mathscr{L}_{t\to s}\left[\phi^*(t)Q(p,t|x_0)\right] &\approx \begin{cases} b_\gamma \int_0^1 f(u)(s+pu)^{\gamma-1}du, & 0<\gamma<1 \\ \langle t_R\rangle, & 1<\gamma<2. \end{cases} \end{aligned} \tag{D.6}$$

Let us first consider the case $1<\gamma<2$. Plugging (D.6) into (6.6) we find

$$Q(p,s|x_0)_r \approx \frac{1}{\int_0^1 f(u)(s+pu)du} = \frac{1}{s+p\langle u\rangle} \tag{D.7}$$

where $\langle u\rangle = \int_0^1 uf(u)du$. Since $\langle u\rangle = \langle T^+\rangle/t$, the double Laplace transform of $Q(p,s|x_0)_r$ with respect to p and s yields

$$Q(T_+,t|x_0)_r = \delta\left(T_+ - \langle T_+(t|x_0)\rangle_r\right) \tag{D.8}$$

Next, we consider the case $0<\gamma<1$. By setting (D.6) in (6.6) we readily obtain

$$Q(p,s|x_0)_r \approx \frac{\int_0^1 f(u)(s+pu)^{\gamma-1}du}{\int_0^1 f(u)(s+pu)^\gamma du}. \tag{D.9}$$

This result establishes a link between the characteristic function of T_+ under a resetting with the limiting PDF of T_+ in the absence of resetting assuming that the resetting PDF decays as $t^{-1-\gamma}$ for $0<\gamma<1$ as $t\to\infty$, regardless of the other details and structure of the resetting PDF or the specific random walk. We can write Eq. (D.9) in a more useful scaling form

$$Q(p,s|x_0)_r \approx \frac{1}{s} g_\gamma\left(\frac{p}{s}\right) \tag{D.10}$$

where

$$g_\gamma(\chi) = \frac{1}{\chi}\frac{\int_0^1 f(u)(\chi^{-1}+u)^{\gamma-1}du}{\int_0^1 f(u)(\chi^{-1}+u)^{\gamma}du} \tag{D.11}$$

and $\chi = p/s$. The double Laplace inversion from p and s to T_+ and t has the form $Q(T_+,t|x_0)_r \equiv Q(z)_r$ where $z = T_+/t$. To find $Q(z)_r$ we follow the method in Ref. [141] by noting

$$Q(z)_r = -\frac{1}{\pi z}\lim_{\varepsilon\to 0}\mathrm{Im}\left[g_\gamma\left(-\frac{1}{z+i\varepsilon}\right)\right]. \tag{D.12}$$

Calculating the imaginary part of Eq. (D.12) we find

$$Q(z)_r = \frac{\sin(\gamma\pi)}{\pi}\frac{C_\gamma(z)C_{-1+\gamma}(1-z)+C_{-1+\gamma}(z)C_\gamma(1-z)}{C_\gamma(z)^2+2C_\gamma(z)C_\gamma(1-z)\cos(\gamma\pi)+C_\gamma(1-z)^2}. \tag{D.13}$$

with $z = T_+/t$ and $C_\beta(z)$ is given by

$$C_\beta(z) \;=\; \int_0^z f(u)(z-u)^\beta du = z^{\beta+1}\int_0^1 f(zv)(1-v)^\beta dv. \tag{D.14}$$

E

PROBABILITY DENSITY FUNCTIONS OF OCCUPATION TIMES IN HETEROGENEOUS MEDIA

E.1 Derivation of the half occupation time distribution 191
E.1.1 Piecewise heterogeneity 192
E.1.2 Power-law heterogeneity 193
E.2 Derivation of the distribution of the occupation time in an interval 194
E.2.1 Piecewise heterogeneity 194
E.2.2 Power-law heterogeneity 195

In this Appendix, we provide details on the derivation of the probability density functions of occupation times in heterogeneous media, as presented in Chapter 7. In particular, we provide details on the derivation of the half occupation time distribution and the distribution of the occupation time in an interval.

E.1 Derivation of the half occupation time distribution

The FK equation for the characteristic function $Q(p,s|x_0)$ in this case reads (Eq. (7.7))

$$sQ(p,s|x_0) - 1 = D(x_0)\frac{\partial^2 Q(p,s|x_0)}{\partial x_0^2} - p\Theta(x_0)Q(p,s|x_0). \tag{E.1}$$

As we have mentioned in the main text, this equation has to be solved with the appropriate boundary conditions [129]. Which we repeat them here for convenience. If the starting point $x_0 \to +\infty$ the particle will stay on the positive side with $x(t) > 0$ for all finite t implying $T^+(t|x_0 \to +\infty) = t$ and accordingly $Q(T_+, t|x_0 \to +\infty) = \delta(T_+ - t)$, On the other hand, if the starting point $x_0 \to -\infty$ the particle will never reach the positive side and it will stay on the negative half-space implying $T^+(t|x_0 \to -\infty) = 0$ and hence $Q(T_+, t|x_0 \to -\infty) = \delta(T_+)$. Thus, the boundary conditions for $Q(p,s|x_0)$ in Laplace-Laplace space read

$$Q(p,s|x_0 \to +\infty) = \frac{1}{s+p}, \quad Q(p,s|x_0 \to -\infty) = \frac{1}{s}. \tag{E.2}$$

With this we can solve Eq. (E.1) for the different diffusion coefficients $D(x)$ in Eqs. (7.5), and (7.6). Once $Q(p,s|x_0)$ is known, one can find the PDF of $y = T_+/t$ in the long-time limit by using the method in Ref. [141].

E.1.1 Piecewise heterogeneity

For the piecewise diffusion coefficient (7.6) we solve (7.7) in the regions $x_0 < 0$ and $x_0 > 0$, and requiring continuity of Q and its derivative $\partial_{x_0} Q$ across $x_0 = 0$. By setting $x_0 = 0$ we get

$$Q(p,s|0) = \frac{1}{s+p}\left(1 + \frac{p}{s + \rho\sqrt{s(s+p)}}\right) \tag{E.3}$$

where

$$\rho = \sqrt{\frac{D_-}{D_+}}, \tag{E.4}$$

which is the asymmetry parameter. To invert the characteristic function (E.3) back to T_+ and t we note that it has the following scaling behavior

$$Q(p,s|0) = \frac{1}{s} g\left(\frac{p}{s}\right). \tag{E.5}$$

Then the random variable $y = T_+/t$ possesses the distribution

$$Q(y|0) = Q\left(y = \frac{T_+}{t}, t|0\right) = tQ\left(T_+ = yt, t|0\right) \tag{E.6}$$

The above equation can be found again using the same procedure as Eq. (D.11) following Ref. [141]

$$Q(y|0) = -\frac{1}{\pi y} \lim_{\varepsilon \to 0} \mathrm{Im}\left[g\left(-\frac{1}{y + i\varepsilon}\right)\right]. \tag{E.7}$$

Thus, from (E.3)

$$g(\chi) = \frac{1}{1+\chi}\left(1+\frac{\chi}{1+\rho\sqrt{1+\chi}}\right) \tag{E.8}$$

where $\chi = p/s$. Setting $\chi^{-1} = -y - i\varepsilon$ and computing (E.7) we find

$$Q(T_+,t|0) = \frac{1}{t}F\left(\frac{T_+}{t}\right) = \frac{1}{t}\frac{\rho}{\pi\sqrt{\frac{T_+}{t}(1-\frac{T_+}{t})}\left[\frac{T_+}{t}+\rho^2(1-\frac{T_+}{t})\right]} \tag{E.9}$$

Thus, from (E.6), we get, in terms of $y = T_+/t$, the limiting distribution of the half occupation time for the piecewise heterogeneity

$$Q(y|0) = \frac{\rho}{\pi\sqrt{y(1-y)}\,[y+\rho^2(1-y)]}, \quad 0<y<1. \tag{E.10}$$

E.1.2 Power-law heterogeneity

For the power-law diffusion coefficient (7.5) we again solve (7.7) in the regions $x_0 < 0$ and $x_0 > 0$ separately, and set $x_0 = 0$. Thus, the solution for the characteristic function is

$$Q(p,s|0) = \frac{1}{s+p}\left[1+\frac{p/s}{1+\left(\frac{s+p}{s}\right)^{\frac{1}{2-\alpha}}}\right], \quad \alpha<1 \tag{E.11}$$

To invert (E.11) to the real space, we use the same method employed for the piecewise heterogeneity. This is by computing (E.7) we get

$$Q(y|0) = \frac{\sin\left(\frac{\pi}{2-\alpha}\right)}{\pi}\frac{[y(1-y)]^{\frac{1}{2-\alpha}-1}}{y^{\frac{2}{2-\alpha}}+(1-y)^{\frac{2}{2-\alpha}}+2\cos\left(\frac{\pi}{2-\alpha}\right)[y(1-y)]^{\frac{1}{2-\alpha}}} \tag{E.12}$$

It is worth noting that when $\alpha \to 1^-$ the expression for the characteristic function given by Eq. (E.11) reads

$$Q(p,s|0) = \frac{2}{2s+p} \tag{E.13}$$

which after the double Laplace inversion for $y = T_+/t$ reads

$$Q(y|0) = \delta\left(y-\frac{1}{2}\right). \tag{E.14}$$

E.2 Derivation of the distribution of the occupation time in an interval

In the case of the occupation time in an interval, the corresponding FK equation reads (Eq. (7.22))

$$sQ(p,s|x_0)-1=D(x_0)\frac{\partial^2 Q(p,s|x_0)}{\partial x_0^2}-p\Theta(-a<x_0<a)Q(p,s|x_0) \tag{E.15}$$

which again needs to be solved with suitable boundary conditions, which we reproduce here for convenience. For instance, if the starting point is at infinity i.e., $x_0\to\pm\infty$ the particle will never reach the interval so that $Q(T_a,t|x_0\to\pm\infty)=\delta(T_a)$, i.e., $Q(p,s|x_0\to\pm\infty)=1/s$. The initial condition is such that $T_a(t=0|x_0)=0$ so that $Q(p,t=0|x_0)=1$. Therefore, we must explicitly find the solution in the regions I ($x_0<-a$), II ($-a<x_0<0$), III ($0<x_0<a$), and IV ($x_0>a$).

E.2.1 Piecewise heterogeneity

The solution of Eq. (E.15) for the piecewise diffusion coefficient (7.6) is given by (setting $x_0=0$)

$$Q(p,s|0)=\frac{1}{s+p}\left[1+\frac{p}{sF}\right],\quad F=\frac{M_-(s,p)N_+(s,p)+\rho M_+(s,p)N_-(s,p)}{N_+(s,p)+\rho N_-(s,p)} \tag{E.16}$$

where

$$\begin{aligned}M_\pm(s,p)&=\cosh\left(a\sqrt{\frac{s+p}{D_\pm}}\right)+\sqrt{\frac{s+p}{s}}\sinh\left(a\sqrt{\frac{s+p}{D_\pm}}\right)\\ N_\pm(s,p)&=\sinh\left(a\sqrt{\frac{s+p}{D_\pm}}\right)+\sqrt{\frac{s+p}{s}}\cosh\left(a\sqrt{\frac{s+p}{D_\pm}}\right).\end{aligned}$$

Since the double Laplace inversion of $Q(p,s|0)$ cannot be found explicitly, we derive an approximate expression which holds when t and T_a are large. To do this, we consider s and p small and comparable in Eq. (E.16) and find

$$Q(p,s|0)\simeq\frac{1}{s+p}\left[1+\frac{p}{s+\mathscr{C}\sqrt{s(s+p)}}\right],\quad \mathscr{C}=\frac{a\left(\sqrt{\frac{D_+}{D_-}}+\sqrt{\frac{D_-}{D_+}}\right)}{\sqrt{D_+}+\sqrt{D_-}}. \tag{E.17}$$

Performing the double Laplace inversion of (E.17), we find that the PDF of T_a for large t and T_a reads

$$Q(T_a,t|0)\simeq\sqrt{\frac{D_*}{\pi a^2 t}}\exp\left[-\frac{D_* T_a^2}{4a^2 t}\right],\quad D_*=\left(\frac{D_+\sqrt{D_-}+D_-\sqrt{D_+}}{D_++D_-}\right)^2, \tag{E.18}$$

which is Eq. (7.23) in the main text.

E.2.2 Power-law heterogeneity

Finally, we turn to the occupation time in an interval for the power-law diffusion coefficient (7.5). In this case, the expression for the characteristic function in the long-time limit is given by

$$Q(p,s|0) \simeq \frac{s^{-1+\frac{1}{2-\alpha}}}{s^{\frac{1}{2-\alpha}} + \lambda_\alpha p}; \quad \lambda_\alpha = \frac{a^{1-\alpha}}{\left[(2-\alpha)\sqrt{D_0}\right]^{\frac{2-2\alpha}{2-\alpha}}} \frac{\Gamma\left(\frac{1}{2-\alpha}\right)}{\Gamma\left(\frac{3-2\alpha}{2-\alpha}\right)} \tag{E.19}$$

which holds for $\alpha < 1$. Performing the double Laplace inversion of (E.19) with respect to p one finds the scaling form

$$Q(T_a,t|0) \sim \frac{1}{t^{\frac{1}{2-\alpha}}} N_\alpha\left(\frac{T_a}{\lambda_\alpha t^{\frac{1}{2-\alpha}}}\right), \quad N_\alpha(z) = \frac{2-\alpha}{\lambda_\alpha z^{3-\alpha}} l_{\frac{1}{2-\alpha}}\left(\frac{1}{z^{2-\alpha}}\right) \tag{E.20}$$

for $\alpha < 1$, and where $l_\beta(z)$ is the one-sided Lévy stable distribution with index β. In the limit $\alpha \to 1^-$ we see that (E.19) turns into

$$Q(p,s|0) \simeq \frac{1}{s+p} \tag{E.21}$$

which after Laplace inversion yields

$$Q(T_a,t|0) \simeq \delta(T_a - t), \quad \alpha \to 1^-. \tag{E.22}$$

F

SECOND MOMENT OF THE ABSOLUTE AREA UNDER A SBM

In this Appendix, we detail the calculation of the second moment of the absolute area under a SBM, as referenced in Chapter 8. To compute the second moment of the absolute area, we insert the autocorrelation (8.35) into Eq. (8.59) and introduce the new variables $u = \tau_1/\tau_2$ and $v = \tau_2/t$:

$$\left\langle \mathscr{A}^2(t) \right\rangle = \frac{4K}{\pi} t^{\alpha+2} \int_0^1 v^{\alpha+1} dv \left[\frac{\pi}{\alpha+1} - 2\int_0^1 u^{\alpha} \arctan\left(\sqrt{\frac{1}{u^{\alpha}} - 1} \right) du + 2\int_0^1 u^{\alpha/2} \sqrt{1-u^{\alpha}}\, du \right]. \tag{F.1}$$

The integral over v can be easily performed. The first integral inside the parenthesis can be evaluated as follows. First we introduce the new variable $y = \sqrt{u^{-\alpha} - 1}$ to get

$$\int_0^1 u^{\alpha} \arctan\left(\sqrt{\frac{1}{u^{\alpha}} - 1} \right) du = \frac{2}{\alpha} \int_0^{\infty} \frac{y \arctan(y)}{(1+y^2)^{2+1/\alpha}} dy, \tag{F.2}$$

now integrating by parts

$$\frac{2}{\alpha} \int_0^{\infty} \frac{y \arctan(y)}{(1+y^2)^{2+1/\alpha}} dy = \frac{1}{\alpha+1} \int_0^{\infty} \frac{dy}{(1+y^2)^{2+1/\alpha}}. \tag{F.3}$$

Making use of the definition of the beta function (see Eq. 3.194.3 in Ref. [257])

$$\int_0^1 \frac{y^{\mu-1}}{(1+y)^{\rho}} dy = B(\mu, \rho-\mu) = \frac{\Gamma(\mu)\Gamma(\rho-\mu)}{\Gamma(\rho)}, \quad \rho > \mu > 0. \tag{F.4}$$

Again, using this integral, we find for the second integral inside the parentheses

$$\int_0^1 u^{\alpha/2}\sqrt{1-u^{\alpha}}du = \frac{\sqrt{\pi}}{2\alpha}\frac{\Gamma\left(\frac{1}{2}+\frac{1}{\alpha}\right)}{\Gamma\left(2+\frac{1}{\alpha}\right)}. \tag{F.5}$$

Finally, using the property $\Gamma(1+z) = z\Gamma(z)$ we can simplify to get

$$\left\langle \mathscr{A}(t)^2 \right\rangle = \frac{4Kt^{\alpha+2}}{(\alpha+1)(\alpha+2)}\left[1 + \frac{1}{2\sqrt{\pi}}\frac{\Gamma\left(\frac{1}{2}+\frac{1}{\alpha}\right)}{\Gamma\left(2+\frac{1}{\alpha}\right)}\right]. \tag{F.6}$$

which is the result given in Eq. (8.63).

BIBLIOGRAPHY

[1] R. Flaquer-Galmés, D. Campos, and V. Méndez. "Intermittent random walks under stochastic resetting". In: *Physical Review E* 109 (3 Mar. 2024), p. 034103. DOI: 10.1103/PhysRevE.109.034103 (cit. on p. ix).

[2] V. Méndez, R. Flaquer-Galmés Rosa, and D. Campos. "First-passage time of a Brownian searcher with stochastic resetting to random positions". In: *Physical Review E* 109 (4 Apr. 2024), p. 044134. DOI: 10.1103/PhysRevE.109.044134 (cit. on p. ix).

[3] V. Méndez, R. Flaquer-Galmés, and A. Pal. "Occupation-time statistics for non-Markovian random walks". In: *Physical Review E* 111 (4 Apr. 2025), p. 044119. DOI: 10.1103/PhysRevE.111.044119 (cit. on pp. ix, 86, 87).

[4] V. Méndez and R. Flaquer-Galmés. "Statistical properties of stochastic functionals under general resetting". In: *Physical Review E* 112 (4 Oct. 2025), p. 044123. DOI: 10.1103/pcm7-bw2y (cit. on p. ix).

[5] V. Méndez, C. Hervás, and R. Flaquer-Galmés. "Ergodic properties of functionals of Gaussian processes". In: *Physical Review E* 112 (6 Dec. 2025), p. 064111. DOI: 10.1103/qpkk-mgt6 (cit. on p. ix).

[6] V. Méndez and R. Flaquer-Galmés. "Ergodic properties of occupation times in heterogeneous media". In: *Journal of Statistical Mechanics: Theory and Experiment* 2026.1 (Jan. 2026), p. 013203. DOI: 10.1088/1742-5468/ae337d (cit. on p. ix).

[7] V. Méndez, R. Flaquer-Galmés, and J. Cristín. "Area under subdiffusive random walks". In: *Physica A: Statistical Mechanics and its Applications* (June 2026), p. 131719. DOI: 10.1016/j.physa.2026.131719 (cit. on pp. ix, 162).

[8] E. Barkai, R. Flaquer-Galmés, and V. Méndez. "Ergodic properties of Brownian motion under stochastic resetting". In: *Physical Review E* 108 (6 Dec. 2023), p. 064102. DOI: 10.1103/PhysRevE.108.064102 (cit. on pp. ix, 23, 87, 94, 108, 109, 121, 122, 154, 156).

[9] R. Flaquer-Galmés, D. Campos, and J. Cristín. "Magneticlike model for chemotactic navigation in ants". In: *Physical Review Research* 8 (1 Jan. 2026), p. 013116. DOI: 10.1103/fdhh-5jpy (cit. on p. x).

[10] A. Einstein. *Investigations on the Theory of the Brownian Movement*. Ed. by R. Fürth. Trans. by A. D. Cowper. New York: Dover Publications, 1956 (cit. on p. 3).

[11] M. von Smoluchowski. "Zur kinetischen Theorie der Brownschen Molekularbewegung und der Suspensionen". In: *Annalen der Physik* 326.14 (1906), pp. 756–780. DOI: 10.1002/andp.19063261405 (cit. on p. 3).

[12] P. Lévy. "Sur la théorie du mouvement brownien". In: *Rendiconti del Circolo Matematico di Palermo* 146.3 (1908), pp. 530–533. DOI: 10.1007/bf02854204 (cit. on p. 3).

[13] R. Brown. "Mikroskopische Beobachtungen über die im Pollen der Pflanzen enthaltenen Partikeln, und über das allgemeine Vorkommen activer Molecüle in organischen und unorganischen Körpern". In: *Annalen der Physik* 90.10 (1828), pp. 294–313. DOI: 10.1002/andp.18280901016 (cit. on p. 3).

[14] J. B. Perrin. "Mouvement brownien et réalité moléculaire". In: *Annales de Chimie et de Physique*. 8th ser. 18 (1909), pp. 5–114 (cit. on pp. 3, 4).

[15] P. Hänggi and F. Marchesoni. "100 years of Brownian motion". In: *Chaos: An Interdisciplinary Journal of Nonlinear Science* 15.2 (June 2005), p. 026101. DOI: 10.1063/1.1895505 (cit. on pp. 3, 4).

[16] R. M. Mazo. *Brownian Motion: Fluctuations, Dynamics, and Applications*. Oxford University Press, Oct. 2008. ISBN: 9780199556441. DOI: 10.1093/acprof:oso/9780199556441.001.0001 (cit. on p. 3).

[17] R. Metzler and J. Klafter. "The random walk's guide to anomalous diffusion: a fractional dynamics approach". In: *Physics Reports* 339.1 (2000), pp. 1–77. DOI: 10.1016/S0370-1573(00)00070-3 (cit. on pp. 4, 10, 11, 80–82).

[18] X. Bian, C. Kim, and G. E. Karniadakis. "111 years of Brownian motion". In: *Soft Matter* 12.30 (Aug. 2016), pp. 6331–6346. DOI: 10.1039/c6sm01153e (cit. on pp. 3, 4).

[19] American Institute of Physics. *250 Years of Brownian Motion*. https://pubs.aip.org/collection/525821/250-Years-of-Brownian-Motion. AIP Publishing collection (cit. on p. 4).

[20] F. Cecconi et al. "Brownian motion and diffusion: From stochastic processes to chaos and beyond". In: *Chaos: An Interdisciplinary Journal of Nonlinear Science* 15.2 (June 2005), p. 026102. DOI: 10.1063/1.1832773 (cit. on p. 4).

[21] A. V. Chechkin et al. "Brownian yet Non-Gaussian Diffusion: From Superstatistics to Subordination of Diffusing Diffusivities". In: *Physical Review X* 7 (2 Apr. 2017), p. 021002. DOI: 10.1103/PhysRevX.7.021002 (cit. on pp. 4, 10, 126).

[22] R. Metzler et al. "Anomalous diffusion models and their properties: non-stationarity, non-ergodicity, and ageing at the centenary of single particle tracking". In: *Phys. Chem. Chem. Phys.* 16 (44 2014), pp. 24128–24164. DOI: 10.1039/C4CP03465A (cit. on pp. 4, 12, 24, 77, 127, 142, 176).

[23] E. W. Montroll and G. H. Weiss. “Random Walks on Lattices. II”. In: *Journal of Mathematical Physics* 6.2 (Feb. 1965), pp. 167–181. DOI: 10.1063/1.1704269 (cit. on pp. 4, 11, 80, 81).

[24] S. Redner. *A Guide to First-Passage Processes*. Cambridge University Press, 2001. DOI: 10.1017/CBO9780511606014 (cit. on pp. 5, 14, 15, 31).

[25] M. Kac. “On distributions of certain Wiener functionals”. In: *Transactions of the American Mathematical Society* 65.1 (1949), pp. 1–13. DOI: 10.1090/s0002-9947-1949-0027960-x (cit. on pp. 5, 20).

[26] N. G. van Kampen. “Chapter IV - Markov processes”. In: *Stochastic Processes in Physics and Chemistry*. Ed. by N. Van Kampen. Third Edition. North-Holland Personal Library. Amsterdam: Elsevier, 2007, pp. 73–95. DOI: 10.1016/B978-044452965-7/50007-6 (cit. on p. 7).

[27] V. Méndez, D. Campos, and F. Bartumeus. *Stochastic Foundations in Movement Ecology*. Berlin, Heidelberg: Springer Berlin Heidelberg, Jan. 2014. DOI: 10.1007/978-3-642-39010-4 (cit. on pp. 7, 14, 34).

[28] M. Woringer et al. “Anomalous Subdiffusion in Living Cells: Bridging the Gap Between Experiments and Realistic Models”. In: *Frontiers in Physics* 8 (2020), p. 134. DOI: 10.3389/fphy.2020.00134 (cit. on p. 10).

[29] W. R. Holmes. “Subdiffusive Dynamics Lead to Depleted Particle Densities near Cellular Borders”. In: *Biophysical Journal* 116.8 (2019), pp. 1538–1546. DOI: 10.1016/j.bpj.2019.02.021 (cit. on p. 10).

[30] P. Tan et al. “Gradual Crossover from Subdiffusion to Normal Diffusion: A Many-Body Effect in Protein Surface Water”. In: *Physical Review Letters* 120 (2018), p. 248101. DOI: 10.1103/PhysRevLett.120.248101 (cit. on p. 10).

[31] S. Fomin, V. Chugunov, and T. Hashida. “Mathematical Modeling of Anomalous Diffusion in Porous Media”. In: *Fractional Differential Calculus* 1.1 (2011), pp. 1–28. DOI: 10.7153/fdc-01-01 (cit. on p. 10).

[32] X. Zhang et al. “Fractal Study on the Effective Diffusion Coefficient of Gases in Rough Porous Media”. In: *Journal of Materials Engineering and Performance* 33 (2024), pp. 10781–10793. DOI: 10.1007/s11665-023-08731-6 (cit. on p. 10).

[33] J. Xu et al. “Fractal Analysis of Surface Diffusion Effects on Gas Permeability of Fractal Porous Media in the Slip Flow Regime”. In: *Fractals* 33 (2025), p. 2540228. DOI: 10.1142/S0218348X25402285 (cit. on p. 10).

[34] J. Dong, N. Du, and Z. Yang. “Ultraslow diffusion revisited: Logarithmic scaling in single-term fractional diffusion models for anomalous transport of complex systems”. In: *Applied Mathematics Letters* 173 (Feb. 2026), p. 109749. DOI: 10.1016/j.aml.2025.109749 (cit. on p. 10).

[35] D. Molina-Garcia et al. “Crossover from anomalous to normal diffusion: truncated power-law noise correlations and applications to dynamics in lipid bilayers”. In: *New Journal of Physics* 20.10 (Oct. 2018), p. 103027. DOI: 10.1088/1367-2630/aae4b2 (cit. on p. 10).

[36] T. Akimoto et al. “Anomalous statistics in the Langevin equation with fluctuating diffusivity: from Brownian yet non-Gaussian diffusion to anomalous diffusion and ergodicity breaking”. In: *Reports on Progress in Physics* 89.1 (Jan. 2026), p. 014602. DOI: 10.1088/1361-6633/ae358c (cit. on p. 10).

[37] E. Barkai, R. Metzler, and J. Klafter. “From continuous time random walks to the fractional Fokker-Planck equation”. en. In: *Physical Review E* 61.1 (Jan. 2000), pp. 132–138. DOI: 10.1103/PhysRevE.61.132 (cit. on p. 11).

[38] S. Burov and E. Barkai. “Occupation Time Statistics in the Quenched Trap Model”. In: *Phys. Rev. Lett.* 98 (25 June 2007), p. 250601. DOI: 10.1103/PhysRevLett.98.250601 (cit. on p. 11).

[39] V. Nguyen Ba Vy. *Théorie de l’addition des variables aléatoires*. Vol. 1. Monographies des probabilités. Publiés sous la direction de E. Borel. Paris: Gauthier-Villars, 1937. DOI: 10.19182/remvt.9071 (cit. on p. 11).

[40] A. Reynolds. “Liberating Lévy walk research from the shackles of optimal foraging”. In: *Physics of Life Reviews* 14 (2015), pp. 59–83. DOI: 10.1016/j.plrev.2015.03.002 (cit. on p. 11).

[41] G. Margolin and B. Berkowitz. “Application of Continuous Time Random Walks to Transport in Porous Media”. en. In: *The Journal of Physical Chemistry B* 104.16 (Apr. 2000), pp. 3942–3947. DOI: 10.1021/jp993721x (cit. on p. 11).

[42] F. Höfling and T. Franosch. “Anomalous transport in the crowded world of biological cells”. In: *Reports on Progress in Physics* 76.4 (Mar. 2013), p. 046602. DOI: 10.1088/0034-4885/76/4/046602 (cit. on p. 11).

[43] J. Nelson. “Continuous-time random-walk model of electron transport in nanocrystalline TiO 2 electrodes”. en. In: *Physical Review B* 59.23 (June 1999), pp. 15374–15380. DOI: 10.1103/PhysRevB.59.15374 (cit. on p. 11).

[44] J.-W. Yang, Z.-G. Yu, and L. Shi. “A new fractional-order anomalous epidemic model on complex networks based on continuous-time random walk and its dynamics”. en. In: *Chaos: An Interdisciplinary Journal of Nonlinear Science* 35.11 (Nov. 2025), p. 113112. DOI: 10.1063/5.0288024 (cit. on p. 11).

[45] E. Scalas. “The application of continuous-time random walks in finance and economics”. en. In: *Physica A: Statistical Mechanics and its Applications* 362.2 (Apr. 2006), pp. 225–239. DOI: 10.1016/j.physa.2005.11.024 (cit. on p. 11).

[46] J. Masoliver et al. “The CTRW in finance: Direct and inverse problems with some generalizations and extensions”. In: *Physica A: Statistical Mechanics and its Applications* 379.1 (2007), pp. 151–167. DOI: 10.1016/j.physa.2007.01.001 (cit. on p. 11).

[47] M. J. Saxton. “Anomalous Subdiffusion in Fluorescence Photobleaching Recovery: A Monte Carlo Study”. In: *Biophysical Journal* 81.4 (2001), pp. 2226–2240. DOI: 10.1016/S0006-3495(01)75870-5 (cit. on p. 12).

[48] J. Szymański et al. “Movement of Proteins in an Environment Crowded by Surfactant Micelles: Anomalous versus Normal Diffusion”. In: *The Journal of Physical Chemistry B* 110.14 (Apr. 2006), pp. 7367–7373. DOI: 10.1021/jp055626w (cit. on p. 12).

[49] J. Wu and K. M. Berland. “Propagators and Time-Dependent Diffusion Coefficients for Anomalous Diffusion”. In: *Biophysical Journal* 95.4 (2008), pp. 2049–2052. DOI: 10.1529/biophysj.107.121608 (cit. on p. 12).

[50] R. Kazakevičius and A. Kononovicius. “Anomalous diffusion and long-range memory in the scaled voter model”. In: *Physical Review E* 107 (2 Feb. 2023), p. 024106. DOI: 10.1103/PhysRevE.107.024106 (cit. on p. 12).

[51] L. F. Richardson. “Atmospheric diffusion shown on a distance-neighbour graph”. In: *Proceedings of the Royal Society of London. Series A, Containing Papers of a Mathematical and Physical Character* 110.756 (1926), pp. 709–737. DOI: 10.1098/rspa.1926.0043 (cit. on pp. 12, 13, 126).

[52] A. S. Bodrova et al. “Ultraslow scaled Brownian motion”. In: *New Journal of Physics* 17.6 (June 2015), p. 063038. DOI: 10.1088/1367-2630/17/6/063038 (cit. on p. 12).

[53] A. Bontas. “Wiener’s spiral and some other interesting curves in Hilbert space”. In: *KOINON: The International Journal of Classical Numismatic Studies* 26 (1940), pp. 115–118. DOI: 10.32028/k.v5i.1660 (cit. on p. 12).

[54] B. B. Mandelbrot and J. W. Van Ness. “Fractional Brownian motions, fractional noises and applications”. In: *SIAM Review* 10.4 (1968), pp. 422–437. DOI: 10.1137/1010093 (cit. on p. 12).

[55] M. Magdziarz et al. “Fractional Brownian Motion Versus the Continuous-Time Random Walk: A Simple Test for Subdiffusive Dynamics”. In: *Physical Review Letters* 103.18 (2009), p. 180602. DOI: 10.1103/PhysRevLett.103.180602 (cit. on p. 12).

[56] J.-H. Jeon et al. “In vivo anomalous diffusion and weak ergodicity breaking of lipid granules”. In: *Physical Review Letters* 106.4 (2011), p. 048103. DOI: 10.1103/PhysRevLett.106.048103 (cit. on p. 12).

[57] J.-H. Jeon et al. “Anomalous diffusion of phospholipids and cholesterols in a lipid bilayer and its origins”. In: *Physical Review Letters* 109.18 (2012), p. 188103. DOI: 10.1103/PhysRevLett.109.188103 (cit. on p. 12).

[58] J.-H. Jeon et al. “Anomalous diffusion and power-law relaxation of the time averaged mean squared displacement in worm-like micellar solutions”. In: *New Journal of Physics* 15.4 (2013), p. 045011. DOI: 10.1088/1367-2630/15/4/045011 (cit. on p. 12).

[59] S. M. A. Tabei et al. “Intracellular transport of insulin granules is a subordinated random walk”. In: *Proceedings of the National Academy of Sciences* 110.13 (2013), pp. 4911–4916. DOI: 10.1073/pnas.1221962110 (cit. on p. 12).

[60] T. Mikosch et al. “Is network traffic appriximated by stable Lévy motion or fractional Brownian motion?” In: *The Annals of Applied Probability* 12.1 (2002), pp. 23–68. DOI: 10.1214/aoap/1015961155 (cit. on p. 12).

[61] F. Comte and E. Renault. “Long memory in continuous-time stochastic volatility models”. In: *Mathematical Finance* 8.4 (1998), pp. 291–323. DOI: 10.1111/1467-9965.00057 (cit. on p. 12).

[62] F. Biagini et al. *Stochastic calculus for fractional Brownian motion and applications*. Springer, 2008. DOI: 10.1007/978-1-84628-797-8 (cit. on pp. 12, 13).

[63] J. F. Reverey et al. “Superdiffusion dominates intracellular particle motion in the supercrowded cytoplasm of pathogenic Acanthamoeba castellanii”. In: *Scientific Reports* 5.1 (2015), p. 11690. DOI: 10.1038/srep11690 (cit. on p. 13).

[64] D. Krapf et al. “Spectral content of a single non-Brownian trajectory”. In: *Physical Review X* 9.1 (2019), p. 011019. DOI: 10.1103/PhysRevX.9.011019 (cit. on pp. 13, 126).

[65] G. Rangarajan and M. Ding. *Processes with long-range correlations: Theory and applications*. Vol. 621. Springer, 2008, pp. 167–180. DOI: 10.1007/3-540-44832-2_9 (cit. on p. 13).

[66] T. Srokowski. “Non-Markovian Lévy diffusion in nonhomogeneous media”. In: *Physical Review E* 75 (5 May 2007), p. 051105. DOI: 10.1103/PhysRevE.75.051105 (cit. on pp. 13, 127).

[67] A. G. Cherstvy, A. V. Chechkin, and R. Metzler. “Anomalous diffusion and ergodicity breaking in heterogeneous diffusion processes”. In: *New Journal of Physics* 15.8 (Aug. 2013), p. 083039. DOI: 10.1088/1367-2630/15/8/083039 (cit. on pp. 13, 78, 126, 127).

[68] N. Leibovich and E. Barkai. “Infinite ergodic theory for heterogeneous diffusion processes”. In: *Physical Review E* 99 (4 Apr. 2019), p. 042138. DOI: 10.1103/PhysRevE.99.042138 (cit. on pp. 13, 17, 27, 127, 137, 139, 146, 153).

[69] M. Radice. “First-passage functionals of Brownian motion in logarithmic potentials and heterogeneous diffusion”. In: *Physical Review E* 108 (4 Oct. 2023), p. 044151. DOI: 10.1103/PhysRevE.108.044151 (cit. on pp. 13, 127).

[70] P. Singh. “Extreme value statistics and arcsine laws for heterogeneous diffusion processes”. In: *Physical Review E* 105 (2 Feb. 2022), p. 024113. DOI: 10.1103/PhysRevE.105.024113 (cit. on pp. 13, 21, 124, 127, 131, 132, 139).

[71] X. Wang, W. Deng, and Y. Chen. “Ergodic properties of heterogeneous diffusion processes in a potential well”. In: *The Journal of Chemical Physics* 150.16 (Apr. 2019), p. 164121. DOI: 10.1063/1.5090594 (cit. on pp. 13, 14, 126, 127, 133).

[72] M. Dentz et al. “Diffusion and trapping in heterogeneous media: An inhomogeneous continuous time random walk approach”. In: *Advances in Water Resources* 49 (2012), pp. 13–22. DOI: 10.1016/j.advwatres.2012.07.015 (cit. on pp. 13, 126).

[73] C. Loverdo et al. “Quantifying Hopping and Jumping in Facilitated Diffusion of DNA-Binding Proteins”. In: *Physical Review Letters* 102 (18 May 2009), p. 188101. DOI: 10.1103/PhysRevLett.102.188101 (cit. on pp. 13, 126).

[74] P. Lançon et al. “Drift without flux: Brownian walker with a space-dependent diffusion coefficient”. In: *Europhysics Letters (EPL)* 54.1 (2001), pp. 28–34. DOI: 10.1209/epl/i2001-00103-6 (cit. on pp. 13, 126).

[75] J. Pešek et al. “Mathematical model suitable for efficient simulation of thin semi-flexible polymers in complex environments”. In: *Soft Matter* 12 (14 2016), pp. 3360–3387. DOI: 10.1039/C5SM03106K (cit. on p. 13).

[76] S. Regev, N. Grønbech-Jensen, and O. Farago. “Isothermal Langevin dynamics in systems with power-law spatially dependent friction”. In: *Physical Review E* 94 (1 July 2016), p. 012116. DOI: 10.1103/PhysRevE.94.012116 (cit. on p. 13).

[77] C. W. Gardiner. *Handbook of stochastic methods for physics, chemistry and the natural sciences*. Third. Vol. 13. Springer Series in Synergetics. Berlin: Springer-Verlag, 2004, pp. xviii+415. ISBN: 3-540-20882-8. DOI: 10.1007/978-3-662-02452-2 (cit. on p. 13).

[78] E. Bertin and F. Bardou. *Lévy Statistics and Laser Cooling: How Rare Events Bring Atoms to Rest*. Vol. 76. 7. Cambridge University Press, 2001, pp. 630–636. DOI: 10.1119/1.2888543 (cit. on p. 13).

[79] O. Farago and N. Grønbech-Jensen. “On the connection between dissipative particle dynamics and the Itô-Stratonovich dilemma”. In: *The Journal of Chemical Physics* 144.8 (Feb. 2016), p. 084102. DOI: 10.1063/1.4942114 (cit. on p. 13).

[80] A. J. Bray. “Random walks in logarithmic and power-law potentials, nonuniversal persistence, and vortex dynamics in the two-dimensional XY model”. In: *Physical Review E* 62 (1 July 2000), pp. 103–112. DOI: 10.1103/PhysRevE.62.103 (cit. on p. 13).

[81] S. Pieprzyk, D. M. Heyes, and A. C. Brańka. “Spatially dependent diffusion coefficient as a model for pH sensitive microgel particles in microchannels”. In: *Biomicrofluidics* 10.5 (Oct. 2016), p. 054118. DOI: 10.1063/1.4964935 (cit. on p. 13).

[82] A. M. Berezhkovskii and D. E. Makarov. “Communication: Coordinate-dependent diffusivity from single molecule trajectories”. In: *The Journal of Chemical Physics* 147.20 (Nov. 2017), p. 201102. DOI: 10.1063/1.5006456 (cit. on p. 13).

[83] T. Kühn et al. “Protein Diffusion in Mammalian Cell Cytoplasm”. In: *PLoS ONE* 6.8 (Aug. 2011). Ed. by S. Agarwal, pp. 1–12. DOI: 10.1371/journal.pone.0022962 (cit. on pp. 13, 77, 78, 126).

[84] B. Kaulakys and M. Alaburda. “Modeling scaled processes and $1/f^{\beta}$ noise using nonlinear stochastic differential equations”. In: *Journal of Statistical Mechanics: Theory and Experiment* 2009.02 (Feb. 2009), P02051. DOI: 10.1088/1742-5468/2009/02/P02051 (cit. on p. 13).

[85] P. C. Bressloff and S. D. Lawley. “Temporal disorder as a mechanism for spatially heterogeneous diffusion”. In: *Physical Review E* 95 (6 June 2017), p. 060101. DOI: 10.1103/PhysRevE.95.060101 (cit. on pp. 14, 127).

[86] A. Pacheco-Pozo et al. “Langevin Equation in Heterogeneous Landscapes: How to Choose the Interpretation”. In: *Physical Review Letters* 133 (6 Aug. 2024), p. 067102. DOI: 10.1103/PhysRevLett.133.067102 (cit. on pp. 14, 127).

[87] B. P. van Milligen et al. “On the applicability of Fick’s law to diffusion in inhomogeneous systems”. In: *European Journal of Physics* 26.5 (Sept. 2005), pp. 913–925. DOI: 10.1088/0143-0807/26/5/023 (cit. on pp. 14, 127).

[88] R. Metzler, G. Oshanin, and S. Redner. *First-Passage Phenomena and Their Applications*. WORLD SCIENTIFIC, 2014. DOI: 10.1142/9104 (cit. on p. 14).

[89] G.-W. Li and X. S. Xie. “Central dogma at the single-molecule level in living cells”. In: *Nature* 475.7356 (July 2011), pp. 308–315. DOI: 10.1038/nature10315 (cit. on p. 14).

[90] M. R. Evans, S. N. Majumdar, and G. Schehr. “Stochastic resetting and applications”. In: *Journal of Physics A: Mathematical and Theoretical* 53.19 (Apr. 2020), p. 193001. DOI: 10.1088/1751-8121/ab7cfe (cit. on pp. 16, 18, 19, 31, 43).

[91] M. R. Evans and S. N. Majumdar. “Diffusion with optimal resetting”. In: *Journal of Physics A: Mathematical and Theoretical* 44.43 (2011), p. 435001. DOI: 10.1088/1751-8113/44/43/435001 (cit. on pp. 16, 31, 40, 54, 58).

[92] L. Kusmierz et al. “First Order Transition for the Optimal Search Time of Lévy Flights with Resetting”. In: *Physical Review Letters* 113 (22 Nov. 2014), p. 220602. DOI: 10.1103/PhysRevLett.113.220602 (cit. on p. 16).

[93] A. Pal. “Diffusion in a potential landscape with stochastic resetting”. In: *Physical Review E* 91.1 (1 Jan. 2015), p. 012113. DOI: 10.1103/PhysRevE.91.012113 (cit. on pp. 16, 102).

[94] D. Campos and V. Méndez. “Phase transitions in optimal search times: How random walkers should combine resetting and flight scales”. In: *Physical Review E* 92 (6 Dec. 2015), p. 062115. DOI: 10.1103/PhysRevE.92.062115 (cit. on p. 16).

[95] U. Bhat, C. De Bacco, and S. Redner. “Stochastic search with Poisson and deterministic resetting”. In: *Journal of Statistical Mechanics: Theory and Experiment* 2016.8 (2016), p. 083401. DOI: 10.1088/1742-5468/2016/08/083401 (cit. on p. 16).

[96] A. Pal, A. Kundu, and M. R. Evans. “Diffusion under time-dependent resetting”. In: *Journal of Physics A: Mathematical and Theoretical* 49.22 (2016), p. 225001. DOI: 10.1088/1751-8113/49/22/225001 (cit. on pp. 16, 20, 42).

[97] S. Reuveni. “Optimal Stochastic Restart Renders Fluctuations in First Passage Times Universal”. In: *Physical Review Letters* 116 (17 Apr. 2016), p. 170601. DOI: 10.1103/PhysRevLett.116.170601 (cit. on pp. 16, 70, 108).

[98] M. R. Evans and S. N. Majumdar. “Run and tumble particle under resetting: a renewal approach”. In: *Journal of Physics A: Mathematical and Theoretical* 51.47 (2018), p. 475003. DOI: 10.1088/1751-8121/aae74e (cit. on p. 16).

[99] A. Nagar and S. Gupta. “Stochastic resetting in interacting particle systems: A review”. In: *Journal of Physics A: Mathematical and Theoretical* 56.28 (2023), p. 283001. DOI: 10.1088/1751-8121/acda6c (cit. on p. 16).

[100] M. R. Evans and S. N. Majumdar. “Diffusion with Stochastic Resetting”. In: *Physical Review Letters* 106.16 (16 Apr. 2011), p. 160601. DOI: 10.1103/PhysRevLett.106.160601 (cit. on pp. 16–18, 31, 40, 43–45, 52, 57).

[101] B. Żbik and B. Dybiec. “Lévy flights and Lévy walks under stochastic resetting”. In: *Physical Review E* 109 (4 Apr. 2024), p. 044147. DOI: 10.1103/PhysRevE.109.044147 (cit. on p. 16).

[102] M. Radice and G. Cristadoro. “Optimizing leapover lengths of Lévy flights with resetting”. In: *Physical Review E* 110 (2 Aug. 2024), p. L022103. DOI: 10.1103/PhysRevE.110.L022103 (cit. on p. 16).

[103] S. N. Majumdar et al. “Record statistics for random walks and Lévy flights with resetting”. In: *Journal of Physics A: Mathematical and Theoretical* 55.3 (Dec. 2021), p. 034002. DOI: 10.1088/1751-8121/ac3fc1 (cit. on p. 16).

[104] P. C. Bressloff. “Occupation time of a run-and-tumble particle with resetting”. In: *Physical Review E* 102 (4 Oct. 2020), p. 042135. DOI: 10.1103/PhysRevE.102.042135 (cit. on pp. 16, 77).

[105] V. Méndez et al. “Continuous time random walks under Markovian resetting”. In: *Physical Review E* 103 (2 Feb. 2021), p. 022103. DOI: 10.1103/PhysRevE.103.022103 (cit. on pp. 16, 122).

[106] S. Ray and S. Reuveni. “Resetting transition is governed by an interplay between thermal and potential energy”. In: *The Journal of Chemical Physics* 154.17 (May 2021), p. 171103. DOI: 10.1063/5.0049642 (cit. on pp. 16, 20).

[107] S. Ahmad et al. “First passage of a particle in a potential under stochastic resetting: A vanishing transition of optimal resetting rate”. In: *Phys. Rev. E* 99 (2 Feb. 2019), p. 022130. DOI: 10.1103/PhysRevE.99.022130 (cit. on p. 16).

[108] S. Reuveni, M. Urbakh, and J. Klafter. “The role of substrate unbinding in michaelis-menten enzymatic reactions”. In: *Proceedings of the National Academy of Sciences* 106.2 (2014), 677a. DOI: 10.1073/pnas.1318122111 (cit. on p. 16).

[109] A. Nagar and S. Gupta. “Diffusion with stochastic resetting at power-law times”. In: *Physical Review E* 93 (6 June 2016), p. 060102. DOI: 10.1103/PhysRevE.93.060102 (cit. on pp. 16, 18, 108).

[110] V. Méndez and D. Campos. “Characterization of stationary states in random walks with stochastic resetting”. en. In: *Physical Review E* 93.2 (Feb. 2016), p. 022106. DOI: 10.1103/PhysRevE.93.022106 (cit. on pp. 17, 108).

[111] T. D. Keidar et al. “Adaptive resetting for informed search strategies and the design of non-equilibrium steady-states”. en. In: *Nature Communications* 16.1 (Aug. 2025), p. 7259. DOI: 10.1038/s41467-025-62398-2 (cit. on p. 17).

[112] G. Mercado-Vásquez, D. Boyer, and S. N. Majumdar. “Freezing transitions of Brownian particles in confining potentials”. In: *Journal of Statistical Mechanics: Theory and Experiment* 2022.6 (June 2022), p. 063203. DOI: 10.1088/1742-5468/ac764c (cit. on p. 17).

[113] M. R. Evans, S. N. Majumdar, and K. Mallick. “Optimal diffusive search: nonequilibrium resetting versus equilibrium dynamics”. In: *Journal of Physics A: Mathematical and Theoretical* 46.18 (Apr. 2013), p. 185001. DOI: 10.1088/1751-8113/46/18/185001 (cit. on pp. 17, 102, 124).

[114] A. Pal and S. Reuveni. “First Passage under Restart”. In: *Physical Review Letters* 118 (3 Jan. 2017), p. 030603. DOI: 10.1103/PhysRevLett.118.030603 (cit. on pp. 19, 20).

[115] A. Masó-Puigdellosas, D. Campos, and V. Méndez. “Transport properties and first-arrival statistics of random motion with stochastic reset times”. In: *Physical Review E* 99 (1 Jan. 2019), p. 012141. DOI: 10.1103/PhysRevE.99.012141 (cit. on pp. 19, 102, 108, 124).

[116] A. Pal, Ł. Kuśmierz, and S. Reuveni. “Invariants of motion with stochastic resetting and space-time coupled returns”. In: *New Journal of Physics* 21.11 (Nov. 2019), p. 113024. DOI: 10.1088/1367-2630/ab5201 (cit. on p. 19).

[117] G. García-Valladares et al. “Stochastic resetting with refractory periods: pathway formulation and exact results”. In: *Physica Scripta* 99.4 (Mar. 2024), p. 045234. DOI: 10.1088/1402-4896/ad317b (cit. on p. 19).

[118] É. Roldán and S. Gupta. “Path-integral formalism for stochastic resetting: Exactly solved examples and shortcuts to confinement”. In: *Phys. Rev. E* 96 (2 Aug. 2017), p. 022130. DOI: 10.1103/PhysRevE.96.022130 (cit. on p. 19).

[119] G. García-Valladares et al. “Optimal resetting strategies for search processes in heterogeneous environments”. In: *New Journal of Physics* 25.11 (Nov. 2023), p. 113031. DOI: 10.1088/1367-2630/ad06da (cit. on p. 19).

[120] J. C. Sunil et al. “The cost of stochastic resetting”. In: *Journal of Physics A: Mathematical and Theoretical* 56.39 (Sept. 2023), p. 395001. DOI: 10.1088/1751-8121/acf3bb (cit. on p. 20).

[121] M. Biroli et al. “Extreme Statistics and Spacing Distribution in a Brownian Gas Correlated by Resetting”. In: *Physical Review Letters* 130.20 (May 2023). DOI: 10.1103/physrevlett.130.207101 (cit. on p. 20).

[122] S. Carmi, L. Turgeman, and E. Barkai. “On Distributions of Functionals of Anomalous Diffusion Paths”. In: *Journal of Statistical Physics* 141.6 (Dec. 1, 2010), pp. 1071–1092. DOI: 10.1007/s10955-010-0086-6 (cit. on pp. 20, 77, 87, 90, 97, 113, 124, 131, 146).

[123] X. Wu, W. Deng, and E. Barkai. “Tempered fractional Feynman-Kac equation: Theory and examples”. In: *Physical Review E* 93.3 (Mar. 2016), p. 032151. DOI: 10.1103/PhysRevE.93.032151 (cit. on p. 20).

[124] M. Bandyopadhyay, S. Gupta, and D. Segal. “DNA breathing dynamics: Analytic results for distribution functions of relevant Brownian functionals”. In: *Phys. Rev. E* 83 (3 Mar. 2011), p. 031905. DOI: 10.1103/PhysRevE.83.031905 (cit. on pp. 20, 23).

[125] M. Kac. “On Some Connections between Probability Theory and Differential and Integral Equations”. In: *Second Berkeley Symposium on Mathematical Statistics and Probability*. Ed. by J. Neyman. University of California Press, Jan. 1951, pp. 189–215. DOI: 10.1525/9780520411586-016 (cit. on pp. 20, 142–144).

[126] M. Yor. *Some Aspects of Brownian Motion.* 1992. DOI: 10.1007/978-3-0348-8954-4 (cit. on p. 20).

[127] H. Geman and M. Yor. “BESSEL PROCESSES, ASIAN OPTIONS, AND PERPETUITIES”. In: *Mathematical Finance* 3.4 (1993), pp. 349–375. DOI: 10.1111/j.1467-9965.1993.tb00092.x (cit. on p. 20).

[128] A. Comtet, J. Desbois, and C. Texier. “Functionals of Brownian motion, localization and metric graphs”. In: *Journal of Physics A: Mathematical and General* 38.37 (Aug. 2005), R341. DOI: 10.1088/0305-4470/38/37/R01 (cit. on p. 20).

[129] S. N. Majumdar. “Brownian Functionals in Physics and Computer Science”. In: *The Legacy of Albert Einstein* 89 (2005), p. 2076. DOI: 10.1142/9789812772718_0006 (cit. on pp. 20, 21, 23, 94, 97, 128, 192).

[130] A. Baule and R. Friedrich. “Investigation of a generalized Obukhov model for turbulence”. In: *Physics Letters A* 350.3 (2006), pp. 167–173. DOI: 10.1016/j.physleta.2005.10.017 (cit. on pp. 20, 24).

[131] S. N. Majumdar and A. J. Bray. “Large-deviation functions for nonlinear functionals of a Gaussian stationary Markov process”. In: *Physical Review E* 65 (5 May 2002), p. 051112. DOI: 10.1103/PhysRevE.65.051112 (cit. on pp. 20, 23, 24).

[132] L. Turgeman, S. Carmi, and E. Barkai. “Fractional Feynman-Kac Equation for Non-Brownian Functionals”. In: *Physical Review Letters* 103 (19 Nov. 2009), p. 190201. DOI: 10.1103/PhysRevLett.103.190201 (cit. on p. 20).

[133] S. Sabhapandit, S. N. Majumdar, and A. Comtet. “Statistical properties of functionals of the paths of a particle diffusing in a one-dimensional random potential”. In: *Physical Review E* 73.5 (2006), p. 051102. DOI: 10.1103/PhysRevE.73.051102 (cit. on pp. 21, 22, 146).

[134] E. Barkai. “Residence Time Statistics for Normal and Fractional Diffusion in a Force Field”. In: *Journal of Statistical Physics* 123.4 (May 1, 2006), pp. 883–907. DOI: 10.1007/s10955-006-9109-8 (cit. on pp. 21, 77, 90, 102, 124, 129, 138, 146).

[135] S. Carmi and E. Barkai. “Fractional Feynman-Kac equation for weak ergodicity breaking”. In: *Physical Review E* 84 (6 Dec. 2011), p. 061104. DOI: 10.1103/PhysRevE.84.061104 (cit. on p. 21).

[136] P. Singh and A. Kundu. “Generalised ’Arcsine’ laws for run-and-tumble particle in one dimension”. In: *Journal of Statistical Mechanics: Theory and Experiment* 2019.8 (Aug. 2019), p. 083205. DOI: 10.1088/1742-5468/ab3283 (cit. on pp. 21, 77).

[137] A. C. Barato et al. “Arcsine Laws in Stochastic Thermodynamics”. In: *Physical Review Letters* 121.9 (Aug. 2018), p. 090601. DOI: 10.1103/PhysRevLett.121.090601 (cit. on p. 21).

[138] P. Lévy. “Sur certains processus stochastiques homogènes”. fr. In: *Compositio Mathematica* 7 (1940), pp. 283–339 (cit. on pp. 21, 97, 118, 119, 129).

[139] J. Lamperti. “An occupation time theorem for a class of stochastic processes”. In: *Transactions of the American Mathematical Society* 88.2 (1958), pp. 380–387. DOI: 10.1090/s0002-9947-1958-0094863-x (cit. on pp. 22, 97, 118, 122, 131).

[140] G. Bel and E. Barkai. “Weak Ergodicity Breaking in the Continuous-Time Random Walk”. In: *Physical Review Letters* 94.24 (24 June 2005), p. 240602. DOI: 10.1103/PhysRevLett.94.240602 (cit. on pp. 22, 24, 25).

[141] C. Godrèche and J.-M. Luck. “Statistics of the Occupation Time of Renewal Processes”. In: *Journal of Statistical Physics* 104 (Nov. 2001), pp. 489–524. DOI: 10.1023/A:1010364003250 (cit. on pp. 22, 27, 77, 108, 109, 153, 189, 192).

[142] S. N. Majumdar and A. Comtet. “Local and Occupation Time of a Particle Diffusing in a Random Medium”. In: *Physical Review Letters* 89.6 (6 July 2002), p. 060601. DOI: 10.1103/PhysRevLett.89.060601 (cit. on p. 22).

[143] N. Agmon. “The residence time equation”. In: *Chemical Physics Letters* 497.4 (2010), pp. 184–186. DOI: 10.1016/j.cplett.2010.08.019 (cit. on p. 22).

[144] N. Agmon. “Residence times in diffusion processes”. In: *The Journal of Chemical Physics* 81.8 (Oct. 1984), pp. 3644–3647. DOI: 10.1063/1.448113 (cit. on p. 22).

[145] L. A. Shepp. “On the Integral of the Absolute Value of the Pinned Wiener Process”. In: *The Annals of Probability* 10.1 (Feb. 1982). DOI: 10.1214/aop/1176993926 (cit. on pp. 23, 24).

[146] M. Perman and J. A. Wellner. “On the distribution of Brownian areas”. In: *The Annals of Applied Probability* 6.4 (1996), pp. 1091–1111. DOI: 10.1214/aoap/1035463325 (cit. on p. 23).

[147] L. Takacs. “On the Distribution of the Integral of the Absolute Value of the Brownian Motion”. In: *The Annals of Applied Probability* 3.1 (Feb. 1993). DOI: 10.1214/aoap/1177005514 (cit. on pp. 23, 24).

[148] D. M. Cifarelli. “Contributi intorno ad un test per l’omogeneità tra due campioni”. In: *Giornale degli Economisti e Annali di Economia* 34.3/4 (1975), pp. 233–249. DOI: 10.5962/bhl.title.4903 (cit. on p. 24).

[149] B. L. Altshuler, A. G. Aronov, and D. E. Khmelnitskii. “Effects of electron-electron collisions with small energy transfers on quantum localisation”. In: *Journal of Physics C: Solid State Physics* 15.36 (Dec. 1982), p. 7367. DOI: 10.1088/0022-3719/15/36/018 (cit. on p. 24).

[150] S. Chandrasekhar. “Stochastic Problems in Physics and Astronomy”. In: *Reviews of Modern Physics* 15.1 (1943), pp. 1–89. DOI: 10.1103/revmodphys.15.1 (cit. on pp. 24, 165).

[151] D. G. Kendall et al. *Processus Stochastiques et Mouvement Brownien*. Vol. 53. 1/2. Paris: Gauthier–Villars, 1940, p. 293. DOI: 10.2307/2334089 (cit. on p. 24).

[152] J.-P. Bouchaud. “Weak ergodicity breaking and aging in disordered systems”. In: *Journal de Physique I* 2.9 (1992), pp. 1705–1713. DOI: 10.1051/jp1:1992238 (cit. on p. 24).

[153] X. Brokmann et al. “Statistical Aging and Nonergodicity in the Fluorescence of Single Nanocrystals”. In: *Physical Review Letters* 90 (12 Mar. 2003), p. 120601. DOI: 10.1103/PhysRevLett.90.120601 (cit. on p. 24).

[154] S. Burov, R. Metzler, and E. Barkai. “Aging and nonergodicity beyond the Khinchin theorem”. In: *Proceedings of the National Academy of Sciences* 107.30 (2010), pp. 13228–13233. DOI: 10.1073/pnas.1003693107 (cit. on p. 24).

[155] A. Lubelski, I. M. Sokolov, and J. Klafter. “Nonergodicity Mimics Inhomogeneity in Single Particle Tracking”. In: *Physical Review Letters* 100 (25 June 2008), p. 250602. DOI: 10.1103/PhysRevLett.100.250602 (cit. on p. 24).

[156] A. V. Weigel et al. “Ergodic and nonergodic processes coexist in the plasma membrane as observed by single-molecule tracking”. In: *Proceedings of the National Academy of Sciences* 108.16 (2011), pp. 6438–6443. DOI: 10.1073/pnas.1016325108 (cit. on p. 24).

[157] F. Bardou et al. “Subrecoil laser cooling and Lévy flights”. In: *Physical Review Letters* 72 (2 Jan. 1994), pp. 203–206. DOI: 10.1103/PhysRevLett.72.203 (cit. on p. 25).

[158] Y. He et al. “Random Time-Scale Invariant Diffusion and Transport Coefficients”. In: *Physical Review Letters* 101 (5 July 2008), p. 058101. DOI: 10.1103/PhysRevLett.101.058101 (cit. on pp. 25, 27, 153).

[159] A. G. Cherstvy et al. “Time averages and their statistical variation for the Ornstein-Uhlenbeck process: Role of initial particle distributions and relaxation to stationarity”. In: *Physical Review E* 98 (2 Aug. 2018), p. 022134. DOI: 10.1103/PhysRevE.98.022134 (cit. on p. 26).

[160] T. Akimoto, A. G. Cherstvy, and R. Metzler. “Ergodicity, rejuvenation, enhancement, and slow relaxation of diffusion in biased continuous-time random walks”. In: *Physical Review E* 98 (2 Aug. 2018), p. 022105. DOI: 10.1103/PhysRevE.98.022105 (cit. on p. 26).

[161] A. G. Cherstvy and R. Metzler. “Ergodicity breaking and particle spreading in noisy heterogeneous diffusion processes”. In: *The Journal of Chemical Physics* 142.14 (Apr. 2015), p. 144105. DOI: 10.1063/1.4917077 (cit. on p. 26).

[162] P. G. Meyer and R. Metzler. “Stochastic processes in a confining harmonic potential in the presence of static and dynamic measurement noise”. In: *New Journal of Physics* 25.6 (June 2023), p. 063003. DOI: 10.1088/1367-2630/acd94f (cit. on p. 26).

[163] R. Metzler and M. Weiss. “Discriminating stochastic processes for the assessment of materials properties by diffusion measurements”. In: *Physical Chemistry Chemical Physics* 27 (27 2025), pp. 14350–14358. DOI: 10.1039/D5CP01378J (cit. on p. 26).

[164] F. Rehfeldt and M. Weiss. “The random walker’s toolbox for analyzing single-particle tracking data”. In: *Soft Matter* 19 (28 2023), pp. 5206–5222. DOI: 10.1039/D3SM00557G (cit. on p. 26).

[165] V. Tejedor et al. “Quantitative Analysis of Single Particle Trajectories: Mean Maximal Excursion Method”. In: *Biophysical Journal* 98.7 (2010), pp. 1364–1372. DOI: 10.1016/j.bpj.2009.12.4282 (cit. on p. 26).

[166] E. Barkai. “Fractional Fokker-Planck equation, solution, and application”. In: *Physical Review E* 63 (4 Mar. 2001), p. 046118. DOI: 10.1103/PhysRevE.63.046118 (cit. on p. 27).

[167] O. Bénichou et al. “Intermittent search strategies”. In: *Reviews of Modern Physics* 83 (1 Mar. 2011), pp. 81–129. DOI: 10.1103/RevModPhys.83.81 (cit. on pp. 31, 34, 38, 40).

[168] F. Bartumeus et al. *The physics of foraging: an introduction to random searches and biological encounters*. Ed. by M. D. McDonnell. Vol. 9. 9. Cambridge University Press, 2011, e106373. DOI: 10.1371/journal.pone.0106373 (cit. on pp. 31, 34).

[169] D. L. Kramer and R. L. McLaughlin. “The Behavioral Ecology of Intermittent Locomotion1”. In: *American Zoologist* 41.2 (Aug. 2015), pp. 137–153. DOI: 10.1093/icb/41.2.137 (cit. on pp. 31, 34).

[170] M. Coppey et al. “Kinetics of target site localization of a protein on DNA: a stochastic approach”. In: *Biophysical Journal* 87.3 (Sept. 2004), pp. 1640–1649. DOI: 10.1529/biophysj.104.045773 (cit. on pp. 31, 34).

[171] I. Gomez Portillo, D. Campos, and V. Méndez. “Intermittent random walks: Transport regimes and implications on search strategies”. In: *Journal of Statistical Mechanics: Theory and Experiment* 2011 (Feb. 2011), P02033. DOI: 10.1088/1742-5468/2011/02/P02033 (cit. on pp. 31, 34, 37, 49).

[172] O. Bénichou et al. “A stochastic model for intermittent search strategies”. In: *Journal of Physics: Condensed Matter* 17.49 (2005), S4275. DOI: 10.1088/0953-8984/17/49/020 (cit. on pp. 31, 34, 38, 40, 49).

[173] G. Oshanin et al. “Efficient search by optimized intermittent random walks”. In: *Journal of Physics A: Mathematical and Theoretical* 42.43 (Oct. 2009), p. 434008. DOI: 10.1088/1751-8113/42/43/434008 (cit. on pp. 31, 34, 38).

[174] M. A. Lomholt et al. “Lévy strategies in intermittent search processes are advantageous”. In: *Proceedings of the National Academy of Sciences* 105.32 (July 2008), pp. 11055–11059. DOI: 10.1073/pnas.0803117105 (cit. on pp. 31, 34, 40, 49).

[175] O. Vilk et al. “Phase Transition in a Non-Markovian Animal Exploration Model with Preferential Returns”. In: *Physical Review Letters* 128 (14 Apr. 2022), p. 148301. DOI: 10.1103/PhysRevLett.128.148301 (cit. on pp. 31, 34).

[176] M. D. Cameron et al. “Pronounced Fidelity and Selection for Average Conditions of Calving Area Suggestive of Spatial Memory in a Highly Migratory Ungulate”. In: *Frontiers in Ecology and Evolution* 8 (2020). DOI: 10.3389/fevo.2020.564567 (cit. on pp. 31, 52).

[177] B. Van Moorter et al. “Memory keeps you at home: a mechanistic model for home range emergence”. In: *Oikos* 118.5 (2009), pp. 641–652. DOI: 10.1111/j.1600-0706.2008.17003.x (cit. on pp. 31, 52).

[178] F. H. González, A. P. Riascos, and D. Boyer. “Diffusive transport on networks with stochastic resetting to multiple nodes”. In: *Physical Review E* 103.6 (2021), p. 062126. DOI: 10.1103/physreve.103.062126 (cit. on pp. 31, 52).

[179] P. Julián-Salgado, L. Dagdug, and D. Boyer. “Diffusion with two resetting points”. In: *Physical Review E* 109 (2 Feb. 2024), p. 024134. DOI: 10.1103/PhysRevE.109.024134 (cit. on pp. 31, 52).

[180] J. Q. Toledo-Marín and D. Boyer. “First passage time and information of a one-dimensional Brownian particle with stochastic resetting to random positions”. In: *Physica A: Statistical Mechanics and its Applications* 625 (2023), p. 129027. DOI: 10.1016/j.physa.2023.129027 (cit. on pp. 31, 52).

[181] K. S. Olsen. “Steady-state moments under resetting to a distribution”. In: *Physical Review E* 108 (4 Oct. 2023), p. 044120. DOI: 10.1103/PhysRevE.108.044120 (cit. on pp. 31, 52).

[182] A. M. Reynolds. “On the intermittent behaviour of foraging animals”. In: *Europhysics Letters (EPL)* 75.4 (2006), p. 517. DOI: 10.1209/epl/i2006-10157-x (cit. on p. 34).

[183] D. W. Stephens and J. R. Krebs. *Foraging theory*. Princeton, N.J.: Princeton University Press, 1986. ISBN: 0691084416 (alk. paper). DOI: 10.2307/j.ctvs32s6b (cit. on p. 34).

[184] A. C. Kamil and A. B. Bond. *Foraging behavior*. Springer Science & Business Media, 2012, pp. 106–126. DOI: 10.1093/acprof:oso/9780195377804.003.0007 (cit. on p. 34).

[185] T. Zhou, P. Xu, and W. Deng. “Continuous-time random walks and Lévy walks with stochastic resetting”. In: *Physical Review Research* 2 (1 Jan. 2020), p. 013103. DOI: 10.1103/PhysRevResearch.2.013103 (cit. on p. 34).

[186] A. Abdullahi et al. “Stochastic models in seed dispersals: random walks and birth–death processes”. In: *Journal of Biological Dynamics* 13.1 (2019), pp. 345–361. DOI: 10.1080/17513758.2019.1605003 (cit. on p. 34).

[187] F. G. Schmitt and L. Seuront. “Multifractal random walk in copepod behavior”. In: *Physica A: Statistical Mechanics and its Applications* 301.1 (2001), pp. 375–396. DOI: 10.1016/S0378-4371(01)00429-0 (cit. on p. 34).

[188] O. Bénichou et al. “Intermittent search process and teleportation”. In: *The Journal of Chemical Physics* 126.23 (June 2007), p. 234109. DOI: 10.1063/1.2741516 (cit. on p. 34).

[189] M. J. Skaug, J. Mabry, and D. K. Schwartz. “Intermittent Molecular Hopping at the Solid-Liquid Interface”. In: *Physical Review Letters* 110 (25 June 2013), p. 256101. DOI: 10.1103/PhysRevLett.110.256101 (cit. on p. 34).

[190] A. Cavagna. “Supercooled liquids for pedestrians”. In: *Physics Reports* 476.4 (2009), pp. 51–124. DOI: 10.1016/j.physrep.2009.03.003 (cit. on p. 34).

[191] E. R. Weeks and D. A. Weitz. “Subdiffusion and the cage effect studied near the colloidal glass transition”. In: *Chemical Physics* 284.1 (2002). Strange Kinetics, pp. 361–367. DOI: 10.1016/S0301-0104(02)00667-5 (cit. on p. 34).

[192] S. Rajasekar and K. P. N. Murthy. “Dynamical evolution of escape probability in the presence of Sinai disorder”. In: *Physical Review E* 57 (2 Feb. 1998), pp. 1315–1318. DOI: 10.1103/PhysRevE.57.1315 (cit. on p. 34).

[193] P. de Anna et al. “Flow Intermittency, Dispersion, and Correlated Continuous Time Random Walks in Porous Media”. In: *Physical Review Letters* 110 (18 May 2013), p. 184502. DOI: 10.1103/PhysRevLett.110.184502 (cit. on p. 34).

[194] P. K. Kang et al. “Pore-scale intermittent velocity structure underpinning anomalous transport through 3-D porous media”. In: *Geophysical Research Letters* 41.17 (2014), pp. 6184–6190. DOI: 10.1002/2014GL061475 (cit. on p. 34).

[195] R. Pastore et al. “Many facets of intermittent dynamics in colloidal and molecular glasses”. In: *Colloids and Surfaces A: Physicochemical and Engineering Aspects* 532 (2017). 30th European Colloid and Interface Society Meeting, Rome 2016, pp. 87–96. DOI: 10.1016/j.colsurfa.2017.06.019 (cit. on p. 34).

[196] S.-N. Chow, X. Ye, and H. Zhou. “Potential induced random teleportation on finite graphs”. In: *Computational Optimization and Applications* 61.3 (July 2015), pp. 689–711. DOI: 10.1007/s10589-015-9727-7 (cit. on p. 34).

[197] P. Grassberger. “Self-Trapping Self-Repelling Random Walks”. In: *Physical Review Letters* 119 (14 Oct. 2017), p. 140601. DOI: 10.1103/PhysRevLett.119.140601 (cit. on p. 34).

[198] A. Ramezanpour. “Intermittent exploration on a scale-free network”. In: *Europhysics Letters (EPL)* 77.6 (2007), p. 60004. DOI: 10.1209/0295-5075/77/60004 (cit. on p. 34).

[199] G. Oshanin et al. “Intermittent random walks for an optimal search strategy: one-dimensional case”. In: *Journal of Physics: Condensed Matter* 19.6 (Jan. 2007), p. 065142. DOI: 10.1088/0953-8984/19/6/065142 (cit. on pp. 34, 37, 49).

[200] F. Rojo, C. E. Budde, and H. S. Wio. “Optimal intermittent search strategies”. In: *Journal of Physics A: Mathematical and Theoretical* 42.12 (Feb. 2009), p. 125002. DOI: 10.1088/1751-8113/42/12/125002 (cit. on p. 34).

[201] D. Boyer and C. Solis-Salas. “Random Walks with Preferential Relocations to Places Visited in the Past and their Application to Biology”. In: *Physical Review Letters* 112.24 (24 June 2014), p. 240601. DOI: 10.1103/PhysRevLett.112.240601 (cit. on p. 52).

[202] S. N. Majumdar, S. Sabhapandit, and G. Schehr. “Random walk with random resetting to the maximum position”. In: *Phys. Rev. E* 92 (5 Nov. 2015), p. 052126. DOI: 10.1103/PhysRevE.92.052126 (cit. on p. 52).

[203] O. Tal-Friedman, Y. Roichman, and S. Reuveni. “Diffusion with partial resetting”. In: *Phys. Rev. E* 106 (5 Nov. 2022), p. 054116. DOI: 10.1103/PhysRevE.106.054116 (cit. on p. 52).

[204] B. Besga et al. “Optimal mean first-passage time for a Brownian searcher subjected to resetting: Experimental and theoretical results”. In: *Physical Review Research* 2 (3 July 2020), p. 032029. DOI: 10.1103/PhysRevResearch.2.032029 (cit. on p. 52).

[205] T. M. Michelitsch et al. “Random walks with stochastic resetting in complex networks: A discrete-time approach”. In: *Chaos: An Interdisciplinary Journal of Nonlinear Science* 35.1 (Jan. 2025), p. 013119. DOI: 10.1063/5.0238517 (cit. on pp. 52, 109).

[206] G. Tucci et al. “Controlling particle currents with evaporation and resetting from an interval”. In: *Physical Review Research* 2.4 (Oct. 2020). DOI: 10.1103/physrevresearch.2.043138 (cit. on p. 52).

[207] F. Mori, K. S. Olsen, and S. Krishnamurthy. “Entropy production of resetting processes”. In: *Physical Review Research* 5 (2 May 2023), p. 023103. DOI: 10.1103/PhysRevResearch.5.023103 (cit. on p. 52).

[208] T. T. Da Silva. “Effects of a moving barrier on the first-passage time of a diffusing particle under stochastic resetting”. In: *Communications in Nonlinear Science and Numerical Simulation* 145 (June 2025), p. 108732. DOI: 10.1016/j.cnsns.2025.108732 (cit. on p. 52).

[209] C. Manzo and M. F. Garcia-Parajo. “A review of progress in single particle tracking: from methods to biophysical insights”. In: *Reports on Progress in Physics* 78.12 (Oct. 2015), p. 124601. DOI: 10.1088/0034-4885/78/12/124601 (cit. on pp. 77, 126).

[210] J. J. E. Maris et al. “Single-molecule observation of diffusion and catalysis in nanoporous solids”. In: *Adsorption* 27.3 (Apr. 2021), pp. 423–452. DOI: 10.1007/s10450-020-00292-7 (cit. on pp. 77, 78, 126).

[211] B. P. English et al. “Single-molecule investigations of the stringent response machinery in living bacterial cells”. In: *Proceedings of the National Academy of Sciences* 108.31 (Aug. 2011), E365–73. DOI: 10.1073/pnas.1102255108 (cit. on pp. 77, 126).

[212] A. Pal et al. “Local time of diffusion with stochastic resetting”. In: *Journal of Physics A: Mathematical and Theoretical* 52.26 (2019), p. 264002. DOI: 10.1088/1751-8121/ab2069 (cit. on pp. 77, 98, 103).

[213] T. Sadhu, M. Delorme, and K. J. Wiese. “Generalized Arcsine Laws for Fractional Brownian Motion”. In: *Physical Review Letters* 120.4 (2018), p. 040603. DOI: 10.1103/PhysRevLett.120.040603 (cit. on pp. 77, 152).

[214] M. Kimura and T. Akimoto. “Occupation time statistics of the fractional Brownian motion in a finite domain”. In: *Physical Review E* 106.6 (2022), p. 064132. DOI: 10.1103/PhysRevE.106.064132 (cit. on pp. 77, 153, 155, 156).

[215] G. Margolin and E. Barkai. “Nonergodicity of Blinking Nanocrystals and Other Lévy-Walk Processes”. In: *Physical Review Letters* 94 (8 Mar. 2005), p. 080601. DOI: 10.1103/PhysRevLett.94.080601 (cit. on p. 77).

[216] R. Dey et al. “Experimental verification of arcsine laws in mesoscopic nonequilibrium systems”. In: *Physical Review E* 106.5 (2022), p. 054113. DOI: 10.1103/PhysRevE.106.054113 (cit. on p. 77).

[217] S. Paramanick et al. “Arcsine Laws of Light”. In: *PRX Life* 132.13 (2024), p. 133801. DOI: 10.1103/PRXLife.2.033007 (cit. on p. 77).

[218] G. Bel and E. Barkai. “Weak ergodicity breaking with deterministic dynamics”. In: *Europhysics Letters (EPL)* 74.1 (Feb. 22, 2006), p. 15. DOI: 10.1209/epl/i2005-10501-8 (cit. on p. 77).

[219] A. G. Cherstvy and R. Metzler. “Population splitting, trapping, and nonergodicity in heterogeneous diffusion processes”. In: *Physical Chemistry Chemical Physics* 15 (46 2013), pp. 20220–20235. DOI: 10.1039/C3CP53056F (cit. on pp. 78, 126, 127, 139, 176).

[220] V. M. Kenkre, E. W. Montroll, and M. F. Shlesinger. “Generalized master equations for continuous-time random walks”. In: *Journal of Statistical Physics* 9.1 (Sept. 1, 1973), pp. 45–50. DOI: 10.1007/BF01016796 (cit. on pp. 80, 81).

[221] T. Sandev, R. Metzler, and A. Chechkin. “From continuous time random walks to the generalized diffusion equation”. In: *Fractional Calculus and Applied Analysis* 21.1 (Feb. 2018), pp. 10–28. DOI: 10.1515/fca-2018-0002 (cit. on p. 81).

[222] M. Abramovitz and I. A. Stegun. *Handbook of Mathematical functions. With Formulas, Graphs and Mathematical Tables*. Vol. 128. 4. Dover, 1964, p. 593. DOI: 10.2307/2343473 (cit. on pp. 83, 115).

[223] J. Chover and W. Feller. *An introduction to probability theory and its applications. Vol. II.* Vol. 62. Second edition 319. New York: John Wiley & Sons Inc., 1971, pp. xxiv+669. DOI: 10.2307/2283695 (cit. on pp. 83, 188).

[224] R. Gorenflo et al. *Mittag-Leffler Functions, Related Topics and Applications*. Springer Berlin Heidelberg, 2020. ISBN: 9783662615508. DOI: 10.1007/978-3-662-61550-8 (cit. on pp. 83, 121, 184).

[225] F. den Hollander et al. “Properties of additive functionals of Brownian motion with resetting”. In: *Journal of Physics A: Mathematical and Theoretical* 52.17 (Apr. 2019), p. 175001. DOI: 10.1088/1751-8121/ab0efd (cit. on pp. 98, 101, 108, 110).

[226] J. M. Meylahn, S. Sabhapandit, and H. Touchette. “Large deviations for Markov processes with resetting”. In: *Physical Review E* 92 (6 Dec. 2015), p. 062148. DOI: 10.1103/PhysRevE.92.062148 (cit. on pp. 98, 108, 110).

[227] V. Stojkoski et al. “Autocorrelation functions and ergodicity in diffusion with stochastic resetting”. In: *Journal of Physics A: Mathematical and Theoretical* 55.10 (2022), p. 104003. DOI: 10.1088/1751-8121/ac4ce9 (cit. on p. 102).

[228] D. Gupta, C. A. Plata, and A. Pal. “Work Fluctuations and Jarzynski Equality in Stochastic Resetting”. In: *Physical Review Letters* 124.11 (2020), p. 110608. DOI: 10.1103/PhysRevLett.124.110608 (cit. on p. 103).

[229] S. Eule and J. J. Metzger. “Non-equilibrium steady states of stochastic processes with intermittent resetting”. In: *New Journal of Physics* 18.3 (Mar. 2016), p. 033006. DOI: 10.1088/1367-2630/18/3/033006 (cit. on p. 108).

[230] A. V. Chechkin and I. M. Sokolov. “Random Search with Resetting: A Unified Renewal Approach”. In: *Physical Review Letters* 121 (5 Aug. 2018), p. 050601. DOI: 10.1103/PhysRevLett.121.050601 (cit. on p. 108).

[231] V. P. Shkilev and I. M. Sokolov. “Subdiffusive continuous time random walks with power-law resetting”. In: *Journal of Physics A: Mathematical and Theoretical* 55.48 (Dec. 2022), p. 484003. DOI: 10.1088/1751-8121/aca450 (cit. on p. 108).

[232] A. S. Bodrova and I. M. Sokolov. “Continuous-time random walks under power-law resetting”. In: *Physical Review E* 101 (6 June 2020), p. 062117. DOI: 10.1103/PhysRevE.101.062117 (cit. on pp. 108, 122).

[233] W. Wang et al. “Renewal theory with fat-tailed distributed sojourn times: Typical versus rare”. In: *Physical Review E* 98 (4 Oct. 2018), p. 042139. DOI: 10.1103/PhysRevE.98.042139 (cit. on p. 109).

[234] T. J. Kozubowski. “Fractional moment estimation of linnik and mittag-leffler parameters”. In: *Mathematical and Computer Modelling* 34.9 (2001), pp. 1023–1035. DOI: 10.1016/S0895-7177(01)00115-7 (cit. on pp. 121, 175, 176).

[235] K. A. Penson and K. Górska. “Exact and Explicit Probability Densities for One-Sided Lévy Stable Distributions”. In: *Physical Review Letters* 105 (21 Nov. 2010), p. 210604. DOI: 10.1103/PhysRevLett.105.210604 (cit. on p. 121).

[236] R. Weron. “On the Chambers-Mallows-Stuck method for simulating skewed stable random variables”. In: *Statistics &; Probability Letters* 28.2 (1996), pp. 165–171. DOI: 10.1016/0167-7152(95)00113-1 (cit. on pp. 121, 176).

[237] M. Guéneau, S. N. Majumdar, and G. Schehr. “Optimal mean first-passage time of a run-and-tumble particle in a class of one-dimensional confining potentials”. In: *Europhysics Letters* 145.6 (Mar. 2024), p. 61002. DOI: 10.1209/0295-5075/ad2ba3 (cit. on p. 124).

[238] M. Yang and M. Ripoll. "Drift velocity in non-isothermal inhomogeneous systems". In: *The Journal of Chemical Physics* 136.20 (May 2012), p. 204508. DOI: 10.1063/1.4723685 (cit. on p. 126).

[239] J. Mittal et al. "Layering and Position-Dependent Diffusive Dynamics of Confined Fluids". In: *Physical Review Letters* 100 (14 Apr. 2008), p. 145901. DOI: 10.1103/PhysRevLett.100.145901 (cit. on p. 126).

[240] A. Weron et al. "Ergodicity breaking on the neuronal surface emerges from random switching between diffusive states". In: *Scientific Reports* 7.1 (July 2017), p. 5404. DOI: 10.1038/s41598-017-05911-y (cit. on p. 126).

[241] K. Norregaard et al. "Manipulation and Motion of Organelles and Single Molecules in Living Cells". In: *Chemical Reviews* 117.5 (Mar. 2017), pp. 4342–4375. DOI: 10.1021/acs.chemrev.6b00638 (cit. on p. 126).

[242] A. G. Cherstvy, A. V. Chechkin, and R. Metzler. "Particle invasion, survival, and non-ergodicity in 2D diffusion processes with space-dependent diffusivity". In: *Soft Matter* 10 (10 2014), pp. 1591–1601. DOI: 10.1039/C3SM52846D (cit. on p. 126).

[243] B. J. West et al. "Stochastic processes with non-additive fluctuations: I. Itô and Stratonovich calculus and the effects of correlations". In: *Physica A: Statistical Mechanics and its Applications* 97.2 (1979), pp. 211–233. DOI: 10.1016/0378-4371(79)90103-1 (cit. on p. 127).

[244] X. Wang, Y. Chen, and W. Deng. "Feynman-Kac equation revisited". In: *Physical Review E* 98 (5 Nov. 2018), p. 052114. DOI: 10.1103/PhysRevE.98.052114 (cit. on p. 127).

[245] N. G. van Kampen and W. P. Reinhardt. *Stochastic processes in physics and chemistry*. Vol. 1. 2. Elsevier, 1992, pp. 78–80. DOI: 10.1063/1.2915501 (cit. on pp. 142, 145, 163).

[246] W. Deng and E. Barkai. "Ergodic properties of fractional Brownian-Langevin motion". In: *Physical Review E* 79.1 (1 Jan. 2009), p. 011112. DOI: 10.1103/PhysRevE.79.011112 (cit. on pp. 142, 152).

[247] J.-H. Jeon and R. Metzler. "Fractional Brownian motion and motion governed by the fractional Langevin equation in confined geometries". In: *Physical Review E* 81.2 (2010), p. 021103. DOI: 10.1103/PhysRevE.81.021103 (cit. on pp. 142, 152).

[248] A. I. Khinchin. *Mathematical Foundations of Statistical Mechanics*. Trans. by R. A. Silverman and M. D. Friedman. Vol. 66. 2. Dover, New York, 1949, p. 159. DOI: 10.2307/2310044 (cit. on p. 147).

[249] S. B. Yuste, E. Abad, and C. Escudero. "Diffusion in an expanding medium: Fokker-Planck equation, Green's function, and first-passage properties". In: *Physical Review E* 94 (3 Sept. 2016), p. 032118. DOI: 10.1103/PhysRevE.94.032118 (cit. on p. 150).

[250] P. J. Colmenares. “Effect of time-dependent temperature and field-bath interaction on the diffusion of generalized Brownian motion”. In: *Physical Review E* 111 (4 Apr. 2025), p. 044126. DOI: 10.1103/PhysRevE.111.044126 (cit. on p. 150).

[251] M. Herberthson, P. J. Basser, and E. Özarslan. “Time-dependent diffusion in one-dimensional disordered media decorated by permeable membranes: Theoretical findings backed by simulations and a new disorder class”. In: *Physics of Fluids* 37.6 (June 2025), p. 067159. DOI: 10.1063/5.0272370 (cit. on p. 150).

[252] K. J. Wiese, S. N. Majumdar, and A. Rosso. “Perturbation theory for fractional Brownian motion in presence of absorbing boundaries”. In: *Physical Review E* 83 (6 June 2011), p. 061141. DOI: 10.1103/PhysRevE.83.061141 (cit. on p. 152).

[253] T. Vojta and A. Warhover. “Probability density of fractional Brownian motion and the fractional Langevin equation with absorbing walls”. In: *Journal of Statistical Mechanics: Theory and Experiment* 2021.3 (2021), p. 033215. DOI: 10.1088/1742-5468/abe700 (cit. on p. 152).

[254] D. A. Darling and M. Kac. “On occupation times for Markoff processes”. In: *Transactions of the American Mathematical Society* 84 (1957), pp. 444–458. DOI: 10.1090/s0002-9947-1957-0084222-7 (cit. on p. 153).

[255] H. Safdari et al. “Aging scaled Brownian motion”. In: *Physical Review E* 91 (4 Apr. 2015), p. 042107. DOI: 10.1103/PhysRevE.91.042107 (cit. on pp. 153, 154).

[256] E. Perrin et al. “Fast and exact synthesis for 1-D fractional Brownian motion and fractional Gaussian noises”. In: *IEEE Signal Processing Letters* 9.11 (2002), pp. 382–384. DOI: 10.1109/LSP.2002.805311 (cit. on p. 177).

[257] I. S. Gradshteyn et al. *Table of integrals, series, and products*. Amsterdam: Academic Press, 2015. DOI: 0123849330 (cit. on p. 198).